MASARYK UNIVERSITY

FACULTY OF SCIENCE

DEPARTMENT OF CHEMISTRY

LASER-MATTER INTERACTION AS A KEY PROCESS FOR SAMPLING BY LASER ABLATION

HABILITATION THESIS

MARKÉTA HOLÁ

BRNO 2024

Science and everyday life cannot and should not be separated.

Rosalind Elsie Franklin

ACKNOWLEDGEMENTS

At this point, I would like to thank those who made this habilitation thesis possible. I would like to start with my family, as they occupy a central position in my life. Family may seem like an obstacle to many in a scientific career, but on the other hand, it can be a great asset. My family taught me to solve unexpected problems immediately, manage time, and work efficiently. They also taught me patience and how to find joy in seemingly small and insignificant moments in life. I thank my husband, David, who has always been and will always be my support; my children, Monika and Šimon, who constantly teach me what is important in life. I thank my parents for the care they gave me and unwavering belief in me. My dad, who is unfortunately no longer here, would be extremely proud of me. I must also mention our dog, Dusty, a constant reminder that every day can be filled with happiness, yet also with responsibility for others.

The fact that I have reached this point in my scientific career is mainly due to my colleagues at the Masaryk University, whom I consider to be my second family. I am particularly grateful to prof. Viktor Kanický, who was and is a great role model for me both in terms of science and humanity. I am grateful to prof. Vítězslav Otruba, an excellent scientist and the supervisor of my diploma and doctoral theses. Special thanks go to my long-time colleague and friend, Tomáš Vaculovič, who is a great support for me every day. I thank my other colleagues, Karel Novotný and Aleš Hrdlička, who constantly surprise me with their patience and composure in solving problems. I also thank other colleagues, Lucie Šimoníková, Michaela Kuchynka, Veronika Faltusová and others. I would like to thank my colleague Jakub Ondráček form CAS for devoting his time to unconventional connection of aerosol devices and laser ablation.

Sport forms an integral part of my life, providing physical and mental balance. I am grateful to my friends, many of whom are also colleagues, for creating an environment that fosters sporting achievements and life-enriching experiences. Their support motivates me to train, especially for our cycling adventures.

ABSTRACT

This habilitation thesis contains 12 related publications, all focused on the use of laser ablation as a sampling method for inductively coupled plasma mass spectrometry. It presents the range of applications for laser ablation inductively coupled plasma mass spectrometry (LA-ICP-MS) technique and provides a detailed analysis of laser ablation parameters and their influence on laser-matter interaction and subsequent aerosol formation. The quality of this aerosol is crucial for the accuracy and precision of the analysis. Parameters such as wavelength, laser pulse duration, fluence or choice of ablation mode are discussed. The thesis also highlights the significance of the sample's physical, chemical, and surface properties. Additionally, it discusses various methods for studying the processes that occur during the interaction of the laser pulse with the sample. These methods include the study of ablation craters, the characterization of the generated aerosol, in particular the determination of the particle size distribution and the time-resolved signal processing of the monitored isotopes.

CONTENT

1 Introduction

Inductively coupled plasma mass spectrometry (ICP-MS) is a widespread method in inorganic analysis allowing the determination of elements in trace and ultra-trace concentrations. It is also popular for the possibility of accurate determination of isotope ratios, which are used, for example, in geochronology, bioarchaeology, food science, biology, ecology, etc. In a typical arrangement, samples in liquid form are introduced into the ICP-MS spectrometer. This is advantageous for initially liquid samples, such as water. However, for solid samples, this necessitates a preceding digestion process, limiting the analysis to the determination of the bulk content of analytes. Laser ablation (LA) offers an alternative sampling method, expanding the application of ICP-MS to localised analysis of very small areas on solid samples without prior digestion.

Sampling by laser ablation operates on the principle of laser pulse interaction with the sample surface, removing part of the material which is then transported by carrier gas to the inductively coupled plasma. The extent and nature of this interaction are influenced by both the conditions of the laser ablation and the sample's properties. Numerous variables can be adjusted, including the optimization of laser parameters, the selection of the ablation cell, the flow rate and type of carrier gas, or the modification of the sample surface.

Understanding the process of laser-matter interaction enables control over various process variables. These include efficient coupling of the laser beam to the sample, reproducible ablation, control of the volume of material removed, minimization of preferential ablation, achievement of stoichiometric ablation, and control over the size distribution of laser-generated particles. Gaining an overview of the complexity of laser ablation process is extremely beneficial for optimizing the sampling conditions and the processing of the measured data, opening the way to obtain accurate and precise results using the LA-ICP-MS technique.

1.1 Structure of the thesis

This habilitation thesis is a collection of 12 papers that deal with the fundamental study of the laser beam interaction with the surface of a solid sample, and its consequences for the formation of an aerosol suitable for dosing into ICP-MS. The papers have been produced continuously throughout my scientific career, reflecting my enduring interest in this area. It aims to consolidate essential knowledge about laser ablation sampling and its various applications, while also investigating the parameters that influence the ablation process. Seemingly minor insights can contribute significantly to our understanding of the physical and chemical processes involved in using a laser as a sampling tool for mass spectrometry.

The initial sections of this work provide a comprehensive overview of laser ablation sampling, detailing its fundamental principles and potential applications [1-3]. The core of this thesis is devoted to examining specific aspects that influence the ablation process, including the laser wavelength [4], pulse duration [4], pulse energy [5, 6], ablation mode [7, 8], as well as the matrix [8-11] and surface properties of the sample [5, 6, 12]. To facilitate understanding of these core topics, the thesis also includes a summary of techniques used to diagnose the interaction processes between laser radiation and the sample. This involves detailed characterization of ablation craters [5-11], analysis of the aerosol generated by laser ablation [4-12], and the processing of LA-ICP-MS signals [1-8, 11, 12].

This habilitation thesis not only collects a range of research findings but also places them in a wider scientific context, including references to the work of other research groups dealing with similar research topics. The primary focus of this work is on nanosecond laser ablation, in accordance with the capabilities of our laboratory, thus representing a specific subsection of the extensive domain of LA-ICP-MS.

For clarity and easy orientation in cited works, my contributions selected for the habilitation thesis are listed as the first 12 publications and are highlighted in blue and bold within the text.

1.2 Summary of publications used in the thesis

So far, I have published 47 papers (according to the WOS database), 42 of which are in peer-reviewed journals and 5 in conference proceedings. Among these 42 publications, I am the main or corresponding author for 15 of them. Due to the focus of my habilitation thesis, I have selected 12 publications and provide an overview that summarizes my contributions to them. This summary pays particular attention to aspects such as experimental work, student supervision, manuscript preparation, and research direction.

1. Wertich, V.*, Kubeš, M., Leichmann, J., **Holá, M.**, Haifler, J., Mozola, J., Hršelová, P., Jaroš, M., Trace element signatures of uraninite controlled by fluid-rock interactions: A case study from the Eastern Moldanubicum (Bohemian Massif), *Journal of Geochemical Exploration*. 2022, 243, 107111. *DOI 10.1016/j.gexplo.2022.107111* (IF 3.9)
Contribution: Experimental work, evaluation of data, participation in manuscript writing
(Experimental work 30 %, Supervision 10 %, Manuscript 20 %, Research direction 20 %)

2. Holá, M., Kalvoda, J.*, Nováková, H., Škoda, R., Kanický, Possibilities of LA-ICP-MS technique for the spatial elemental analysis of the recent fish scales: Line scan vs. depth profiling, *Applied Surface Science*. 2011, 257(6), 1932-1940. *DOI 10.1016/j.apsusc.2010.09.029* (IF 6.7)
Contribution: Design of experiments, experimental work, evaluation of data, participation in manuscript writing
(Experimental work 50 %, Supervision 60 %, Manuscript 40 %, Research direction 30 %)

3. Holá, M., Novotný, K.*, Dobeš, J., Krempl, I., Wertich, V., Mozola, J., Kubeš, M., Faltusová, V., Leichmann, J., Kanický, Dual imaging of uranium ore by Laser Ablation Inductively Coupled Plasma Mass Spectrometry and Laser Induced Breakdown Spectroscopy, *Spectrochim. Acta B*. 2021, 186, 106312. *DOI 10.1016/j.sab.2021.106312* (IF 3.3)
Contribution: Design of experiments, experimental work, evaluation of data, participation in manuscript writing
(Experimental work 30 %, Supervision 50 %, Manuscript 30 %, Research direction 50 %)

4. Možná, V., Pisonero, J.*, **Holá, M.**, Kanický, V., Günther, D., Quantitative analysis of Fe-based samples using ultraviolet nanosecond and femtosecond laser ablation-ICP-MS, *J. Anal. At. Spectrom.* 2006, 21(11), 1194–1201. *DOI 10.1039/b606988f* (IF 3.4)
Contribution: Supervision, consultation, participation in manuscript writing
(Experimental work -, Supervision 30 %, Manuscript 15 %, Research direction 20 %)

5. Holá, M., Salajková, Z., Hrdlička, A., Pořízka, P., Novotný, K., Čelko, L., Šperka, P., Prochazka, D., Novotný, J., Modlitbová, P., Kanický, Kaiser, J., Feasibility of Nanoparticle-Enhanced Laser Ablation Inductively Coupled Plasma Mass Spectrometry. *Anal. Chem.* 2018, 90(20), 11820–11826. *DOI 10.1021/acs.analchem.8b01197* (IF 7.4)
Contribution: Design of experiments, experimental work, evaluation of data, manuscript writing
(Experimental work 50 %, Supervision 60 %, Manuscript 80 %, Research direction 70 %)

6. Salajková, Z.*, **Holá, M.**, Prochazka, D., Ondráček, J., Pavliňák, D., Čelko, L., Gregar, F., Šperka, P., Pořízka, P., Kanický, De Giacomo, A., Kaiser, J., Influence of sample surface topography on laser ablation process, *Talanta.* 2021, 222, 121512. *DOI 10.1016/j.talanta.2020.121512* (IF 6.1)
Contribution: Design of experiments, experimental work, evaluation of data, manuscript writing
(Experimental work 40 %, Supervision 60 %, Manuscript 80 %, Research direction 80 %)

7. Nováková, H., **Holá, M.***, Vojtíšek-Lom, M., Ondráček, J., Kanický, V., Online monitoring of nanoparticles formed during nanosecond laser ablation, *Spectrochim. Acta B*. 2016, 125, 52–60. *DOI 10.1016/j.sab.2016.09.017* (IF 3.3)
Contribution: Design of experiments, experimental work, evaluation of data, manuscript writing
(Experimental work 50 %, Supervision 80 %, Manuscript 70 %, Research direction 90 %)

8. Holá, M.*, Ondráček, J., Nováková, H., Vojtíšek-Lom, M., Hadravová, R., Kanický, V., The influence of material properties on highly time resolved particle formation for nanosecond laser ablation, *Spectrochim. Acta B*. 2018, 148, 193–204, *DOI 10.1016/j.sab.2018.07.001* (IF 3.3)
Contribution: Design of experiments, experimental work, evaluation of data, manuscript writing
(Experimental work 60 %, Supervision 80 %, Manuscript 80 %, Research direction 90 %)

9. Holá, M.*, Konečná, V., Mikuška, P., Kaiser, J., Kanický, V., Influence of physical properties and chemical composition of sample on formation of aerosol particles generated by nanosecond laser ablation at 213 nm, *Spectrochim. Acta B*. 2010, 65(1), 51–60. *DOI 10.1016/j.sab.2009.11.003* (IF 3.3)
Contribution: Design of experiments, experimental work, evaluation of data, manuscript writing
(Experimental work 60 %, Supervision 80 %, Manuscript 80 %, Research direction 90 %)

10. Holá, M.*, Konečná, V., Mikuška, P., Kaiser, J.*, Páleníková, K., Průša, S., Hanzlíková, R., Kanický, V., Study of aerosols generated by 213 nm laser ablation of cobalt-cemented hard metals, *J. Anal. At. Spectrom.* 2008, 23(10), 1341–1349. *DOI 10.1039/B802906G* (IF 3.4)
Contribution: Design of experiments, experimental work, evaluation of data, manuscript writing
(Experimental work 60 %, Supervision 80 %, Manuscript 80 %, Research direction 90 %)

11. Holá, M.*, Mikuška, P., Hanzlíková, R., Kaiser, J., Kanický, V., Tungsten carbide precursors as an example for influence of a binder on the particle formation in the nanosecond laser ablation of powdered materials, *Talanta.* 2010, 80(5), 1862–1867. *DOI 10.1016/j.talanta.2009.10.035* (IF 6.1)
Contribution: Design of experiments, experimental work, evaluation of data, manuscript writing
(Experimental work 70 %, Supervision 80 %, Manuscript 80 %, Research direction 80 %)

12. Holá, M., Salajková, Z., Hrdlička, A.*, M., Ondráček, J., Novotný, K., Pavliňák, D., Vojtíšek-Lom, M., Čelko, L., Pořízka, P., Kanický, V., Prochazka, D., Novotný, J., Kaiser, J., The effect of nanoparticle presence on aerosol formation during nanoparticle-enhanced laser ablation inductively coupled plasma mass spectrometry, *J. Anal. At. Spectrom.* 2020, 35(12), 2893-2900. *DOI 10.1039/d0ja00324g* (IF 3.4)
Contribution: Design of experiments, experimental work, evaluation of data, manuscript writing
(Experimental work 50 %, Supervision 50 %, Manuscript 80 %, Research direction 90 %)

2 Laser ablation

2.1 A sampling tool for ICP-MS

Laser ablation, as an alternative sampling technique for Inductively Coupled Plasma Mass Spectrometry, finds applications across a wide range of scientific fields. Its basic principle involves irradiating the sample with a laser to induce an ablation process, resulting in the removal of a small amount of material. This ablated material is then transported to the inductively coupled plasma (ICP), where it is vaporized, atomized, and ionized. The resulting ions are subsequently analysed and detected in a mass spectrometer and signal of individual isotopes is recorded [13, 14]. Different approaches to sample analysis can be taken depending on the specific analytical requirements. According to the Web of Science database, most applications are related to the geological sciences, with 12,500 out of a total of 17,000 articles pertaining to the geological applications of LA-ICP-MS.

One such approach is *spot ablation*, where the pulsed laser repeatedly removes material from a single spot. It's essential to monitor data consistency of the time-resolved LA-ICP-MS signal: any sharp drop or rise in the value of the observed isotope may indicate the presence of an impurity or inhomogeneity, potentially biasing the results. **Figure 1** presents an example of a time-resolved signal for isotopes measured in an uraninite mineral sample, achieved using a nanosecond (ns) laser with a wavelength of 213 nm, a beam diameter of 50 µm, a fluence of 9 J cm^{-2}, and a laser repetition rate of 10 Hz. The data in **Figure 1a** indicate minimal risk of contamination at the ablation site from fluid or mineral inclusions hidden beneath the surface. Conversely, isotopic records in **Figure 1b** that varies from the described correct isotopic recordings hint at the presence of a mineral or fluid inclusion. Such inclusions would significantly alter the geochemical composition of the measured uraninite, and therefore, the data must be excluded from the overall recorded data set [1].

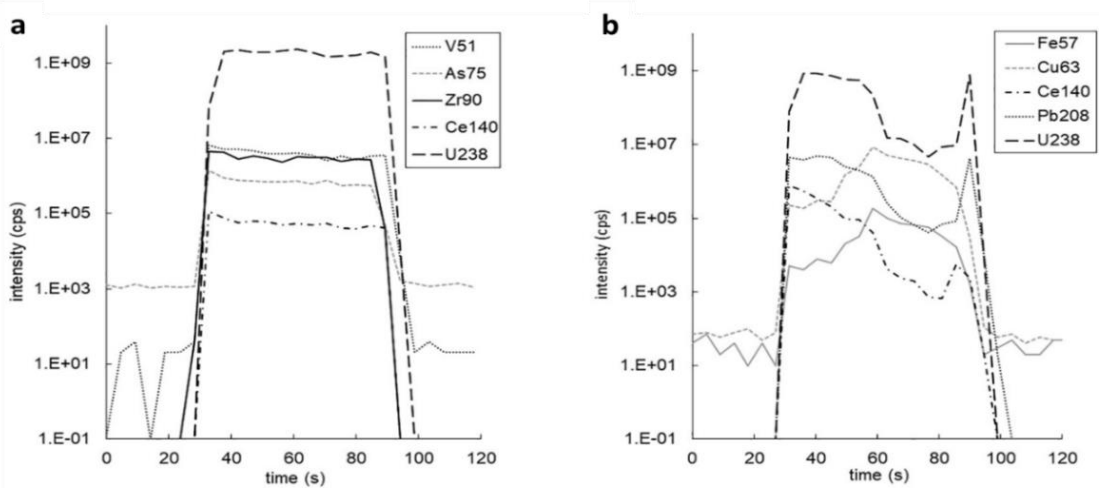

Fig. 1. a) LA-ICP-MS spot analysis record of uraninite displaying the correct shape; and b) record of uraninite spot analysis contaminated by chalcopyrite mineral inclusions hidden beneath the surface [1].

As can be seen from the description of spot ablation, the laser beam gradually penetrates the depth of the analysed sample. This can be advantageously used for monitoring changes in the sample's composition at various depths – termed depth profiling.

Depth profiling is another technique employed in LA-ICP-MS. This method also involves applying laser pulses to a single spot, but instead of targeting just one layer, it monitors the evolution of the sample's composition over time, revealing compositional changes at various depths. By knowing the ablation rate (the amount of material removed per pulse), the thickness of individual layers can be defined [15]. For instance, in metallurgical applications, depth profiling can accurately determine the thickness and composition of layers down to nanometres, particularly when using a femtosecond laser [16]. In natural samples, such as bones and teeth, depth profiling can provide insights into an organism's evolution or exposure to various factors. An example is the study of otoliths, where depth profiling is a microchemical technique revealing life history patterns in fish [17]. Fish scales, as another bony structure, can be similarly analysed, although their complex structure makes this less common. Nevertheless, scale analysis offers a non-lethal approach that is valuable for studying water contamination and migration patterns throughout the life of fish. **Figure 2** shows a dorsal view of the scale structure and the location of the performed LA-ICP-MS analyses [2]. Depth profiling results of the anterior part scales from common carp (Cyprinus carpio) show a concentration gradient of selected elements throughout the scale's thickness, with a clear distinction between the external hydroxyapatite layer and the basal collagen plate (**Figure 3a – 3c**). It was also discovered that the scale surface can accumulate heavy metals, effectively preventing their penetration into the deeper structure (**Figure 3c - 3d**) [2]. Generally, the LA-ICP-MS method ranks among the depth profiling techniques, which have the advantage of simple sample preparation (similar to the technique of Glow discharge spectrometry [18]). In

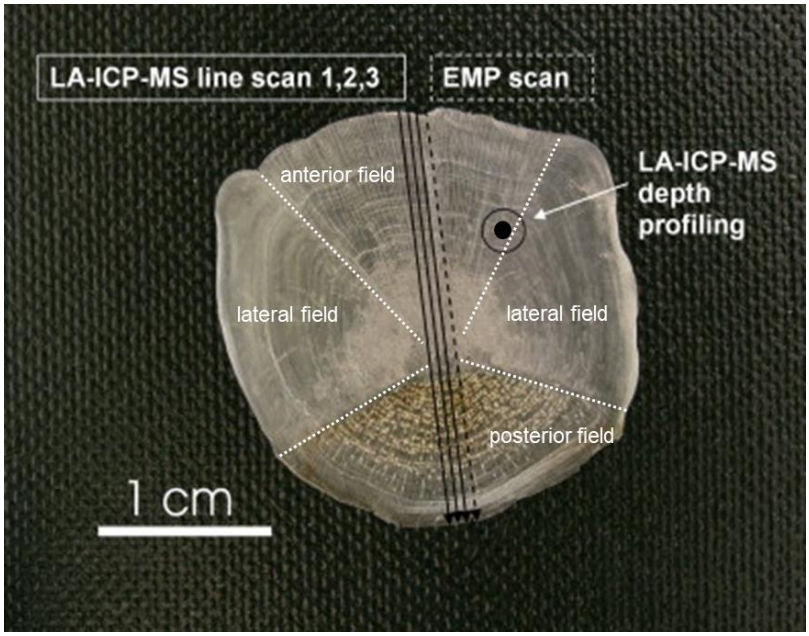

Fig. 2. Dorsal view of the fish scale of the common carp with marked posterior and anterior part. The anterior part, divided in the anterior and lateral fields, is covered by other fish scales while the posterior field is in contact with water; Marked trajectories for LA-ICP-MS and EMP analysis [2].

contrast, commonly used microscopic methods require a cross-section to be made first, which can be technically and time-consuming.

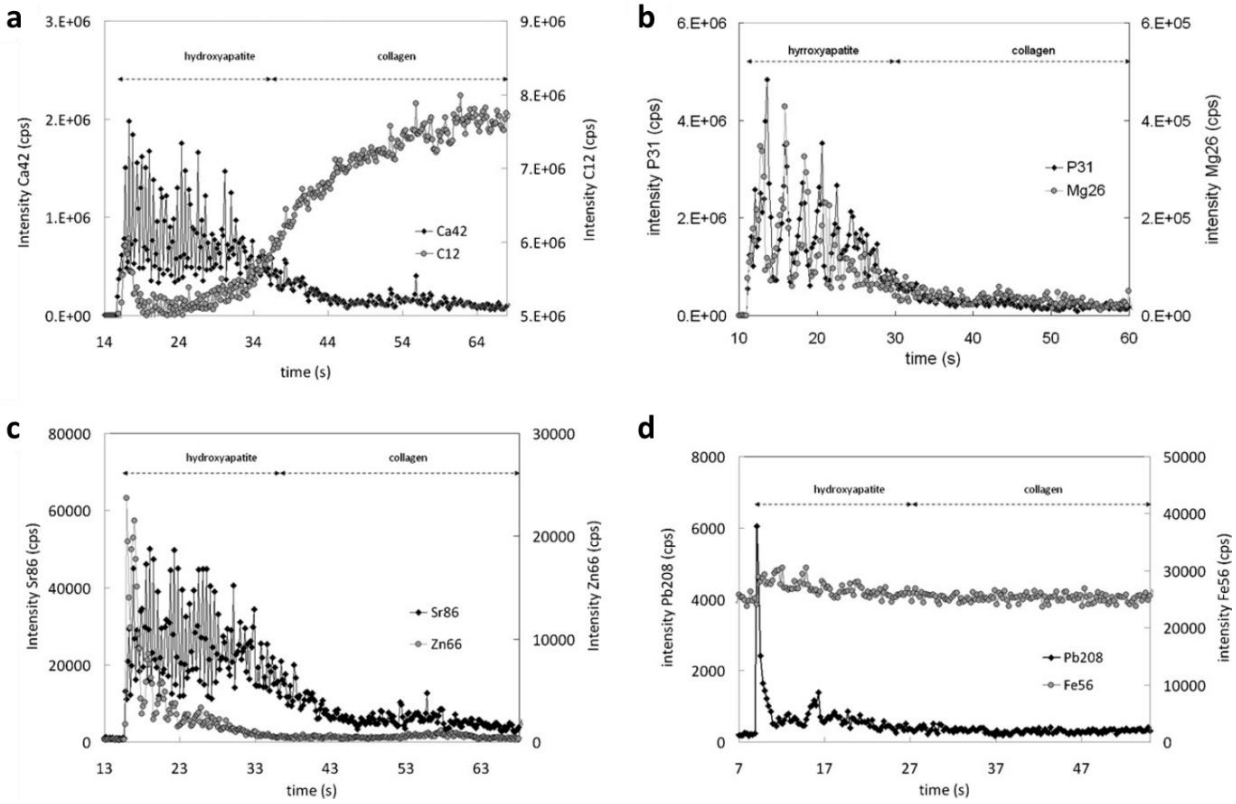

Fig. 3. LA-ICP-MS depth profiling on the posterior part of the fish scale (common carp) for following pairs of isotopes: a) ^{42}Ca and ^{12}C; b) ^{31}P and ^{26}Mg; c) ^{86}Sr and ^{66}Zn; d) ^{208}Pb and ^{56}Fe. Laser wavelength of 213 nm, 100 µm spot size, repetition rate of 4 Hz, fluence of 3.5 J cm^{-2} [2].

The application of a specific number of pulses to one spot allows for the determination of either the average composition of a sample or its depth profile. An alternative approach involves performing a *linear scan* across a selected part of the sample. This technique serves various purposes: it can determine the average composition of a larger sample area, such as a specific zone [19], or it can be employed to identify variations in element distribution across different zones. This is particularly beneficial for tasks like determining mineral zonation [20], assessing element concentrations in growth lines (such as tree rings [21], otoliths [22], urinary stones [23], etc.), detecting impurities or heterogeneities in industrial products [24, 25], defining archaeological artefacts [26] or other analyses. The parameters defining a linear scan are similar to those for spot ablation: spot size, number of pulses, repetition rate and fluence. A key additional parameter is the scan speed. This speed, combined with the other parameters, dictates the degree of pulse overlap, spatial resolution, and the overall duration of the analysis.

The use of line scans in LA-ICP-MS provides valuable insights, again, with fish scale analysis serving as a pertinent example [2]. Performing a line scan across the entire fish scale, perpendicular to the growth rings as illustrated in **Figure 2**, enables analysis of both the anterior

part, which is covered by other scales, and the posterior part, which is in direct contact with the water. This type of analysis, as detailed in **Table 1**, reveals a distinct distribution of elements in the two regions.

Specifically, certain trace metals like Zn and Mn, as well as matrix elements such as Ca and P, and predominant cation substituents like Mg and Sr, were found to be more concentrated in the posterior part. This discrepancy is largely attributed to the higher prevalence of the mineral phase in the posterior region, which facilitates increased substitution and vacancy filling. Additionally, certain trace metal elements, namely Fe and Pb, exhibited symmetrical distributions with elevated levels near the scale's periphery. Such patterns likely reflect variations in diet or environmental pollution exposures over time.

Table 1 LA-ICP-MS line scan analysis of fish scale; average values for each region [2].

Isotope	Concentration ($\mu g g^{-1}$)								
	Line scan 1			Line scan 2			Line scan 3		
	Whole scale	Anterior part	Posterior part	Whole scale	Anterior part	Posterior part	Whole scale	Anterior part	Posterior part
^{26}Mg	5160	4410	6440	5170	4560	6160	5460	4780	6550
^{31}P	136,000	131,000	145,000	142,000	137,000	150,000	138,000	134,000	145,000
^{42}Ca	244,000	234,000	259,000	243,000	233,000	259,000	244,000	234,000	260,000
^{55}Mn	33.9	28.4	43.4	34.5	28.7	44.0	34.2	28.1	44.2
^{56}Fe	10.1	7.82	14.0	8.65	6.45	12.2	4.67	4.91	4.27
^{66}Zn	564	412	827	630	467	892	539	398	770
^{86}Sr	276	249	323	283	262	316	294	271	331
^{208}Pb	0.565	0.563	0.566	0.577	0.606	0.530	0.675	0.677	0.670

The application of multiple line scans covering selected area of a sample is used for the *imaging method*. In this approach, a specified area on the sample surface is scanned using parallel lines, where the combination of spot size, line spacing, scan speed, and repetition rate defines the spatial resolution of the resulting elemental/isotopic maps and the time of analysis. However, producing a high-quality image is not without challenges. Common artifacts like blur, smear, aliasing, and noise can compromise the integrity of the image. Various studies and techniques have been developed to reduce or eliminate these undesired effects, ensuring clearer and more accurate visual representations of elemental distributions [27].

Detailed imaging with LA-ICP-MS is very popular for biological applications [28, 29], characterization of steels [30, 31] or alloys [32], archaeology [33], geological applications [34, 35], and others. An example is the analysis in the uraninite mineral zone [3]. A specific area of 2 × 3 mm was methodically analysed using a 213 nm laser. For the line scans, parameters such as a 20 µm spot diameter, a scan speed of 20 µm s^{-1}, a 10 Hz repetition rate, and a fluence of 10 J cm^{-2} were chosen, achieving a spatial resolution of 20 µm. The scan rate of 20 µm s^{-1} was purposely chosen to match the dwell time (1 s) to the time required to traverse the diameter of the ablation crater (20 µm), effectively preventing any smearing of the LA-Q-ICP-MS signal along the x-axis.

The visualization of individual isotopes offers invaluable insights, particularly evident when examining lead isotopes. Lead presents an interesting isotopic spectrum, with non-radiogenic ^{204}Pb coexisting with radiogenic isotopes of ^{206}Pb and ^{207}Pb, which originate from the decay of

^{238}U and ^{235}U respectively. Additionally, ^{208}Pb is a product of ^{232}Th's radiogenic decay. Non-radiogenic lead ^{204}Pb is not related exclusively to the structure of uraninite but also forms isolated clusters, likely as compounds with sulphur or selenium, while radiogenic isotopes of lead also copy their parent nuclides. Therefore, the most abundant and homogeneous is represented by the isotope ^{206}Pb as the decay product of the isotope ^{238}U (relative abundance of 99.274%), which is the main component of uraninite. The heterogenous distribution of ^{207}Pb and even more apparently ^{208}Pb within uraninite aggregates, considered to have originated in one-time period, is worth mentioning due to usage of lead isotope ratios for radiometric dating. In this context, intra-grain scale isotopic variations within fresh uraninite aggregates, showing no visible effect of post-crystallization alteration. All isotopic maps are presented in **Figure 4**.

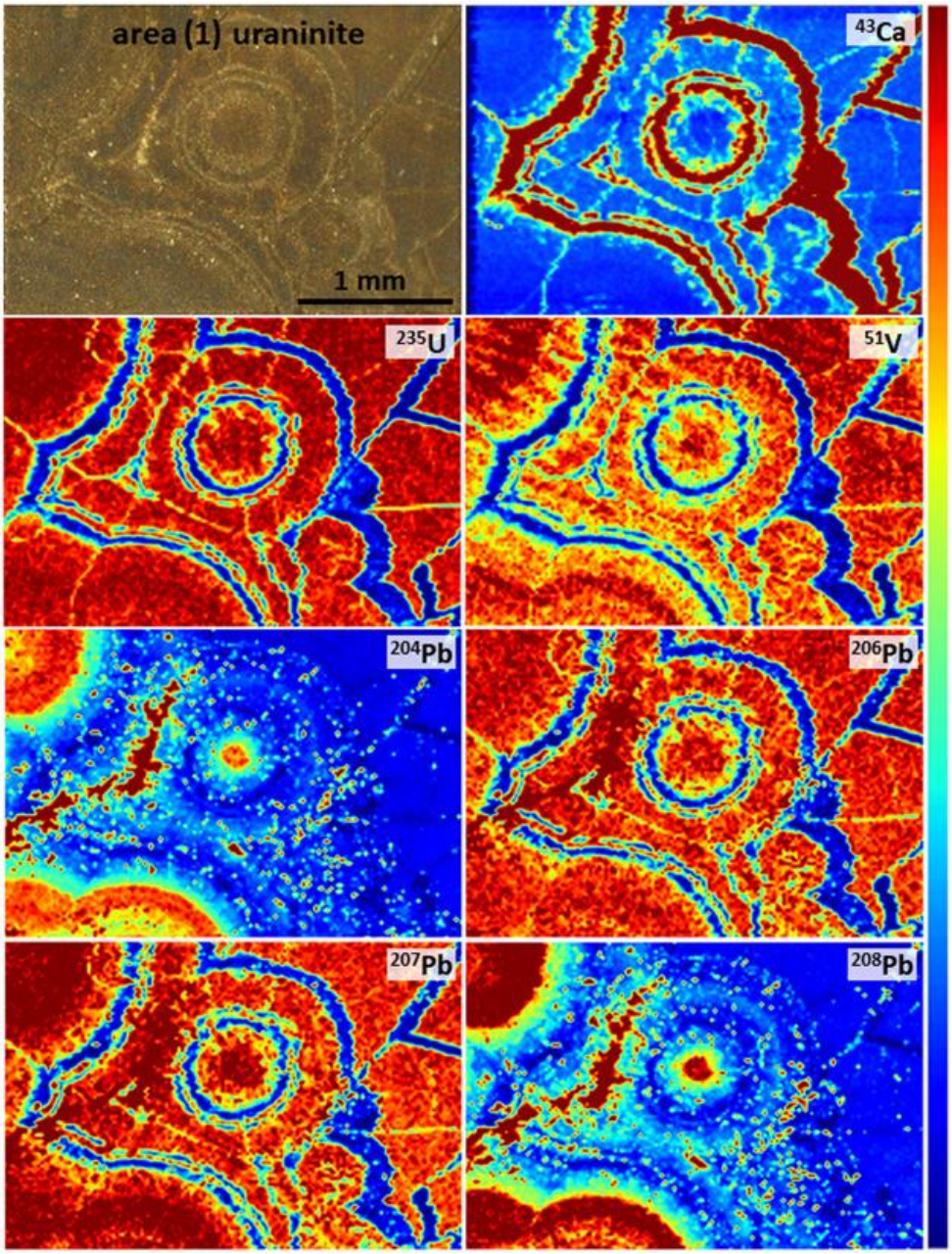

Fig. 4. Photography of analysed sample area (1) and distribution of selected isotopes in uraninite obtained by LA-ICP-MS. Normalised intensities in cps, blue colour as minimum, red as maximum [3].

2.2 If laser ablation were the ideal sampling method...

Laser ablation, as an alternative sampling technique for ICP-MS, offers numerous benefits over the conventional nebulization of liquid samples. This technique provides many significant advantages, making it an ideal tool for accurate and efficient material analysis. The most notable advantage is the minimization of sample preparation requirements. Because laser ablation allows for direct sampling of solid samples into ICP-MS, the need to convert samples into solution is eliminated. This significantly saves time, as complex preparation processes are replaced by almost instantaneous analysis. Furthermore, it eliminates the need for chemicals, making the process more efficient while reducing the risk of contamination or sample loss during preparation. Moreover, the focused laser beam permits highly localised and spatially resolved analyses, enabling detailed examination of sample heterogeneity on a microscopic scale. Additionally, the combination of laser ablation and ICP-MS is conservative in terms of sample usage, consuming only a minimal quantity of material. This aspect is crucial when dealing with rare or limited samples. In an ideal scenario, the material released by laser pulses accurately reflects the composition of the original sample.

In summary, under ideal conditions, laser ablation serves as a unique, rapid, efficient, and highly accurate method for analysing a wide range of materials for scientific and industrial purposes. However, achieving these ideal conditions is not straightforward, and LA-ICP-MS analysis is usually complicated by factors such as fractionation or matrix effects.

2.3 Fractionation

In fact, the laser-matter interaction is a complex process depending on both the laser ablation conditions (pulse duration, wavelength, repetition rate, pulse energy, spot size) and the sample's physical and chemical properties [4, 8, 9, 11, 36, 37]. Generally, the laser beam can interact with the material in two basic ways – thermal (photothermal) and non-thermal (photochemical) [38, 39]. For longer pulses (nanosecond ablation), heat conduction, melting, evaporation, and plasma formation are the dominant processes. The energy of the laser is absorbed by the sample surface and forms a temperature field due to the heat conduction. Depending on the achieved temperature, the material melts, evaporates, or is transferred to a plasma state. Laser ablation parameters, especially pulse duration and pulse energy, affect the proportionality of evaporation and sputtering of the melt as the main processes of nanosecond laser ablation [40]. The physical and chemical properties of the sample can significantly influence the laser energy absorption (absorption coefficient for the specific wavelength), the heat transfer (thermal conductivity) [8, 9, 41, 42] and degree of plasma shielding (attenuation of the incoming laser radiation by plasma). On the other hand, the sample heating by the laser irradiation significantly modifies the optical and thermo-physical properties, such as surface reflectivity, electrical and thermal conductivity, surface tension, and latent heat of vaporization [43]. Thermal and non-thermal processes create

particles of the sampled aerosol by different principles; therefore, their size distribution and composition differ (a more detailed description of the mechanism of particle formation is described in Chapter 3.5). The particle size is important due to the transportation efficiency and its impact on vaporization, atomization, and ionization efficiency within the ICP. This insight is key to understanding possible non-stoichiometric sampling, so-called fractionation.

In the context of argon ICP, which operates as an atmospheric pressure ion source, the process of laser ablation sampling is likewise conducted in an environment of atmospheric pressure of an ambient gas. In such a setting, the formation of the plasma generated by the laser at the site of ablation is confined to a small volume, typically just a few cubic millimetres. Subsequent expansion leads to material redeposition onto the sample substrate post the laser pulse. Additionally, factors such as transport losses and the condensation of the plasma plume on the ablation cell sidewalls or on sputtered particles can lead to a reduction in the efficiency of ablation. These aspects can potentially alter the yield of the ablation process and affect the accuracy of the elemental concentrations measured.

LA-ICP-MS is a time-resolved method that provides a transient signal corresponding to the ablation conditions in terms of time. For spot ablation, it depends on the number of pulses applied, i.e., the first pulse on an intact sample surface will not provide the same analytical signal as a pulse generated after many repetitions. Here, thermal effects, melting of a thin layer of the sample, which can be gradually depleted of more volatile components, and deepening of the crater (higher aspect ratio) play a role. Fractionation during analysis can be quantified using the Fractionation Index (FI). The FI is given by the intensity of any element rationed to an "internal standard" from the second half of the signal, divided by its intensity ratio during the first half of the signal [44]. An example of FI calculations for 43 elements contained in the glass standard SRM NIST610 for different laser wavelengths is shown in Chapter 3.1 in **Figure 9** [45].

2.4 How to diagnose the laser-sample interaction?

To obtain high quality analytical results by LA-ICP-MS, it is very important to ensure controlled sampling by laser ablation into the ICP mass spectrometer. Because the laser beam is focused on a very small area (tens to thousands of square μm), and the sample is placed in a closed chamber, monitoring the quality of laser ablation using conventional laser system equipment is very difficult. A microscope camera, which is part of the ablation system, is used for the basic assessment of the ablation process. This can detect undesirable phenomena such as breakage, cracking or crumbling of the sample, or, conversely, resistance to the laser beam used. For a detailed diagnosis of the sampling process, other procedures must be used typically based on:

- Characterization of the ablation crater
- Characterization of the generated aerosol
- Processing of the time-resolved ICP-MS signal

2.4.1 Characterization of the ablation crater

The depth, shape, structure, and chemical composition of an ablation crater are key indicators of the laser-matter interaction. Analysing these parameters can precisely define the processes involved and serve as a benchmark for 'correct' sampling with laser pulses. However, the disadvantage of using craters to diagnose ablation processes is that they are assessed offline after the analysis, usually once the sample has been removed from the ablation chamber. Consequently, any adjustments to conditions for improved sampling are implemented only after an analysis has 'failed'.

A more stable analytical signal is produced with smaller values of the crater aspect ratio (depth/diameter), ideally less than 1. At higher values (>5), there is ineffective removal of material from the crater's base, resulting in a sharp decline in the time signal [46]. Factors such as the number of pulses and fluence used can influence the resultant crater depth, which also varies depending on the sample material. Insights into the behaviour of the ablation process can be gleaned from the shape, structure, and volume of the ablation crater. This allows for estimations of the ablation rate, the degree of sample melting, or the extent of reverse condensation of evaporated material. The amount of material released during laser ablation can be specified from the ablation crater volume, relative to the amount of material remaining around the crater as a rim.

For basic diagnostics, ablation craters are typically first visualised using an optical or scanning electron microscope (SEM). The microscope images enable the detection of undesired effects such as cracking or large fragments being dislodged from the sample and allow for an estimation of the melting extent around the crater area. The next stage involves determining the precise shape and volume of the ablation crater, usually using profilometric methods, either based on the mechanical principle or more often on the optical basis. Consider **Figure 5**, where laser ablation was executed using a ns laser at 213 nm under the following conditions: a laser spot diameter of 100 μm, a fluence of 13 J cm^{-2} and a repetition rate of 10 Hz [9]. **Figure 5** illustrates the ablation craters on different materials after 600 pulses. From the SEM images (**Figure 5A1, B1, C1**), it is possible to see the degree of melting of the materials. This is evident especially for steel sample (**Figure A1**) both from the structure of the ablation crater rim and from the presence of large, deposited particles that arise directly from the melt of the sample and are indicative of thermal effects. The optical profilometer provides a 3D model of the craters (**Figure 5A2, B2, C2**) that shows the height of the rim, the character of the crater bottom, and calculates the total volume. The most illustrative view may be a representative cross-section through the crater, where a degree of thermal effects and presumably fractionation effects in LA-ICP-MS analysis can be diagnosed from the elevated crater rim or the molten crater bottom (**Figure 5A3, B3, C3**) [9].

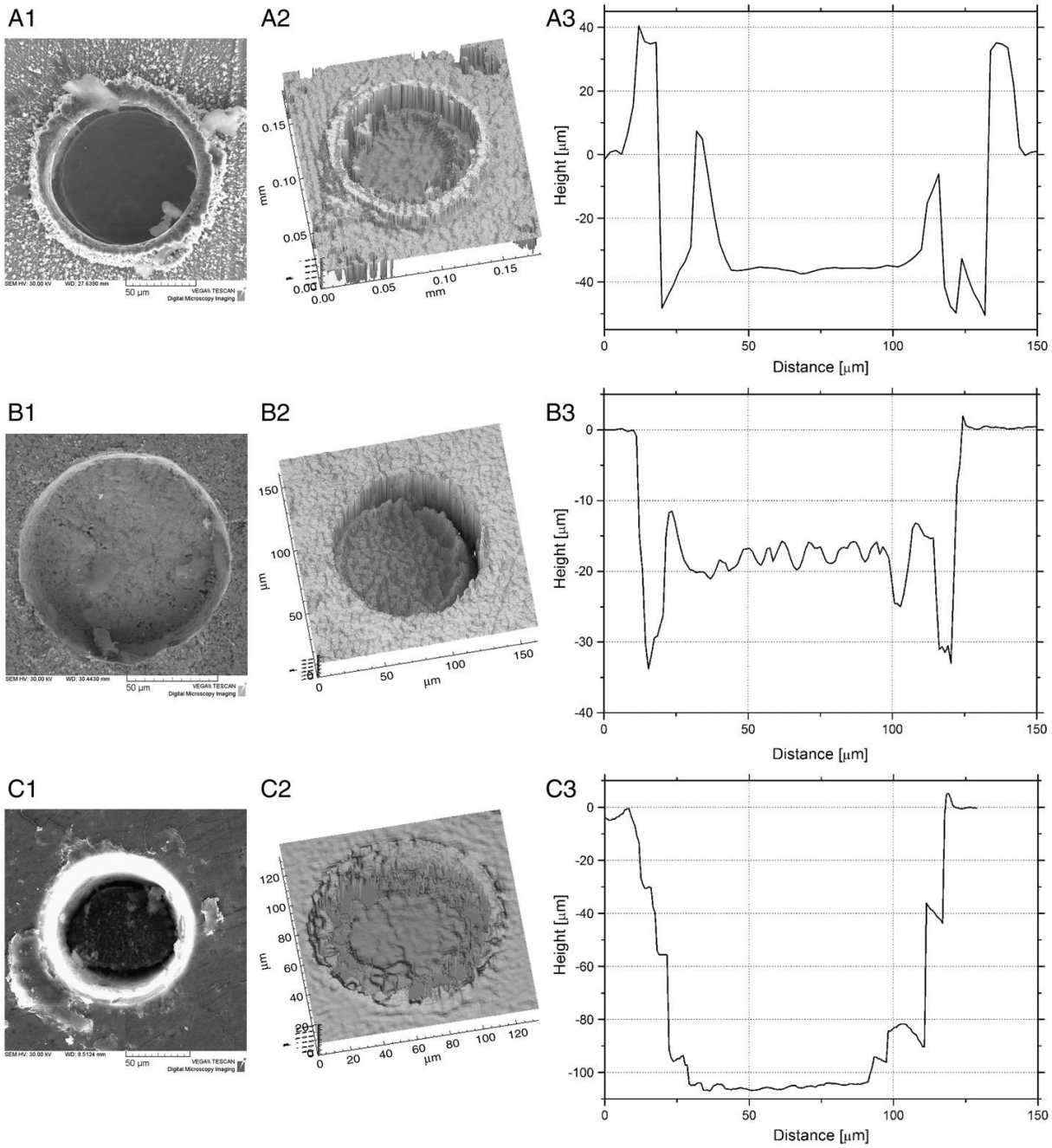

Fig. 5. SEM (1) and optical micrograph (2) of the ablation craters together with a representative cross-section (3) on steel sample (A), tungsten carbide (B) and glass (C) using 213 nm laser ablation [9].

Each material exhibits unique behaviour when sampled using a laser. While its inherent properties remain constant, the variable parameters of laser ablation can be adjusted. These include the size of the ablation crater, the ablation mode, fluence, repetition rate, and the number of applied pulses. In the process of optimizing the LA-ICP-MS method, characterising the ablation crater is a crucial step in identifying the most suitable sampling conditions. The ideal outcome is to achieve a symmetrical ablation crater, cylindrical in shape with a flat bottom, showing no signs of melting, crumbling, or other forms of damage. Under such conditions, an aerosol suitable for analysis by ICP-MS can be produced.

2.4.2 Characterization of the generated aerosol

The quality of generated aerosol is crucial for conducting correct and accurate analyses in LA-ICP-MS. The purpose of laser ablation is to generate particles that match the composition of the sample and are of a size that can be efficiently transported and vaporized in the ICP. Knowledge of particle sizes and their number distribution in laser-generated aerosols is required for a better understanding of non-stoichiometric effects observed with LA-ICP-MS. These effects are commonly encompassed under the term 'fractionation', which is influenced by a variety of factors ranging from the conditions of laser ablation to the effects in the ICP. However, the initial step towards understanding these complex processes is to gather information about the properties of particles generated under specific LA conditions. Subsequently, one can examine changes induced by transport or ICP effects. Since aerosol study is only feasible after particles have exited the ablation cell, the influence of particle transport is invariably included. Nonetheless, theoretical models of particle formation can be developed based on recognized patterns [43].

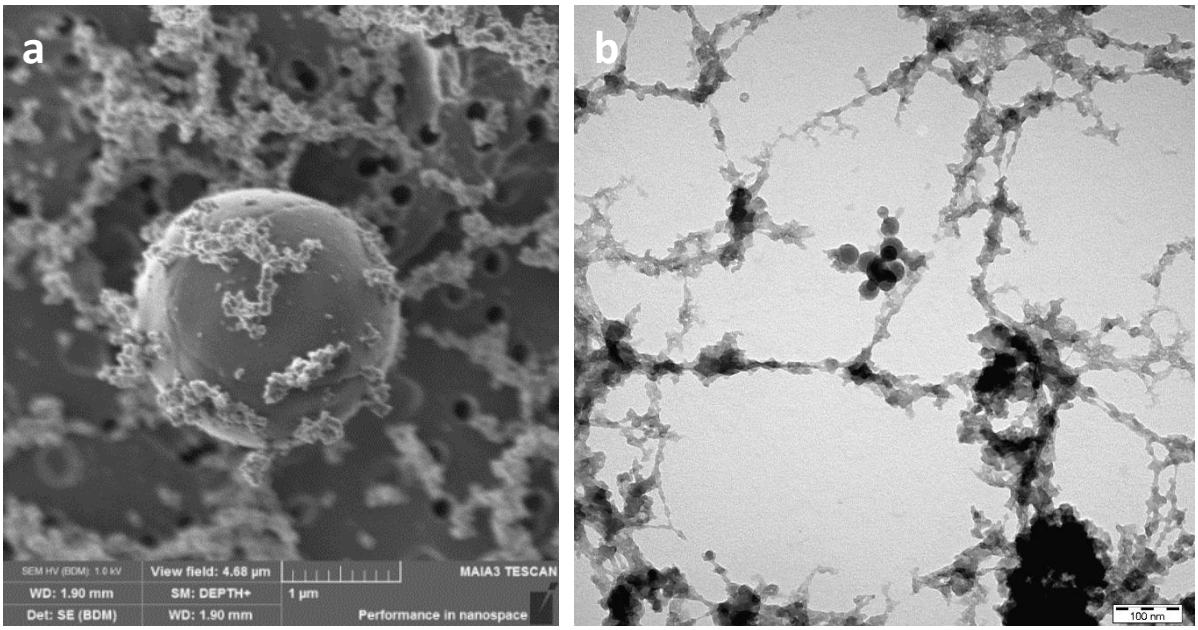

Fig. 6. Visualization of collected LA particles of a) steel sample by SEM; b) glass SRM NIST610 by TEM.

Laser-generated aerosol can be studied via different offline or online techniques. Offline methods involve collecting particles on special filters, grids, or discs for subsequent analysis. The efficiency of sample collection can be enhanced using an electrostatic sampler [47], or by segregating and depositing particles on substrates according to their aerodynamic diameter, such as with a cascade impactor [48, 49]. These offline methods not only allow for visual determination of particle shapes and size via various microscopic methods such as Scanning Electron Microscopy (SEM), Transmission Electron Microscopy (TEM), Electron Probe Micro Analysis (EPMA) but also enable the study of particle composition through subsequent

chemical analysis (ICP-MS, Particle-induced X-ray Emission (PIXE), etc.) of collected material [9, 10, 47, 48, 50, 51]. The particles visualised on the filter and on the grid are shown in **Figure 6a** and **Figure 6b**, respectively.

The stoichiometry of the ablation can be checked by bulk analyses of all particles using a dissolution method. Furthermore, Energy Dispersive X-ray spectroscopy (EDX) enables the acquisition of the composition analysis of specific particles on the filter, which is invaluable for elucidating fractionation processes [10,11,47,51-53]. However, a major limitation of offline methods is the inability to monitor the evolution of particle formation over time; all samples represent the mass accumulated over the entire sampling period.

To characterise particles generated by laser ablation, aerosol spectrometers operating online are also utilised. These devices help mitigate alterations in the aerosol structure that might occur with offline methods, such as filter sampling. Some systems even enable simultaneous measurement of particle size distribution (PSD) and ICP-MS signal at a high time resolution [8]. An example of such an arrangement is presented in **Figure 7**. The selection of an aerosol spectrometer typically depends on the size range of the particles being measured. Nevertheless, it is crucial to consider the detection principle of the spectrometer to prevent misinterpretation of results, especially for non-spherical clusters [49].

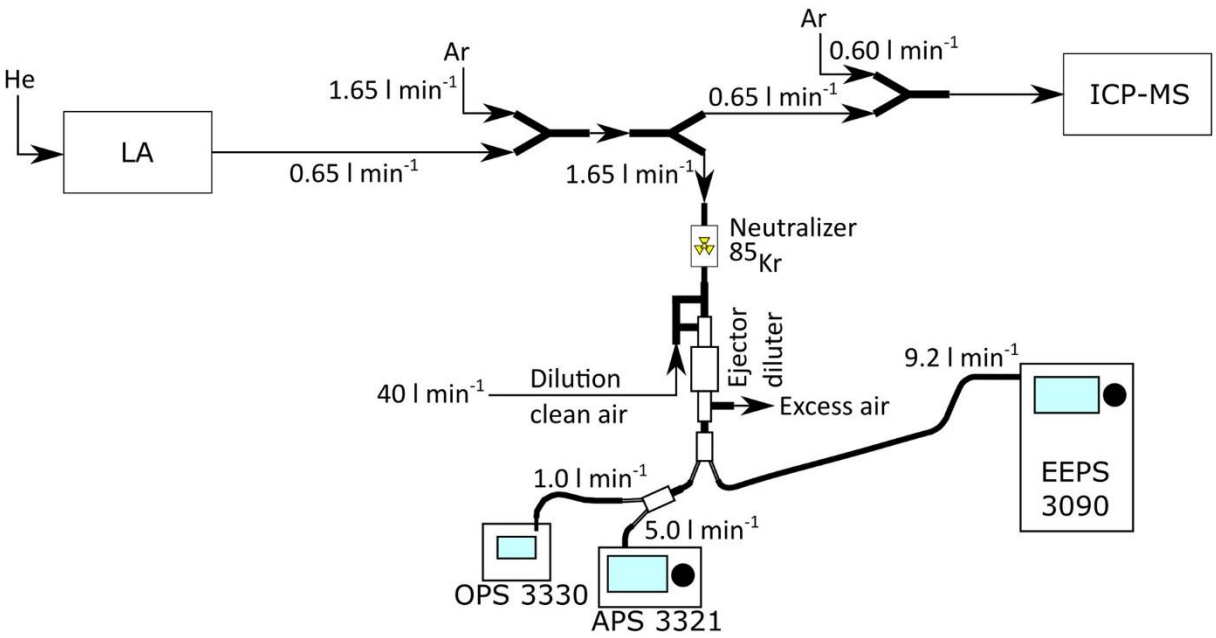

Fig. 7. Schematics of measurement set-up for laser ablation system coupled with ICP-MS and aerosol spectrometers, Engine Exhaust Particle Sizer (EEPS), Aerodynamic particle sizer (APS) and Optical Particle Sizer (OPS) [8].

Various techniques are available for analysing the physical properties of aerosol particles produced during laser ablation. These include electrostatic classifiers with particle detectors

(such as condensation particle counters or electrometers), photometric devices, and cascade impactors for offline analysis. Each instrument offers unique advantages and has certain limitations. For instance, the Scanning Mobility Particle Sizer (SMPS) provides excellent particle sizing resolution but has limitations in time resolution [54, 55]. Fast Mobility Particle Sizers (FMPS or EEPS) deliver high time resolution but have fewer particle size bins and require calibration due to the initial unipolar electrical charging of particles [56]. Photometric devices are user-friendly but heavily rely on the optical properties of the sampled aerosol [57]. Cascade impactors, regarded as a standard for gravimetric analysis, provide limited size resolution and only offer integral values over time (offline analysis) [58].

Different techniques based on various physical principles are used to detect particle concentration, such as Condensation Particle Counters (CPC), Optical Particle Sizers (OPS), Optical Particle Counters (OPC), and electrometers. Particle sizing primarily employs two main principles: mobility in an electrostatic field (Differential Mobility Analyzer (DMA)) [54, 55] and aerodynamic behaviour in accelerated flow (Aerodynamic Particle Sizer (APS)). By integrating particle counters and sizers, a comprehensive aerosol spectrometer can be assembled. The SMPS system is commonly used for submicrometric particle diameters (nanometres to 1 μm) [59, 60], while APS systems measure particles in the 0.5–20 μm range. For processes with rapid changes in particle concentration, the Fast Mobility Particle Sizer (FMPS) combines principles of electrostatic field mobility with concentration detection via electrometers [7, 8, 61].

It is essential to note that different methods for PSD estimation provide complementary data by measuring distinct physical characteristics of particles. For instance, comparing offline impactor techniques with DMA (SMPS) and OPC can reveal different interpretations of agglomerated nanoparticles in laser-generated aerosol. DMA measures physical diameters based on mobility in an electrostatic field and may overestimate the volume-equivalent diameter for porous particles, impacting accurate mass determination. In contrast, OPC assesses particle diameters based on optical equivalent diameter, significantly influenced by the particles' optical properties [57]. If the optical properties of the measured material differ from the calibration standard (typically polystyrene latex spheres), the results can vary significantly, often underestimating the real particle sizes [49]. Therefore, when using any aerosol instrument, the user must be aware of the measurement method employed and consider its advantages and limitations in interpreting the data.

It should also be noted that planning and conducting experiments to measure the size distribution and concentration of laser-generated particles pose significant challenges. This is particularly because the aerosol devices employed are primarily designed for measuring aerosols in air. As a result, the flow rates of the sampled gas, along with the concentration and characteristics of the particles, differ considerably when these devices are adapted for use in laser ablation. These differences necessitate careful consideration and adaptation of

experimental protocols to ensure accurate measurements in the context of laser-generated aerosols. An illustration of the plan and implementation of such an experiment, highlighting these specific challenges and adaptations, is demonstrated in **Figure 8**.

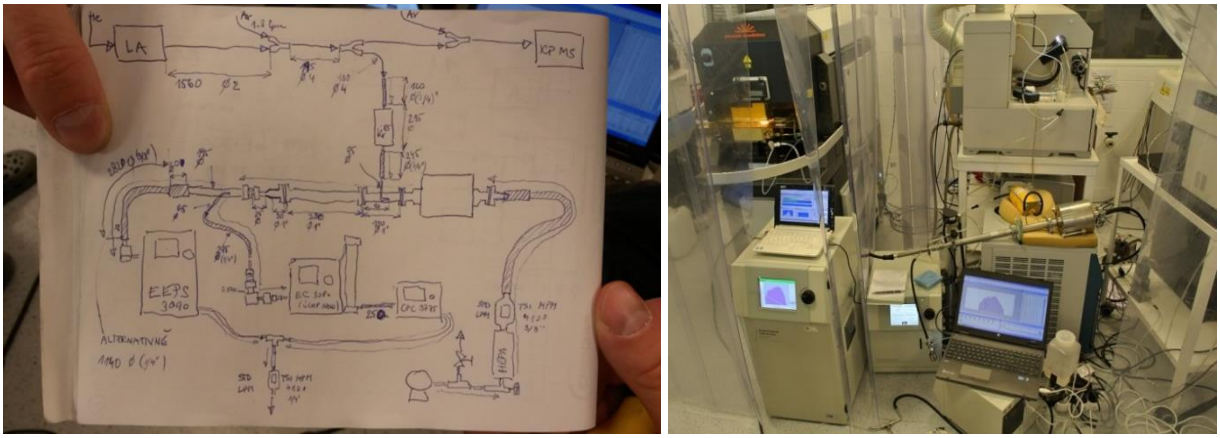

Fig. 8. From experimental planning to implementation - measurement of aerosol properties in the Laboratory of Atomic Spectrochemistry.

2.4.3 Processing of the time-resolved ICP-MS signal

The characteristic of the time-resolved signal of the measured isotope not only mirrors the original composition of the sample but also reflects the effects and changes that occur throughout the LA-ICP-MS measurement process. This includes the interaction of the laser with the sample, the formation of solid particles, their transport, subsequent vaporization, and ionization, as well as the behaviour of these ions in the mass analyser and their detection. Consequently, careful processing of the measured data is crucial for achieving high-quality analytical results.

A detailed analysis of the analytical signal can, for instance, identify the degree of fractionation, as discussed in Chapter 2.3. This fractionation can then be compensated for using specialised evaluation software designed for LA-ICP-MS analyses [62]. The nature of the signal varies depending on the analytical requirements and, therefore, the established conditions. As a result, there will be differences in output between bulk analysis and spatially resolved analysis as already presented in Chapter 2.1. Signal progression also reveal undesirable sample inhomogeneities, which must be excluded from the results, as illustrated in **Figure 1b**. Furthermore, signal instability, indicative of changes in conditions during the analysis, should be corrected using a normalization method (internal standard, sum normalization…) [63].

Currently, data processing in LA-ICP-MS is facilitated by specialised software tailored to specific applications in this field. This includes both commercial software options, such as *Iolite* (Elemental Scientific) [64] or *HDIP* (Teledyne Photon Machines), and software initially developed for internal use in laboratories which has subsequently been made available to the public such as *Ilaps* designed in our laboratory [65] or *LAtools* [66].

3 Parameters affecting the laser ablation process

The laser-matter interaction is a complex process influenced by both the laser ablation conditions and the physical and chemical properties of the sample. Some laser parameters are dictated by the construction of the ablation system used (wavelength, pulse duration) and so their variability becomes strongly dependent on the available experimental setup [67]. While the properties of samples are often challenging to alter, in some instances, modifications are possible, such as surface treatment or the addition of a binder to powder samples. Numerous studies have explored a variety of laser ablation conditions and their combinations, contributing significantly to the understanding and definition of the very complex processes that occur during laser ablation sampling. Parameters that most affect ablation process are discussed in the following chapters.

3.1 Laser wavelength

It is generally accepted that shorter wavelengths are more suitable for LA-ICP-MS [13] due to higher photon energies, which are efficient at breaking bonds and ionizing the solid sample. The use of shorter wavelengths typically results in higher ablation rates and reduced fractionation [68]. This effect is particularly noticeable when ablating minerals or transparent glasses, where the better absorption of shorter UV radiation compared to longer wavelengths is significant. With shorter wavelengths, lateral resolution can be improved, detection limits can be lowered, and the application of LA can be expanded to different types of minerals [69].

Comparing different laser wavelengths usually entails using distinct ablation systems, meaning that factors other than just the wavelength must be considered. These include variations in pulse duration, fluence, beam profile, laser light polarization, and the volume and shape of the ablation chamber. To isolate the influence of wavelength on the LA process, one approach is to use a single solid-state laser source (like a 1064 nm Nd:YAG laser) and generate higher harmonics (532 nm, 266 nm, 213 nm, 193 nm), keeping all other laser parameters constant. Studies focusing on the effect of wavelength on LA-ICP-MS attribute the reduction in fractionation effects with shorter wavelengths to the PSD. When applied to glass reference materials, a higher fraction of smaller particles in the aerosol was generated by exposure to shorter laser wavelengths. Since the incomplete vaporization of large particles in ICP is a primary source of elemental fractionation [70], the absence or reduced presence of particles larger than 200 nm when using 193 nm laser is reflected in more stable transient signals and smaller variations in intensity ratios, indicating reduced time-dependent elemental fractionation [4].

Many studies investigating the impact of laser wavelength have used NIST 61X series glass reference materials as samples, where the material's transparency is a significant factor. Even within the UV region, reducing the wavelength is crucial for the ICP response and time-

dependent fractionation. This is evident from **Figure 9** which compares the fractionation index (see definition in Chapter 2.3) for 43 elements with respect to ^{42}Ca during the ablation of NIST 610 at wavelengths of 266 nm, 213 nm, and 193 nm. The FI was calculated from the intensity ratios of the second 30 s and first 30 s of one-minute ablation with a repetition of 4 Hz. A fractionation index of one indicates no time-dependent fractionation.

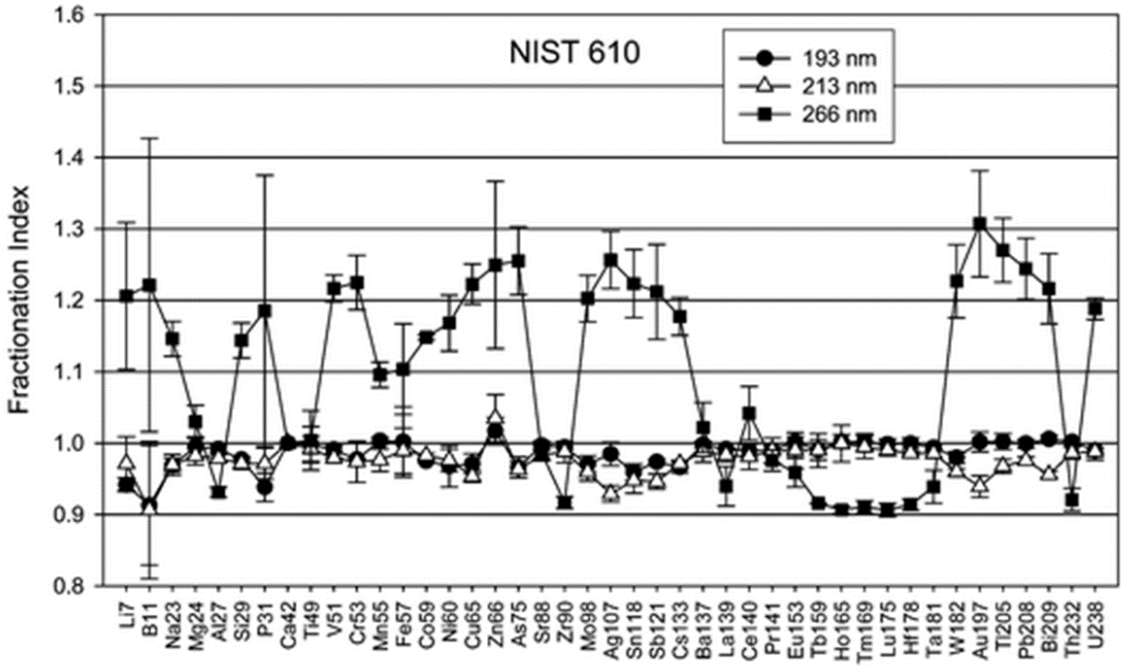

Fig. 9. Fractionation index for 43 elements with respect to ^{42}Ca for the ablation of NIST 610. Error bars represent the standard deviation (1σ) from 5 measurements for each wavelength [45].

The applicability of these findings to other types of samples, beyond glass reference materials, has been verified, for example, with metallic, Fe-based materials [4]. Using a 193 nm excimer laser has been shown to significantly reduce the formation of particles larger than 150 nm, which are commonly present up to 350 nm when using a 266 nm Nd:YAG laser (as measured by OPS in the 65 nm - 1 µm range). **Figure 10** illustrates the PSD for both types of lasers.

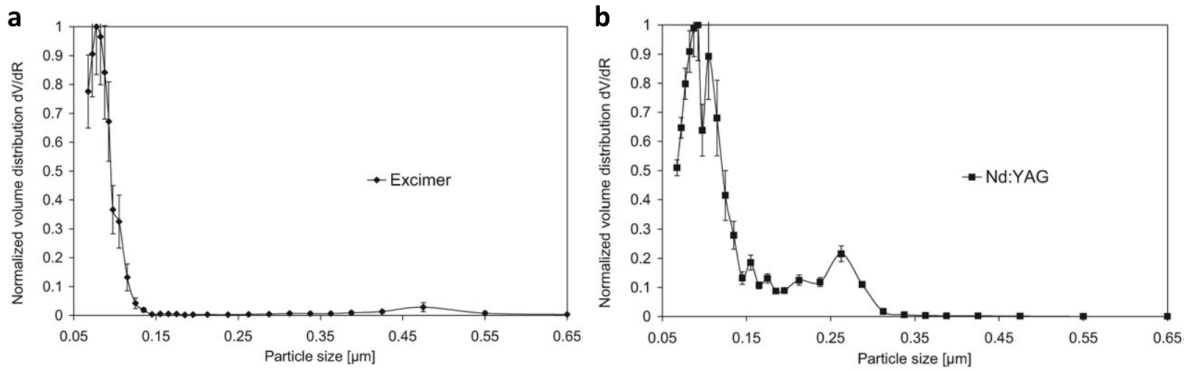

Fig. 10. Normalised particle size distribution of the generated aerosol measured during LA of Fe-based samples: a) 193 nm UV-ns-(ArF*); b) 266 nm UV-ns-(Nd:YAG) [4].

3.2 Laser pulse duration

The pulse duration is a parameter that significantly affects the ablation process. However, it is an immutable characteristic, determined by the design of the laser system. Hence, this parameter is essentially predetermined at the time of selecting or purchasing a laser setup for LA-ICP-MS. Lasers are generally classified into three groups based on the pulse duration: nanosecond, picosecond, and femtosecond. Research consistently indicates that reducing the pulse duration positively affects the accuracy and precision of analytical results [71]. This is because shorter laser pulses provide less time for thermal effects to induce fractionation.

In femtosecond laser ablation, the energy transfer occurs in two stages. The first stage happens in the initial few femtoseconds of the laser pulse, during which the sample's surface layer absorbs photons and undergoes photon ionization processes, exciting the electrons. The second stage lasts a few hundred femtoseconds to picoseconds and involves the transfer of absorbed energy to the lattice through electron-phonon coupling. This leads to thermal evaporation of the sample, known as 'strong ablation', or to the direct removal of heavy atoms and ions, termed 'soft ablation'. Both ablation processes can occur simultaneously, with the contribution of each depending on the laser intensity and the ablation thresholds of the sample [72].

Longer laser pulses, such as those in the nanosecond and picosecond ranges, increase the proportion of thermal effects, causing non-stoichiometric ablation (preferential vaporization of volatile components) [10, 37, 71, 73]. The heat transfer during these longer pulses results in material melting. The mechanical interaction between the molten liquid and plasma leads to the formation of large particles in the aerosol (up to units of micrometres), a process known as hydrodynamic sputtering. The extent of the hydrodynamic sputtering depends on the melt thickness creating the upper layer of the ablation crater surface. Typically, greater heat diffusion and lower fluences lead to increased melt thickness, thereby prolonging the solidification time and consequently enhancing fractionated evaporation and hydrodynamic sputtering. The thermal diffusivity of materials, such as metal and glass, can result in a melt layer approximately an order of magnitude thicker in metals under fluences below 10 J cm^{-2} [74]. The amount and size of the droplets formed depend on the thickness of the melt layer, and models of hydrodynamic sputtering have been developed for various ablation conditions [75].

An explanation for the reduction in fractionation when using a shorter pulse can be given by comparing PSD and particle composition. The direct removal of material in a gas phase leads to a gas-to-particle conversion, resulting in primary nanoparticles within the nucleation size range (< 30 nm) and their agglomerates, which can reach sizes of hundreds of nanometres [7, 8]. In contrast, particles created by thermal effects and thermodynamic sputtering attain sizes of up to several micrometres and are typically characterised by spherical symmetry [4, 10, 37].

Alternative methods for measuring ablated particles have shown that the chemical composition of these particles varies depending on their size and, consequently, their origin [10, 76]. Primary nanoparticles and their agglomerates are often enriched with more volatile components, whereas refractory components tend to accumulate in larger particles. This trend was also confirmed in cobalt-cemented tungsten carbide, a system comprising both high- and low-volatile components. Large particles showed enrichment with tungsten, a less volatile element, while clusters of smaller particles exhibited obvious depletion of W and enrichment of Co. The condensation of Co on larger spherical particles is also distinctly visible [10].

This situation is illustrated in **Figure 11**, where the 5x4 mm filter area is covered by network of nanoparticles, their clusters, and one large spherical particle. **Figure 11a**, captured using Back-scattered Electrons (BSE), shows the overall distribution, while **Figures 11b-11d**, obtained via Energy Dispersive X-ray Spectrometry (EDS), depict the elemental distribution within the particles. The EDS mapping highlights the evident accumulation of tungsten in spherical particles and the uniform distribution of cobalt in agglomerates. The original composition of the sample was (% wt): C 6.13, Co 3.33, Ta 1.03, Nb 0.42, and W 89.09.

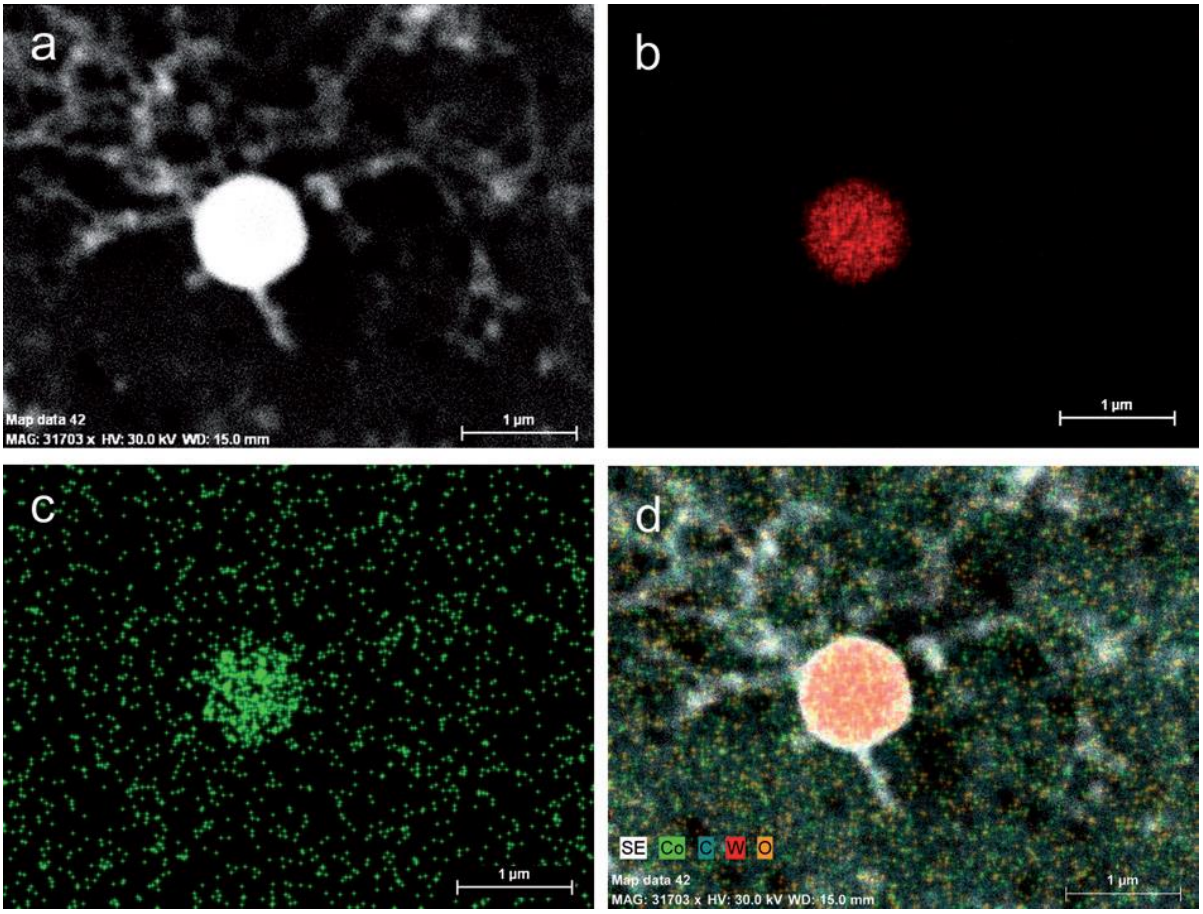

Fig. 11. The elemental distribution maps of particles collected from sample no. 1457HF3, measured on a 5 x 4 mm filter area; a) BSE picture of the particles on the filter, b) tungsten and c) cobalt detected in this area, and d) common map of major elements (W, Co, C, O) [10].

The employment of femtosecond (fs) laser pulses (fs-LA) enables the elimination or significant reduction of micrometric-scale particle formation, a common occurrence with nanosecond (ns) pulses (ns-LA). The interaction mechanisms of fs-LA with a target are associated with a reduction in thermal effects, leading to decreased material melting. For instance, during UV-fs-LA of Fe-based sample, only nano-sized agglomerates ranging from 50–250 nm were observed (**Figure 12b**), while UV-ns-LA generated an aerosol showing a bimodal distribution composed of micro-sized molten spherical particles and nano-sized agglomerates (**Figure 12a**) [4].

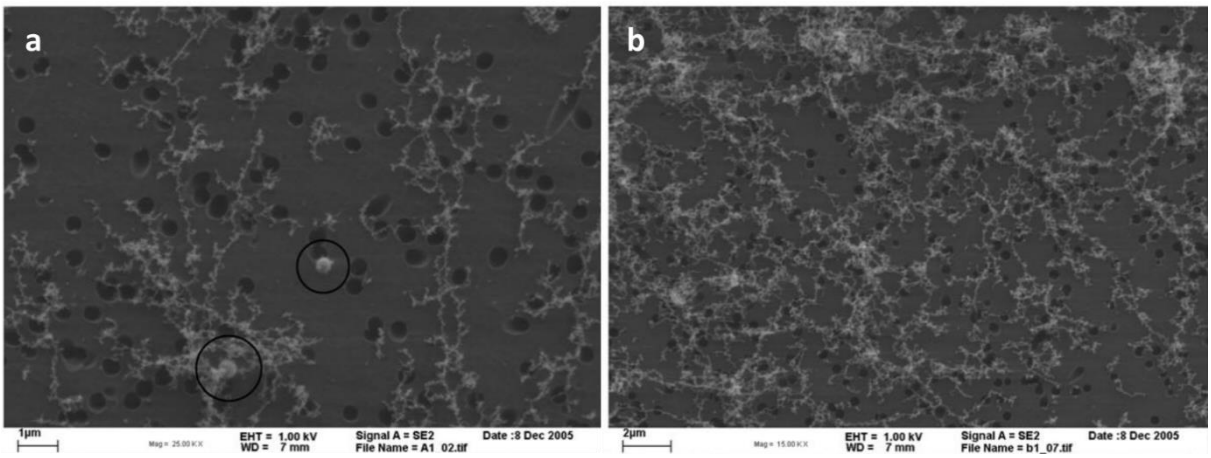

Fig. 12. SEM images of the collected aerosol particles obtained for an Fe metal sample using: a) UV-ns-(Nd:YAG)LA; b) UV-fs-(Ti-sapphire)LA. These images show the different kinds of transported particles observed for each laser system but are not representative of the total transported mass [4].

Shortening the pulse duration can lead to a significant increase in the accuracy and precision of the analytical method. A case in point is the analysis of Fe-based samples using lasers with almost identical wavelengths but differing pulse durations (Nd:YAG 266 nm, 4 ns and Ti-sapphire 265 nm, 150 fs). Matrix-matched (within metallic samples) and non-matrix matched calibrations were employed for analysing Fe-based samples, using a silicate glass (SRM NIST 610) as non-matrix matched calibration sample (glass-metals). Notably, improved analytical results in terms of precision and accuracy were achieved using femtosecond laser ablation, particularly when using similar matrices for calibration. Furthermore, non-matrix matched calibration employed for quantification provided more accurate results (5–15% RSD) compared to UV-ns-LA-ICP-MS (5–30% RSD) [4]. For a comprehensive summary of these results, refer to **Table 2**.

Table 2 Elemental content values, relative standard deviations (n=6) and accuracy values (bias from reference content) found for SRM JK27A using matrix and non-matrix matched calibration. a) UV-ns (Nd:YAG)-LA-ICP-MS; b) UV-fs (Ti-sapphire)-LA-ICP-MS [4].

(a) ns-Nd:YAG laser

SRM JK27A		Matrix matched calibration with SRM JK2D			Non-matrix matched calibration with SRM NIST 610		
Element	Ref. content/μg g^{-1}	Content/μg g^{-1}	Precision RSD (%)	Accuracy (%)	Content/μg g^{-1}	Precision RSD (%)	Accuracy (%)
Al	169	195	20	15	217	21	28
Si	4110	4.34×10^3	5	6	4.99×10^3	3	21
P	222	259	6	17	234	10	6
Cr	167 600	1.65×10^5	2	1	1.89×10^5	8	13
Mn	15 890	1.52×10^4	3	4	2.04×10^4	7	29
Ni	120 400	1.18×10^5	3	2	1.19×10^5	2	1
Cu	1990	1.81×10^3	2	9	2.46×10^3	3	24
Mo	25 310	2.55×10^4	9	1	1.91×10^4	5	24

(b) fs-Ti sapphire laser

SRM JK27A		Matrix matched calibration with SRM JK2D			Non-matrix matched calibration with SRM NIST 610		
Element	Ref. content/μg g^{-1}	Content/μg g^{-1}	Precision RSD (%)	Accuracy (%)	Content/μg g^{-1}	Precision RSD (%)	Accuracy (%)
Al	169	156	2	8	188	12	11
Si	4110	4.10×10^3	2	0.2	4.35×10^3	2	6
P	222	220	4	1	212	2	5
Cr	167 600	1.66×10^5	2	1	1.60×10^5	3	4
Mn	15 890	1.59×10^4	1	0.4	1.52×10^4	3	4
Ni	120 400	1.20×10^5	3	0.1	1.14×10^5	3	5
Cu	1990	1.98×10^3	1	1	1.91×10^3	3	4
Mo	25 310	2.47×10^4	4	2	2.14×10^4	2	15

3.3 Laser fluence

Fluence, defined as laser energy per unit area, significantly influences the nature of laser ablation sampling. It affects not only the amount of mass ablated but also the degree of fractionation. Unlike pulse duration, where shorter times are generally recommended, there is no universal guideline for setting fluence, and it must be carefully tailored for each sample. The appropriate fluence value depends on the combination of the sample properties (especially its absorption at the applied laser wavelength, thermal conductivity, and melting point) and laser parameters, such as wavelength, pulse duration, or spot size. Generally, samples that have higher optical transparency for the wavelength of the applied laser require higher fluence. However, high fluences for samples with high thermal conductivity and low melting points may induce melting and splashing of the sample that might result in deviations from the expected element ratio [77]. This is especially true when applying repeated pulses to the same spot, as the overall process also depends on the number of pulses used [14].

A different scenario arises when scanning the sample surface along a line. Here, by adjusting the crater size, scanning speed, and repetition rate, the degree of overlap of individual laser shots is selected. Consequently, laser ablation partly occurs on the previously ablated surface and partly on the untouched surface. It is possible to set a scanning speed where the craters do not overlap, meaning the molten surface of the sample does not affect subsequent pulses.

Such a model was applied to the study [6] which demonstrates that the final representation of individual elements in the Al alloy sample varies based on the laser fluence used. Using higher fluences of ns laser reduces preferential vaporization of volatile components. The change in the response of measured analytes persists even after the application of several pre-shots. In the case of metallic materials where extreme melting occurs, the composition may permanently change due to surface re-melting, especially at lower fluences. The experiment was performed

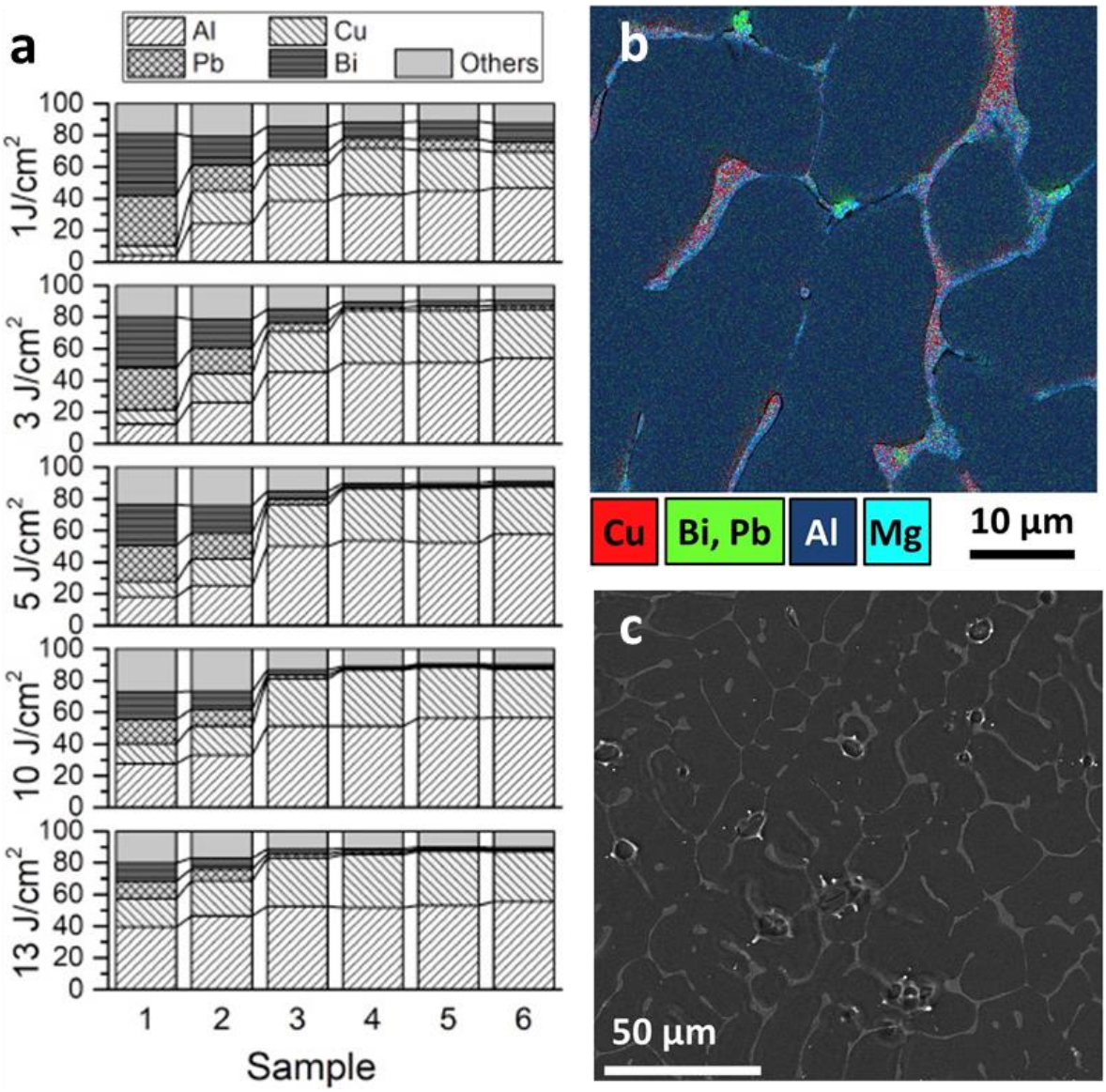

Fig. 13. a) The total elemental representation (expressed as a percentage of sum of signal intensities) for BAM 311 sample with different surface roughness: 1 polished (14.0), 2 #2000 (73.0), 3 #1200 (190.0), 4 #500 (335.0), 5 #220 (875.7) and 6 #80 (2717.3); b) The image of a polished BAM 311 surface: EDX map of elemental distribution. Cu (red) and Mg (turquoise) form dendrites. Bi and Pb (green) are captured together in small inclusions within dendrites. Al (blue) is mainly contained in the space between them; c) SEM image of the polished BAM 311 sample surface ablated by 1 J cm^{-2} spot by spot of 110 µm diameter [6].

on the BAM 311 sample (composition in m/m %: Al 92 %, Cu 4.7 %, Pb 0.05 %, Bi 0.05 %, other elements ~ 3 %) prepared with different surface roughness to also demonstrate the effect of surface topography on laser ablation. The influence of surface properties on laser-matter interaction is a separate phenomenon, covered in Chapter 3.6. To illustrate the effect of fluence, compare the composition of the ICP-MS response of individual analytes within columns 1 – 6 in **Figure 13a**, which represent the same sample with varying surface topography. Focusing on column 1, corresponding to the polished sample (preparation of surfaces by the usual procedure), a substantial change in the composition of the registered signal with increasing fluence is evident. Lower fluences lead to higher representation of volatile components (especially Pb and Bi), which are present in the sample in minor quantities compared to aluminium, the predominant element in the alloy. This can be explained by two factors. Firstly, the different physical properties of elements: Pb and Bi are extremely volatile with melting points of 207ºC for Pb and 271ºC for Bi. Secondly, their distribution within the matrix differs from other elements. **Figure 13b** shows that the alloy exhibits a dendritic structure that was created during the unidirectional solidification process. Due to different melting points and solidification ratios of elements, the dendrites are enriched with Cu, Bi and Pb. Although globally homogeneous, this dendritic structure introduces micro-heterogeneity to the sample, creating regions with varying melting and boiling points or optical properties, potentially causing fractionation. This effect is most pronounced at low fluences, where preferential ablation occurs primarily in the areas of dendrites, as illustrated in **Figure 13c**.

Irrespective of the sample properties, fluence remains one of the most critical variable parameters in laser ablation. Optimizing fluence is essential to achieve precise (minimal fractionation effect) and accurate (sufficient mass ablated) analytical results. The appropriate fluence value is primarily related to the sample matrix, laser pulse duration, and the number of applied pulses.

3.4 Ablation mode and spot size

In LA-ICP-MS, two ablation modes are commonly used. The first is the *spot ablation mode*, where a specific number of laser pulses are repeatedly directed at a single point. The number of pulses can vary based on the nature of the analysis, ranging from a single pulse (known as single pulse ablation) to hundreds or even thousands of pulses. These pulses generate the aerosol necessary for trace analysis from that specific area or to create a depth profile. The second frequently used mode is the *scanning mode*, where the sample is moved at a predefined speed, typically linearly. The combination of the set laser repetition rate and spot size with this speed determines the degree of overlap between individual pulses.

It has been observed that the settings of the ablation mode can significantly influence the formation of aerosols and, consequently, the resulting analytical signal. For instance, in spot ablation, the spot size impacts not only the quantity of generated particles but also their size distribution [7]. When monitoring particles generated by spot ablation with a ns laser on the SRM NIST 610 sample, a shift in PSD peak, corresponding to the nucleation of nanoparticles (around 10-20 nm), was noted towards larger sizes with increasing applied spot diameter (**Figure 14a**). This shift is attributed to the greater amount of material evaporated. The second peak in the PSD, indicative mostly of the coagulation/agglomeration of primary nanoparticles (at 190 nm), remains constant in position irrespective of the spot size, although the concentration of particles changes. As anticipated, the particle concentration of all sizes escalates with an enlarging spot.

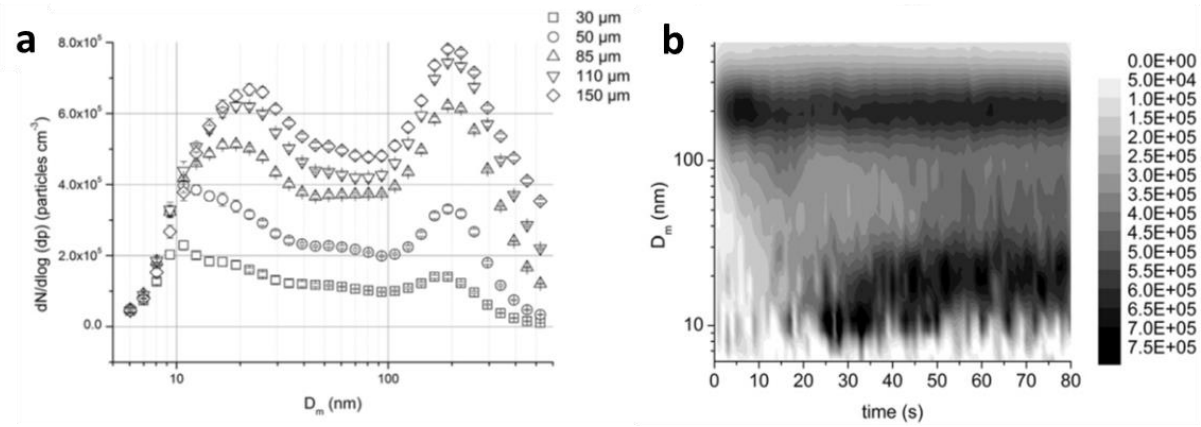

Fig. 14. a) EEPS particle size distribution graphs (average of 80 s spot ablation) for different spot sizes, the error bars indicate standard deviation of 5 measurements; b) Distribution map for temporal behaviour of particle number concentration in individual size channels for spot size of 85 µm. The particle concentration scale is shown to the right of the graph dN/dlog(dp) (particles cm^{-3}) [7].

In **Figure 14b**, temporal changes in the PSD during spot ablation with an 85 µm spot size are depicted. There is a noticeable increase in the production of particles with diameter (D_m) of approximately 190 nm within the first 10 seconds of spot laser ablation. The production of primary nanoparticles begins roughly 20 seconds after the start of ablation, corresponding to 200 pulses applied. Furthermore, the number concentration of particles with $D_m < 50$ nm rises as the crater becomes deeper. Such behaviour at the start of surface layer ablation is consistent with the theory that nanoparticles are scavenged by larger particles originating from the intact material surface. As the crater deepens, the production of larger particles decreases [78], leading to a relative increase in the concentration of smaller nanoparticles. Overall, the dynamics of spot ablation change continuously during the ablation process.

The temporal record of PSD for spot ablation reveals differences in laser interaction with the original sample surface compared to a layer of material altered by preceding laser pulses. This

phenomenon is also observable for the scanning mode of laser ablation, specifically regarding the degree of laser spot overlap, i.e., the ratio of original to already ablated material within a single pulse. At the same laser repetition rate, this means that slower scanning speeds will more closely resemble spot ablation. This was confirmed using SRM NIST 610 for spot ablation and various scanning speeds, all employing an 85 µm spot size and a 10 Hz repetition rate (**Figure 15a**) [7]. Slower scanning speeds led to an increased production of primary nanoparticles and a closer resemblance to spot ablation, where the sample remains static. The peak for agglomerated particles consistently remains at 190 nm across different speeds, mirroring the findings in spot ablation. **Figure 15b** illustrates that the ablation process in line scan mode is more stable compared to spot ablation mode. In the case of a scan speed of 40 µm s^{-1}, the scan ablation stabilizes after the initial 10 seconds.

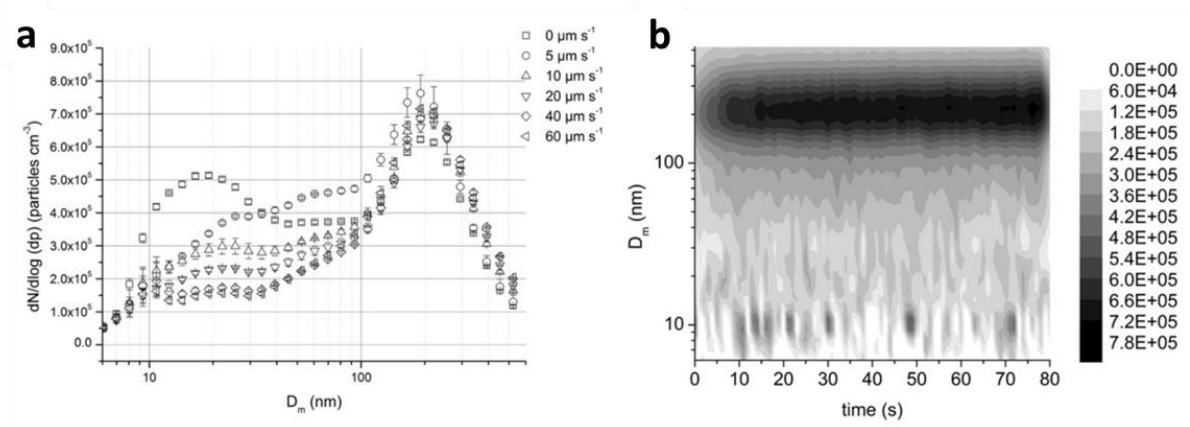

Fig. 15. a) EEPS particle size distribution graphs (average of 80 s spot ablation) for different scan speeds, the error bars indicate standard deviation of 5 measurements; b) Distribution map for temporal behaviour of particle number concentration in individual size channels for scan speed of 40 µm s^{-1}. The particle concentration scale is shown to the right of each graph dN/dlog(dp) (particles cm^{-3}) [7].

When comparing spot and line scanning ablation modes using the APS instrument, capable of measuring PSD in the range of 540 nm - 17 µm, it was found that line scan ablation produces up to 10 times more particles in this size range, as evidenced in **Figure 16** for 85 µm spot ablation vs. scanning ablation at a speed of 40 µm s^{-1}. Such an increase in large particles causes a considerable rise in the overall volume of the sampled material introduced into the ICP, thereby enhancing the response of measured analytes in line scan ablation mode [7].

Differences in aerosol PSD between spot and line scan ablation have also been the subject of another study [8], which further explores the comparison of particle formation relative to the sample matrix. This aspect will be discussed in greater detail in the subsequent chapter.

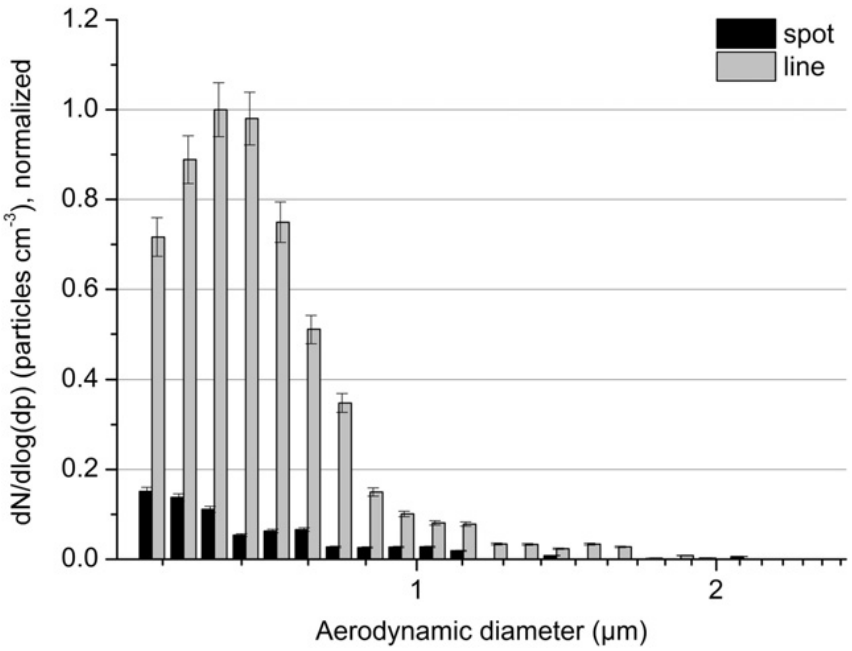

Fig. 16. Particle size distribution by Aerodynamic Particle Sizer for spot ablation mode (85 µm) and line scan (40 µm s^{-1}) of SRM NIST 610; the error bars indicate standard deviation of 5 measurements [7].

3.5 Sample matrix

The laser-matter interaction is significantly influenced by the sample's physical and chemical properties. These include, for example, the absorption coefficient, which determines the extent of laser energy absorption at a specific wavelength, the thermal conductivity of the sample affecting heat transfer, and the degree of plasma shielding, which refers to the attenuation of incoming laser radiation [79]. Conversely, laser irradiation can substantially alter the sample's optical and thermo-physical properties, leading to changes in surface reflectivity, electrical and thermal conductivity, surface tension, and latent heat of vaporization.

Depending on the sample matrix, there is a specific interaction between laser radiation and the formation of aerosol particles, occurring predominantly through two fundamental processes. Firstly, the aerosol is formed via a gas-to-particle conversion process, typically resulting in smaller particle sizes. Studies investigating particle formation have revealed that nanoparticles produced by vapor nucleation are generally smaller than 100 nm (subject to variations based on laser and sample parameters) before cluster agglomeration commences [80]. Detailed observation of nanoparticle formation is challenging due to the irregular shapes and undefined density of the clusters they form.

Secondly, the aerosol is formed through heat transfer processes that cause material melting, followed by liquid-plasma interaction, leading to the creation of larger particles in the aerosol through hydrodynamic sputtering. The extent of hydrodynamic sputtering is dependent on the

thickness of the molten layer forming the upper part of the ablation crater surface. Increased heat diffusion and lower fluences typically result in a thicker melt layer, extending the solidification time and enhancing fractionated evaporation and hydrodynamic sputtering [74]. The thickness of this melt layer is a determining factor for the quantity and size of the generated droplets. For example, the thermal diffusivity difference in materials such as metals and glass can lead to a melt layer about an order of magnitude thicker in metals under fluences below 10 J cm^{-2} [74]. This principle is influenced not only by the sample matrix but also by the parameters of the laser radiation, particularly wavelength and pulse duration.

Some observations have been able to approximately delineate particle formation during the condensation process using ns lasers. Commonly, two size distribution modes are observed [75, 81]. The size of particles in the primary mode is mainly influenced by the ablation mode [7, 8], with smaller sizes noted for line ablation, and is largely independent of the type of ablated material. This is attributed to a similar mechanism of primary particle formation across all materials, involving evaporation followed by the condensation of vapours, under conditions set by the laser ablation setup (including laser settings, carrier gas, etc.). In contrast, the size of particles in the accumulation mode is material-dependent, as illustrated in **Figure 17** when comparing metal and glass. Notably, for SRM NIST 610, the accumulation mode of the PSD shifts to larger sizes (200 and 220 nm for spot and line ablation, respectively) compared to steel F4 material (120 and 160 nm for spot and line ablation, respectively) for both ablation modes.

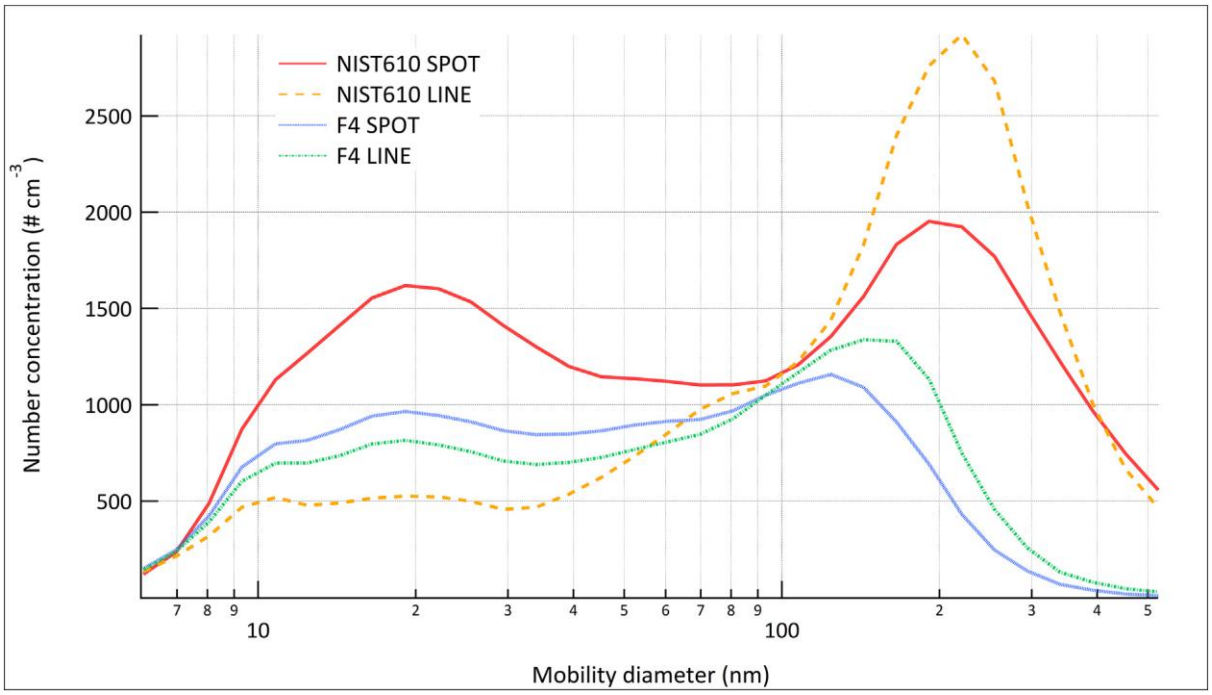

Fig. 17. Average PSD for laser ablation of different materials (glass NIST610 and steel F4) and different ablation modes (measured by EEPS). Ablation conditions: ns laser (193 nm), 110 µm spot size, 8 J cm^{-2}, 10 Hz, scan speed of 20 µm s^{-1} [8].

Furthermore, the overall size distribution exhibits lower concentrations for the ablation of steel material. The greater tendency of SRM NIST 610 for clustering compared to steel F4 was confirmed through particle observation using TEM, as illustrated in **Figure 18**. NIST 610 was observed to predominantly form clusters consisting of a single type of particle, whereas F4 produced two distinct particle types. The large spherical particles, characteristic of hydrodynamic sputtering of the liquid layer, can reach sizes of up to several micrometres.

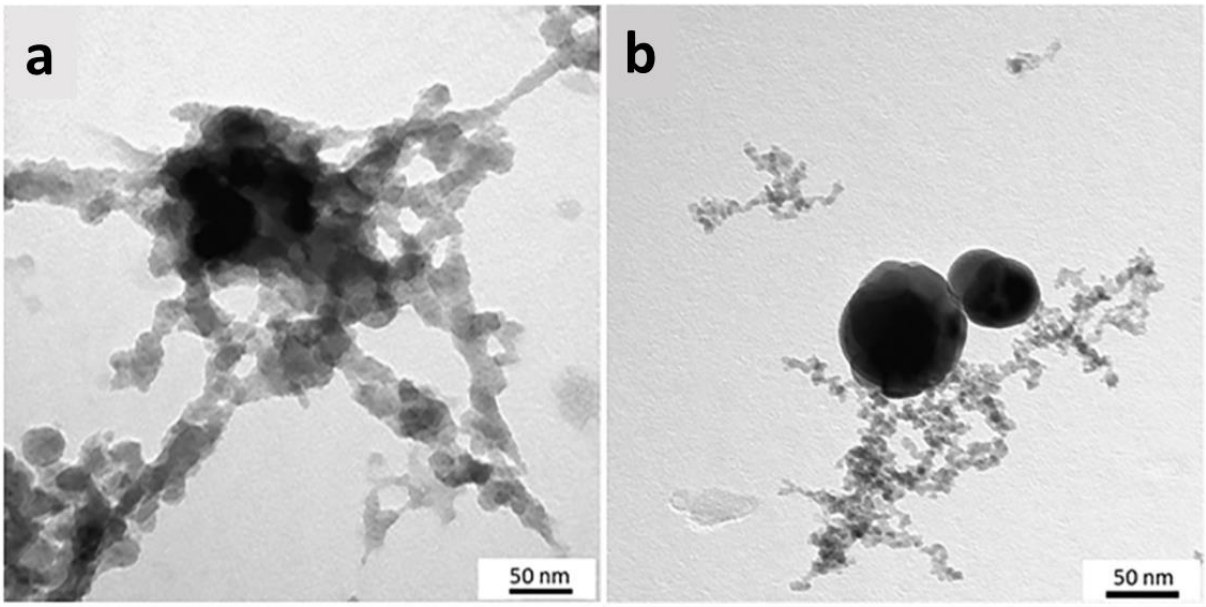

Fig. 18. TEM image of particles produced by spot ns laser ablation (193 nm, 110 µm spot size, 8 J cm^{-2}, 10 Hz) a) SRM NIST 610, b) steel F4 [8].

Although the quantity of particles generated by hydrodynamic sputtering may seem insignificant compared to the total number of particles, their considerable size - up to several micrometres - means that they constitute a significant portion of the total aerosol volume. Both the quantity and size of these particles are influenced not only by the laser ablation parameters but also significantly by the material's matrix. This is particularly evident when comparing different materials under identical ablation conditions. **Figure 19** shows PSD in the size range of 0.25–2.5 µm, encompassing the entire range for particles produced by hydrodynamic sputtering [9]. Three materials with different matrices are presented: metal (steel), metal-ceramic (Co-cemented tungsten carbide hardmetal), and non-metal (glass) sample. In the steel sample, the highest number concentration of particles is observed, along with the presence of particles reaching the largest sizes. In contrast, the glass sample exhibits the smallest particles in the lowest concentrations. This variation is linked to the thermal conductivity of the samples; a higher thermal conductivity leads to the formation of a thicker molten material layer on the surface, serving as a source for material sputtering.

The extent of thermal effects on a sample can be evaluated by examining the structure and dimensions of the ablation crater. Significant melting of the sample becomes apparent through the characteristics of the crater's bottom, its rim, and the particles deposited around it. These features can be observed using a confocal microscope or profilometer, or through electron microscope imagery as shown in **Figure 5**. **Figure 20** presents a comparative analysis of two ablation craters created under identical conditions but on different material types. The SRM NIST610 glass produces a regular crater, devoid of signs of a molten bottom or an expanded rim, and the resultant particles resemble agglomerates of primary nanoparticles (**Figure 20a, c**). Conversely, a metal sample displays pronounced melting, especially evident at the crater's rim and bottom, as well as in the abundance of deposited particles (**Figure 20b, d**). These particles are indicative of thermodynamic sputtering of the melt. Additionally, they serve as 'traps' for capturing primary particles, reducing the efficiency of particle transport to the ICP.

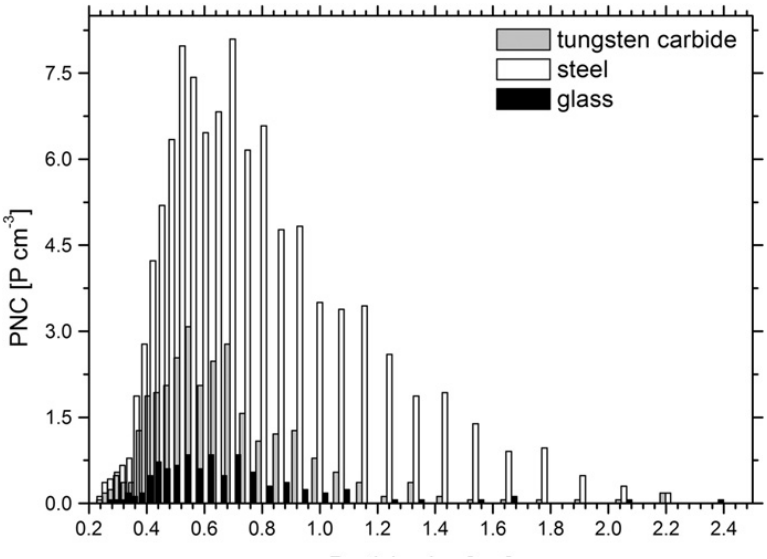

Fig. 19. Particle size distribution graph measured by optical aerosol spectrometer Welas® for large spherical particles (Co-cemented tungsten carbide sample no. 3648 K, steel no. 54666, and glass no. U12) [9].

The process of matrix unification effectively reduces the disparities in ablation mechanisms among different samples. This effect was clearly demonstrated in a study involving Co-tungsten carbide precursor powder samples [11]. For laser ablation, these samples were prepared as pressed pellets, either without a binder or using silver as both a binder and a matrix unifier. The analysis focusing on particle formation and ablation crater characteristics highlighted the significant role played by the matrix unifier. Notably, it led to a reduction in variations in the total particle concentration among the samples, with the relative standard deviation (RSD) decreasing from 46% to 19%, as shown in **Figure 21**. Similarly, the disparities in the volumes of the ablation craters were also minimised, with the RSD dropping from 36% to 16% [11].

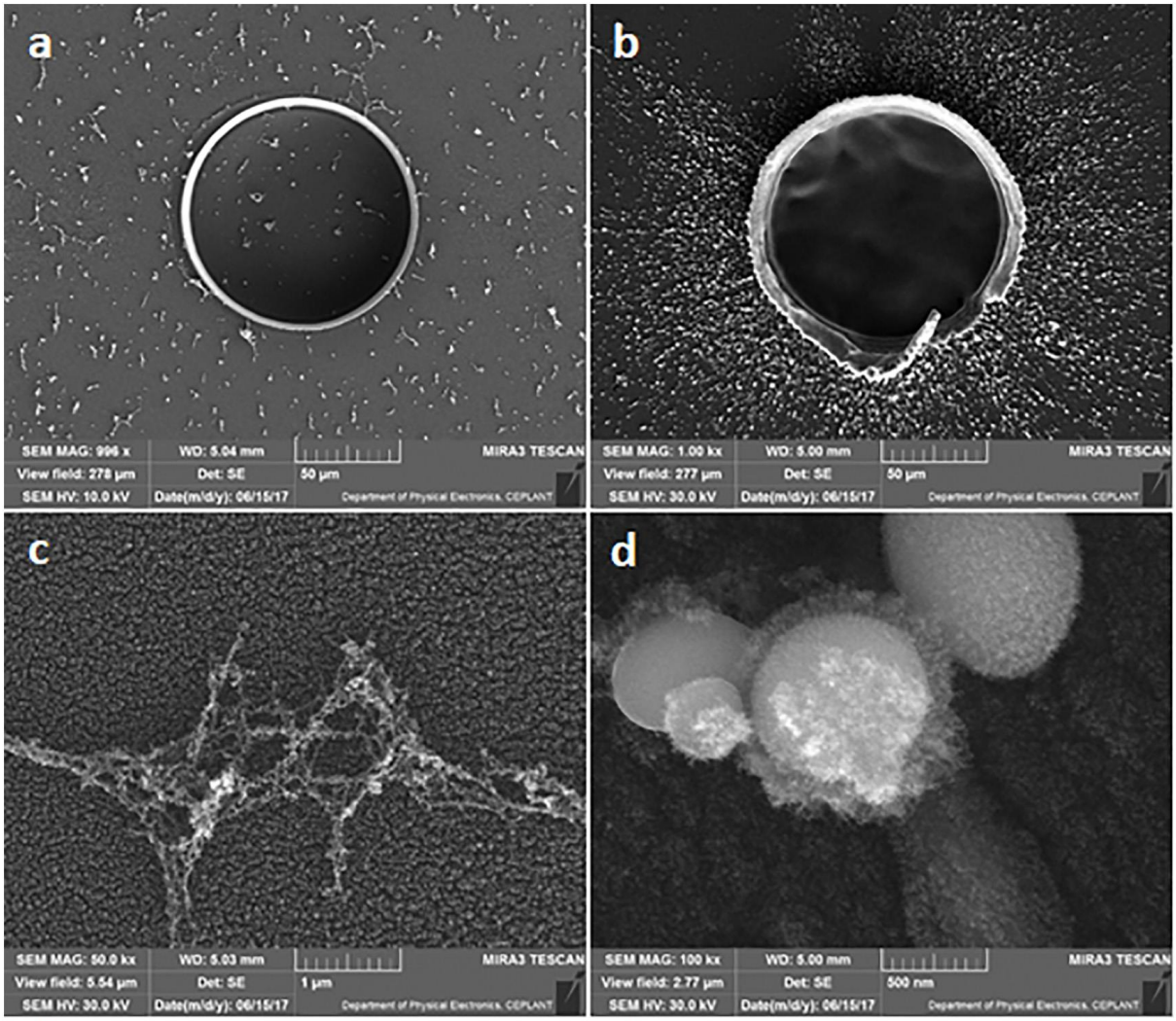

Fig. 20. SEM of the ablation craters after 100 pulses a) NIST 610, b) steel F4 and detail of deposited particles c) NIST 610, d) steel F4 [8].

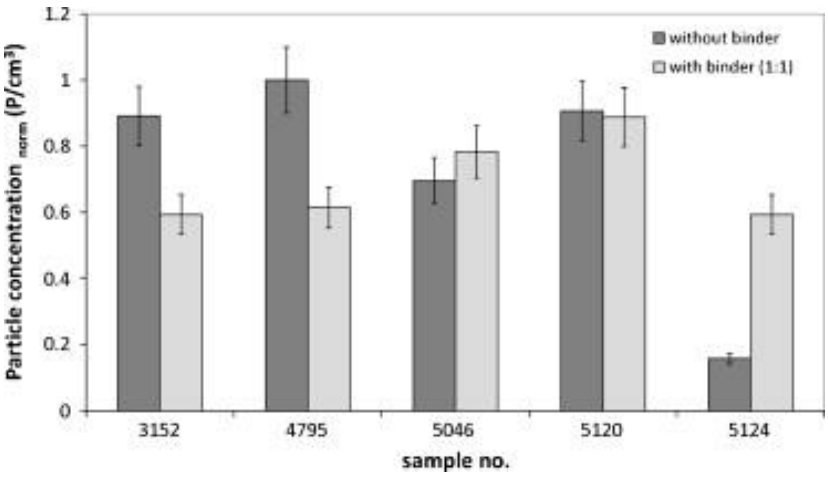

Fig. 21. Total concentration of particles (10 nm–17 µm) formed during the laser ablation of non-matrix-unified (without binder) and matrix-unified (with Ag binder) Co-tungsten carbide samples. The error-bars signify the standard deviation of three parallel measurements of each sample [11].

3.6 Sample surface

While the intrinsic chemical and physical properties of a sample are typically unalterable, its surface - which directly interacts with laser radiation - can often be modified prior to analysis. There are exceptions, such as porous samples, biological specimens, cultural heritage artefacts, or powdered materials. A standard approach to sample preparation involves surface polishing using diamond paste to achieve a smooth finish. Research has demonstrated that intentional surface treatments, aimed at modifying optical or thermal characteristics, can enhance the analytical performance of LA-based techniques.

For example, roughening the sample surface can amplify the LA-ICP-MS signal. This enhancement is attributed to decreased material reflectivity and increased energy transfer from the laser pulse through the material's sharp edges [6]. In the referenced study, certified glass standard reference material (SRM) NIST 610 and aluminium alloy standard BAM 311 (BAM, Germany) were utilised as samples. Different levels of surface roughness were achieved through wet grinding or polishing with various silicon carbide papers (ranging from #80 to #2000) or diamond pastes of 3 µm and 1 µm. The resulting surface roughness values for these samples are listed in **Table 3**.

Table 3 Surface roughness measured by an optical 3D microscope for samples with different grinding set up [6].

Ra [nm]	#80	#220	#500	#1200	#2000	polished
BAM 311	2717.3	875.7	335.0	190.0	73.0	14.0
NIST 610	2601.8	514.5	136.8	24.2	8.1	1.2

The LA-ICP-MS response for measured isotopes was assessed across different fluences (1, 3, 5, 10, and 13 J cm^{-2}). Each measurement was carried out as a "spot by spot" (no pulse overlap) line scan of 5 mm length and 10 repetitions. The average counts per second (cps) for each isotope were calculated along with the standard deviation (SD). Subsequently, these values were compared across isotopes and varying fluences. By comparing the cps of samples with specific roughness against those of polished samples, changes in signal response were estimated. As the ratio between cps of samples with specific surface roughness and the cps of polished samples exceeded one in most cases, it is referred to as 'enhancement'. The correlation between enhancement and surface roughness is depicted in **Figure 22**.

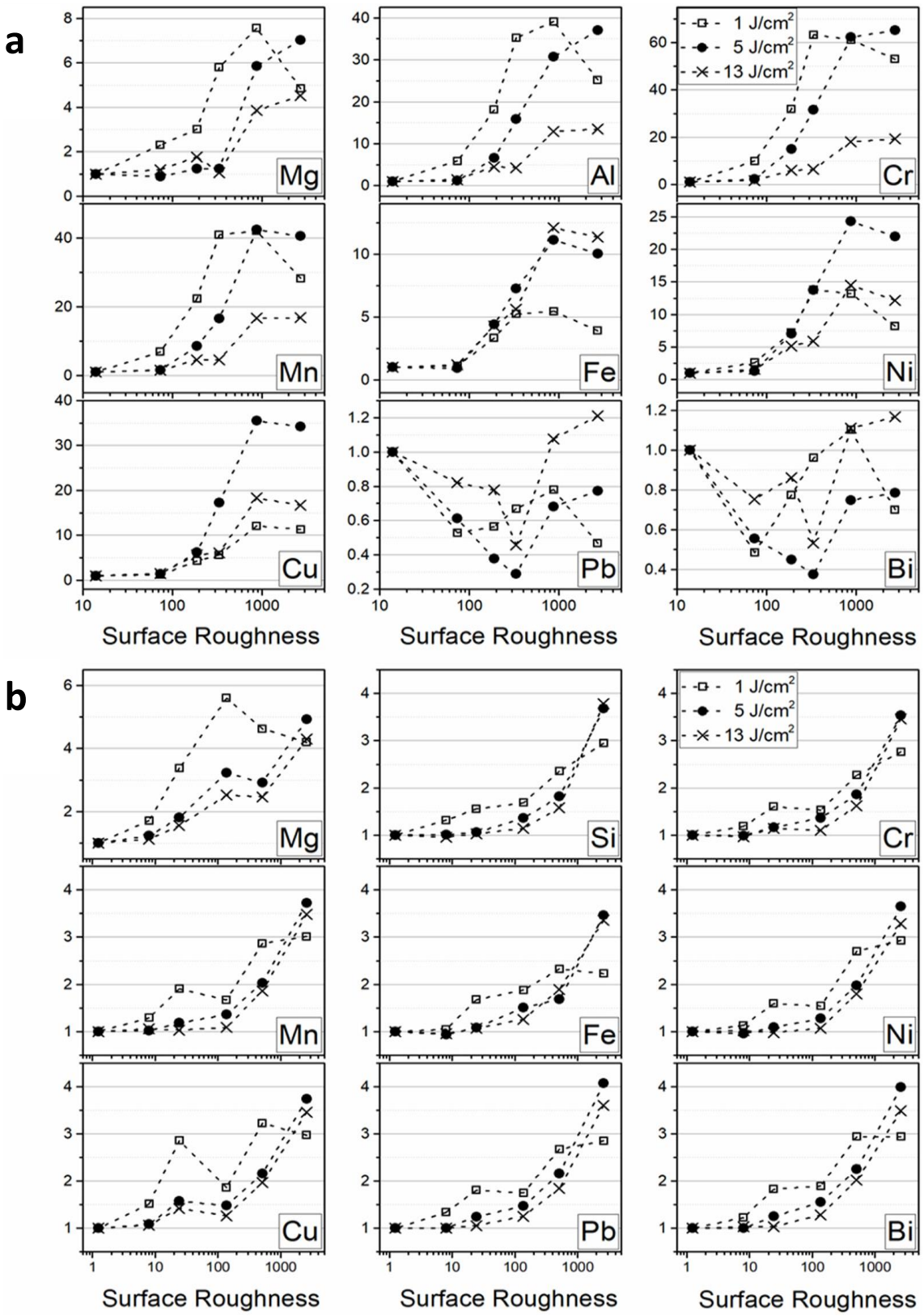

Fig. 22. The ratio between cps of samples with specific surface roughness and the cps of polished samples for selected isotopes as a function of surface roughness a) BAM 311; b) NIST 610 [6].

Beyond the effect of fluence, surface roughness contributed significantly to signal enhancement. Higher analytical ICP-MS signals for measured isotopes suggest an increase in ion production from the aerosol. This aerosol formed by the interaction of the laser pulses with the sample, can either be larger in volume or have a different structural composition. To quantify the total mass generated by LA, a DustTrack DrX monitor was used. It measured the aerosol mass produced from ablating both a polished sample and a sample with #220 roughness (exhibiting the highest enhancement) across various fluences (1, 3, 5, 10, and 13 J cm^{-2}) for both material types. The analysis revealed that the Al alloy sample with #220 roughness generated an increase in aerosol mass exceeding an order of magnitude, achieving up to fifty times the mass compared to the polished sample. In contrast, NIST 610 demonstrated an increase in aerosol production by less than an order of magnitude (as shown in **Table 4**). These results are consistent with the signal enhancement observed for both materials, validating that samples with higher surface roughness produce a larger mass of aerosol particles.

Table 4 Ablated mass [mg m^{-3}] during laser ablation with various fluencies (1, 3, 5, 10 and 13 J cm^{-2}) and reflectivity of polished sample and sample #220 (with the highest enhancement in case of alloy) [6].

[J/cm2]	NIST 610 [mg/m^3]		BAM 311 [mg/m^3]	
	Polished	220	Polished	220
1	0.020	0.136	0.007	0.093
3	0.033	0.167	0.005	0.211
5	0.045	0.143	0.005	0.234
10	0.053	0.147	0.005	0.275
13	0.058	0.146	0.008	0.295
Reflectivity	100%	60%	100%	44%

Another approach to enhance analyte signals involves applying metal nanoparticles to the sample surface, a technique referred to as NE-LA-ICP-MS (Nanoparticle-Enhanced Laser Ablation Inductively Coupled Plasma Mass Spectrometry) [5]. In experiments using Aluminium alloy AW 2030 as the model sample (with a composition by weight %: 92% Al, 3.9% Cu, 1.2% Pb, 0.8% Mg, 0.6% Mn, and 0.1% Fe), the application of metal nanoparticles in the form of dried droplets led to a significant amplification of the analyte signal, as shown in **Figure 23**. This enhancement exceeded two orders of magnitude while reducing the detection limits by an order of magnitude. The extent of signal amplification was observed to vary with the applied fluence. **Table 5** presents a comparative analysis of detection limits for various fluences, contrasting the clean surface of aluminium alloy AW 2030 with a surface coated with 40 nm AgNPs.

The observed improvements on metallic targets might suggest a role for surface plasmon resonance and an intensification of the electric field between the nanoparticles (NPs) and the surface [82]. However, the ICP-MS signal increases monotonously with the surface NP concentration, which is atypical for surface plasmon resonance, where emission usually decreases beyond a critical NP concentration. An examination of the ablation craters revealed that the presence of nanoparticles does not necessarily lead to increased material removal but does alter the crater's structure. **Figure 24a** illustrates the contrast between a crater formed by a single laser pulse (213 nm, 100 µm diameter, with fluence of 4.5 J cm^{-2}) at the boundary of a clean sample surface and an area with dried droplets containing 40 nm AgNPs. The presence of NPs appears to result in smoother ablation craters with less material splashing. This observation led to the hypothesis of potential variations in aerosol structure, later confirmed by a study showing different particle size distributions between a polished sample surface and a surface coated with gold nanoparticles of various sizes [12]. When employing the NE-LA-ICP-MS method, a larger proportion of smaller particles (<30 nm) was produced, at the expense of particles around 100 nm and larger (**Figure 24b**). This phenomenon can be attributed to two main factors: firstly, different clustering mechanisms employed by the two methods; and secondly, reduced thermal effects during NE-LA, leading to fewer large spherical particles typically formed by the solidification of sprayed sample melt, a process known as hydrodynamic sputtering. The experimental findings conclusively demonstrate that the NE-LA-ICP-MS method produces a higher proportion of smaller particles (<30 nm) in comparison to conventional LA-ICP-MS, approaching an ideal monodisperse aerosol that can be efficiently vaporized in the ICP. This discovery provides a foundation for future research aimed at developing strategies to reduce the undesirable effects of fractionation in LA.

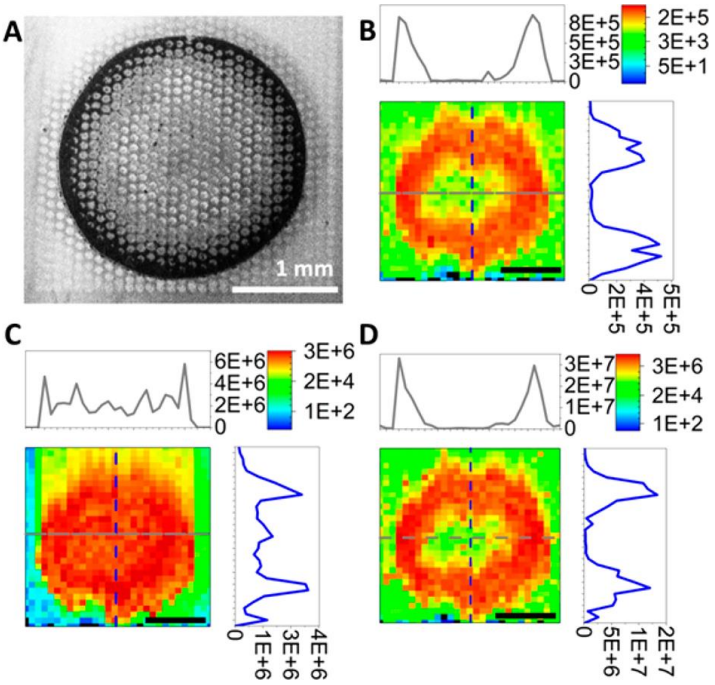

Fig. 23. a) Photograph of the ablated area with a dried droplet of 40 nm AgNPs and craters on the aluminium alloy (AW 2030) sample for a fluence of 4.5 J cm^{-2}; and ICP-MS intensity maps with xy cross-sections for analyte b) Mg; c) Ag; and d) Pb [5].

Table 5 LODs (µg g^{-1}) for different fluences (J cm^{-2}) without and with 40 nm AgNPs on the sample surface (comparing LA-ICP-MS and NE-LA-ICP-MS methods) [5]

fluence	Mg	Mn	Fe	Cu	Pb
		Without NPs			
0.2	120	440	1300	5400	4.9
0.3	110	360	970	4800	4.0
0.4	50	190	730	2500	2.2
1.0	42	87	440	1100	1.5
2.0	51	51	450	580	2.5
3.0	60	35	350	450	2.1
3.7	30	26	250	340	1.7
4.5	46	23	270	280	3.0
		With 40 nm AgNPs			
0.2	3.3	73	750	250	0.15
0.3	5.5	77	610	430	0.29
0.4	5.2	60	490	370	0.27
1.0	2.8	30	280	220	0.15
2.0	2.9	20	170	160	0.16
3.0	1.7	11	120	84	0.10
3.7	1.9	14	140	110	0.11
4.5	1.9	12	130	98	0.12

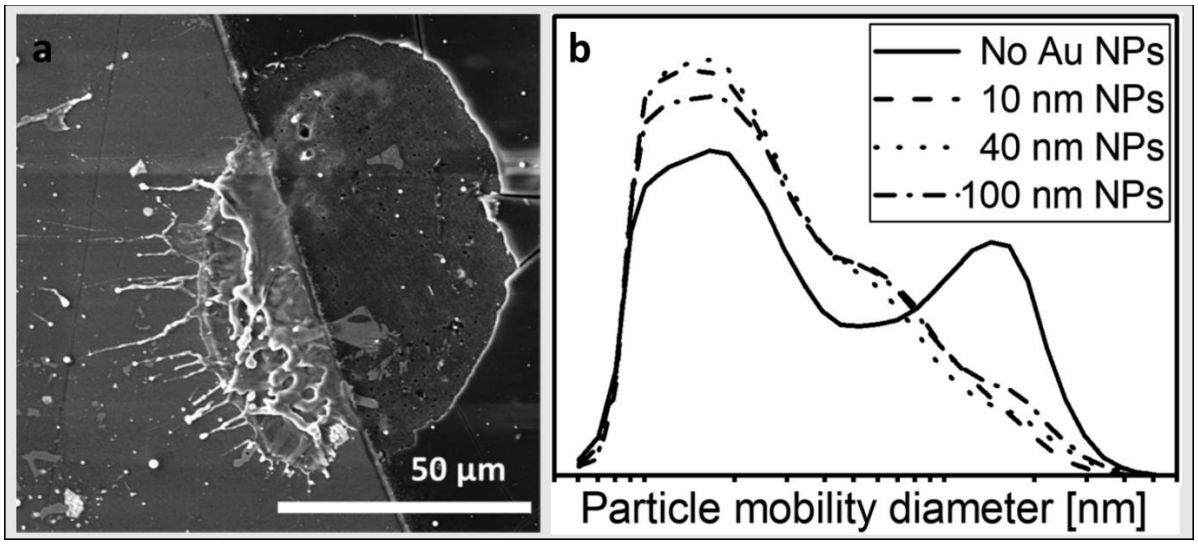

Fig. 24. a) Crater image by SEM-BSE for a fluence of 4.5 J cm^{-2} on the interface of the droplet with 40 nm AgNPs (right) and the surface without NPs (left) [5]; b) Particle size distribution measured by EEPS (5.6–560 nm, arbitrary concentration units) of LA and NE-LA aerosol using different sizes of nanoparticles for fluences 1 J cm^{-2} [12].

4 Conclusion and outlook

This habilitation thesis comprehensively deals with the sampling of solid materials by laser ablation for mass spectrometry with inductively coupled plasma (LA-ICP-MS) emphasizing the prevalent application of the most used nanosecond lasers. It seeks to contribute to the elucidation of the complex dynamics between the laser pulse and the sample. It indicates how numerous parameters, such as laser wavelength, pulse duration, fluence, ablation mode, scan speed, and laser beam size, as well as physical and chemical properties - especially the matrix and surface - critically affect this interaction.

The research included in the habilitation thesis shows that the use of shorter laser wavelengths, specifically the reduction from 266 nm to 193 nm, significantly limits the formation of particles larger than 150 nm during the ablation of metal samples. This finding underscores the potential for improved precision in particle size control during aerosol generation. The study further shows that the duration of the laser pulses significantly affects the thermal dynamics during ablation. Longer pulses in the nanosecond and picosecond range enhance non-stoichiometric ablation due to preferential evaporation of volatile components, resulting in significant material melting. This molten material mechanically interacts with the plasma, leading to the production of larger particles by hydrodynamic sputtering and thereby affecting the particle size distribution and composition of the aerosol. The use of femtosecond laser pulses has been shown to be helpful in mitigating microparticle formation - a prevalent problem with longer nanosecond pulses - by reducing thermal effects and minimizing material melting. This advance in pulsed laser ablation not only refines aerosol particle sizes, but also increases the analytical accuracy and precision of the LA-ICP-MS method.

In addition, adjustments in the fluence and ablation mode are shown to play a pivotal role. Higher fluences with nanosecond lasers reduce preferential evaporation of volatiles on metal samples, independent of surface topography. The findings also confirm that the setting of the ablation mode, especially the spot size in spot ablation or the scan speed in scanning ablation, significantly affects the particle size distribution and thus directly affects the analytical signal. This work further confirmed that matrix and sample surface modifications are key to optimizing the laser-matter interaction. Surface treatments such as roughening, or deposition of metal nanoparticles can significantly affect the amount and size of produced particles due to changes in the optical and thermal properties of the surface. These modifications not only enhance the analytical signal, but also substantially reduce the detection limits.

The work underlines the basic factors influencing the course of laser-matter interaction and the formation of sample aerosol using methods such as diagnostics of ablation craters, measurement of aerosol particle size and concentration, and analysis of analytical signals. Other parameters such as carrier gas type and flow rate, ablation cell geometry and laser repetition rate are

certainly very important, and all these factors require thorough optimization for accurate and precise application of the LA-ICP-MS method.

In conclusion, the LA-ICP-MS technique is in a state of constant development. The move to shorter-wavelength, shorter-pulse lasers is designed to alleviate fractionation issues, along with the development of new calibration standards and advanced results processing that account for factors such as fractionation, matrix effects, and sample inhomogeneities. These advancements propel the method towards faster analyses, enhanced spatial resolution, reduced detection limits, and expanded applicability. The method is increasingly used not only for the analysis of trace elements, but also for the precise determination of the isotopic ratio and the identification and quantification of proteins after their labelling. This thesis significantly contributes to a deeper understanding of laser-matter interactions, pivotal for the continuous improvement and expansion of LA-ICP-MS applications across different scientific disciplines.

5 References

1. V. Wertich, M. Kubes, J. Leichmann, M. Holá, J. Haifler, J. Mozola, P. Hrselová, M. Jaros. "Trace element signatures of uraninite controlled by fluid-rock interactions: A case study from the Eastern Moldanubicum (Bohemian Massif)". Journal of Geochemical Exploration. 2022. 243: 107111. doi:10.1016/j.gexplo.2022.107111.
2. M. Hola, J. Kalvoda, H. Novakova, R. Skoda, V. Kanicky. "Possibilities of LA-ICP-MS technique for the spatial elemental analysis of the recent fish scales: Line scan vs. depth profiling". Applied Surface Science. 2011. 257(6): 1932-1940. doi:10.1016/j.apsusc.2010.09.029.
3. M. Hola, K. Novotny, J. Dobes, I. Krempl, V. Wertich, J. Mozola, M. Kubes, V. Faltusova, J. Leichmann, V. Kanicky. "Dual imaging of uranium ore by Laser Ablation Inductively Coupled Plasma Mass Spectrometry and Laser Induced Breakdown Spectroscopy". Spectrochimica Acta Part B-Atomic Spectroscopy. 2021. 186: 106312. doi:10.1016/j.sab.2021.106312.
4. V. Mozna, J. Pisonero, M. Hola, V. Kanicky, D. Guenther. "Quantitative analysis of Fe-based samples using ultraviolet nanosecond and femtosecond laser ablation-ICP-MS". Journal of Analytical Atomic Spectrometry. 2006. 21(11): 1194-1201. doi:10.1039/b606988f.
5. M. Hola, Z. Salajkova, A. Hrdlicka, P. Porizka, K. Novotny, L. Celko, P. Sperka, D. Prochazka, J. Novotny, P. Modlitbova, V. Kanicky, J. Kaiser. "Feasibility of Nanoparticle-Enhanced Laser Ablation Inductively Coupled Plasma Mass Spectrometry". Analytical Chemistry. 2018. 90(20): 11820-11826. doi:10.1021/acs.analchem.8b01197.
6. Z. Salajkova, M. Hola, D. Prochazka, J. Ondracek, D. Pavlinak, L. Celko, F. Gregar, P. Sperka, P. Porizka, V. Kanicky, A. Giacomo, J. Kaiser. "Influence of sample surface topography on laser ablation process". Talanta. 2021. 222: 121512. doi:10.1016/j.talanta.2020.121512.
7. H. Novakova, M. Hola, M. Vojtisek-Lom, J. Ondracek, V. Kanicky. "Online monitoring of nanoparticles formed during nanosecond laser ablation". Spectrochimica Acta Part B-Atomic Spectroscopy. 2016. 125: 52-60. doi:10.1016/j.sab.2016.09.017.
8. M. Hola, J. Ondracek, H. Novakova, M. Vojtisek-Lom, R. Hadravova, V. Kanicky. "The influence of material properties on highly time resolved particle formation for nanosecond laser ablation". Spectrochimica Acta Part B-Atomic Spectroscopy. 2018. 148: 193-204. doi:10.1016/j.sab.2018.07.001.
9. M. Hola, V. Konecna, P. Mikuska, J. Kaiser, V. Kanicky. "Influence of physical properties and chemical composition of sample on formation of aerosol particles generated by nanosecond laser ablation at 213 nm". Spectrochimica Acta Part B-Atomic Spectroscopy. 2010. 65(1): 51-60. doi:10.1016/j.sab.2009.11.003.
10. M. Hola, V. Konecna, P. Mikuska, J. Kaiser, K. Palenikova, S. Prusa, R. Hanzlikova, V. Kanicky. "Study of aerosols generated by 213 nm laser ablation of cobalt-cemented hard metals". Journal of Analytical Atomic Spectrometry. 2008. 23(10): 1341-1349. doi:10.1039/b802906g.
11. M. Hola, P. Mikuska, R. Hanzlikova, J. Kaiser, V. Kanicky. "Tungsten carbide precursors as an example for influence of a binder on the particle formation in the nanosecond laser ablation of powdered materials". Talanta. 2010. 80(5): 1862-1867. doi:10.1016/j.talanta.2009.10.035.
12. M. Hola, Z. Salajkova, A. Hrdlicka, J. Ondracek, K. Novotny, D. Pavlinak, M. Vojtisek-Lom, L. Celko, P. Porizka, V. Kanicky, D. Prochazka, J. Novotny, J. Kaiser. "The effect of nanoparticle presence on aerosol formation during nanoparticle-enhanced laser ablation inductively coupled plasma mass spectrometry". Journal of Analytical Atomic Spectrometry. 2020. 35(12): 2893-2900. doi:10.1039/d0ja00324g.
13. R.E. Russo, X.L. Mao, H.C. Liu, J. Gonzalez, S.S. Mao. "Laser ablation in analytical chemistry - a review". Talanta. 2002. 57(3): 425-451. doi:10.1016/s0039-9140(02)00053-x.
14. C.C. Garcia, H. Lindner, K. Niemax. "Laser ablation inductively coupled plasma mass spectrometry-current shortcomings, practical suggestions for improving performance, and experiments to guide future development". Journal of Analytical Atomic Spectrometry. 2009. 24(1): 14-26. doi:10.1039/b813124b.

15. E. Vanícková, M. Holá, K. Rapouch, D. Pavlinák, R. Kopecká, V. Kanicky. “LA-ICP-MS analysis of metal layers on samples of cultural heritage”. Chemical Papers. 2019. 73(12): 2923-2936. doi:10.1007/s11696-019-00745-6.
16. J. Pisonero, J. Koch, M. Wälle, W. Hartung, N.D. Spencer, D. Günther. “Capabilities of femtosecond laser ablation inductively coupled plasma mass spectrometry for depth profiling of thin metal coatings”. Analytical Chemistry. 2007. 79(6): 2325-2333. doi:10.1021/ac062027s.
17. M.L. Warburton, M.R. Reid, C.H. Stirling, G. Closs. “Validation of depth-profiling LA-ICP-MS in otolith applications”. Canadian Journal of Fisheries and Aquatic Sciences. 2017. 74(4): 572-581. doi:10.1139/cjfas-2016-0063.
18. L. Lobo, B. Fernández, R. Pereiro. “Depth profile analysis with glow discharge spectrometry”. Journal of Analytical Atomic Spectrometry. 2017. 32(5): 920-930. doi:10.1039/c7ja00055c.
19. J. Kalvoda, T. Kumpan, M. Hola, O. Babek, V. Kanicky, R. Skoda. “Fine-scale LA-ICP-MS study of redox oscillations and REEY cycling during the latest Devonian Hangenberg Crisis (Moravian Karst, Czech Republic)”. Palaeogeography Palaeoclimatology Palaeoecology. 2018. 493: 30-43. doi:10.1016/j.palaeo.2017.12.034.
20. S.F. Foley, D.E. Jacob, H.S.C. O'Neill. “Trace element variations in olivine phenocrysts from Ugandan potassic rocks as clues to the chemical characteristics of parental magmas”. Contributions to Mineralogy and Petrology. 2011. 162(1): 1-20. doi:10.1007/s00410-010-0579-y.
21. M. Danek, T. Bell, C.P. Laroque. “SOME CONSIDERATIONS IN THE RECONSTRUCTION OF LEAD LEVELS USING LASER ABLATION: LESSONS FROM THE DESIGN STAGE OF AN URBAN DENDROCHEMISTRY STUDY, ST. JOHN'S, CANADA”. Geochronometria. 2015. 42(1): 217-231. doi:10.1515/geochr-2015-0024.
22. M. Sanborn, K. Telmer. “The spatial resolution of LA-ICP-MS line scans across heterogeneous materials such as fish otoliths and zoned minerals”. Journal of Analytical Atomic Spectrometry. 2003. 18(10): 1231-1237. doi:10.1039/b302513f.
23. K. Proksova, K. Novotny, J. Kaiser, M. Galiova, T. Vaculovic, V. Kanicky. “Study of elemental distribution in urinary stones by Laser Ablation Inductively Coupled Plasma Mass Spectrometry (LA-ICP-MS)”. Journal of Biochemical Technology. 2010. 2(5): S106-S107.
24. A.G. Coedo, T. Dorado, I. Padilla, J.C. Fariñas. “Study of heterogeneities in steels and determination of soluble and total aluminium and titanium concentration by laser ablation inductively coupled plasma mass spectrometry”. Talanta. 2007. 71(5): 2108-2120. doi:10.1016/j.talanta.2006.10.027.
25. A.V. Izmer, M.V. Zoriy, C. Pickhardt, W. Quadakkers, V. Shemet, L. Singheiser, J.S. Becker. “LA-ICP-MS studies of cross section of NiCrAlY-based coatings on high-temperature alloys”. Journal of Analytical Atomic Spectrometry. 2005. 20(9): 918-923. doi:10.1039/b505459c.
26. C. Vlachou-Mogire, B. Stern, J.G. McDonnell. “The application of LA-ICP-MS in the examination of the thin plating layers found in late Roman coins”. Nuclear Instruments & Methods in Physics Research Section B-Beam Interactions with Materials and Atoms. 2007. 265(2): 558-568. doi:10.1016/j.nimb.2007.09.040.
27. J.T. van Elteren, V.S. Selih, M. Sala. “Insights into the selection of 2D LA-ICP-MS (multi)elemental mapping conditions”. Journal of Analytical Atomic Spectrometry. 2019. 34(9): 1919-1931. doi:10.1039/c9ja00166b.
28. P.A. Doble, R.G. de Vega, D.P. Bishop, D.J. Hare, D. Clases. “Laser Ablation-Inductively Coupled Plasma-Mass Spectrometry Imaging in Biology”. Chemical Reviews. 2021. 121(19): 11769-11822. doi:10.1021/acs.chemrev.0c01219.
29. P. Stepka, M. Kratochvilova, M. Kuchynka, M. Raudenska, H.H. Polanska, T. Vicar, T. Vaculovic, M. Vaculovicova, M. Masarik. “Determination of Renal Distribution of Zinc, Copper, Iron, and Platinum in Mouse Kidney Using LA-ICP-MS”. Biomed Research International. 2021. 2021: 6800294. doi:10.1155/2021/6800294.
30. Q.H. Luo, H.Z. Wang. “Elemental Quantitative Distribution and Statistical Analysis on Cross Section of Stainless Steel Sheet by Laser Ablation Inductively Coupled Plasma Mass Spectrometry”. Journal of Iron and Steel Research International. 2015. 22(8): 730-737. doi:10.1016/s1006-706x(15)30064-9.
31. T. Warchilová, V. Dillingerová, R. Skoda, T. Simo, O. Matal, T. Vaculovic, V. Kanicky. “Corrosion of nickel-based structural materials for nuclear reactors by molten fluoride salt: From bulk content of

corrosion products to elemental imaging of corrosion changes". Spectrochimica Acta Part B-Atomic Spectroscopy. 2018. 148: 113-117. doi:10.1016/j.sab.2018.06.010.
32. S. Wagner, C. Hummel, J. Santner, M. Puschenreiter, J. Irrgeher, W.W. Wenzel, S.M. Borisov, T. Prohaska. "In situ spatiotemporal solute imaging of metal corrosion on the example of magnesium". Analytica Chimica Acta. 2022. 1212: 339910. doi:10.1016/j.aca.2022.339910.
33. J.T. van Elteren, S. Panighello, V.S. Selih, E.F. Orsega. "Optimization of 2D LA-ICP-MS Mapping of Glass with Decorative Colored Features: Application to Analysis of a Polychrome Vessel Fragment from the Iron Age". Recent Advances in Laser Ablation Icp-Ms for Archaeology. 2016. 53-71. doi:10.1007/978-3-662-49894-1_4.
34. A. Gundlach-Graham, M. Burger, S. Allner, G. Schwarz, H.A.O. Wang, L. Gyr, D. Grolimund, B. Hattendorf, D. Günther. "High-Speed, High-Resolution, Multielemental Laser Ablation-Inductively Coupled Plasma-Time-of-Flight Mass Spectrometry Imaging: Part I. Instrumentation and Two-Dimensional Imaging of Geological Samples". Analytical Chemistry. 2015. 87(16): 8250-8258. doi:10.1021/acs.analchem.5b01196.
35. D. Chew, K. Drost, J.H. Marsh, J.A. Petrus. "LA-ICP-MS imaging in the geosciences and its applications to geochronology". Chemical Geology. 2021. 559: 119917. doi:10.1016/j.chemgeo.2020.119917.
36. M. Ohata, D. Tabersky, R. Glaus, J. Koch, B. Hattendorf, D. Gunther. "Comparison of 795 nm and 265 nm femtosecond and 193 nm nanosecond laser ablation inductively coupled plasma mass spectrometry for the quantitative multi-element analysis of glass materials". Journal of Analytical Atomic Spectrometry. 2014. 29(8): 1345-1353. doi:10.1039/c4ja00030g.
37. H.R. Kuhn, D. Gunther. "Elemental fractionation studies in laser ablation inductively coupled plasma mass spectrometry on laser-induced brass aerosols". Analytical Chemistry. 2003. 75(4): 747-753. doi:10.1021/ac0259919.
38. D. Bäuerle. Laser processing and chemistry. 2011.
39. R.E. Russo, X.L. Mao, J.J. Gonzalez, V. Zorba, J. Yoo. "Laser Ablation in Analytical Chemistry". Analytical Chemistry. 2013. 85(13): 6162-6177. doi:10.1021/ac4005327.
40. K.H. Leitz, B. Redlingshofer, Y. Reg, A. Otto, M. Schmidt. "Metal Ablation with Short and Ultrashort Laser Pulses". Lasers in Manufacturing 2011: Proceedings of the Sixth International Wlt Conference on Lasers in Manufacturing, Vol 12, Pt B. 2011. 12: 230-238. doi:10.1016/j.phpro.2011.03.128.
41. P.M. Outridge, W. Doherty, D.C. Gregoire. "Ablative and transport fractionation of trace elements during laser sampling of glass and copper". Spectrochimica Acta Part B-Atomic Spectroscopy. 1997. 52(14): 2093-2102. doi:10.1016/s0584-8547(97)00112-2.
42. M. Hola, V. Otruba, V. Kanicky. "Influence of binders on infrared laser ablation of powdered tungsten carbide pressed pellets in comparison with sintered tungsten carbide hardmetals studied by inductively coupled plasma atomic emission spectrometry". Spectrochimica Acta Part B-Atomic Spectroscopy. 2006. 61(5): 515-524. doi:10.1016/j.sab.2006.03.007.
43. D. Marla, U.V. Bhandarkar, S.S. Joshi. "A model of laser ablation with temperature-dependent material properties, vaporization, phase explosion and plasma shielding". Applied Physics a-Materials Science & Processing. 2014. 116(1): 273-285. doi:10.1007/s00339-013-8118-0.
44. B.J. Fryer, S.E. Jackson, H.P. Longerich. "DESIGN, OPERATION AND ROLE OF THE LASER-ABLATION MICROPROBE COUPLED WITH AN INDUCTIVELY-COUPLED PLASMA - MASS-SPECTROMETER (LAM-ICP-MS) IN THE EARTH-SCIENCES". Canadian Mineralogist. 1995. 33: 303-312.
45. M. Guillong, I. Horn, D. Gunther. "A comparison of 266 nm, 213 nm and 193 nm produced from a single solid state Nd : YAG laser for laser ablation ICP-MS". Journal of Analytical Atomic Spectrometry. 2003. 18(10): 1224-1230. doi:10.1039/b305434a.
46. O.V. Borisov, X.L. Mao, R.E. Russo. "Effects of crater development on fractionation and signal intensity during laser ablation inductively coupled plasma mass spectrometry". Spectrochimica Acta Part B-Atomic Spectroscopy. 2000. 55(11): 1693-1704. doi:10.1016/s0584-8547(00)00272-x.
47. R. Glaus, R. Kaegi, F. Krumeich, D. Gunther. "Phenomenological studies on structure and elemental composition of nanosecond and femtosecond laser-generated aerosols with implications on laser ablation inductively coupled plasma mass spectrometry". Spectrochimica Acta Part B-Atomic Spectroscopy. 2010. 65(9-10): 812-822. doi:10.1016/j.sab.2010.07.005.

48. R. Jaworski, E. Hoffmann, H. Stephanowitz. “Collection and separation of particles by size from laser ablated material”. International Journal of Mass Spectrometry. 2002. 219(2): 373-379. doi:10.1016/s1387-3806(02)00768-6.
49. H.R. Kuhn, J. Koch, R. Hargenroder, K. Niemax, M. Kalberer, D. Gunther. “Evaluation of different techniques for particle size distribution measurements on laser-generated aerosols”. Journal of Analytical Atomic Spectrometry. 2005. 20(9): 894-900. doi:10.1039/b504563k.
50. E.C. Hathorne, R.H. James, P. Savage, O. Alard. “Physical and chemical characteristics of particles produced by laser ablation of biogenic calcium carbonate”. Journal of Analytical Atomic Spectrometry. 2008. 23(2): 240-243. doi:10.1039/b706727e.
51. J. Kosler, M. Wiedenbeck, R. Wirth, J. Hovorka, P. Sylvester, J. Mikova. “Chemical and phase composition of particles produced by laser ablation of silicate glass and zircon - implications for elemental fractionation during ICP-MS analysis”. Journal of Analytical Atomic Spectrometry. 2005. 20(5): 402-409. doi:10.1039/b41629b.
52. G. Alloncle, N. Gilon, C. Legens, C.P. Lienemann, B. Rebours, L. Sorbier, S. Morin, R. Revel. “Following the evolution of morphology, composition and crystallography of alumina based catalysts after laser ablation: Implications for analysis by LA-ICP-AES”. Applied Surface Science. 2009. 255(22): 8978-8985. doi:10.1016/j.apsusc.2009.05.160.
53. D. Fliegel, M. Klementova, J. Kosler. “Phase and Composition Changes of Titanite during Laser Ablation Inductively Coupled Plasma Mass Spectrometry Analysis”. Analytical Chemistry. 2010. 82(10): 4272-4277. doi:10.1021/ac902284y.
54. E.O. Knutson, Whitby, K.T. “Aerosol classification by electric mobility: apparatus, theory, and applications”. 1975. 6: 443-451.
55. A. Wiedensohler, A. Wiesner, K. Weinhold, W. Birmili, M. Hermann, M. Merkel, T. Muller, S. Pfeifer, A. Schmidt, T. Tuch, F. Velarde, P. Quincey, S. Seeger, A. Nowak. “Mobility particle size spectrometers: Calibration procedures and measurement uncertainties”. Aerosol Science and Technology. 2018. 52(2): 146-164. doi:10.1080/02786826.2017.1387229.
56. H. Tammet, A. Mirme, E. Tamm. “Electrical aerosol spectrometer of Tartu University”. Atmospheric Research. 2002. 62(3-4): 315-324. doi:10.1016/s0169-8095(02)00017-0.
57. W.W. Szymanski, A. Nagy, A. Czitrovszky. “Optical particle spectrometry-Problems and prospects”. Journal of Quantitative Spectroscopy & Radiative Transfer. 2009. 110(11): 918-929. doi:10.1016/j.jqsrt.2009.02.024.
58. A. Berner, C. Lurzer, F. Pohl, O. Preining, P. Wagner. “SIZE DISTRIBUTION OF THE URBAN AEROSOL IN VIENNA”. Science of the Total Environment. 1979. 13(3): 245-261. doi:10.1016/0048-9697(79)90105-0.
59. D.W. Lee, M.D. Cheng. “Particle generation by ultraviolet-laser ablation during surface decontamination”. Journal of the Air & Waste Management Association. 2006. 56(11): 1591-1598.
60. Z. Marton, L. Landstrom, M. Boman, P. Heszler. “A comparative study of size distribution of nanoparticles generated by laser ablation of graphite and tungsten”. Materials Science & Engineering C-Biomimetic and Supramolecular Systems. 2003. 23(1-2): 225-228. doi:10.1016/s0928-4931(02)00272-2.
61. B.P. Lee, Y.J. Li, R.C. Flagan, C. Lo, C.K. Chan. “Sizing Characterization of the Fast-Mobility Particle Sizer (FMPS) Against SMPS and HR-ToF-AMS”. Aerosol Science and Technology. 2013. 47(9): 1030-1037. doi:10.1080/02786826.2013.810809.
62. C. Paton, J.D. Woodhead, J.C. Hellstrom, J.M. Hergt, A. Greig, R. Maas. “Improved laser ablation U-Pb zircon geochronology through robust downhole fractionation correction”. Geochemistry Geophysics Geosystems. 2010. 11: Q0aa06. doi:10.1029/2009gc002618.
63. X. Lin, W. Guo, L.L. Jin, S.H. Hu. “Review: Elemental Analysis of Individual Fluid Inclusions by Laser Ablation-ICP-MS”. Atomic Spectroscopy. 2020. 41(1): 1-10. doi:10.46770/as.2020.01.001.
64. C. Paton, J. Hellstrom, B. Paul, J. Woodhead, J. Hergt. “Iolite: Freeware for the visualisation and processing of mass spectrometric data”. Journal of Analytical Atomic Spectrometry. 2011. 26(12): 2508-2518. doi:10.1039/c1ja10172b.

65. V. Faltusova, T. Vaculovic, M. Hola, V. Kanicky. “Ilaps - python software for data reduction and imaging with LA-ICP-MS”. Journal of Analytical Atomic Spectrometry. 2022. 37(4): 733-740. doi:10.1039/d1ja00383f.
66. O. Branson, J.S. Fehrenbacher, L. Vetter, A.Y. Sadekov, S.M. Eggins, H.J. Spero. “LAtools: A data analysis package for the reproducible reduction of LA-ICPMS data”. Chemical Geology. 2019. 504: 83-95. doi:10.1016/j.chemgeo.2018.10.029.
67. J.C. Wright, M.J. Wirth. “PRINCIPLES OF LASERS”. Analytical Chemistry. 1980. 52(9): 1087-1095. doi:10.1021/ac50059a004.
68. D. Figg, M.S. Kahr. “Elemental fractionation of glass using laser ablation inductively coupled plasma mass spectrometry”. Applied Spectroscopy. 1997. 51(8): 1185-1192. doi:10.1366/0003702971941728.
69. T.E. Jeffries, W.T. Perkins, N.J.G. Pearce. “COMPARISONS OF INFRARED AND ULTRAVIOLET-LASER PROBE MICROANALYSIS INDUCTIVELY-COUPLED PLASMA-MASS SPECTROMETRY IN MINERAL ANALYSIS”. Analyst. 1995. 120(5): 1365-1371. doi:10.1039/an9952001365.
70. C.Y. Liu, X.L. Mao, J. Gonzalez, R.E. Russo. “Study of particle size infkuence on laser ablation inductively coupled plasma mass spectrometry using an in-line cascade impactor”. Journal of Analytical Atomic Spectrometry. 2005. 20(3): 200-203. doi:10.1039/b414422h.
71. S.D. Zhang, M.H. He, Z.B. Yin, E.Y. Zhu, W. Hang, B.L. Huang. “Elemental fractionation and matrix effects in laser sampling based spectrometry”. Journal of Analytical Atomic Spectrometry. 2016. 31(2): 358-382. doi:10.1039/c5ja00273g.
72. P.K. Diwakar, S.S. Harilal, N.L. LaHaye, A. Hassanein, P. Kulkarni. “The influence of laser pulse duration and energy on ICP-MS signal intensity, elemental fractionation, and particle size distribution in NIR fs-LA-ICP-MS”. Journal of Analytical Atomic Spectrometry. 2013. 28(9): 1420-1429. doi:10.1039/c3ja50088h.
73. C. Liu, X.L. Mao, S.S. Mao, X. Zeng, R. Greif, R.E. Russo. “Nanosecond and ferntosecond laser ablation of brass: Particulate and ICPMS measurements”. Analytical Chemistry. 2004. 76(2): 379-383. doi:10.1021/ac035040a.
74. R. Hergenroder. “A model of non-congruent laser ablation as a source of fractionation effects in LA-ICP-MS”. Journal of Analytical Atomic Spectrometry. 2006. 21(5): 505-516. doi:10.1039/b600698a.
75. R. Hergenroder. “Hydrodynamic sputtering as a possible source for fractionation in LA-ICP-MS”. Journal of Analytical Atomic Spectrometry. 2006. 21(5): 517-524. doi:10.1039/b600705h.
76. H.R. Kuhn, D. Gunther. “Laser ablation-ICP-MS: particle size dependent elemental composition studies on filter-collected and online measured aerosols from glass”. Journal of Analytical Atomic Spectrometry. 2004. 19(9): 1158-1164. doi:10.1039/b404729j.
77. Q.Z. Bian, C.C. Garcia, J. Koch, K. Niemax. “Non-matrix matched calibration of major and minor concentrations of Zn and Cu in brass, aluminium and silicate glass using NIR femtosecond laser ablation inductively coupled plasma mass spectrometry”. Journal of Analytical Atomic Spectrometry. 2006. 21(2): 187-191. doi:10.1039/b513690c.
78. H.R. Kuhn, M. Guillong, D. Gunther. “Size-related vaporisation and ionisation of laser-induced glass particles in the inductively coupled plasma”. Analytical and Bioanalytical Chemistry. 2004. 378(4): 1069-1074. doi:10.1007/s00216-003-2346-7.
79. X.L. Mao, W.T. Chan, M. Caetano, M.A. Shannon, R.E. Russo. “Preferential vaporization and plasma shielding during nano-second laser ablation”. Applied Surface Science. 1996. 96-8: 126-130. doi:10.1016/0169-4332(95)00420-3.
80. T. Ohkubo, M. Kuwata, B. Luk'yanchuk, T. Yabe. “Numerical analysis of nanocluster formation within ns-laser ablation plume”. Applied Physics a-Materials Science & Processing. 2003. 77(2): 271-275. doi:10.1007/s00339-003-2135-3.
81. H.R. Kuhn, D. Gunther. “The agglomeration state of nanosecond laser-generated aerosol particles entering the ICP”. Analytical and Bioanalytical Chemistry. 2005. 383(3): 434-441. doi:10.1007/s00216-005-0021-x.
82. S.W. Zeng, D. Baillargeat, H.P. Ho, K.T. Yong. “Nanomaterials enhanced surface plasmon resonance for biological and chemical sensing applications”. Chemical Society Reviews. 2014. 43(10): 3426-3452. doi:10.1039/c3cs60479a.

6 Abbreviations

APS	Aerodynamic Particle Sizer
BSE	Back-Scattered Electrons
CPC	Condensation Particle Counter
CPS	Counts Per Second
D_m	Mobility diameter (measured by Differential Mobility Analyser)
DMA	Differential Mobility Analyser
EEPS	Engine Exhaust Particle Sizer
EDS	Energy Dispersive X-ray Spectroscopy
EDX	Energy Dispersive X-ray Spectroscopy
EPMA	Electron Probe Micro Analysis
FI	Fractionation Index
FMPS	Fast Mobility Particle Sizer
ICP	Inductively Coupled Plasma
ICP-MS	Inductively Coupled Plasma Mass Spectrometry
LA	Laser Ablation
LA-Q-ICP-MS	Laser Ablation with Quadrupole Inductively Coupled Plasma Mass Spectrometry
LA-ICP-MS	Laser Ablation with Inductively Coupled Plasma Mass Spectrometry
LOD	Limit of Detection
Nd:YAG	Neodymium-doped Yttrium Aluminium Garnet; $Nd:Y_3Al_5O_{12}$
NE-LA	Nanoparticle-Enhanced Laser Ablation
NP	Nanoparticle
OPC	Optical Particle Counter
OPS	Optical Particle Sizer
PIXE	Particle-induced X-ray Emission
PNC	Particle Number Concentration
PSD	Particle Size Distribution
SD	Standard Deviation
SEM	Scanning Electron Microscopy
SMPS	Scanning Mobility Particle Sizer
SRM	Standard Reference Material
TEM	Transmission Electron Microscopy

7 Attachment

The appendix contains a set of papers commenting on this habilitation thesis in the order listed in Chapter 1.2.

PAPER 1

Trace element signatures of uraninite controlled by fluid-rock interactions: A case study from the Eastern Moldanubicum (Bohemian Massif)

Wertich, V.*, Kubeš, M., Leichmann, J., **Holá, M.**, Haifler, J., Mozola, J., Hršelová, P., Jaroš, M.

Journal of Geochemical Exploration. 2022, 243, 107111. DOI 10.1016/j.gexplo.2022.107111

Contribution:

LA-ICP-MS design of experiments and measurements, data evaluation, participation in manuscript writing.

Journal of Geochemical Exploration 243 (2022) 107111

Contents lists available at ScienceDirect

Journal of Geochemical Exploration

journal homepage: www.elsevier.com/locate/gexplo

Trace element signatures of uraninite controlled by fluid-rock interactions: A case study from the Eastern Moldanubicum (Bohemian Massif)

Vojtěch Wertich [a,b,*], Martin Kubeš [a,b], Jaromír Leichmann [a], Markéta Holá [c], Jakub Haifler [a], Juraj Mozola [a], Pavla Hršelová [d], Michal Jaroš [e]

[a] Department of Geological Sciences, Masaryk University, Kotlářská 267/2, Brno 61137, Czech Republic
[b] Czech Geological Survey, Klárov 3, Prague, 11821, Czech Republic
[c] Department of Chemistry, Masaryk University, Kamenice 753/5, Brno 62500, Czech Republic
[d] Department of Mineralogy and Petrography, Moravian Museum, Zelný trh 6, Brno 65937, Czech Republic
[e] Diamo S. E., Branch GEAM, 592 51 Dolní Rožínka, Czech Republic

ARTICLE INFO

Keywords:
Uraninite
Trace elements
Geochemistry signatures
Fluid-rock interaction
REE
HFSE

ABSTRACT

The eastern part of the Moldanubian Zone (Bohemian Massif, Czech Republic) hosts the Western Moravian uranium (U) province where U exploitation was active from 1957 to 2017 with total production about 24,000 t of U. A set of 369 laser ablation-inductively coupled plasma mass spectrometry (LA-ICP-MS) analyses were performed to simultaneously assay 50 chemical elements in samples of unaltered uraninite from this U province, alongside 246 electron microprobe analyses (EMPA) to determine the major and minor element compositions of the latter. Such large sets of analyses allowed comparisons to be made and a possible classification of individual deposits and/or ore fields based on the major, minor, and trace elements compositions of uraninite. According to the results, uraninite samples from individual U ore fields or even deposits exhibited contrasting trace element signatures. For example, minor elements such as Ca differed significantly (median of CaO 3.1–9.0 wt%), while ∑REE and Y, which are common substituents in uraninite, reached median values on 4.3–6495 and 6.5–1552 ppm, respectively. The REE chondrite normalized patterns along with Eu anomalies (Eu_N/Eu_N^* 0.06–1.50) of uraninite varied significantly among the studied deposits. The Zr contents commonly ranged over only a few ppm. However, the uraninite samples from two deposits of the ore province (Rozsochy and Rožná-Jasan) yielded anomalously high Zr contents (medians of thousands of ppm and maximum contents of up to 2 wt%) which are not common for hydrothermal uraninite. Furthermore, significant variations were also observed in the concentrations of Nb, Ti, and V, for example. All deposits in the province have very similar mineralogical, ore textural, or structural features (low temperature shear zone hosted U veins) as well as timing of mineralization events (Permian age). Such significant trace element variations in uraninite within one U ore province are uncommon and may underline the limitations of using the trace element compositions of uraninite as a tool for provenance studies or determining the function of a type of U deposit. We suggest that factors such as the physico-chemical conditions, lithological controls, and fluid-rock interaction processes on a deposit/ore field scale can significantly control the minor and trace element compositions of uraninite.

1. Introduction

Uraninite can be hosted in diverse geological environments and on different scales, from occurring as an accessory mineral in intrusive rocks to forming high-grade orebodies in a range of uranium (U) deposit types (Dahlkamp, 1993; Cuney, 2008). Various opinions on the genesis and classification of U deposit types have been developed over the past 50 years (Ruzicka, 1971; Dahlkamp, 1978; Dahlkamp, 1993; Nash et al., 1981; Cuney and Kyser, 2009). The latest geological classification compiled by the International Atomic Energy Agency (IAEA, 2018) subdivided U deposits into 15 main types and over 50 subtypes.

With the recent development of fast low detection limit analytical techniques such as laser ablation-inductively coupled plasma mass spectrometry (LA-ICP-MS) or secondary ion mass spectrometry (SIMS), studies using trace elements systematics in uraninite as a possible function of a deposit type (Mercadier et al., 2011; Alexandre et al., 2015;

* Corresponding author at: Department of Geological Sciences, Masaryk University, Kotlářská 267/2, Brno 61137, Czech Republic.
E-mail address: wertich@sci.muni.cz (V. Wertich).

https://doi.org/10.1016/j.gexplo.2022.107111
Received 4 July 2022; Received in revised form 13 October 2022; Accepted 14 October 2022
Available online 20 October 2022

Eglinger et al., 2013) or provenance source (Depiné et al., 2013; Frimmel et al., 2014; Spano et al., 2017) have emerged. Minor and trace elements can be incorporated into uraninite due to its complex formula $(U^{4+}_{1-x-y-z}U^{6+}_{x}REE^{3+}_{y}M^{2+}_{z})O_{2+x-(0.5y)-z}$ (Janeczek and Ewing, 1992a) and presence within it of structural defects and ionic substitutions. Moreover, processes connected to the radioactive decay of U to Pb, oxidation of U^{4+} to U^{6+}, alterations under oxidizing or reducing conditions, as well other processes (Janeczek and Ewing, 1992a; Janeczek and Ewing, 1992b; Finch and Ewing, 1992; Janeczek and Ewing, 1995; Alexandre and Kyser, 2005; Ballouard et al., 2017) allow the uraninite structure to host (or lose) a variety of elements and not only those with an ionic radius close to the 1 Å of U^{4+} (e.g. REE^{3+} 1.116–0.98, Y^{3+}1.019 Å, Ca^{2+} 1.12 Å, Th^{4+} 1.5 Å, VIII coordination; Shannon, 1976). Considering the associations and quantity of major, minor, and trace elements and its comparison between uraninite from individual deposit types, previous authors have reported that among other trace elements, the chondrite normalized values of rare earth elements (REE) can serve as useful tools for specifying the provenance and/or type of deposit (e.g., Bonhoure et al., 2007; Mercadier et al., 2011; Frimmel et al., 2014; Alexandre et al., 2015). On the other hand, in their research of uraninite from the unconformity-related deposits of the Athabasca basin, Martz et al. (2019a) outlined the disadvantages of this method due to the mobile behavior of REE and some other elements during post-crystallization alteration processes in uraninite.

The eastern margin of the Moldanubian Zone (Central Europe, Czech Republic, Bohemian Massif) hosts the Western Moravian U province which has a long history of U mining (1957–2017) and has yielded an overall production about 24,000 t of U (Arapov et al., 1984). Although the province has been considered in many studies (Arapov et al., 1984; Ruzicka, 1993; Kříbek et al., 2009; Kříbek et al., 2022; Dahlkamp, 2016), some variations in the described deposit types and the genesis/origin of the U mineralization are still not fully understood. To contribute to this topic, we gathered samples of unaltered uraninite mineralizations from all major deposits of this province. The main contribution of this study is its very large set of >600 point analyses measured on 23 uraninite samples to assess the possible differentiation or uniformity of the major, minor, and trace element signatures of uraninite from the whole mining province. The results reveal unusual trace elements signatures for low-

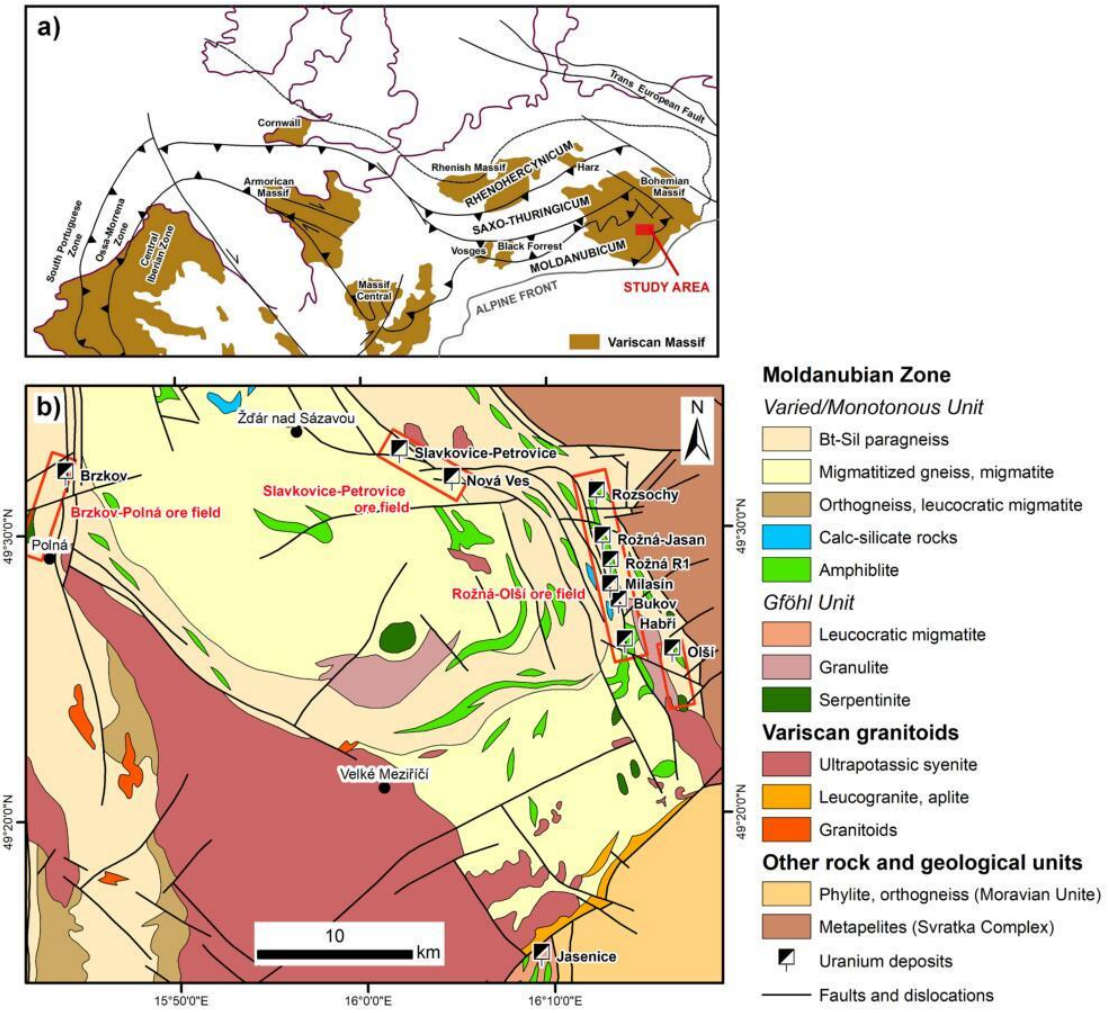

Fig. 1. a) Generalized tectonic scheme of Variscan massifs in western and central Europe with the location of the study area (edited after Franke, 2000); and b) geological map of the eastern part of the Moldanubian Zone (area of the Western Moravian uranium province) showing the locations of the ore fields (red rectangles) and of individual deposits and formal mines from where the studied samples were obtained (the map is edited after Tajčmanová et al., 2006). (For interpretation of the references to colour in this figure legend, the reader is referred to the web version of this article.)

temperature uraninite samples as well as significant trace element variations between individual ore fields considered to represent the same deposit type formed during the same time period.

2. Geological setting

The investigated U ore fields are located within the eastern part of the Moldanubian Zone (Fig. 1a and b) which traditionally divided into three major tectonostratigraphic units that are distinguished by contrasting lithological assemblages and different metamorphic conditions: the Monotonous, Varied, and Gföhl units (Dudek and Fediuková, 1974; Matte et al., 1990; Lardeaux et al., 2014). The Monotonous and Varied mid-crustal amphibolite facies units consist predominantly of migmatitic cordierite-biotite-sillimanite paragneisses along with minor orthogneisses and amphibolites; abundant intercalations/lenses of calc-silicate rocks, marble, quartzite, and graphitic gneiss are only characteristic of the Varied unit. In addition, boudins of retrogressed eclogites and spinel peridotite have been found particularly at the boundary between the two (Faryad et al., 2015). The sedimentary protoliths of both mid-crustal assemblages have been attributed Neoproterozoic-Early Paleozoic sedimentation ages (Košler et al., 2014). On the other hand, the lower crustal/upper mantle Gföhl unit, which is found structurally on the top of the Moldanubian sequence, consists mostly of anatectic orthogneisses and migmatites (Cooke and O'Brien, 2001; Hasalová et al., 2008), amphibolites with mid-ocean ridge basalt (MORB)-like composition associated with high-pressure (HP) felsic granulites (Tajčmanová et al., 2006; Vrána et al., 2013), and characteristically encloses minor eclogite bodies, and spinel and/or garnet-bearing peridotites and pyroxenites (Medaris et al., 2005; Medaris et al., 2006; Kusbach et al., 2015; Kubeš et al., 2022). The magmatic protolith of the Gföhl gneisses (sensu Fuchs, 1976) has been assigned Cambrian-Devonian ages (Friedl et al., 2004; Schulmann et al., 2005).

The Variscan metamorphic evolution of the Moldanubian Zone, with a peak stage at ~340 Ma (O'Brien and Rötzler, 2003; Janoušek and Holub, 2007), was accompanied by extensive plutonic activity occurring in contrasting geodynamic settings, mostly from the Late Devonian to the Carboniferous (e.g., Finger et al., 1997; Timmerman, 2008; Žák et al., 2014). The ultrapotassic magmatism is specifically a characteristic feature of the Gföhl unit, as exemplified by extensive occurrences of so-called durbachites which are typically found within the whole Variscan Orogenic Belt in western central Europe (Fig. 1a; e.g., von Raumer et al., 2013; Soder and Romer, 2018). For instance, the largest durbachite (ultrapotassic syenite) intrusion occurring in the Bohemian Massif, the Třebíč pluton (338 ± 3 Ma, U—Pb zircon; Janoušek et al., 2020), was originally around twice larger than today and its marginal part reached the tectonic boundary between the Moldanubian Zone and the Svratka Complex where the studied U deposits are located (Leichmann et al., 2017). The tectonic boundary between the high-grade Gföhl unit and the Svratka Complex, predominantly consisting of metapelites, corresponds to a low angle thrust between the two Moldanubian subunits (Tajčmanová et al., 2006).

3. Uranium ore deposits in the eastern part of the Moldanubian Zone

The U province in the eastern part of the Moldanubian Zone (also referred as the Western Moravian U province) can be divided into three major ore fields, in addition to some isolated U deposits and/or occurrences (Arapov et al., 1984; Dahlkamp, 2016). The studied samples were obtained from the U deposits of the Rožná-Olší, Slavkovice-Petrovice, and Brzkov-Polná ore fields (Fig. 1b). Only the Jasenice deposit located further to the south on the eastern edge of the ultrapotassic syenite Třebíč pluton (Fig. 1b) was not included in this research due to the unavailability of unaltered uraninite samples. The nomenclature of the samples used in the study is based on a specification or localization of the mine or exploration/mining shafts from which they were collected (e.g., shaft Rožná R-1, Bukov mine, Rozsochy mine etc.).

The deposits of this province are referred to as U veins in shear and fault zones (Ruzicka, 1993), share zone-hosted hydrothermal U mineralization (Kříbek et al., 2009), or as structure-bound monometallic vein subtypes of metamorphite U deposit types (IAEA, 2018). Kříbek et al. (2009) and René (2008) have also previously documented features of hydrothermal decomposition of U- and REE-bearing accessory minerals, subsequent U and REE mobilization, and a possible role of Permo-Carboniferous basinal fluids which link U mineralization in the ore province to a basement-hosted unconformity-type (Hecht and Cuney, 2000; Martz et al., 2019b). The mineralized shear zone and faults trend in a NNW-SSE direction in the case of the Rožná-Olší ore field and then become more westward-oriented toward the Slavkovice-Petrovice ore field (Fig. 1b). The Brzkov-Polná ore field (Fig. 1b) is located further to the west, on several smaller NW-SE trending structures situated within the large NNE-SSW oriented Přibyslav mylonite zone.

Kříbek et al. (2009) distinguished a pre-ore, ore, and post-ore substage of the uraniferous hydrothermal event that formed the Rožná deposit. The pre-ore substage was dated by Kříbek et al. (2009) as having occurred from 296.3 ± 7.5 to 281 ± 5.4 Ma by K—Ar ages of pre-ore authigenic K-feldspar. The pre-ore substage was characterized by temperatures of about 300 °C and its fluid inclusion compositions point to the large-scale mixing of basinal brines with meteoric water (Kříbek et al., 2009). Kříbek et al. (2009) suggested that U was leached from surrounding Moldanubian rocks during this substage. The temperature of the ore-substage itself decreased to 150–170 °C based on fluid inclusion and chlorite thermometry. Low-temperature ore-forming fluids and a gradual evolution toward cooler and higher salinity basinal brine-type fluids were documented in the same deposit by Hein et al. (2002). Uraninite isotopic bulk-phase U—Pb dating conducted on the unaltered uraninite from vein-type ores of the Rožná deposit (Anderson et al., 1988) yielded ages ranging from 270 to 280 Ma. K—Ar illite (277.2 ± 5.5 to 264 ± 4.3) and chemical U—Pb dating of hydrothermal monazite (268 ± 50 Ma) from the Rožná deposit further confirmed Permian ages for the uraniferous mineralization events (Kříbek et al., 2009).

There are two major types of U ore mineralization styles with different proportional representations in the individual ore fields of the Western Moravian U province. One is represented by network-disseminated coffinite>uraninite mineralizations occurring in narrow subparallel ore bodies formed along longitudinal, shear, and cataclasite zones. Cataclasite U ore zones are usually enriched in graphite and typical alteration processes include chloritization, pyritization, and carbonatization (Arapov et al.,1984; Kříbek et al., 2009; Dahlkamp, 2016). The ore grade is rather low for network-disseminated ores, ranging from 0.05 to 2 wt% U in the case of the Rožná deposit (Dahlkamp, 2016; Kříbek et al., 2009). The second type of mineralization style was described by Dahlkamp (2016) as a vein-type ore with a characteristic predominance of uraninite over coffinite in carbonates predominantly manifested as calcite veins. A detailed description of this variety was made using samples from the Rožná-Olší ore field where the U veins occurred mostly in tension gashes and horsetail-like structures of subsidiary faults genetically related to the master faults (Kříbek et al., 2009; Dahlkamp, 2016). The ore grades in the veins are considered 2–3 times higher than those of the network-disseminated ores (Dahlkamp, 2016). A third type of ore type (metasomatic type, described especially in the Rožná deposit), developed in albititized, desilicified, and commonly porous rocks hosts disseminated coffinite accompanied to a lesser extent by U-Zr-silicate mineralizations with a rather lower grade of 0.1–0.15 % U (Kříbek et al., 2009; Dahlkamp, 2016).

The description of mineralization styles is valid for all ore fields and/or deposits of the Western Moravian U province; we can observe only different representation of the described ore types on explored/mined resources between individual ore fields. The network-disseminated type of ore was dominant in the Rožná-Olší ore field (about 85 % of the resources), whereas "vein-type" ores accounted only for 10 % of the resources. In contrast, vein-type ores formed the majority of explored

resources in the Slavkovice-Petrovice ore field (80 % vein-type, 20 % network-disseminated ore). Vein-type ores also prevailed in the Brzkov-Polná ore field, accompanied by metasomatic type mineralization (Dahlkamp, 2016).

4. Methods

4.1. Samples

A total of 23 samples were gathered to cover all three ore fields of the Western Moravian U province (16 samples from the Rožná-Olší ore field, six from the Slavkovice-Petrovice ore field, and one from the Brzkov-Polná ore field/Brzkov deposit; see Fig. 1a; Table 1 and Table 2 for details). The samples were obtained from archives of the Moravian Museum and the DIAMO state enterprise (organization dealing with the elimination of the consequences of U mining activities), because the U mines are no longer in operation and therefore inaccessible, with the exception of a few parts of Rožná R1 (central part of the Rožná deposit) and Bukov deposits. The studied samples belong to vein-type ores where the unaltered domains of uraninite can be found (Fig. 3a-d). Selected high-grade ore samples were processed and made into polished thin sections which were subsequently studied by reflected light microscopy and backscattered electron (BSE) imaging to earmark unaltered parts of uraninite suitable for electron microprobe (EMP) and LA-ICP-MS analyses.

4.2. Electron microprobe analyses

The major and minor element chemistry of U mineralization from individual studied ore fields was determined using a Cameca SX 100 EMP analyzer at the Institute of Geological Sciences, Masaryk University Brno, the Czech Republic. The operating conditions for the EMP analyses of the most pure and unaltered uraninite were as follows: an accelerating voltage of 15 kV, a beam current of 20 nA (or 80 nA in case of chemical dating), and a beam size of 2–5 μm. During the analyses in wavelength-dispersive mode, the following standards, elements, and spectral lines were used: UO_2 (U *M*β), wollastonite (Si *K*α, Ca *K*α), vanadinite (V *K*α), almandine (Fe *K*α), alamosite (Pb *M*α), fluorapatite (P *K*α), YAG (Y *L*α), $SrSO_4$ (Sr *L*α, S *K*α), lammerite (As *L*α), ThO_2 (Th *M*α), $ScVO_4$ (Sc *K*α), $LaPO_4$ (La *L*α), $CePO_4$ (Ce *L*α), $PrPO_4$ (Pr *L*β), $NdPO_4$ (Nd *L*β), $SmPO_4$ (Sm *L*β), $GdPO_4$ (Gd *L*β), $DyPO_4$ (Dy *L*α), and $ErPO_4$ (Er *L*α). Only the unaltered parts of uraninite were chosen for analyses based on BSE imaging (Fig. 3a-d). An alteration phenomenon, coffinization, was occasionally observed; it could also be identified in the measured datasets through increased values of SiO_2 and lower UO_2 against unaltered uraninite. Therefore, we used an internal threshold on 5 wt% SiO_2 for both EMPA and LA-ICP-MS measurements. The results that exceeded the threshold were considered to represent uraninite that had already been affected by coffinization processes and were therefore excluded from the dataset. A total of 246 EMP analyses were performed on 23 samples.

Table 1
Electron microprobe analyses (EMPA): median values (wt%) for major and minor elements (UO_2, PbO, SiO_2, CaO). The numbers of samples and numbers of analyses for individual studied deposits used for median values are displayed in brackets (No. of samples / No. of analyses). All analyses used for the calculation of medians as well as other measured elements are included in the electronic supplementary material.

Ore field	Deposit (No. of samples/No. of analyses)	UO_2	PbO	SiO_2	CaO
Brzkov-Polná	Brzkov (1/8)	84.6	3.6	1.5	5.8
Slavkovice-Petrovice	Slavkovice (3/32)	85.8	3.2	1.2	6.7
	Petrovice (2/33)	84.2	3.2	1.6	7.5
	Nová Ves (1/12)	84.5	3.7	0.9	6.9
Rožná-Olší (Northern part)	Rozsochy (2/36)	82.8	2.8	3.5	3.1
	Rožná-Jasan (1/20)	83.6	3.0	3.1	4.0
Rožná-Olší (Central and Southern part)	Rožná R-1 (5/29)	84.3	3.5	1.2	5.7
	Milasín (3/25)	84.5	3.1	0.6	6.8
	Bukov (2/19)	84.9	3.8	0.8	5.7
	Habří (2/26)	84.9	3.2	0.7	6.3
	Olší (1/6)	82.5	3.1	1.7	9.0
Total No. samples / No. of analyses	23 / 246				

Electron microprobe dating of uraninite was performed using the approach of Montel et al. (1996). Given the zero or negligible Th contents of the samples, only U and Pb were involved effectively. Corrections of the spectral interferences of Th and Y on Pb *M*α and Th on U *M*β were considered in the analytical protocol. However, these overlaps were insignificant in the case of the compositions measured in this study. The calculation provided an apparent age for every analytical point. The weighted mean and 95 % confidence uncertainty for each compositional domain were calculated using the Isoplot v. 4.15 program (Ludwig, 2003).

4.3. Laser ablation-inductively coupled plasma mass spectrometry

Analyses of the major, minor, and trace elements of the samples were also conducted by LA-ICP-MS. The system consisted of a LSX-213 G2+ laser ablation device (Teledyne Cetac Technologies, USA) and Agilent 7900 ICP-MS analyzer with an octopole reaction cell (Agilent Technologies, Japan). The laser operated at a wavelength of 213 nm with a pulse duration ~4 ns. Using helium as a carrier gas with a flow rate of 0.9 l min^{-1}, the aerosol was washed out a 2-volume ablation cell (HelEx) and transported through a FEP (fluorinated ethylene propylene) tube (i.d. 2 mm, length 1 m) to the ICP-MS. The mass spectrometer operated with a forwarded power of 1550 W, an Ar gas flow rate of 15 l min^{-1} (outer plasma gas), and Ar makeup gas flow rate of 1 l min^{-1}. Spot ablations with a 50 μm spot diameter, repetition rate of 10 Hz, and fluence of 9 J cm^{-2} was performed for 60 s. The fifty following isotopes representing both the major components and trace elements of the samples were monitored with a total integration time of 4.5 s: ^{24}Mg, ^{29}Si, ^{31}P, ^{43}Ca, ^{45}Sc, ^{47}Ti, ^{51}V, ^{52}Cr, ^{55}Mn, ^{57}Fe, ^{60}Ni, ^{63}Cu, ^{66}Zn, ^{71}Ga, ^{72}Ge, ^{75}As, ^{78}Se, ^{85}Rb, ^{88}Sr, ^{89}Y, ^{90}Zr, ^{93}Nb, ^{95}Mo, ^{107}Ag, ^{118}Sn, ^{121}Sb, ^{137}Ba, ^{139}La, ^{140}Ce, ^{141}Pr, ^{146}Nd, ^{147}Sm, ^{153}Eu, ^{157}Gd, ^{159}Tb, ^{163}Dy, ^{165}Ho, ^{165}Er, ^{169}Tm, ^{172}Yb, ^{175}Lu, ^{178}Hf, ^{181}Ta, ^{182}W, ^{206}Pb, ^{207}Pb, ^{208}Pb, ^{209}Bi, ^{232}Th, ^{238}U.

Prior to processing the measured data for quantification, the time-resolved LA-ICP-MS spectra for individual measured isotopes were monitored. The correct isotope composition is recorded when the signal is only slightly declining when ablating one spot, corresponding to the gradual depression of the ablation crater (Fig. 2a). Such an ablation record indicates that there was only a minimal risk of an ablation spot being contaminated by fluid or mineral inclusions hidden under the surface. On the other hand, isotope records showing deviations from the described correct isotope records (Fig. 2b) could indicate the presence of a mineral or fluid inclusion that would strongly affect the geochemical composition of the measured uraninite and therefore such spots were not further considered in the measured datasets. The correct ablation records (Fig. 2a) were evaluated using the Ilaps software (Faltusová et al., 2022) which has been especially developed for data reduction and imaging (Holá et al., 2021) with LA-ICP-MS. External calibration was performed using the standard reference materials (SRM) NIST 610 and NIST 612. A total of 369 LA-ICP-MS analyses were performed on 19 samples.

5. Results

5.1. Texture of uraninite samples

All analyzed uraninite samples represent the abovementioned vein-type ores and share very similar textures characterized by massive and often colloform/botryoidal textures (Fig. 3b and Fig. 3c) surrounded or crosscut by veinlets of hydrothermal calcite (Fig. 3a-d). Uraninite is

Table 2
Laser ablation-inductively coupled mass spectrometry (LA-ICP-MS) analyses of selected trace elements (Ti, V, ∑REE, Y, Zr, Nb, and Th) with median values shown in ppm. The number of samples and number of analyses for individual studied deposits used for the median values are displayed in brackets (No. of samples / No. of analyses). Numerous analyses of Ti, Zr, Nb, Th yielded results which were below the detection limit (<LOD), especially in the Slavkovice-Petrovice ore field and the central and southern parts of the Rožná-Olší ore field. All analyses are included in the electronic supplementary material.

Ore field	Deposit (No. of samples / No. of analyses)	Ti	V	Y	Zr	Nb	W	∑REE	Th
Brzkov-Polná	Brzkov (1/20)	976	1433	1267	46	12	325	6495	0.3
Slavkovice-Petrovice	Slavkovice (3/63)	17	3479	20	0.31	1.02	279	11	0.01
	Petrovice (2/36)	28	2917	6.5	0.15	0.19	405	4.3	0.02
	Nová Ves (1/20)	54	4609	83	0.3	2.4	225	76	<LOD
Rožná-Olší (Northern part)	Rozsochy (2/25)	1294	3137	1552	3614	1868	477	1056	32
	Rožná-Jasan (2/49)	825	2117	496	2743	11	454	467	1.1
Rožná-Olší (Central and Southern part)	Rožná R-1 (2/35)	23	14,490	283	0.5	1.0	101	521	0.8
	Milasín (2/41)	21	12,607	135	5.3	0.4	53	229	0.39
	Bukov (2/42)	4.8	10,176	30	0.3	0.04	61	30	0.006
	Habří (1/19)	80	14,265	158	1.6	0.76	91	587	0.22
	Olší (1/19)	5.1	4678	51	0.19	0.13	28	96	0.08
Total No of samples/No. of analyses	19 / 369								

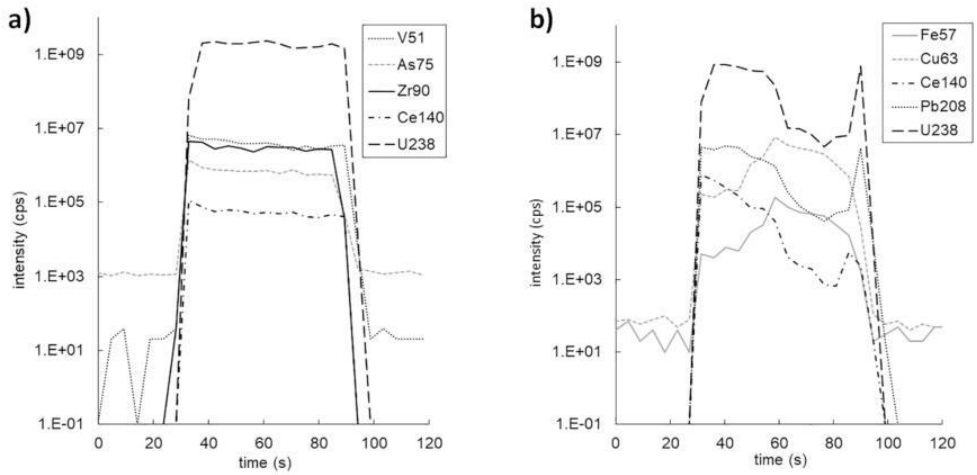

Fig. 2. a) Laser ablation-inductively coupled mass spectrometry (LA-ICP-MS) record of uraninite with the correct shape; and b) LA-ICP-MS record of uraninite point analysis contaminated by chalcopyrite mineral inclusions hidden under surface. Such analyses (b) were not further considered in the measured datasets.

occasionally locally brecciated and accompanied by coffinites (Fig. 3a) or is affected by secondary coffinitization. The detected sulphides consist mostly of pyrite (Fig. 3b), chalcopyrite, and less commonly galena, Fig. 3d); these predominantly belong to the pre-(uranium)ore stage and are commonly spatially associated with later uraninite. Conversely, Cu sulphoselenide (Fig. 3b), Ni—Co arsenide, montroseite, or Fe (Oxy)hydroxides are post-dating uraninite mineralizations in the studied samples. Uraninite mineralization is commonly hosted in thick hydrothermal carbonate veins predominantly composed of calcite.

5.2. Major and minor elements

Only the domains of unaltered uraninite in each sample were considered for a detailed investigation of the uraninite compositions from individual ore fields and/or deposits. This is evidenced by the relatively high and uniform UO_2 and low SiO_2 contents of the analyzed samples, with median values ranging between 82.45 and 85.79 wt% and 0.61–3.48 wt% for UO_2 and SiO_2, respectively (Fig. 4a, Fig. 4c, and Table 1). Only a few distinctions may be noted in the case of the UO_2 concentrations; for example, the Slavkovice deposit is characterized by the highest UO_2 contents (median 85.79 wt%; Table 1), whereas uraninite from the Rozsochy and Rožná-Jasan deposits in the northern part of the Rožná-Olší ore field show decreased contents with median values of 82.84 and 83.65 wt%, respectively (Fig. 4a and Table 1). Taken as a whole, the SiO_2 contents in uraninite vary considerably among the individual deposits and ore fields (Fig. 4c). For instance, the lowest values were recorded in samples from the Milasín, Habří, and Bukov deposits (median 0.6–0.8 wt%; Fig. 4c and Table 1), occurring in the central part of the Rožná-Olší ore field. In contrast, samples from the northern part of the same ore field represented by the Rozsochy and Rožná-Jasan deposits yielded much higher values (median 3.5 and 3.1 wt%, respectively; Fig. 4c and Table 1). Limited variations are also noticeable in the PbO contents, with more pronounced differences among the deposits from the Rožná-Olší ore field (median 2.81–3.89 wt%; Fig. 4b and Table 1). In turn, the samples from the Brzkov deposit and Slavkovice-Petrovice ore fields exhibit relatively similar PbO concentrations (median 3.21–3.7 wt%; Fig. 4b and Table 1). In the case of CaO, an interesting trend can be seen within samples from the Rožná-Olší ore field, apparently related to the geographical location of the deposits themselves. Note that a significant CaO enrichment occurs in uraninite especially in the south and central part of the Rožná-Olší and Slavkovice-Petrovice ore fields (Fig. 4d).

Electron microprobe analyses were performed to determine the U-(Th)-Pb chemical ages of several selected uraninite samples covering all studied ore fields. The calculated apparent ages yielded a relatively wider range from ca 230 Ma to 310 Ma throughout the dataset. The majority of compositions from Brzkov yielded somewhat higher but homogeneous apparent ages of 296 ± 3 Ma (weighted mean ± 95 %

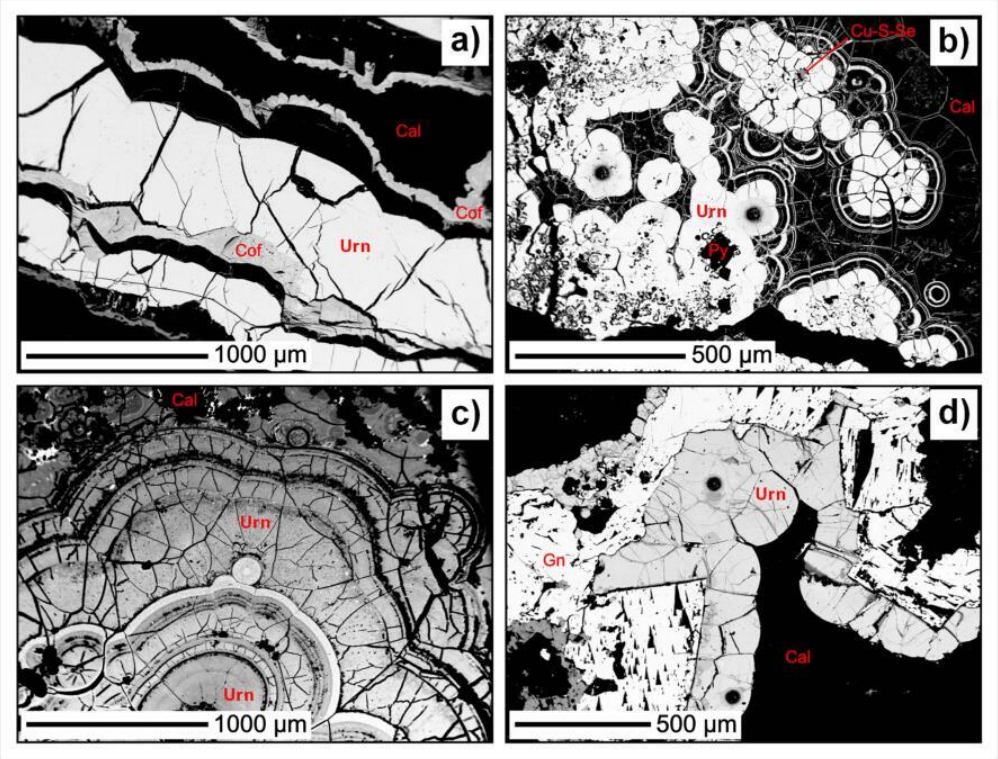

Fig. 3. Backscattered electron (BSE) images of selected uraninite samples from the a) Rožná-Jasan, b) Habří, c) Slavkovice, and d) Brzkov deposits (see Fig. 1b) illustrating the massive and colloform textures of the analyzed uraninites. A different BSE contrast scaling was used in figure c) to show the subtle variations between the individual "layers" of colloform uraninite aggregates. The laser ablation craters within the unaltered parts of the uraninite samples are shown in figures b) and d); Urn – uraninite, Cof – coffinite, Cal – calcite, Py – pyrite, Gn – galena, Cu-S-Se – copper sulphoselenide.

confidence uncertainty). A representative sample from the Slavkovice deposit (Slavkovice-Petrovice ore field) yielded an apparent chemical age of 278 ± 3 Ma. The ages of two samples from deposits in the northern part of the Rožná-Olší ore field were also determined. The calculated apparent ages of the samples from Rozsochy and Rožná-Jasan, which were slightly enriched in SiO_2 (Fig. 4c), are somewhat younger at 250 ± 5 Ma and 237 ± 3 Ma, respectively. The apparent age of most samples from the central part of the Rožná-Olší ore field (Rožná R-1) was calculated at 253 ± 8 Ma and the ages of the samples from Olší, the southernmost deposit of this ore field, yielded an apparent age of 277 ± 10 Ma.

5.3. Trace elements

The highest total REE contents (ΣREE) were typically recorded in uraninite samples from the Brzkov deposit, commonly exceeding 1 wt% with an overall median value of 6495 ppm (Fig. 5a and Table 2). The ∑REE contents in uraninite from the Rožná-Olší ore field vary from low (median on 96 and 30 ppm for Olší and Bukov, respectively; Table 2) to relatively high median values of 521 ppm for Rožná R-1 or 1056 ppm for the Rozsochy deposit in the northern part of the ore field (Fig. 5a). On the other hand, the uraninites from the Slavkovice-Petrovice ore field yielded the lowest ∑REE contents. The median values of ∑REE in uraninite from the Slavkovice, Petrovice, and Nová Ves deposits are 22, 4.3, and 76 ppm, respectively (Fig. 5a and Table 2).

Four distinctive trends can be observed in the chondrite normalized (McDonough and Sun, 1995) REE patterns of the deposits/ore fields from the eastern part of the Moldanubian Zone (Fig. 5c and d). An enrichment of LREE over HREE (La_N/Yb_N 3.41–19.65) with a maximum of Ce to Nd (Fig. 5c) was typically recorded in the uraninite samples from the Brzkov deposit. The relatively flat REE chondrite normalized patterns of all three deposits of the Slavkovice-Petrovice ore field (Fig. 5d) illustrate somewhat lower concentrations of LREE (La_N/Yb_N 0.52–13.13, median 1.07; Fig. 5d) and only a minimal enrichment of MREE and HREE (La_N/Gd_N 0.04–4.68, median 0.91, maximum from Gd to Tm; Fig. 5d). A LREE dominated pattern (La_N/Yb_N 1.30–44.42, median 4.94, Fig. 5c) with maximum on La and decreasing trend toward HREE with small positive Gd anomaly can be observed in all samples from the central and southern parts of the Rožná-Olší ore field (Fig. 5c). Exceptions are the samples from the northern part of the Rožná-Olší ore field, where uraninite from the Rožná-Jasan and Rozsochy have distinctive patterns of HREE enrichment (La_N/Yb_N 0.29–2.34 and 0.01–1.02, respectively, Fig. 5d) with strong negative Eu anomalies (Eu_N/Eu_N^* 0.37–0.64 and 0.11–0.55, respectively, Fig. 5d).

The abundance of Y (Fig. 5b and Table 2) follows the trend of REEs with only one exception; the uraninite samples from the Rozsochy deposit have higher Y concentrations (median 1552 ppm; Fig. 5b and Table 2) than those from Brzkov (median 1267 ppm; Fig. 5b and Table 2) which have the highest REE contents. Although the Th contents (Fig. 6a) in the uraninite samples from all studied deposits in the eastern part of the Moldanubian Zone are very low to undetectable (the detection limit of Th was 0.001 ppm), the trend is relatively similar to those of Y or REEs (Fig. 5a; Fig. 5b; Fig. 6a). The maximum values of Th were measured in uraninite samples from the northern part of the Rožná-Olší ore field – the Rozsochy and Rožná-Jasan deposits with median values on 32 and 1.1 ppm, respectively (Fig. 6a and Table 2). The samples from Rozsochy and Rožná-Jasan can be distinguished from those of other deposits also by their concentrations of other elements; notably, their enrichment in Zr

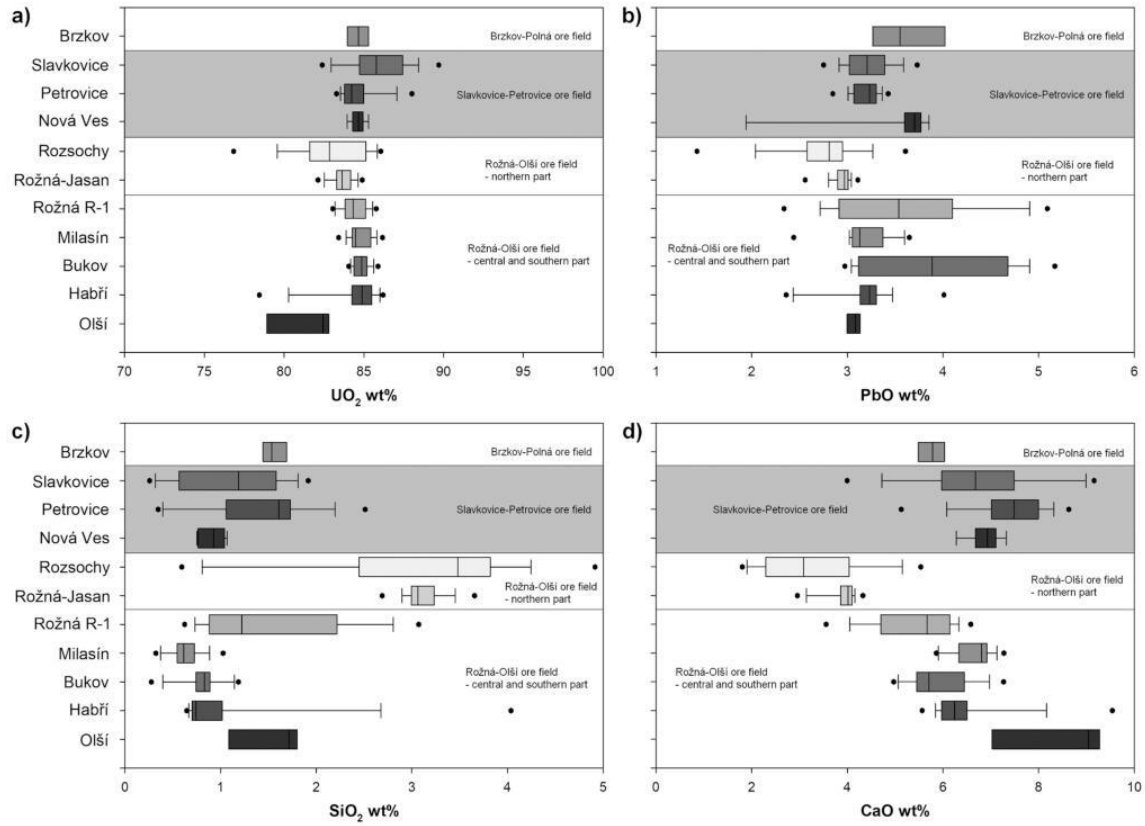

Fig. 4. Box-and-whisker plots for major elements in uraninite from individual uranium deposits (and ore fields) analyzed by electron microprobe analysis (EMPA): a) UO_2; b) PbO; c) SiO_2; and d) CaO. The boxes are framed by 25th and 75th percentiles; the line within the box indicates the median value. The whiskers display the 10th and 90th percentiles and outliers are shown as one symbol representing the 5th and 95th percentiles.

(median 3614 and 2743 ppm, respectively; Fig. 6b) and Nb contents, especially in samples from the Rozsochy deposit (median 1868 ppm; Fig. 6d). The samples from all other studied deposits are characterized by low to very low contents of Zr and Nb, with median values ranging over 0.15–46 and 0.04–12 ppm, respectively (Fig. 6b, Fig. 6d, and Table 2).

The Ti contents of the uraninite samples allowed to separate the studied deposits into two major groups. Uraninites from the Slavkovice-Petrovice and Rožná-Olší ore fields, omitting its northern part, yielded low Ti contents which were below the detection limit of 1.1 ppm in many analyses (median range 4.8–80 ppm; Fig. 6c and Table 2). In contrast, the uraninites from Brzkov, Rozsochy, and Rožná-Jasan have much higher Ti contents with median values on 976, 1294, and 825 ppm, respectively (Table 2).

Differences between individual ore fields or deposits could also be observed to a certain degree among their V and W contents (Table 2). Beside the selected trace elements, some other measured elements also exhibit concentrations of hundreds or even thousands of ppm (e.g., Na, Mg, P, Mn, Fe, As, Sr, or Ba; see the supplementary materials). However, with only a few exceptions, there are not such significant differences between individual ore fields or deposits as was shown by the concentrations of selected trace elements.

6. Discussion

6.1. Division of regional groups based on uraninite geochemistry

The EMPA and LA-ICP-MS analyses clearly indicate that the minor and trace elements associations in the studied uraninite samples are not uniform among the deposits of the eastern part of the Moldanubian Zone (the Western Moravian U province). Box-and-whiskers plots for individual elements along with chondrite normalized REE patterns allowed us to earmark four groups based on uraninite minor and trace elements association that in fact, are also regionally conditioned (Fig. 1b and Fig. 7). Different geochemical signatures of uraninite are not randomly dispersed in the Western Moravian U province, but there is a solid interconnection of the identified groups with individual deposits or even ore fields (Fig. 7).

The southern and central parts of the Rožná-Olší ore field can be distinguished as one group characterized by distinctive chondrite normalized REE patterns (Fig. 5c and Fig. 7), high V concentrations (Table 2), significant CaO contents (Fig. 4d and Table 1), and a depletion of high field strength elements (HFSE) (Fig. 6a-d and Table 2). A sharp change in the geochemical signature was identified in the uraninite samples from the northern part of the Rožná-Olší ore field represented by the Rozsochy and Rožná-Jasan deposits. The principal difference with other groups is represented by a strong HFSE enrichment (Fig. 5a; Fig. 5b; Fig. 6a-d and Table 2), entirely different REE patterns with a distinct Eu anomaly and an increase of HREE (Fig. 5d), low CaO contents (Fig. 4d and Table 1), and slightly higher SiO_2 contents (Fig. 4c and

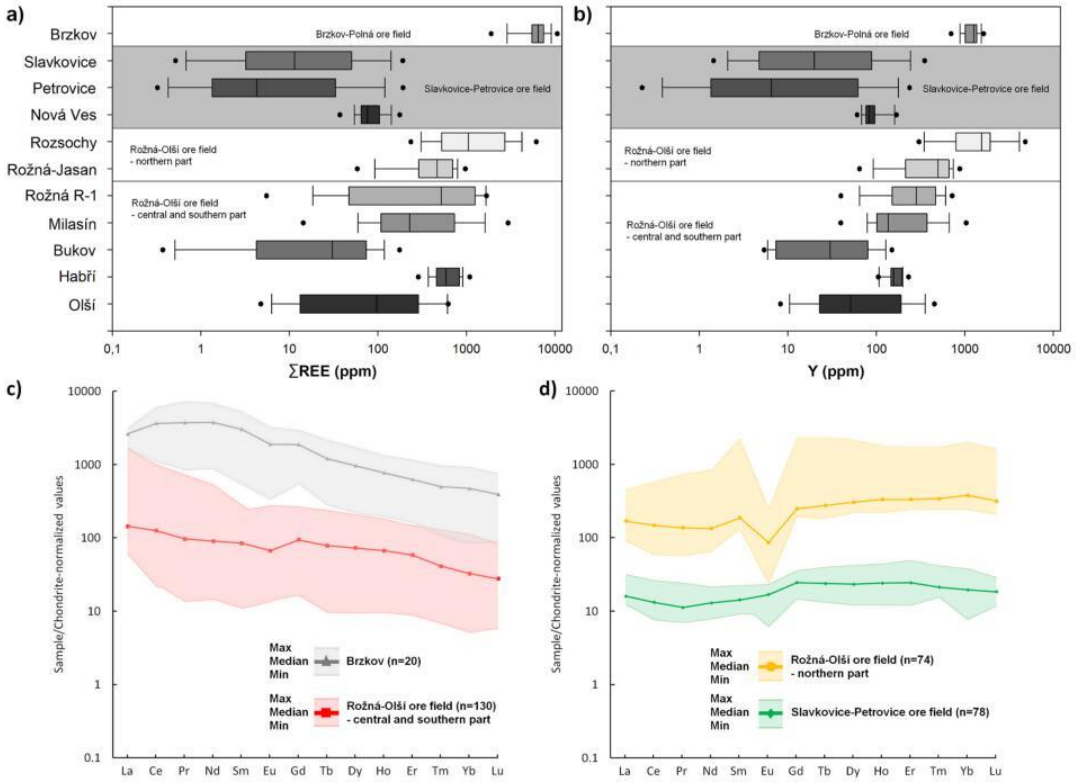

Fig. 5. Box-and-whisker plots for ∑REE (a) and Y (b) in uraninites from individual uranium deposits and ore fields of the eastern part of the Moldanubian Zone analyzed by laser ablation-inductively coupled plasma mass spectrometry (LA-ICP-MS). ∑REE is calculated as the sum of all lanthanides (La—Lu). The boxes are framed by the 25th and 75th percentiles; the line within the box indicates the median value. The whiskers display the 10th and 90th percentiles and outliers are shown as one symbol representing the 5th and 95th percentiles; b) chondrite normalized (McDonough and Sun, 1995) REE patterns illustrating four distinctive trends for uranium deposits/ore fields from the eastern part of the Moldanubian Zone. The lines represent the median values calculated from all analyses of a given group and the coloured fields are delimited at the top by maximum and at the bottom by minimum values for individual normalized REEs (n = x in brackets indicates the number of analyses for each group).

Table 1). The uraninite samples from Slavkovice-Petrovice ore field, located some 5 km to the NW from the northern end of the Rožná-Olší ore field, have contrasting minor and trace element compositions characterized by overall low contents of trace elements (Table 2) and relatively flat REE patterns with a slight M- and HREE enrichment (Fig. 5d and Fig. 7). Significant is their high CaO contents (Table 1) and somewhat increased W concentrations (Table 2) relative to the deposits of the central and southern parts of the Rožná-Olší ore field. The signatures of the studied uraninites from the Brzkov deposit (Fig. 1b), which related to the more westerly Přibyslav mylonite zone, show some similarities with those of the northern part of the Rožná-Olší ore field, especially in their slightly increased HFSE contents (Fig. 6 a-d). However, the chondrite normalized REE pattern (Fig. 5c) as well as the overall high contents of ∑REE (Fig. 5a and Table 2) are the main distinctive feature of this group.

6.2. Major and minor element chemistry – role of alteration, substitution, and lithological controls

Coffinitization, the most common alteration process affecting uraninite under reducing conditions (Janeczek and Ewing, 1992b; Alexandre and Kyser, 2005), represents a prevailing form of hydrothermal alteration of uraninite observed in samples from the investigated ore fields and may significantly influence the major and trace element compositions of the former. Coffinite contains significant amounts of SiO_2, hydroxyl groups, and incomparably lower concentrations of UO_2 relative to uraninite (Guo et al., 2015; René et al., 2019; Szenknect et al., 2020). The uraninite samples from Rožná-Jasan and Rozsochy have somewhat elevated SiO_2 contents (Fig. 4c) and, in contrast, the SiO_2 depleted uraninite samples from the Slavkovice-Petrovice ore field show strong negative correlation between SiO_2 and UO_2 (Fig. 8a; Pearson's coefficients of −0.74, −0.86, and -0.77, respectively). The SiO_2 contents in uraninite, especially when manifesting a negative correlation with UO_2, may indicate the onset of the coffinization process. However, the high UO_2 contents (Fig. 4a, Table 1) and low concentrations of non-structural elements such as SiO_2 (Fig. 4c, Table 1), along with the BSE imaging (Fig. 3a-d) of the studied uraninite samples reflect only negligible and/or strongly limited effects of post-crystallization alteration and thus allowed us to assess and compare their primary compositions.

Both EMPA and LA-ICP-MS analyses confirm Ca (CaO) as the element with the highest concentration after U (UO_2) among all measured elements (Table 1). Only 2–5 μm EMPA beam size and the LA-ICP-MS ablation records of Ca identical to U records advocate uraninite geochemical signature unaffected by contamination caused e.g., by micro inclusions of hydrothermal calcite that represent the main gangue mineral in all studied uraninite samples and often intimately grown together with uraninite (Fig. 3a-d). Ca^{2+} (1.112 Å) has a very similar ionic radius to that of U^{4+} (1 Å, Shannon, 1976), and thus, it can structurally substitute for ions as has frequently been discussed in the literature (Janeczek and Ewing, 1992a; Alexandre and Kyser, 2005;

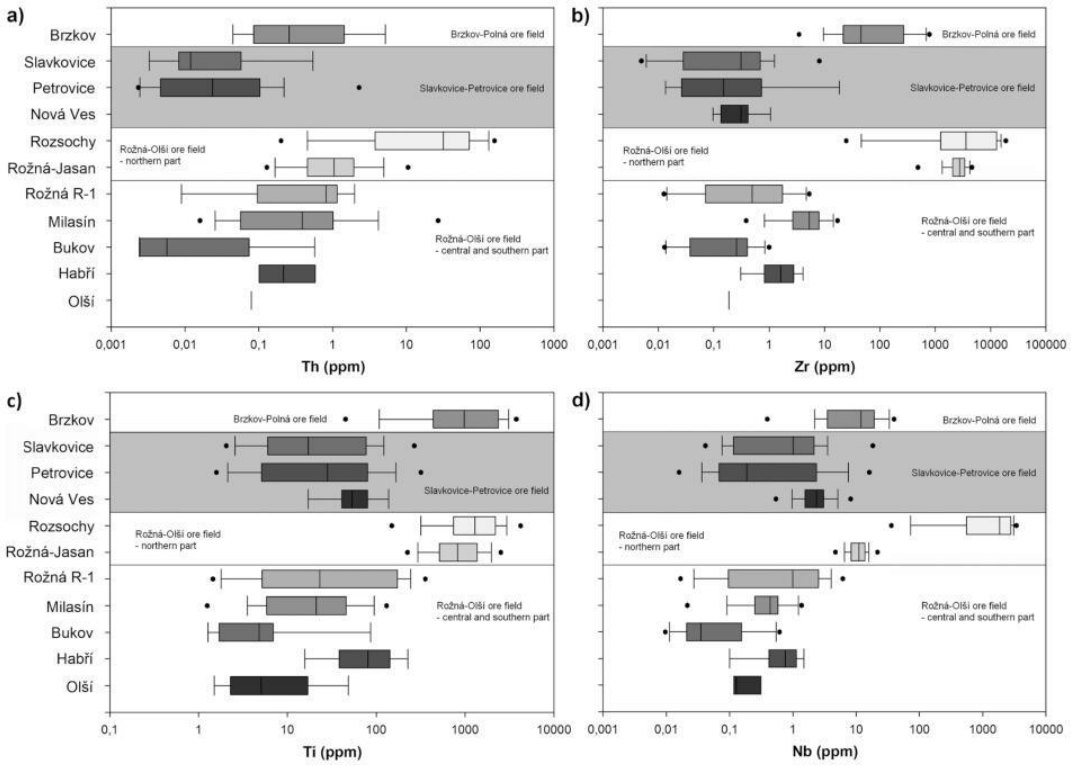

Fig. 6. Box-and-whisker diagram displaying the concentration of selected high field strength elements (HFSE); (a) Th, (b) Zr, (c) Ti, and (d) Nb in uraninite samples from individual uranium deposits (and ore fields) in the eastern part of the Moldanubian Zone measured by laser ablation-inductively coupled plasma mass spectrometry (LA-ICP-MS). The boxes are framed by the 25th and 75th percentiles; the line within the box indicates the median value. The whiskers display the 10th and 90th percentiles and outliers are shown as one symbol representing the 5th and 95th percentiles.

Frimmel et al., 2014; Alexandre et al., 2015). The strong negative correlation of CaO and UO_2 (Fig. 8b, Pearson's coefficient -0.89) observed in the uraninite samples from the Slavkovice-Petrovice ore field may suggest a such crystallographic control. However, the samples from other localities do not manifest such a strong negative correlation, and the uraninite samples from Rozsochy even exhibit a somewhat positive correlation between UO_2 and CaO (Fig. 8b). Moreover, the CaO contents show significant variations between individual localities along with a gradual change recorded by increasing CaO contents from north to south in the Rožná-Olší ore field (Fig. 4d). We suggest that such chemical variations may be caused by the interaction of U ore-forming fluids with Ca-rich lithologies such as marbles or erlans (calc-silicate rock) occurring in varying degrees throughout the entire studied area (the Varied group of the Moldanubian Zone). For example, Bajer (1970) and Šurán et al. (1965) previously discussed in reports from the U exploration campaign of the Slavkovice-Petrovice ore field that marbles and erlans played a significant role in U ore formation when slightly inclined uraninite veins often followed the sequences of these Ca-rich lithologies. This finding is further supported by the CaO concentrations (median 6.7–7.5 wt%, Fig. 4d and Table 1) measured in the uraninite samples from the Slavkovice-Petrovice ore field. Similarly, lenses of marbles and erlans were previously also described in samples from the Rožná and Olší mines (Arapov et al., 1984; Kříbek et al., 2009).

6.3. Chemical U-(Th)-Pb dating of uraninite

The time span of the calculated uraninite U-(Th)-Pb chemical ages from the individual studied deposits appears to be relatively wide (230 to 310 Ma, as seen in Fig. 9). The interpretation of whether the apparent ages calculated from uraninite compositions represent a real geological event (uraninite crystallization) or if they are instead artifacts of post-crystallization gains or losses of mass can be a challenging task (e.g., Kempe, 2003; Alexandre and Kyser, 2005; Alexandre et al., 2015; Ozha et al., 2017). For example, the significant drop in the calculated apparent age due to increasing SiO_2 contents documented by Martz et al. (2019a) could agree with the relatively lower apparent ages (Fig. 9) calculated for the slightly SiO_2 enriched (Fig. 4c and Fig. 8a) uraninite samples from the Rozsochy and Rožná-Jasan deposits. The EMP analyses of all studied uraninite samples from the Rozsochy deposit show a negative correlation between PbO and SiO_2 (Pearson's coefficient of −0.69) that could indicate Pb loss and increasing SiO_2 contents (possibly onset of coffinization). Such a process may have a significant influence on the U-(Th)-Pb chemical age calculations resulting in somewhat lower apparent ages. However, a very good agreement with previously published isotopic bulk-phase U—Pb uraninite dating (270–280 Ma, Anderson et al., 1988), K—Ar ages of illite from ore substage alteration (264 ± 4.3 to 277 ± 5.5, Kříbek et al., 2009), and authigenic monazite (268 ± 50 Ma, Kříbek et al., 2009) from the Rožná deposit as well as the individual studied uraninite samples (especially those with rather low SiO_2 contents) imply that the calculated chemical ages close to ca. 260–280 Ma (Fig. 9) represent the origin of the uraninite mineralization.

6.4. REE and HFSE distribution in uraninites controlled by fluid-rock interaction processes

The REE chondrite normalized patterns characterized by slight LREE enrichment and a decreasing trend toward HREE observed in samples from the central and southern parts of the Rožná-Olší ore field as well as

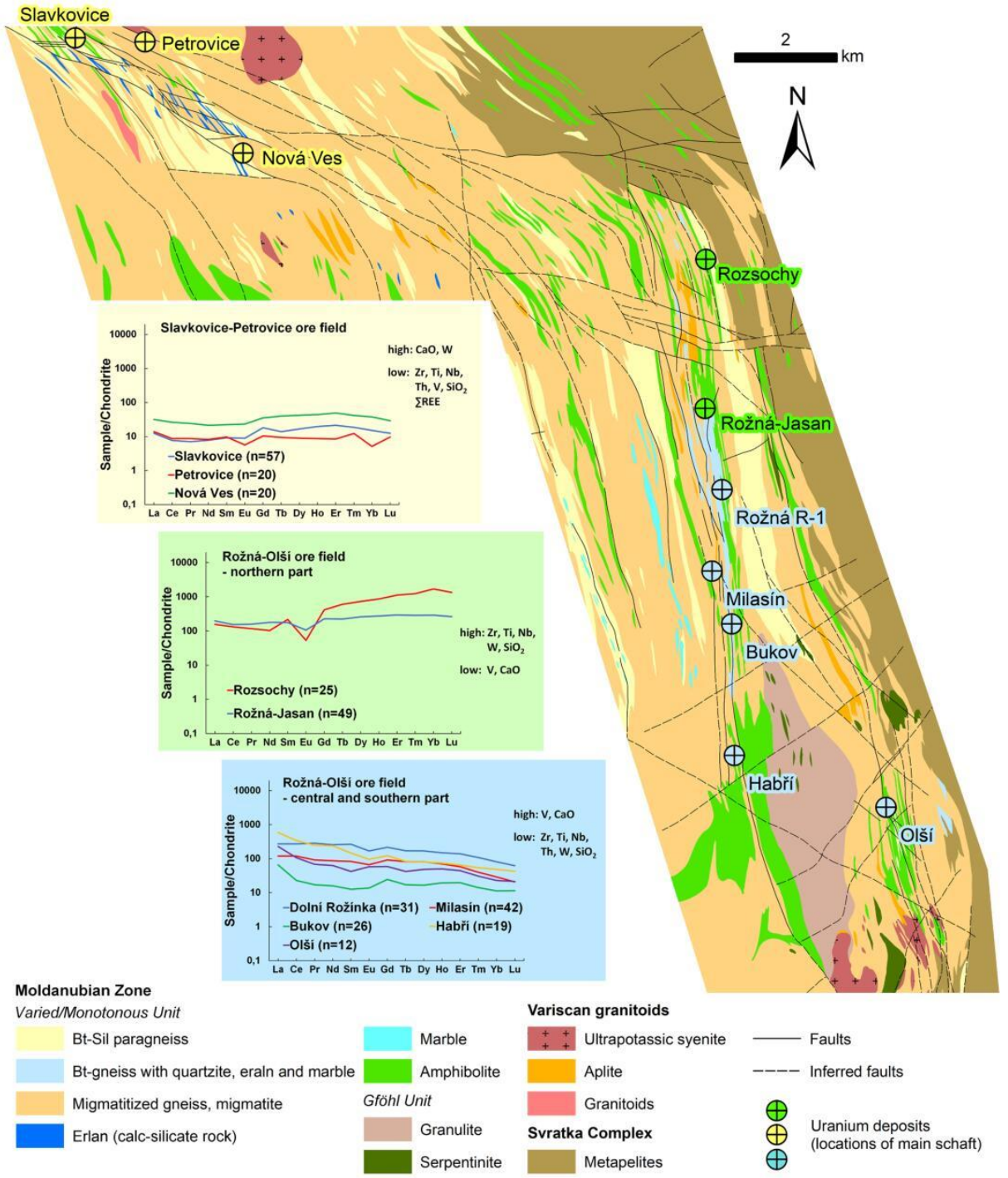

Fig. 7. Geological and tectonic map that cover area of the Slavkovice-Petrovice and Rožná-Olší ore fields. Chondrite normalized REE patterns are shown as the median values of all analyses for individual deposits. The number of analyses used to calculate the medians are indicated in brackets (n = x). Chondrite normalization was performed based on the data of McDonough and Sun (1995) and the map was edited after Arapov et al. (1984).

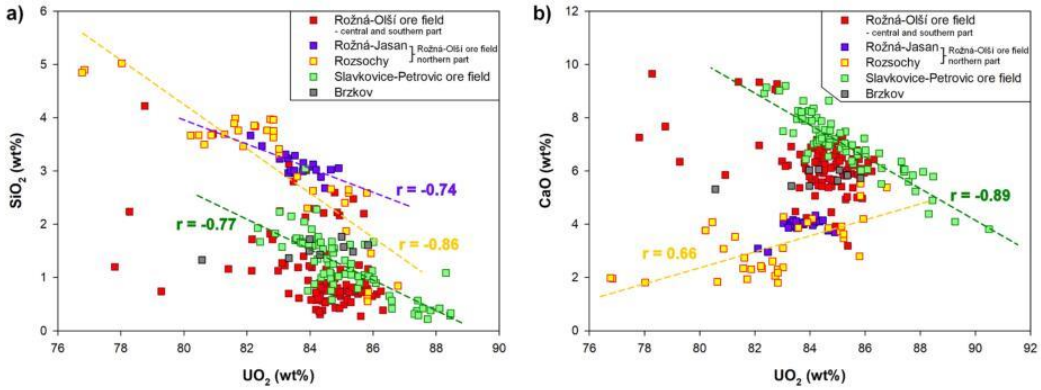

Fig. 8. Binary diagrams of SiO_2 (a) and CaO (b) contents against the UO_2 concentrations of uraninite from the eastern part of the Moldanubian Zone analyzed by electron microprobe analyses (EMPA) with linear regression lines and calculated Pearson's correlation coefficients.

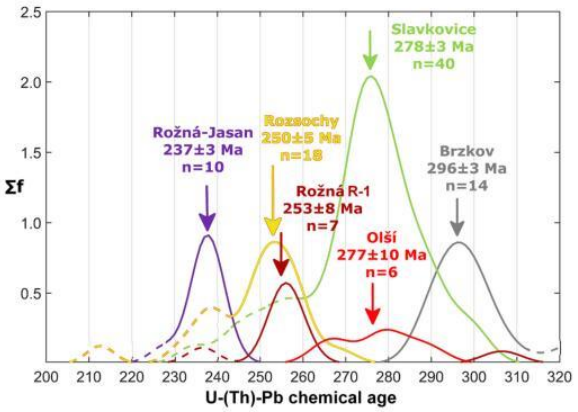

Fig. 9. Frequency distribution curves of the U-(Th)-Pb electron microprobe analysis (EMPA) ages of uraninite. The frequency values shown on the vertical axis are given by the sums of the frequency distribution corresponding to individual point analyses. Certain compositional domains yielded somewhat younger ages (dashed sections of the curves) compared to most compositions from the particular locality; these are interpreted as artifacts caused by slight Pb loss (see text for further details) and were not considered in the statistical evaluation.

the Brzkov deposit (Fig. 5c and Fig. 7) have previously been described by several authors (Mercadier et al., 2011; Frimmel et al., 2014; Alexandre et al., 2015) as being common for vein-type U deposits. It is widely accepted that the REE patterns of uraninites in low-temperature vein-type deposits reflect their potential REE source (e.g., monazite, apatite; Alexandre et al., 2015). Monazites that commonly exhibited LREE-enriched patterns (Henderson, 1984; Dill, 1994; Zhu and O'Nions, 1999; Pérez-Soba et al., 2014) were previously suggested as a potential source of U (and REE) for deposits due to processes related to its alteration and subsequent elemental mobility (e.g., Cuney and Mathieu, 2000; Hecht and Cuney, 2000). Monazites, and to the certain degree titanites, have been considered to be one of the main U sources for the Rožná deposit (Leichmann et al., 2002; Kříbek et al., 2009; Kříbek et al., 2022) since they are the main carriers of U, Th, and LREE in the metapelitic rocks of the eastern part of the Moldanubian Zone.

However, a distinct change in REE chondrite normalized patterns showing LREE depletion, significant Eu anomalies, and a slight enrichment toward HREE (Fig. 5d and Fig. 7) were observed in samples from the northern part of the Rožná-Olší ore field (Rožná-Jasan and Rozsochy deposits). Such a trend has previously ascribed to magmatic/intrusive or Na-metasomatism-related U deposits (Mercadier et al., 2011; Frimmel et al., 2014; Alexandre et al., 2015). The metamorphic host rocks of all the studied U deposits, absence of time-corresponding intrusion (similar to the age of the U mineralization) and low-temperature nature of the U mineralization provide the main evidence against such an intrusion-related origin of the Rozsochy and Rožná-Jasan deposits. On the other hand, the uraninite samples of these two deposits in the northern part of the Rožná-Olší ore field also contain higher abundances of HFSEs (Figs. 5a-b, 6a-d, Table 2) that commonly become concentrated during the final stages of magmatic fractionation processes (e.g., Marks et al., 2008). Such variations in uraninite REE chondrite normalized patterns as well as HFSE concentrations in one ore province could be explained by lithologically controlled processes and fluid-rock interactions rather than in the diversity of genetically related types of U deposits. The lithologies that may play a major role in such processes include the ultrapotassic syenites (durbachites) of the Třebíč pluton and its satellite bodies (Fig. 1b) since they typically exhibit high abundances of REE- and HFSE-bearing phases such as fluorapatites, zircons, titanites, allanites, or thorites (Janoušek et al., 2020). Other supporting evidence includes the original size of the Třebíč pluton which used to be much larger, and indeed, the intrusion probably reached the present position of the U deposits of the Rožná-Olší ore field (Leichmann et al., 2017). In general, zircons exhibit REE chondrite normalized pattern that share some features (negative Eu anomalies, HREE enrichment; e.g., Hoskin and Ireland, 2000; Pérez-Soba et al., 2014) with the REE chondrite normalized patterns observed in the uraninite samples from the northern part of the Rožná-Olší ore field (Rozsochy and Rožná-Jasan deposits; Fig. 5d and Fig. 7). It is likely that the ore-forming fluids could bear these elements as a result of REE and HFSE remobilization from metamict zircons during the formation of the studied U deposits, as previously demonstrated for highly alkaline igneous rocks that are spatially associated with the Třebíč pluton (Kubeš et al., 2021). Indeed, the enhanced mobility of U, Zr, Y, and REEs enabled by the infiltration of oxidized Permo-Carboniferous basinal water into the crystalline rocks of the eastern part of the Moldanubian Zone was previously described by René (2008) and Kříbek et al. (2009) further considered this infiltration as the process that may have prompted U mobility. The role of Permian basinal brines in U extraction was also previously discussed for the genesis of hydrothermal vein U deposits in Variscan granites from the Massif Central, France (e.g., Turpin et al., 1990). More recently, the processes of basinal brines interacting with highly-microfracturated basement rocks were described as being a very important factor for the genesis of unconformity-related U deposits (e.g., Martz et al., 2019b). Such oxidized fluids could have originated from Permian basins that were also unconformably covering the eastern margin of the Moldanubian Zone

(Pešek et al., 2001; McCann et al., 2006), and these fluids could effectively affected, decomposed, and mobilized HFSEs from accessory minerals, particularly metamict zircons from the Třebíč pluton (Kubeš et al., 2021; Janoušek et al., 2020). A remaining question is why such a strong HFSE enrichment was developed only in the uraninite samples of these two particular deposits and not in other deposits of the Rožná-Olší or nearby Slavkovice-Petrovice ore fields. To judge the potential role of local tectonic structures or formerly overlying lithologies which are now eroded is beyond the scope of this study and would require further research. Overall higher REE concentrations (median ca 6500 ppm and the highest values up to 1.1 wt% ∑REE; Fig. 5a, Table 2) and somehow elevated HFSE contents, mainly Y and Ti (Fig. 5b and Fig. 6c) and to a lesser extent also Zr and Nb (Fig. 6b,d) in the uraninite samples from the Brzkov deposit that is located in the vicinity of the Třebíč pluton (Fig. 1b) may further support the essential role of ultrapotassic syenites that likely drove the HFSE enrichment of uraninite in Eastern Moldanubicum.

Although the total REE contents are very low in the uraninite samples from the nearby Slavkovice-Petrovice ore field (Fig. 7), the REE chondrite normalized patterns are entirely different from those of samples derived from the other localities, showing relatively flat patterns resembling a very slight "bell-shaped" enrichment in MREE to HREE (Gd-Tm; Fig. 5d and Fig. 7). Exactly these REEs have ionic radii (from 1.053 Å for Gd^{3+} to 0.994 Å for Tm^{3+}) most similar to that of U^{4+} (1 Å, VIII coordination) (Shannon, 1976). This finding together with the above mentioned strong negative correlation of CaO with UO_2 support the substitutional structural position of these minor and trace elements in the uraninites of the Slavkovice-Petrovice ore field.

6.5. Limited application of trace elements in uraninite as a function of the deposit type

Trace elements, especially REE systematics, in samples of uraninite or U ore concentrates have been considered by many authors as a functional tool for discriminating between different types of U deposits (Bonhoure et al., 2007; Mercadier et al., 2011; Depiné et al., 2013; Frimmel et al., 2014; Alexandre et al., 2015; Spano et al., 2017). The observed variations in trace elements as well as REE in uraninite from one U province (Fig. 5c; Fig. 5d; Fig. 7) raise the question of the extent to which such a tool can be applicable. Taking account that the grouping of "vein-type" U deposits as a deposit type is no longer recommended (e.g., IAEA, 2018), Alexandre et al., 2015 considered the chemical composition of uraninite from vein-type deposits (category) to be the most variable among all studied deposit types. It is in accordance with a variegated geochemical composition and the mineralization/morphological style of the studied samples representing so-called "vein-type" ores (Dahlkamp, 2016; Kříbek et al., 2009; Arapov et al., 1984). On the other hand, the most common LREE dominated chondrite normalized patterns described for the vein-type category (Alexandre et al., 2015; Frimmel et al., 2014; Mercadier et al., 2011) disagree with the observed variations in the REE patterns of individual ore fields and/or deposits in the eastern part of the Moldanubian Zone. Frimmel et al. (2014) and Mercadier et al. (2011) also used a ratio of ∑REE to $(\sum LREE)_N/(\sum REE)_N$ for distinguishing deposit types (Fig. 10). Our data was projected together with uraninite geochemical analyses from different types of U deposits worldwide published in the works of Mercadier et al. (2011), Frimmel et al. (2014), and Eglinger et al. (2013) using the same ∑REE versus LREE/HREE fractionation (Fig. 10).

Very different REE concentrations (∑REE median values 4.3–6495 ppm and LREE/HREE fractionation of 0.03–15.7; Fig. 5a and Fig. 10, respectively) of uraninites in deposits from the eastern part of the

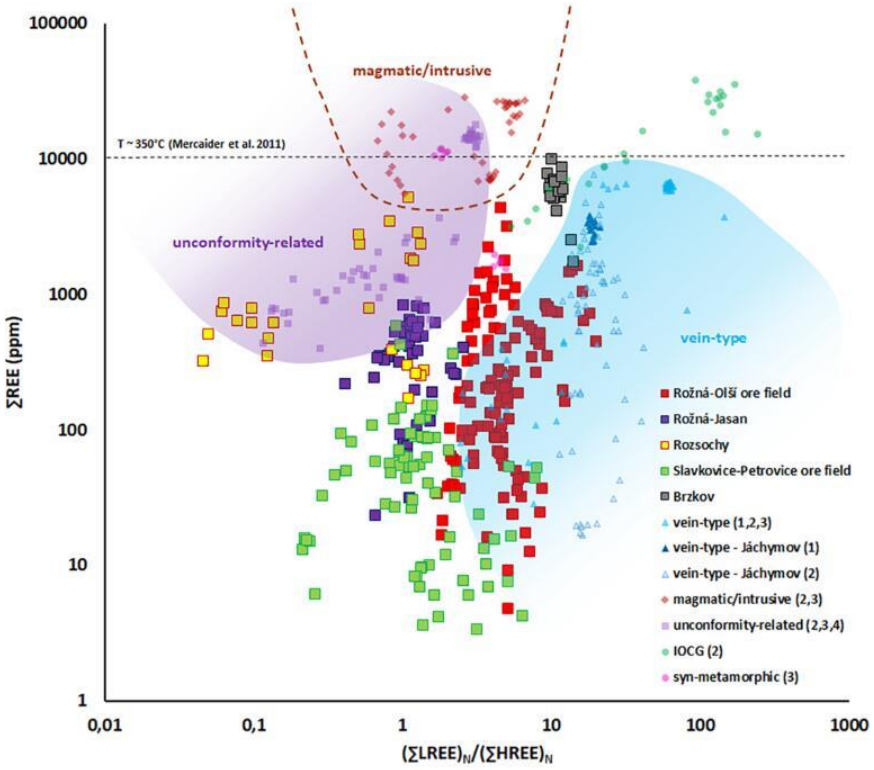

Fig. 10. Total REE abundances versus chondrite normalized LREE/HREE fractionation. The fields of domains for individual deposit types were drawn based on analyses of uraninites located outside the eastern part of the Moldanubian Zone; (1) Jáchymov, Příbram analyzed within the Geobarr project (unpublished); (2) Frimmel et al. (2014); (3) Mercaider et al. (2011); Eglinger et al. (2013). Most of the analyses by Mercadier et al. (2011) were performed using secondary ion mass spectrometry (SIMS) and Gd and Yb could not be measured due to interferences. The total REE abundance of our data and that of Frimmel et al. (2014) were therefore also calculated without Gd and Yb. This was also considered in the calculation of REE fractionation: $\Sigma LREE_N$ (La—Sm); $\Sigma HREE_N$ (Er + Tm + Lu). Chondrite normalization was performed based on the data of McDonough and Sun (1995).

Moldanubian Zone projected the analyzed uraninite samples to almost all field of domains for individual deposit types (Fig. 10). On the other hand, the individual ore fields and/or deposits form clusters similar to the groups which are also distinguished by other minor or trace elements. Possibility, that individual ore fields and/or deposits of the same age and mineralization style within the Western Moravian U province having such diverse ore deposit geneses is unrealistic and points to the rather limited functionality of REE systematics for the discrimination of deposit types. The fractionation of REEs in hydrothermal systems will be rather governed by the various physico-chemical conditions (temperature, ligands, chemical composition) of ore-forming fluids (e.g., Migdisov et al., 2016). However, similarities with other deposit types can further support the hypothesis of a more complex genesis of uranium deposits in the eastern part of the Moldanubian Zone. For example, some analyses from the Rozsochy or Brzkov deposits that are also enriched in HFSEs indicate in the graph (Fig. 10) close positions with analyses of uraninites from magmatic/intrusive type of deposit. Indeed, some influence of the ultrapotassic syenite magmatic suite should be considered when interpreting the origin of these two deposits. The uranium mineralization in the Slavkovice-Petrovice ore field is associated with hydrothermal calcite veins and exhibits well developed botryoidal textures (Fig. 3c) typical for low-temperature uraninites; these deposits are also characterized by the lowest ∑REE contents (Fig. 5a) among all studied deposits and their REE patterns are not unlike those described as being "bell-shaped" (Fig. 5d and Fig. 7) also characteristic of deposits with a low-temperature hydrothermal nature (Mercadier et al., 2011). Moreover, some analyses fall into the domain assigned to unconformity-related deposits (Fig. 10). The link between U ore-forming events in the eastern part of Moldanubian Zone and unconformity-related U deposits can be supported by processes involving the fluid-driven alteration of various mineral phases (e.g., zircons, titanites), mobilization of U and many other trace elements by oxidized fluids and/or basinal brines described from the Rožná deposit (Kříbek et al., 2009, 2022; René, 2008). The same processes of the fluid-driven alteration and HFSE mobilization was described also from marginal part of the ultrapotassic syenites of the Třebíč pluton (Fig. 1b; Kubeš et al., 2021). These processes together with fluid-rock interactions are considered important features in the genesis of unconformity-related U deposits (e.g., Hecht and Cuney, 2000; Martz et al., 2019b). Further considering the timing of the U mineralization (Fig. 9), the basinal fluids probably originated from the now eroded Permian sedimentary basins that covered the area, and the fluids may have interacted with the basement rocks beneath these. These processes of ore-forming fluids interacting with variegated basement lithologies typical for the eastern part of the Moldanubian zone provide suggested explanation for the variations in minor and trace elements in the uraninites of the studied area.

7. Conclusions

A complex study of the geochemical composition of uraninite samples from a whole ore province in the eastern part of the Moldanubian Zone included over 600 combined EMPA and LA-ICP-MS analyses. The following conclusions can be drawn:

- Uraninites from one ore province represented by mineral deposits of the same genesis, mineralization style, and timing exhibit a significant variability in minor and trace elements composition.
- The geochemical signatures of uraninites can be distinctive on an ore field scale. According to the uraninite geochemistry, four groups (Brzkov, Slavkovice-Petrovice ore field, northern part of the Rožná-Olší ore field, and central/southern part of the Rožná-Olší ore field) can be distinguished within the U ore province.
- The described variations in minor elements such as Ca, trace elements, as well as chondrite normalized REE patterns on the ore field or deposit scale also suggest certain limitations for the use of REE patterns in provenance studies or to distinguish deposit types, at least in low-temperature U mineralizing hydrothermal systems.
- HFSE and ∑REE enrichment, as well as the negative Eu anomalies typically observed in uraninite from intrusion/magmatic related deposits, can also be present (e.g., ∑REE up to 1 wt% of, Zr up to 2 wt%) in uraninites from low-temperature vein style mineralizations.
- Backscattered electron imaging, detailed ablation signal observations, very high contents of U (UO_2 medians mostly about 85 wt%), and low concentrations of SiO_2 in all the studied samples except those from the Rozsochy and Rožná-Jasan deposits support a rather minimal rate of alteration and/or risk of 'contamination' of the uraninite samples by hidden fluid and/or mineral inclusions.
- The high concentrations of Ca (e.g., median of 7 wt% of CaO in the samples from the Slavkovice-Petrovice ore field) indicate large amounts of Ca in the environment during uraniferous mineralization events in the eastern part of the Moldanubian Zone. Spatial links between the mineralized structures and Ca-rich lithologies (marbles and calc-silicate rocks) may also suggest the role of lithological controls (fluid-rock interactions) in defining the geochemical composition of the analyzed uraninites.
- The interaction of ore-forming fluids with the variegated lithological compositions present in the eastern part of the Moldanubian Zone as well as with erosion relicts of the formally much larger ultrapotassic syenites of the Třebíč pluton may explain the significant variations in uraninite geochemistry observed in samples from individual ore fields.

Supplementary data to this article can be found online at https://doi.org/10.1016/j.gexplo.2022.107111.

CRediT authorship contribution statement

Conceptualization – Vojtěch Wertich
Data curation – Vojtěch Wertich, Martin Kubeš, Markéta Holá
Formal analysis – Markéta Holá, Jakub Haifler
Funding acquisition – Jaromír Leichmann
Investigation – Vojtěch Wertich
Methodology – Markéta Holá, Jakub Haifler
Resources – Juraj Mozola, Pavla Hršelová, Michal Jaroš
Supervision – Jaromír Leichmann
Visualization – Juraj Mozola
Roles/Writing
– original draft – Vojtěch Wertich, Martin Kubeš, Jakub Haifler
– draft revision – Vojtěch Wertich

Declaration of competing interest

The authors declare that they have no known competing financial interests or personal relationships that could have appeared to influence the work reported in this paper.

Acknowledgements

This research was funded by the Operational Programme Research, Innovation and Education [grant number CZ.02.1.01/0.0/0.0/16_026/0008459 (Geobarr)] of the European Regional Development Fund. The work was further supported by the institutional support of long-term conceptual development of research institutions provided by the Ministry of Culture (ref. MK000094862). We are grateful to the Moravian Museum (namely S. Houzar and J. Toman) and DIAMO state enterprise (namely P. Navrátil) for providing the samples studied here. We gratefully acknowledge constructive and helpful comments from two anonymous reviewers, as well as the editorial work of Stefano Albanese.

References

Alexandre, P., Kyser, T.K., 2005. Effects of cationic substitutions and alteration in uraninite, and implications for the dating of uranium deposits. Can. Mineral. 43 (3), 1005–1017. https://doi.org/10.2113/gscanmin.43.3.1005.

Alexandre, P., Kyser, K., Layton-Matthews, D., Joy, B., Uvarova, Y., 2015. Chemical compositions of natural uraninite. Can. Mineral. 53 (4), 595–622. https://doi.org/10.3749/canmin.1500017.

Anderson, E.B., Ivanov, P.A., Komínek, J., 1988. Ore metasomatism at the uranium veins of the rožná deposit. Geology and Hydrometallurgy of Uranium 12, 70–89 (in Czech).

Arapov, J.A., Bojcov, V.J., Česnokov, N.I., Djakonov, A.V., Halbrštát, J., Jakovjenko, A. M., Kolek, M., Komínek, J., Kozyrev, V.N., Kremčkukov, G.A., Lažanský, M., Milovanov, I.A., Nový, V., Šorf, F., 1984. Uranium deposits of the Czechoslovakia. In: Czechoslovak Uranium Industry. SNTL, Prague, p. 368 pp (in Czech with English summary).

Bajer, B., 1970. Structural-tectonic setting of Slavkovice deposit. In: Mining Příbram – Science and Technics 1970. Symposium of Mining industry workers: Geology of ore deposits. Příbram, pp. 1–31 (in Czech).

Ballouard, C., Poujol, M., Boulvais, P., Mercadier, J., Tartèse, R., Venneman, T., Deloule, E., Jolivet, M., Kéré, I., Cathelineau, M., Cuney, M., 2017. Magmatic and hydrothermal behavior of uranium in syntectonic leucogranites: the uranium mineralization associated with the Hercynian Guérande granite (armorican massif, France). Ore Geol. Rev. 80, 309–331. https://doi.org/10.1016/j.oregeorev.2016.06.034.

Bonhoure, J., Kister, P., Cuney, M., Deloule, E., 2007. Methodology for rare earth element determinations of uranium oxides by ion microprobe. Geostand. Geoanal. Res. 31 (3), 209–225. https://doi.org/10.1111/j.1751-908x.2007.00865.x.

Cooke, R., O'Brien, P., 2001. Resolving the relationship between high P-T rocks and gneisses in collisional terranes: an example from the gföhl gneiss–granulite association in the moldanubian zone. Austria. Lithos 58 (1–2), 33–54. https://doi.org/10.1016/s0024-4937(01)00049-4.

Cuney, M., 2008. The extreme diversity of uranium deposits. Mineral. Deposita 44 (1), 3–9. https://doi.org/10.1007/s00126-008-0223-1.

Cuney, M., Kyser, K., 2009. Recent and not-so-recent developments in uranium deposits and implications for exploration. Mineralogical Association of Canada, Short Course Series Vol. 39. Mineralogical Association of Canada & Society for Geology Applied to Mineral Deposits, ISBN 978-0-921294-48-1.

Cuney, M., Mathieu, R., 2000. Extreme light rare earth element mobilization by diagenetic fluids in the geological environment of the oklo natural reactor zones, Franceville basin. Gabon. Geology 28 (8), 743–746. https://doi.org/10.1130/0091-7613(2000)28<743:ELREEM>2.0.CO;2.

Dahlkamp, F.J., 1978. Classification of uranium deposits. Mineral. Deposita 13 (1). https://doi.org/10.1007/bf00202909.

Dahlkamp, F.J., 1993. Uranium Ore Deposits. 1. Springer-Verlag Berlin Heidelberg, Berlin, ISBN 978-3-540-53264-4. https://doi.org/10.1007/978-3-662-02892-6, 472 pp.

Dahlkamp, F.J., 2016. Uranium Deposits of the World: Europe. 1. In: Springer-Verlag, Berlin Heidelberg, p. 792 pp.. https://doi.org/10.1007/978-3-540-78554-5.

Depiné, M., Frimmel, H.E., Emsbo, P., Koenig, A.E., Kern, M., 2013. Trace element distribution in uraninite from mesoarchean witwatersrand conglomerates (South Africa) supports placer model and magmatogenic source. Mineral. Deposita 48 (4), 423–435. https://doi.org/10.1007/s00126-013-0458-3.

Dill, H., 1994. Can REE patterns and U-Th variations be used as a tool to determine the origin of apatite in clastic rocks? Sediment. Geol. 92 (3–4), 175–196. https://doi.org/10.1016/0037-0738(94)90105-8.

Dudek, A., Fediuková, E., 1974. Eclogites of the bohemian moldanubicum. Neues Jahrbuch für Mineralogie, Abhandlungen 121, 127–159.

Eglinger, A., André-Mayer, A.S., Vanderhaeghe, O., Mercadier, J., Cuney, M., Decrée, S., Feybesse, J.L., Milesi, J.P., 2013. Geochemical signatures of uranium oxides in the lufilian belt: from unconformity-related to syn-metamorphic uranium deposits during the pan-african orogenic cycle. Ore Geol. Rev. 54, 197–213. https://doi.org/10.1016/j.oregeorev.2013.04.003.

Faltusová, V., Vaculovič, T., Holá, M., Kanický, V., 2022. Ilaps – python software for data reduction and imaging with LA-ICP-MS. J. Anal. At. Spectrom. 37 (4), 733–740. https://doi.org/10.1039/d1ja00383f.

Faryad, S.W., Kachlík, V., Sláma, J., Hoinkes, G., 2015. Implication of corona formation in a metatroctolite to the granulite facies overprint of HP-UHP rocks in the moldanubian zone (bohemian massif). J. Metamorph. Geol. 33 (3), 295–310. https://doi.org/10.1111/jmg.12121.

Finch, R.J., Ewing, R.C., 1992. The corrosion of uraninite under oxidizing conditions. J. Nucl. Mater. 190, 133–156. https://doi.org/10.1016/0022-3115(92)90083-w.

Finger, F., Roberts, M.P., Haunschmid, B., Schermaier, A., Steyrer, H.P., 1997. Variscan granitoids of central europe: their typology, potential sources and tectonothermal relations. Mineral. Petrol. 61 (1–4), 67–96. https://doi.org/10.1007/bf01172478.

Franke, W, 2000. The mid-European segment of the Variscides: tectonostratigraphic units, terrane boundaries and plate tectonic evolution. Geological Society, London, Special Publications 179, 35–61. https://doi.org/10.1144/GSL.SP.2000.179.01.05.

Friedl, G., Finger, F., Paquette, J.L., von Quadt, A., McNaughton, N.J., Fletcher, I.R., 2004. Pre-variscan geological events in the austrian part of the bohemian massif deduced from U-Pb zircon ages. Int. J. Earth Sci. 93 (5), 802–823. https://doi.org/10.1007/s00531-004-0420-9.

Frimmel, H.E., Schedel, S., Brätz, H., 2014b. Uraninite chemistry as forensic tool for provenance analysis. Appl. Geochem. 48, 104–121. https://doi.org/10.1016/j.apgeochem.2014.07.013.

Fuchs, V.G., 1976. Zur entwicklung der böhmischen masse. Jahrb. Geol. B.-A. 119, 45–61 (in German).

Guo, X., Szenknect, S., Mesbah, A., Labs, S., Clavier, N., Poinssot, C., Ushakov, S.V., Curtius, H., Bosbach, D., Ewing, R.C., Burns, P.C., Dacheux, N., Navrotsky, A., 2015. Thermodynamics of formation of coffinite, USiO 4. Proceedings of the National Academy of Sciences 112 (21), 6551–6555. https://doi.org/10.1073/pnas.1507441112.

Hasalová, P., Schulmann, K., Lexa, O., Štípská, P., Hrouda, F., Ulrich, S., Týcová, P., 2008. Origin of migmatites by deformation-enhanced melt infiltration of orthogneiss: a new model based on quantitative microstructural analysis. J. Metamorph. Geol. 26 (1), 29–53. https://doi.org/10.1111/j.1525-1314.2007.00743.x.

Hecht, L., Cuney, M., 2000. Hydrothermal alteration of monazite in the Precambrian crystalline basement of the athabasca basin (saskatchewan, Canada): implications for the formation of unconformity-related uranium deposits. Mineral. Deposita 35 (8), 791–795. https://doi.org/10.1007/s001260050280.

Hein, U., Lehmann, B., Kříbek, B., René, M., 2002. Evolution of ore-forming fluids along the Rožná-Olší shear zone, Bohemian Massif, Czech Republic: implication for local uranium deposition and comparison with U-mineralization at Schlema, Erzgebirge, Germany. In: Kříbek, B., Zeman, J. (Eds.), Uranium Deposits: From their Genesis to their Environmental Aspects. Czech Geological Survey, Prague, pp. 61–64.

Henderson, P., 1984. General geochemical properties and abundances of the rare earth elements. Rare Earth Element Geochemistry 1–32. https://doi.org/10.1016/b978-0-444-42148-7.50006-x.

Holá, M., Novotný, K., Dobeš, J., Krempl, I., Wertich, V., Mozola, J., Kubeš, M., Faltusová, V., Leichmann, J., Kanický, V., 2021. Dual imaging of uranium ore by Laser ablation inductively coupled plasma mass spectrometry and laser induced breakdown spectroscopy. Spectrochim. Acta B At. Spectrosc. 186, 106312 https://doi.org/10.1016/j.sab.2021.106312.

Hoskin, P.W., Ireland, T.R., 2000. Rare earth element chemistry of zircon and its use as a provenance indicator. Geology 28 (7), 627–630. https://doi.org/10.1130/0091-7613(2000)28<627:REECOZ>2.0.CO;2.

IAEA, 2018. Geological Classification of Uranium Deposits and Description of selected examples. In: Iaea-TECDOC-1842. IAEA, Vienna. ISBN 978–92–0–101618–8.

Janeczek, J., Ewing, R., 1992a. Structural formula of uraninite. J. Nucl. Mater. 190, 128–132. https://doi.org/10.1016/0022-3115(92)90082-v.

Janeczek, J., Ewing, R., 1992b. Dissolution and alteration of uraninite under reducing conditions. J. Nucl. Mater. 190, 157–173. https://doi.org/10.1016/0022-3115(92)90084-x.

Janeczek, J., Ewing, R., 1995. Mechanisms of lead release from uraninite in the natural fission reactors in Gabon. Geochim. Cosmochim. Acta 59 (10), 1917–1931. https://doi.org/10.1016/0016-7037(95)00117-4.

Janoušek, V., Holub, F.V., 2007. The causal link between HP-HT metamorphism and ultrapotassic magmatism in collisional orogens: case study from the moldanubian zone of the bohemian massif. Proc. Geol. Assoc. 118 (1), 75–86. https://doi.org/10.1016/S0016-7878(07)80049-6.

Janoušek, V., Hanžl, P., Svojtka, M., Hora, J.M., Kochergina, Y.V.E., Gadas, P., Holub, F. V., Gerdes, A., Verner, K., Hrdličková, K., Daly, J.S., Buriánek, D., 2020. Ultrapotassic magmatism in the heyday of the Variscan Orogeny: the story of the Třebíč Pluton, the largest durbachitic body in the Bohemian Massif. In International Journal of Earth Sciences 109 (5), 1767–1810. https://doi.org/10.1007/s00531-020-01872-2.

Kempe, U., 2003. Precise electron microprobe age determination in altered uraninite: consequences on the intrusion age and the metallogenic significance of the kirchberg granite (erzgebirge, Germany). Contrib. Mineral. Petrol. 145, 107–118. https://doi.org/10.1007/s00410-002-0439-5.

Košler, J., Konopásek, J., Sláma, J., Vrána, S., 2014. U-Pb zircon provenance of moldanubian sediments in the bohemian massif. J. Geol. Soc. 171, 83–95. https://doi.org/10.1144/jgs2013-059.

Kříbek, B., Žák, K., Dobeš, P., Leichmann, J., Pudilová, M., René, M., Scharm, B., Scharmová, M., Hájek, A., Holéczy, D., Hein, U.F., Lehmann, B., 2009. The rožná uranium deposit (bohemian massif, Czech republic): shear zone-hosted, late variscan and post-variscan hydrothermal mineralization. Mineral. Deposita 44 (1), 99–128. https://doi.org/10.1007/s00126-008-0188-0.

Kříbek, B., Knésl, I., Dobeš, P., Veselovský, F., Pořádek, P., Škoda, R., Čopjaková, R., Leichmann, J., Košek, F., 2022. The origin of synchysite-(Ce) and sources of rare earth elements in the rožná uranium deposit. Czech Republic. Minerals 12 (6), 690. https://doi.org/10.3390/min12060690.

Kubeš, M., Leichmann, J., Wertich, V., Mozola, J., Holá, M., Kanický, V., Škoda, R., 2021. Metamictization and fluid-driven alteration triggering massive HFSE and REE mobilization from zircon and titanite: direct evidence from EMPA imaging and LA-ICP-MS analyses. Chem. Geol. 586, 120593 https://doi.org/10.1016/j.chemgeo.2021.120593.

Kubeš, M., Leichmann, J., Kotková, J., Čopjaková, R., Holá, M., Sláma, J., 2022. Diversity of origin and geodynamic evolution of the mantle beneath the variscan orogen indicating rapid exhumation within subduction-related mélange (moldanubian zone, bohemian massif). Lithos 422–423 (106726), 1–22. https://doi.org/10.1016/j.lithos.2022.106726.

Kusbach, V., Janoušek, V., Hasalová, P., Schulmann, K., Fanning, C.M., Erban, V., Ulrich, S., 2015. Importance of crustal relamination in origin of the orogenic mantle peridotite–high-pressure granulite association: example from the náměšť granulite massif (bohemian massif, Czech republic). J. Geol. Soc. 172 (4), 479–490. https://doi.org/10.1144/jgs2014-070.

Lardeaux, J.M., Schulmann, K., Faure, M., Janoušek, V., Lexa, O., Skrzypek, E., Edel, J.B., Štípská, P., 2014. The moldanubian zone in the French massif central, vosges/

schwarzwald and bohemian massif revisited: differences and similarities. Geol. Soc. Lond. Spec. Publ. 405 (1), 7–44. https://doi.org/10.1144/SP405.14.
Leichmann, J., Matula, M., Broska, I., Holéczy, D., 2002. Low-degree partial melting of metapelites—another possible implement for selective concentration of uranium: example from the Rožná uranium deposit, Bohemian Massif. In: Uranium deposits: from their genesis to their environmental aspects. Proceedings of the International Workshop. Czech Geological Survey, Prague, ISBN 80-7075-583-0, pp. 75–78.
Leichmann, J., Gnojek, I., Novák, M., Sedlák, J., Houzar, S., 2017. Durbachites from the eastern moldanubicum (bohemian massif): erosional relics of large, flat tabular intrusions of ultrapotassic melts—geophysical and petrological record. Int. J. Earth Sci. 106 (1), 59–77. https://doi.org/10.1007/s00531-016-1296-1.
Ludwig, K.R., 2003. User's Manual for Isoplot 3.00 : A Geochronological Toolkit for Microsoft Excel, Berkeley CA. Special publication / Berkeley Geochronology Centre. No. 4.
Marks, M.A., Coulson, I.M., Schilling, J., Jacob, D.E., Schmitt, A.K., Markl, G., 2008. The effect of titanite and other HFSE-rich mineral (Ti-bearing andradite, zircon, eudialyte) fractionation on the geochemical evolution of silicate melts. Chem. Geol. 257 (1–2), 153–172. https://doi.org/10.1016/j.chemgeo.2008.09.002.
Martz, P., Mercadier, J., Perret, J., Villeneuve, J., Deloule, E., Cathelineau, M., Quirt, D., Doney, A., Ledru, P., 2019a. Post-crystallization alteration of natural uraninites: Implications for dating, tracing, and nuclear forensics. Geochim. Cosmochim. Acta 249, 138–159. https://doi.org/10.1016/j.gca.2019.01.025.
Martz, P., Mercadier, J., Cathelineau, M., Boiron, M.C., Quirt, D., Doney, A., Gerbeaud, O., de Wally, E., Ledru, P., 2019b. Formation of U-rich mineralizing fluids through basinal brine migration within basement-hosted shear zones: a large-scale study of the fluid chemistry around the unconformity-related cigar lake U deposit (saskatchewan, Canada). Chem. Geol. 508, 116–143. https://doi.org/10.1016/j.chemgeo.2018.05.042.
Matte, P., Maluski, H., Rajlich, P., Franke, W., 1990. Terrane boundaries in the bohemian massif: result of large-scale variscan shearing. Tectonophysics 177, 151–170. https://doi.org/10.1016/0040-1951(90)90279-H.
McCann, T., Pascal, C., Timmerman, M., Krzywiec, P., López-Gómez, J., Wetzel, L., Krawczyk, C., Rieke, H., Lamarche, J., 2006. Post-variscan (end carboniferous-early permian) basin evolution in western and central europe. Geol. Soc. Lond. Mem. 32 (1), 355–388. https://doi.org/10.1144/gsl.mem.2006.032.01.22.
McDonough, W., Sun, S.S., 1995. The composition of the earth. Chem. Geol. 120 (3–4), 223–253. https://doi.org/10.1016/0009-2541(94)00140-4.
Medaris, G., Wang, H., Jelínek, E., Mihaljevič, M., Jakeš, P., 2005. Characteristics and origins of diverse variscan peridotites in the gföhl nappe, bohemian massif. Czech Republic. Lithos 82 (1–2), 1–23. https://doi.org/10.1016/j.lithos.2004.12.004.
Medaris, L.G., Beard, B.L., Jelínek, E., 2006. Mantle-derived, UHP garnet pyroxenite and eclogite in the moldanubian gföhl nappe, bohemian massif: a geochemical review, new P-T determinations, and tectonic interpretation. Int. Geol. Rev. 48 (9), 765–777. https://doi.org/10.2747/0020-6814.48.9.765.
Mercadier, J., Cuney, M., Lach, P., Boiron, M.C., Bonhoure, J., Richard, A., Leisen, M., Kister, P., 2011. Origin of uranium deposits revealed by their rare earth element signature. Terra Nova 23 (4), 264–269. https://doi.org/10.1111/j.1365-3121.2011.01008.x.
Migdisov, A., Williams-Jones, A.E., Brugger, J., Caporuscio, F.A., 2016. Hydrothermal transport, deposition, and fractionation of the REE: experimental data and thermodynamic calculations. Chem. Geol. 439, 13–42. https://doi.org/10.1016/j.chemgeo.2016.06.005.
Montel, J.M., Foret, S., Veschambre, M., Nicollet, C., Provost, A., 1996. Electron microprobe dating of monazite. Chem. Geol. 131 (1–4), 37–53. https://doi.org/10.1016/0009-2541(96)00024-1.
Nash, J.T., Granger, H.C., Adams, S.S., 1981. Geology and Concepts of Genesis of Important Types of Uranium Deposits. In: Skinner, B.J. (Ed.), Seventy-Fifth Anniversary Volume. Society of Economic Geologists. https://doi.org/10.5382/av75.04.
O'Brien, P.J., Rötzler, J., 2003. High-pressure granulites: formation, recovery of peak conditions and implications for tectonics. J. Metamorph. Geol. 21 (1), 3–20. https://doi.org/10.1046/j.1525-1314.2003.00420.x.
Ozha, M.K., Pal, D.C., Mishra, B., Desapati, T., Shaji, T.S., 2017. Geochemistry and chemical dating of uraninite in the samarkiya area, central rajasthan, northwestern India – Implication for geochemical and temporal evolution of uranium mineralization. Ore Geol. Rev. 88, 23–42. https://doi.org/10.1016/j.oregeorev.2017.04.010.
Pérez-Soba, C., Villaseca, C., Orejana, D., Jeffries, T., 2014. Uranium-rich accessory minerals in the peraluminous and perphosphorous belvís de monroy pluton (iberian variscan belt). Contrib. Mineral. Petrol. 167 (5) https://doi.org/10.1007/s00410-014-1008-4.
Pešek, J., Holub, V., Jaroš, J., Malý, L., Martínek, K., Prouza, V., Tásler, R., Bek, J., Drábková, J., Kautský, J., Kobr, M., Krásný, J., Mikuláš, R., Opluštil, S., Skoček, V., Sýkorová, I., Šimůnek, Z., Valterová, P., Zajíc, J., 2001. Geology and deposits of upper Paleozoic limnic basins of the Czech Republic. Český geologický ústav, Praha, ISBN 80-7075-470-2, 243 pp (in Czech).
von Raumer, J.F., Finger, F., Veselá, P., Stampfli, G.M., 2013. Durbachites-vaugnerites – a geodynamic marker in the central european variscan orogen. Terra Nova 26 (2), 85–95. https://doi.org/10.1111/ter.12071.
René, M., 2008. Anomalous rare earth element, yttrium and zirconium mobility associated with uranium mineralization. Terra Nova 20 (1), 52–58. https://doi.org/10.1111/j.1365-3121.2007.00786.x.
René, M., Dolníček, Z., Sejkora, J., Škácha, P., Šrein, V., 2019. Uraninite, coffinite and ningyoite from vein-type uranium deposits of the bohemian massif (central european variscan belt). Minerals 9 (2), 123. https://doi.org/10.3390/min9020123.
Ruzicka, V., 1971. In: Geological comparison between east European and Canadian uranium deposits. Series: Geological Survey of Canada. Papers, 1970, p. 48. https://doi.org/10.4095/102392, 196 pp.
Ruzicka, V., 1993. Vein uranium deposits. Ore Geol. Rev. 8 (3–4), 247–276. https://doi.org/10.1016/0169-1368(93)90019-u.
Schulmann, K., Kröner, A., Hegner, E., Wendt, I., Konopásek, J., Lexa, O., Štípská, P., 2005. Chronological constraints on the pre-orogenic history, burial and exhumation of deep-seated rocks along the eastern margin of the variscan orogen – bohemian massif, Czech Republic. Am. J. Sci. 305, 407–448. https://doi.org/10.2475/ajs.305.5.407.
Shannon, R.D., 1976. Revised effective ionic radii and systematic studies of interatomic distances in halides and chalcogenides. Acta Crystallographica Section A 32 (5), 751–767. https://doi.org/10.1107/s0567739476001551.
Soder, C.G., Romer, R.L., 2018. Post-collisional potassic–ultrapotassic magmatism of the variscan orogen: implications for mantle metasomatism during continental subduction. J. Petrol. 59 (6), 1007–1034. https://doi.org/10.1093/petrology/egy053.
Spano, T.L., Simonetti, A., Balboni, E., Dorais, C., Burns, P.C., 2017. Trace element and U isotope analysis of uraninite and ore concentrate: applications for nuclear forensic investigations. Appl. Geochem. 84, 277–285. https://doi.org/10.1016/j.apgeochem.2017.07.003.
Šurán, J., Pluskal, O., Duda, V., 1965. Report on the completion of exploration work at the slavkovice deposit. Uranium industry - geological exploration, nové město na moravě. Příbram. 102 pp. Unpublished report (in Czech).
Szenknect, S., Alby, D., López García, M., Wang, C., Podor, R., Miserque, F., Mesbah, A., Duro, L., Zetterström Evins, L., Dacheux, N., Bruno, J., Ewing, R.C., 2020. Coffinite formation from UO2+x. Sci. Rep. 10 (1) https://doi.org/10.1038/s41598-020-69161-1.
Tajčmanová, L., Konopásek, J., Schlumann, K., 2006. Thermal evolution of the orogenic lower crust during exhumation within a thickened moldanubian root of the variscan belt of central europe. J. Metamorph. Geol. 24 (2), 119–134. https://doi.org/10.1111/j.1525-1314.2006.00629.x.
Timmerman, M.J., 2008. In: Palaeozoic magmatism. The Geology of Central Europe Volume 1: Precambrian and Palaeozoic, pp. 665–748. https://doi.org/10.1144/cev1p.12.
Turpin, L., Leroy, J.L., Sheppard, S.M., 1990. Isotopic systematics (O, H, C, Sr, Nd) of superimposed barren and U-bearing hydrothermal systems in a hercynian granite, massif central. France. Chemical Geology 88 (1–2), 85–98. https://doi.org/10.1016/0009-2541(90)90105-g.
Vrána, S., Janoušek, V., Franěk, J., 2013. Contrasting mafic to felsic HP-HT granulites of the blansky les massif (moldanubian zone of southern bohemia): complexity of mineral assemblages and metamorphic reactions. J. Geosci. 58 (4), 347–378. https://doi.org/10.3190/jgeosci.157.
Žák, J., Verner, K., Janoušek, V., Holub, F.V., Kachlík, V., Finger, F., Hajná, J., Tomek, F., Vondrovic, L., Trubač, J., 2014. A plate-kinematic model for the assembly of the bohemian massif constrained by structural relationships around granitoid plutons. Geol. Soc. Lond., Spec. Publ. 405 (1), 169–196. https://doi.org/10.1144/SP405.9.
Zhu, X.K., O'Nions, R.K., 1999. Monazite chemical composition: some implications for monazite geochronology. Contrib. Mineral. Petrol. 137 (4), 351–363. https://doi.org/10.1007/s004100050555.

PAPER 2

Possibilities of LA-ICP-MS technique for the spatial elemental analysis of the recent fish scales: Line scan vs. depth profiling

Holá, M., Kalvoda, J.*, Nováková, H., Škoda, R., Kanický

Applied Surface Science. 2011, 257(6), 1932-1940. DOI 10.1016/j.apsusc.2010.09.029

Contribution:

LA-ICP-MS design of experiments and measurements, data evaluation, participation in manuscript writing.

Applied Surface Science 257 (2011) 1932–1940

Contents lists available at ScienceDirect

Applied Surface Science

journal homepage: www.elsevier.com/locate/apsusc

Possibilities of LA-ICP-MS technique for the spatial elemental analysis of the recent fish scales: Line scan *vs.* depth profiling

Markéta Holá[a], Jiří Kalvoda[b,*], Hana Nováková[a], Radek Škoda[b], Viktor Kanický[a]

[a] Department of Chemistry, Masaryk University of Brno, Kamenice 5, 625 00 Brno, Czech Republic
[b] Department of Geological Sciences, Masaryk University of Brno, Kotlářská 2, 611 37 Brno, Czech Republic

ARTICLE INFO

Article history:
Received 3 May 2010
Received in revised form 11 August 2010
Accepted 9 September 2010
Available online 18 September 2010

Keywords:
Laser ablation-inductively coupled plasma-mass spectrometry (LA-ICP-MS)
Fish scale
Hydroxyapatite layer
Metal
Spatial distribution

ABSTRACT

LA-ICP-MS and solution based ICP-MS in combination with electron microprobe are presented as a method for the determination of the elemental spatial distribution in fish scales which represent an example of a heterogeneous layered bone structure.

Two different LA-ICP-MS techniques were tested on recent *common carp* (*Cyprinus carpio*) scales:

(a) A line scan through the whole fish scale perpendicular to the growth rings. The ablation crater of 55 μm width and 50 μm depth allowed analysis of the elemental distribution in the external layer. Suitable ablation conditions providing a deeper ablation crater gave average values from the external HAP layer and the collagen basal plate.
(b) Depth profiling using spot analysis was tested in fish scales for the first time. Spot analysis allows information to be obtained about the depth profile of the elements at the selected position on the sample.

The combination of all mentioned laser ablation techniques provides complete information about the elemental distribution in the fish scale samples. The results were compared with the solution based ICP-MS and EMP analyses. The fact that the results of depth profiling are in a good agreement both with EMP and PIXE results and, with the assumed ways of incorporation of the studied elements in the HAP structure, suggests a very good potential for this method.

1. Introduction

1.1. LA-ICP-MS in fish analysis

Laser ablation inductively coupled plasma mass spectrometry (LA-ICP-MS) is a technique commonly used for the direct analysis and microanalysis of solid samples [1–3]. The field of LA-ICP-MS applications is at present very wide – from bulk analysis of various types of materials, local analysis, to depth profiling or spatial elemental analysis [4,5]. The character of the spatial LA-ICP-MS analysis or depth profiling mainly depends on the laser ablation conditions such as size of the ablation spot, pulse energy or shape of the ablation crater [6–8]. With all conditions adjusted for the specific application, the LA-ICP-MS method can even provide information of elemental concentration gradients across small targets or across a defined section of a multilayer sample [9].

The elemental analysis of the age-structured bone structures has become an integral part of environmental science and fisheries. The most common research focuses on the fish otoliths and can provide information about stock discrimination, fish migration, population dynamics or environmental reconstruction [10,11]. The fish scale, as another bone structure, is also used for the same purpose as otoliths but the bone analysis is not so popular. The more complicated structure of the fish scale makes the analysis more intricate and the different scale mineralogy (Ca deficient hydroxyapatite $Ca_{10}(PO_4)_6(OH)_2$) contributes to a higher concentration of most elements. Nevertheless, the scale analysis is a non-lethal method and can thus be very useful for the illustration of both water contamination and migration during the life span of a fish. Since the pioneering work of Countant and Chen [12] focused on the distinction between freshwater and estuarine striped bass, LA-ICP-MS has been used to determine scale chemistry in various applications. Typically it has been used for marine fish such as the spot analysis of a specific area to compare different wild and farmed stocks of salmon [13], the spatial distribution analysis of metals among the growth annuli of the Artic grayling scales [14] and for the identifica-

* Corresponding author.
E-mail addresses: jkalvoda@centrum.cz, dino@sci.muni.cz (J. Kalvoda).

0169-4332/$ – see front matter © 2010 Elsevier B.V. All rights reserved.
doi:10.1016/j.apsusc.2010.09.029

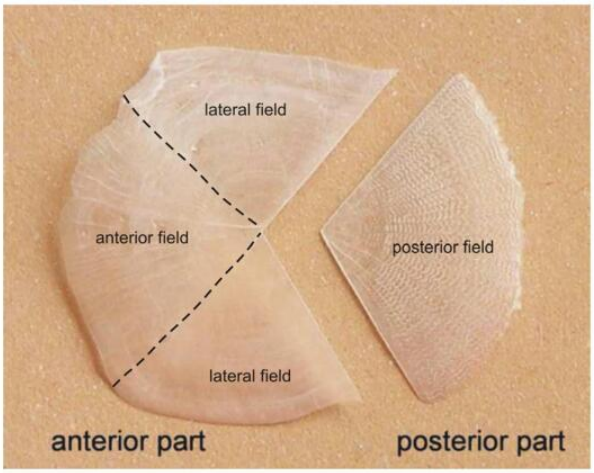

Fig. 1. Dorsal view of the fish scale of the common carp cut to posterior and anterior part for sample dilution. Anterior part divided in the anterior and lateral fields is covered by other fish scales while posterior field is in contact with water.

tion of the migration history of the natal stream origin of westslope cutthroat trout [15] and north sea houting [16].

The correlation between scale and otolith analytical results confirms that the scale method may provide a non-lethal alternative to otoliths for fish chemistry. Another work using LA-ICP-MS analysis proves fish scales as a useful environmental marker [17,18]. Recently, laser ablation of fish scales was applied to the study of environmental contamination and rapid changes in the chemical composition of hydroxyapatite during very early diagenetic processes [19,20] and the fish position in the trophic pyramid [20].

Solution based ICP-MS was applied [21] for the correlation between scales, otoliths and other fish tissues and to study the life-history of juvenile spot [22].

In addition to the already widely applied line or spot scans, a method of depth profiling combined with an electron microprobe was used for the first time in this paper.

1.2. Fish scale morphology and structure

Fish scales are skeletal elements, of dermal origin, that grow shingle-like from pockets within the skin and provide protection. The distinct scale focus (first formed) almost in the center divides the scale into anterior (rostral), posterior (caudal) and lateral fields (Fig. 1). The posterior part covered with epidermis and mucus is exposed (i.e. in contact with water) and firmly embedded in the skin, while anterior and lateral fields are deeply embedded within the dermis and overlapped by other scales [23,24]. The dorsal (external) side of the scale (Fig. 1) is ornamented by concentric ridges called circuli produced at the margin of the scale as the fish grows. Year marks (annuli) are characterized by closely spaced or incomplete circuli at both sides of the scale. As a fish becomes older, growth rate slows down, annuli become closer together and the precise age determination is more difficult [24].

Transverse sections through the scale reveal the characteristic layered organization. Below the epidermal and dermal scale covering, the scale is mainly composed of two superimposed layers. The thin external well-mineralized osseous layer with randomly arranged thin collagen fibres embedded in a proteoglycan matrix which compares to dentin or woven bone [25,26]. Sometimes, a very thin (about 1 μm) hyper-mineralized limiting layer nearly devoid of collagen is distinguished at the surface of the osseous layer analogous to enamel. The basal plate is a thick layer of incompletely mineralized tissue composed of several layers of collagen fibrils organized into a plywood structure [27–35]. While there is a general decrease in thickness of the basal plate from the focus to the growing tip of the scale, the thickness of the osseous layer does not change significantly [36,37].

Similar to bones, the osseous layer is composed of hydroxyapatite (HAP) [25]. Biological apatites occur mainly in the form of poorly crystallized nonstoichiometric nanostructured Ca deficient carbonate-bearing HAP with a high vacancy content and a significant amount of foreign ion substitutions. Consequently, the hydroxyl concentration in biological apatites is considerably lower than in synthetic HAP [38–40] which is also the case for fish scales [34].

2. Samples

2.1. Sample characterization

Two scales were obtained from an individual of the common carp (*Cyprinus carpio*) living in Brno reservoir in South Moravia, Czech Republic. The age of the carp was estimated from the scale growth rings at 2 years. The thickness of the scales and the individual layers were measured from the scale cross-section by backscattering electron microscopy (BSE). The thickness of the external layer changes from 50 to 100 μm; the collagen plate was 70 μm thick (Fig. 4a).

2.2. Sample preparation

The scales were first cleaned of impurities, mucilage and the thin transparent skin exuding the mucilage. The cleaning procedure was based on the sonication by 5% hydrogen peroxide (Perhydrol®, p.a.) in an ultrasonic bath for 5 min and subsequent brushing. The brushing was undertaken using a tooth-brush, the surface of the scale was observed by a binocular microscope. The procedure was repeated three times.

2.2.1. LA-ICP-MS

The spatial LA-ICP-MS analysis requires a sample with sufficient straightness so as to allow application of a linear scan (or raster) across the whole surface area. After cleaning, the scale was moistened by ultra pure water and the wet scale placed between two microscopic slides and dried in the gel dryer (vacuum heated gel dryers) at 60 °C for 1 h. To secure the scale before any wrenching, the bottom part of the scale was fixed on the microscopic slide with double side tape, covered by the second microscopic slide and left under weight-bearing books for few days.

2.2.2. ICP-MS

The scales were air-dried after cleaning (described above). Two scales were analyzed as an entire sample, three scales were cut into to two parts – posterior and anterior, by plastic scissors (Fig. 1). Mineralization was realized by microwave digestion in a mixture of 4 ml of HNO_3 (65%) and 2 ml of H_2O_2 (30%). The solutions were topped up with deionized water up to 100 ml volume.

2.2.3. EMP

For the EMPA measurement two kinds of samples were prepared: (i) the carp scales were fixed to a glass slide by double sided tape and subsequently coated with carbon. (ii) Perpendicular section – the scale sections were mounted in epoxy discs, polished and carbon coated.

3. Experimental

3.1. LA-ICP-MS

Laser ablation was performed using a pulsed Nd:YAG laser system UP 213 (New Wave Research, Inc., Fremont, CA, USA) working at 213 nm wavelength and using a pulse duration of 4.2 ns. The ablation system is equipped with a 33-cm^3 SuperCell (New Wave Research) designed to enable rapid eluting of the ablation-generated aerosol in a large format cell. Helium was used as a carrier gas with a flow rate of 1 l min^{-1}. The aerosol was transported from the ablation cell through a 1-m long polyurethane transport tube (i.d. of 4 mm) to the ICP discharge of the quadrupole mass spectrometer (ICP-MS Agilent 7500ce, Agilent Technologies, Santa Clara, CA, USA).

Line scans were applied throughout the whole fish scale perpendicular to the growth rings. The spot diameter was 40 μm, scan speed 40 μm s^{-1} and a repetition rate of 10 Hz. The integration time of 1.6 s allowed recording of the information about the signal of isotope intensities at each 65 μm of the line (the lateral resolution was 65 μm). The fluence was set to 8 J cm^{-2} and provided an ablation crater of 50 μm depth allowing analysis of the external HAP layer. The following isotopes were monitored during the LA-ICP-MS scan measurements: ^{26}Mg, ^{31}P, ^{42}Ca, ^{55}Mn, ^{56}Fe, ^{66}Zn, ^{86}Sr and ^{208}Pb. The external calibration was performed using the standard reference material (SRM) – SRM NIST 1486 (bone meal powder). The bone meal powder was prepared for the ablation as a pressed pellet without any additional binder using a manual hydraulic press. Calcium was used as an internal standard; the Ca content in each part of the sample was obtained from EMP analysis. The limits of detection for the elements of interest in the line scan were defined as MD = $3\sigma/(S/c)$ (where σ is standard deviation of background, S is signal of isotope and c is concentration of element) on following isotopes: ^{24}Mg 15 μg g^{-1}, ^{31}P 80 μg g^{-1}, ^{42}Ca 70 μg g^{-1}, ^{55}Mn: 1.2 μg g^{-1}, ^{56}Fe: 2.5 μg g^{-1}, ^{66}Zn: 5.9 μg g^{-1}, ^{86}Sr: 8.5 μg g^{-1}, and ^{208}Pb 0.05 μg g^{-1}. The pressed bone standard was used for the signal repeatability calculation. Ten repetitions of line measurements were carried out on the pellet. The RSD reached 4.5%.

The depth profiling was performed using 100 μm spot ablation with a repetition rate of 4 Hz and fluence of 3.5 J cm^{-2}. To obtain signals with sufficient depth resolution, a limited number of isotopes were monitored during one measurement so as not to exceed the integration time of 0.2 s. In this way three groups of isotopes were monitored separately, during three measurements on a different sample area (1st group: ^{42}Ca, ^{31}P, ^{66}Zn, 2nd group: ^{42}Ca, ^{12}C, ^{86}Sr, 3rd group: ^{42}Ca, ^{26}Mg, ^{56}Fe, ^{208}Pb). ^{42}Ca was presented in each group to serve as a "control" isotope. The depth resolution (Δz) was determined from the average ablation rate (AAR) and the number of the laser pulses between 16 and 84% of the maximum intensity of the depth profile graph (Δp): $\Delta z = \Delta p \times$ AAR [41,42]. The depth resolution of C was 25 μm. The rest of the elements allowed depth profiling with a resolution of 10 μm.

3.2. ICP-MS

The ICP-MS instrument Agilent 7500ce (Agilent Technologies, Santa Clara, CA, USA) was used for the analyses of solutions. The instrument was operated with switched-in collision cell in He-mode for elimination of possible polyatomic interferences. Two sets of multielemental calibration solutions were prepared by the appropriate dilution of certified stock solutions Astasol® (made by Analytika, Ltd.) containing (1.000 ± 0.002) g l^{-1} of each element. One set of solutions was used for calibration of major elements (Ca, P, Mg), while the other was employed for trace elements. The following nuclides were selected and used for the ICP-MS analysis: ^{24}Mg, ^{31}P, ^{43}Ca, ^{55}Mn, ^{56}Fe, ^{66}Zn, ^{86}Sr, and ^{208}Pb.

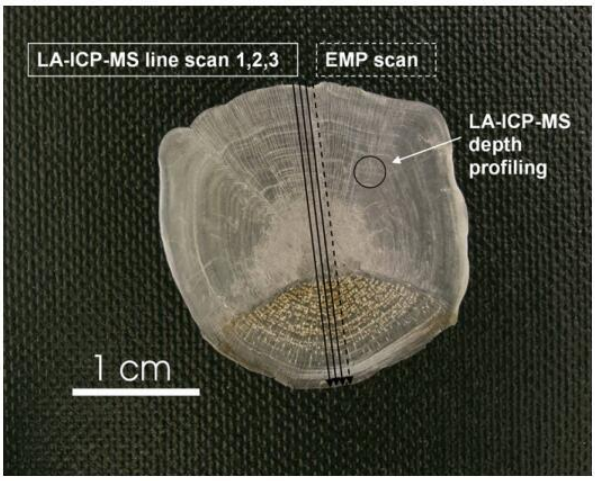

Fig. 2. Fish scale 1 with marked trajectories for LA-ICP-MS and EMP analysis.

3.3. Electron microprobe

Elemental abundances of Na, Ca, P, Fe, Mn, Mg, Si, Al, Sr, Zn, Pb, F and Cl in fish scales were determined using a CAMECA SX100 electron microprobe (Masaryk University and Czech Geological Survey Brno) equipped with a five wavelength dispersive spectrometer (WDS). The WDS analyses were performed on the carbon coated unpolished surface of the scales under the following conditions: accelerating voltage 15 kV, beam current 4 nA, and beam scanned area 50 × 35 μm. The homogeneous synthetic phases and well-defined minerals were used as standards. Raw data was converted into concentrations using the appropriate PAP matrix corrections [43]. The peak counting times were 20 s for Ca and P and 40–60 s for other elements. Under these conditions the average detection limits were as follows: ~1000 μg g^{-1} for F; ~700 μg g^{-1} for Na, Fe, Mn, Zn; ~500–600 μg g^{-1} for P, Mg, Ca, Cl, Sr; ~300 μg g^{-1} for Si, Al.

4. Results and discussion

4.1. Depth profiling

Depth profiling by the LA-ICP-MS method was applied to obtain information about the distribution of elements in different layers of the fish scale. The depth profile of elements of interest gives an illustration about the changes in elemental concentrations and the routes of their binding, i.e. in the structure of HAP or on its surface where nanocrystals of biological apatite display a large specific surface area critically important for the sorption of ions [44].

Depth profile analysis was performed for a limited number of isotopes during one analysis so as not to exceed the integration time of 0.2 s (conditions and groups of isotopes are described in Section 2). The spots for different groups of isotopes were placed at the anterior part of the scale with a spacing of 100 μm (the area for depth profiling is shown in Fig. 2). The results clearly show the concentration gradient of selected elements along the whole scale thickness and the interface between the external layer and basal plate is clearly visible – the most schematic example is given in Fig. 3a with Ca and C profile. Ca is the major element in the HAP layer while C is in the collagen plate.

A similar behavior of the elemental distribution was found for Ca, Mg, P, Fe and Sr (Fig. 3a–c) that are homogenously distributed in the external layer declining close to the collagen internal layer. Ca

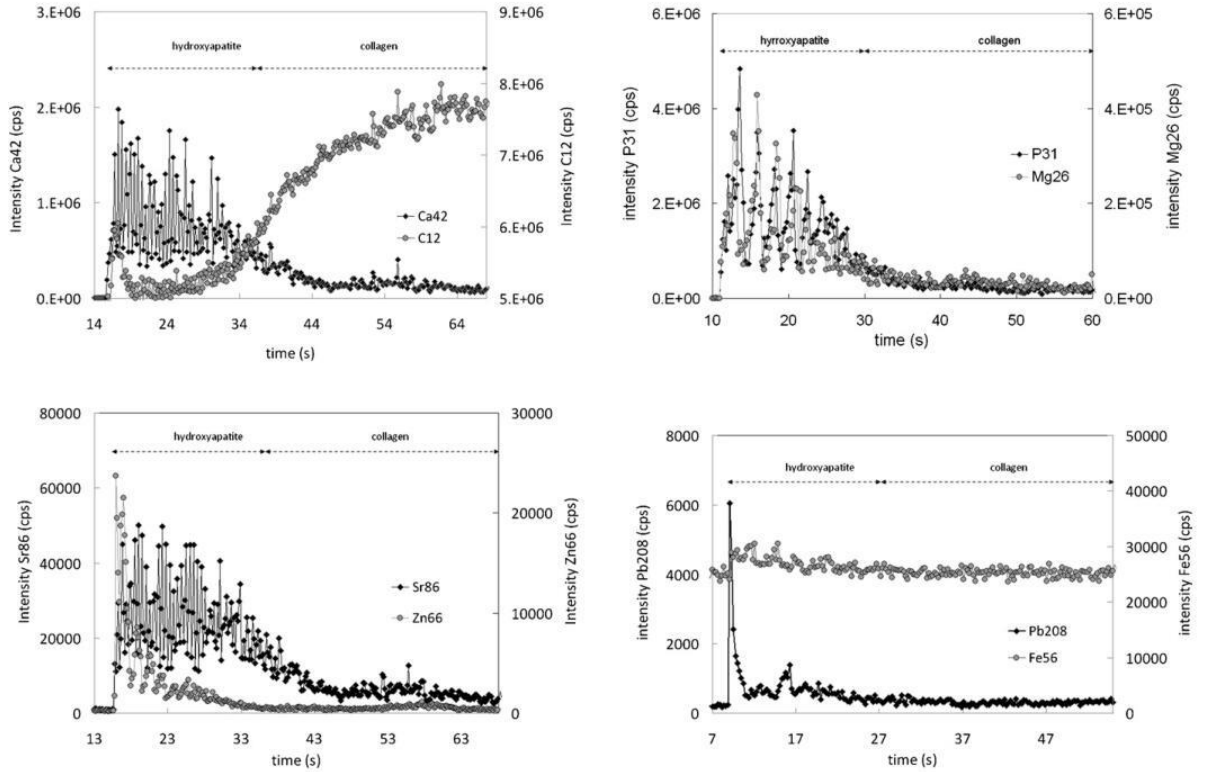

Fig. 3. LA-ICP-MS depth profiling on the posterior part of the fish scale 1 for following pairs of isotopes: ^{42}Ca and ^{12}C (a), ^{31}P and ^{26}Mg (b), ^{86}Sr and ^{66}Zn (c), ^{208}Pb and ^{56}Fe (d).

and P are major constituents of the HAP $Ca_{10}(PO_4)_6(OH)_2$ and both Mg and Sr are among the most common cation substituents in biological apatite replacing Ca in the crystal lattice [45]. The obtained results are well in accord with the character of the incorporation of the mentioned elements in the HAP structure [45–51].

Zn, and Pb representing trace heavy metals showed different behaviors (Fig. 3c, d). The accumulation of these elements on the surface of the HAP layer is clearly observed. Beside the cation substitution in the crystal lattice the surface binding of both Pb and Zn is well known [52–57]. The highest concentration of Zn close to the surface of the fish scale is very similar to the distribution obtained by proton induced X-ray emission (PIXE) in baramundi Lates calcarifer scale [58].

The depth profiling results were compared with the distribution maps made using EMP on the cross-section of the fish scale sample no. 2. The EMP maps (Fig. 4b–h) and LA-ICP-MS results were in very good agreement for all elements by both methods. Moreover, the obtained results are well in accord with the models of the incorporation of studied elements in the HAP.

4.2. Line scan laser ablation

The line scan LA was performed throughout the whole fish scale perpendicular to the growth rings encompassing the anterior part covered by other scales and the posterior part in contact with water. The ablation conditions (described in Section 2) were set to obtain an ablation crater with a 50 μm depth to analyze the HAP layer. Three measurements were done on each of the scales; the lines were placed in parallel 50 μm apart, crossing the focus (Fig. 2).

The line scan with continual motion of the sample allowed recording the information about isotope intensities at each 65 μm along the line. Each point of analysis expressing the integration time was converted into elemental concentrations using the calibration of external standard CRM NIST 1486 and ^{42}Ca as an internal standard. The values of the Ca content were obtained from EMP measurements of the specific position on the scale.

Variation of elements in the focus and anterior and poster elements are illustrated in Fig. 5. There is a difference in the character of the curves between the smaller posterior and the larger anterior part of the scale, where the curves show higher amplitudes. It reflects the fact that the growth rings in the posterior part are denser and the ablation spots thus include a larger ontogenic interval than in the posterior part.

In general, lower contents of elements in the anterior part of the scale (Tables 1 and 2) may reflect either lower thickness of its HAP layer or higher mineralization in the posterior part which is in contact with water. In the first case, the line scans penetrate deeper in the lower part of the HAP layer with more collagen (Fig. 3a) or even in the uppermost part of the collagen layer and thus dilute the content of most of the studied elements. In both cases, stronger mineralization means more possibilities for substitutions and filling of vacancies as Ca-deficient biologic HAP, by nature, induces much adsorption and a little elution of Ca [38,57]. In order to minimize the influence of variations in the HAP content, Fig. 6a–f showing the ratios of studied elements to major constituting element Ca were created.

All elements except Pb show a higher content in the posterior part of the scale. A minor increase is observed in Mg, Sr, Fe, Mn, then a distinct increase in Ca, P and finally a major increase in Zn. As Ca and P are major building elements of HAP. Their increase documents its higher representation. The elements of the first group, Mg,

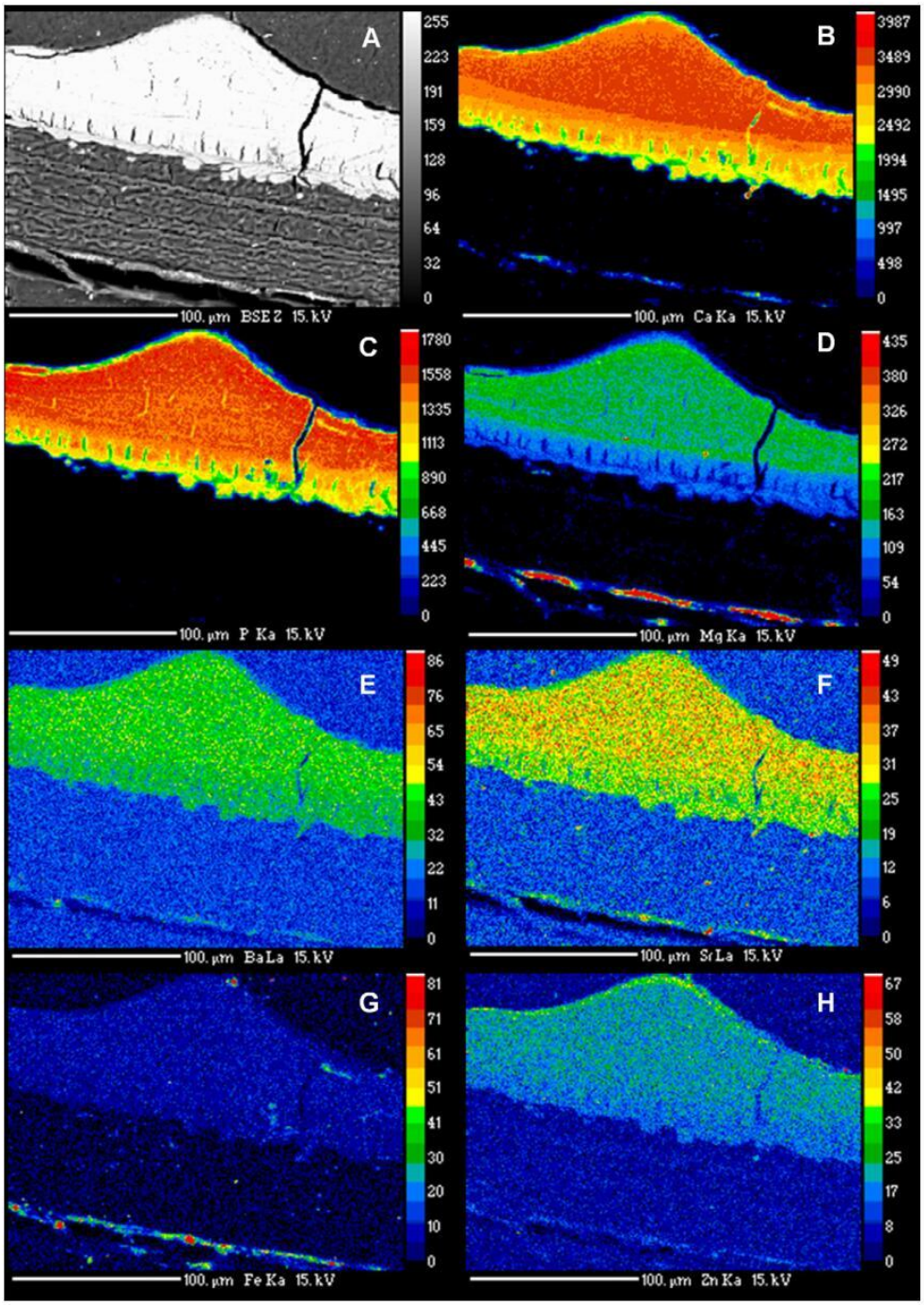

Fig. 4. BSE image of the analyzed area of the scale 1 cross-section (a); EMP spatial distribution maps for Ca (b), P (c), Mg (d), Ba (e), Sr (f), Fe (g) and Zn (h).

Sr, Fe, Mn substitute for Ca and fill in vacancies [45,57], and as illustrated by depth profiling (Fig. 3b–d) and EMP (Fig. 4d, f, and g) are homogenously distributed in the HAP layer. Even though there is a possibility of some uptake of these elements from the surrounding water, its major route is gastrointestinal or via the respiratory tract or even both. Consequently their higher content in the posterior part of the scale can be attributed, in our opinion, to a higher representation of the mineral phase which enables higher substitution and filling of vacancies. In the case of essential direct waterborne uptake, the highest concentrations of elements are to be expected in the posterior scale closest to the focus with the longest exposure, which is not the case.

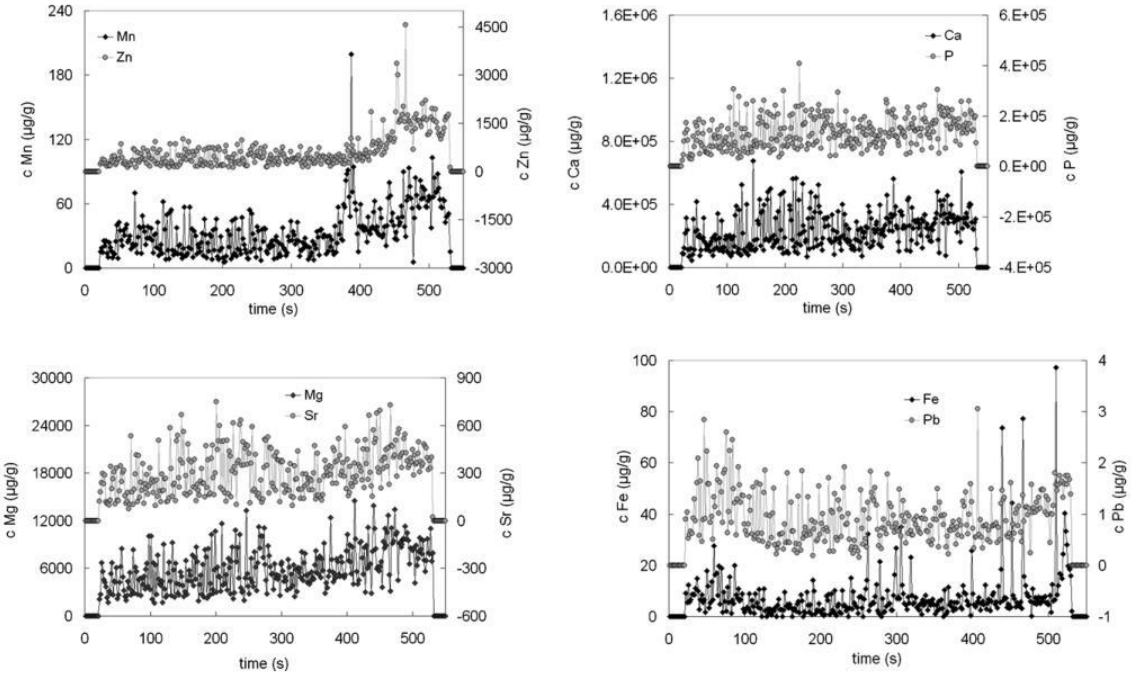

Fig. 5. LA-ICP-MS results of line scan 1 on the scale 1 for Mn and Zn (a), Ca and P (b), Mg and Sr (c), Fe and Pb (d).

Table 1
LA-ICP-MS line scan analysis of fish scale 1 (3 line scans).

Isotope	Concentration ($\mu g\,g^{-1}$)								
	Line scan 1			Line scan 2			Line scan 3		
	Whole scale	Anterior part	Posterior part	Whole scale	Anterior part	Posterior part	Whole scale	Anterior part	Posterior part
^{26}Mg	5160	4410	6440	5170	4560	6160	5460	4780	6550
^{31}P	136,000	131,000	145,000	142,000	137,000	150,000	138,000	134,000	145,000
^{42}Ca	244,000	234,000	259,000	243,000	233,000	259,000	244,000	234,000	260,000
^{55}Mn	33.9	28.4	43.4	34.5	28.7	44.0	34.2	28.1	44.2
^{56}Fe	10.1	7.82	14.0	8.65	6.45	12.2	4.67	4.91	4.27
^{66}Zn	564	412	827	630	467	892	539	398	770
^{86}Sr	276	249	323	283	262	316	294	271	331
^{208}Pb	0.565	0.563	0.566	0.577	0.606	0.530	0.675	0.677	0.670

This interpretation is also supported by relatively symmetric peaks in the distribution of elements like Fe or Mn (Figs. 5a, 5d, 6b, and 6c). The symmetric distribution of Fe with peaks in focus and at the margins of the scale may be influenced by dietary factors connected with either a higher uptake of food rich in these elements or with drinking water with a higher Fe content [59–62]. However, it is beyond the scope of this paper to follow this line in detail.

A high increase in the posterior part is in Zn (Figs. 5a and 6f) which shows a different incorporation in the HAP structure when compared with the previous elements. Zn incorporation into HAP does not only take place by ion exchange and filling vacancies [63]

Table 2
LA-ICP-MS line scan analysis of fish scale 2 (3 line scans).

Isotope	Concentration ($\mu g\,g^{-1}$)								
	Line scan 1			Line scan 2			Line scan 3		
	Whole scale	Anterior part	Posterior part	Whole scale	Anterior part	Posterior part	Whole scale	Anterior part	Posterior part
^{26}Mg	6030	5130	7090	5600	4550	6930	5970	5100	7000
^{31}P	137,000	128,000	150,000	128,000	120,000	140,000	130,000	125,000	139,000
^{42}Ca	238,000	216,000	268,000	232,000	217,000	255,000	238,000	226,000	258,000
^{55}Mn	34.8	24.4	45.8	33.1	25.4	42.6	36.7	26.5	47.7
^{56}Fe	7.77	6.14	9.56	8.85	8.01	10.0	13.0	18.1	8.49
^{66}Zn	674	411	947	655	381	980	601	393	818
^{86}Sr	309	286	341	292	265	330	293	253	341
^{208}Pb	0.938	0.950	0.958	0.926	0.936	0.937	1.01	1.06	0.985

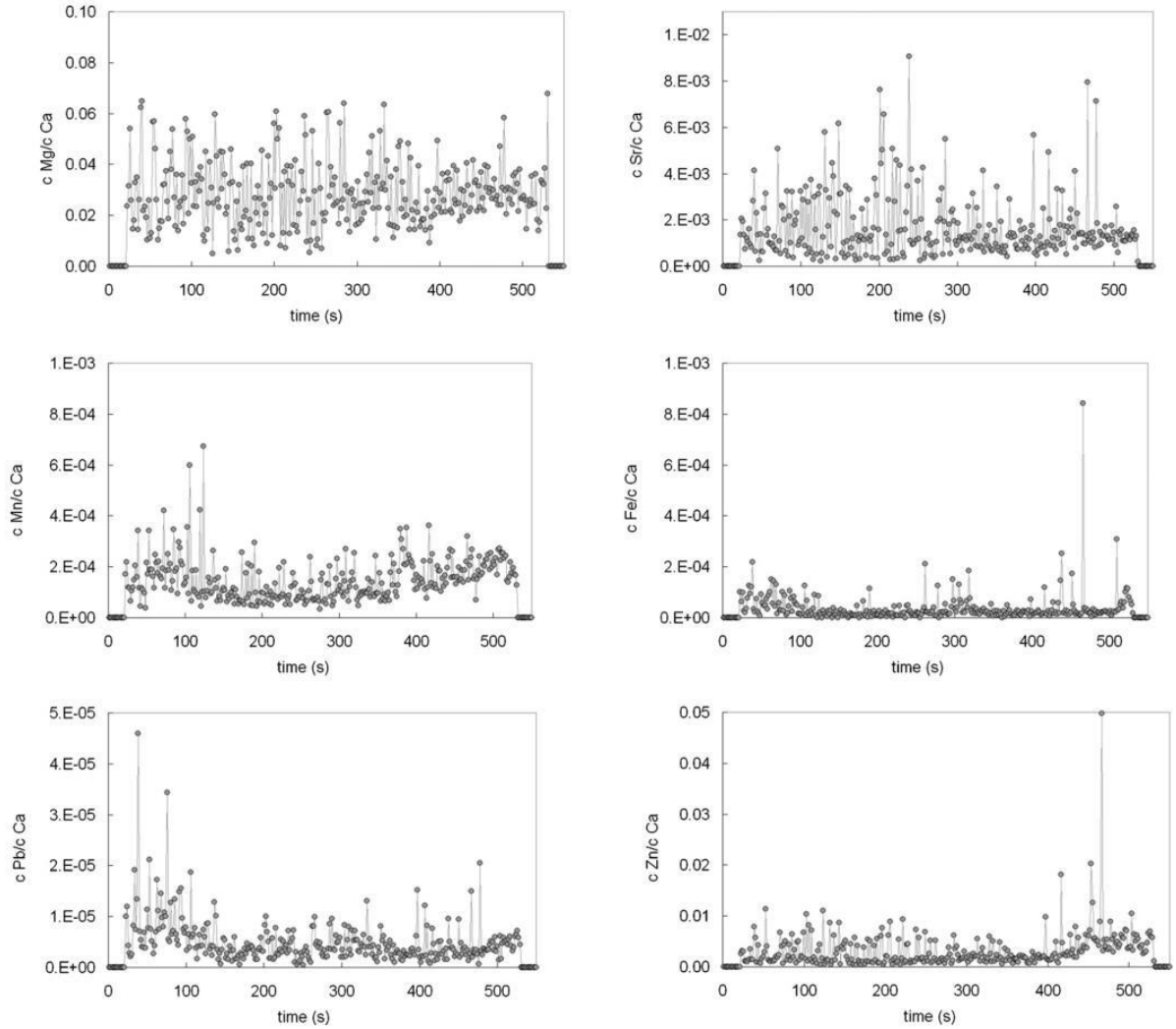

Fig. 6. LA-ICP-MS concentration ratios in line scan 1 for Mg/Ca (a), Mn/Ca (b), Sr/Ca (c), Fe/Ca (d), Pb/Ca (e), and Zn/Ca (f).

but more substantially zinc appears to be sorbed to the surface of the HAP [55] which is also well illustrated by depth profiling and EMP (Figs. 3c and 4h). Such a distribution is not surprising as the fish skin represents another important Zn uptake path beside the gastrointestinal and respiratory tracts [64,59]. In common carp an even higher accumulation of Zn in the skin than in the scales has been documented [65].

Quite different elemental distributions were observed for Pb (Figs. 5d and 6e). It is symmetric with a higher Pb content near the edge of the scale. The distinctly higher values are, however, in the anterior part of the scale. Even though the data concerning Pb are close to detection limits and should be taken with caution, the symmetric distribution supports the idea that the elements are mostly accumulated in the fish scale region that grows during their higher administration via blood circulation, i.e. of digestive or respiratory origin [66,67]. This interpretation may also be supported by the higher representation in anterior part of the scale (Fig. 5d) which is in direct contact with the dermis where the blood vessels provide direct nourishment. The posterior part of the scale is covered only with epidermis [68] where the elements enter only by diffusion from the dermis or from water.

Table 3
EMP line scan analysis of fish scale 1 (1 line scan).

Element/scale part	Concentration ($\mu g\,g^{-1}$)					
	Mn	Fe	P	Sr	Ca	Mg
Whole scale	80	50	120,000	290	248,000	4540
Anterior part	63	45	111,000	253	235,000	3360
Posterior part	104	52	133,000	340	265,000	6180

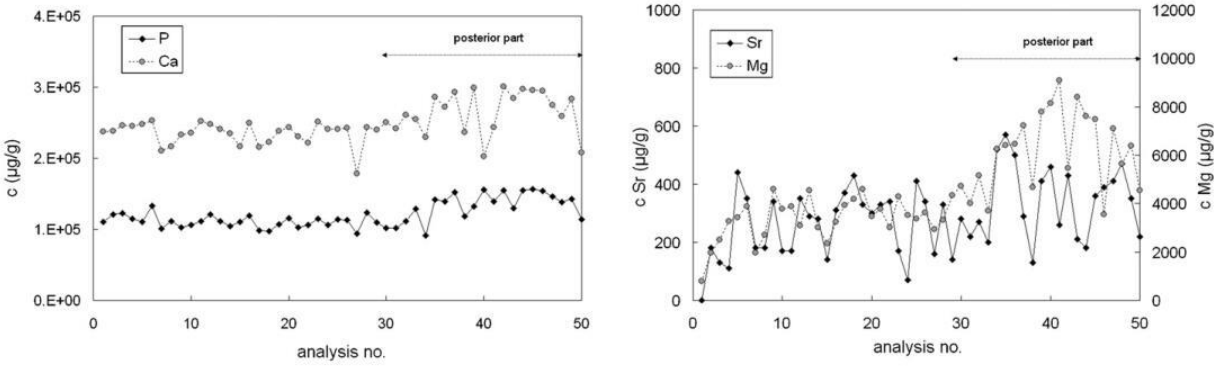

Fig. 7. EMP results of line scan on scale 1 for P and Ca (a), Sr and Mg (b).

Table 4
ICP-MS analysis of 5 diluted fish scales.

Isotope	Concentration of element ($\mu g\,g^{-1}$)							
	Whole scale		Anterior part			Posterior part		
	Scale 1	Scale 2	Scale 3	Scale 4	Scale 5	Scale 3	Scale 4	Scale 5
^{26}Mg	1460	1500	1280	1550	1180	1730	2160	1940
^{31}P	65,200	67,600	41,500	44,600	37,600	51,000	86,100	54,400
^{43}Ca	95,100	98,000	88,600	99,600	86,200	112,000	145,000	123,000
^{55}Mn	<0.9[a]	1.67	<0.9[a]	<0.9[a]	<0.9[a]	<0.9[a]	10.4	14.7
^{56}Fe	<5[a]	<5[a]	<5[a]	<5[a]	<5[a]	<5[a]	<5[a]	<5[a]
^{66}Zn	<14[a]	<14[a]	<14[a]	<14[a]	<14[a]	<14[a]	<14[a]	<14[a]
^{86}Sr	99.1	101.0	89.1	115	105	109	168	152
^{208}Pb	<38[a]	<38[a]	<38[a]	<38[a]	<38[a]	<38[a]	<38[a]	<38[a]

[a] Values are below the detection limit.

To verify the accuracy of LA-ICP-MS results, the scale was also analyzed using EMP. The analysis consisted of 50 points placed near the ablation lines and covering the whole width of the scale with a spacing of 400 µm (Fig. 2). Due to the high EMP (hundreds of $\mu g\,g^{-1}$) limits of detection, a limited selection of elements was detected. Fig. 7a and b shows graphs for Ca, P, Mg and Sr. A similar trend of elemental distribution with LA-ICP-MS is evident for all the mentioned elements.

The content of the elements of interest was also expressed as an average for the whole scale width as well as for the posterior and anterior scale parts. In the case of LA-ICP-MS the calculations were done on 2 different fish scales, each with 3 line scans Tables 1 and 2, and the EMP results for 1 measurement on scale no. 1 are given in Table 3. The EMP values for Mn and Fe are only informative because of detection limits of 320 and 340 $\mu g\,g^{-1}$, respectively.

Summarizing, the data obtained in linear scans is well in accord both with the character of the incorporation of studied elements in HAP and with the character of their uptake in fish. Together, with the good correlation with the EMP analyses, the results illustrate a very good applicability of the LA-ICP-MS method.

4.3. Solution ICP-MS

To confirm the trend of elemental distribution obtained by LA-ICP-MS and EMP, ICP-MS analysis of different parts of scales proceeded after the scale dissolution. Two entire scales were dissolved as well as three scales cut into 2 parts – anterior and posterior (see Fig. 1). These parts were dissolved separately. The solution preparation procedure is described in detail in Section 2.2. Results of solution analysis are shown in Table 4. Lower concentrations of all elements can be seen when compared with the LA-ICP-MS analysis which corresponds to the fact that when using LA-ICP-MS, only the external HAP layer containing dominantly all the analyzed elements is studied while the solution ICP-MS analysis also comprises the organic collagen layer. In other words the HAP layer is diluted with collagen in the case of solution analysis. However the trend of elemental distribution compared favorably with the LA-ICP-MS and EMP results because the increased content of Mn, Ca, P, Mg and Sr were determined in the posterior part of the fish scales as opposed to the anterior part. Values for iron, zinc and lead were under the detection limits (see Table 4).

5. Conclusion

The method, LA-ICP-MS, for spatial elemental analysis of fish scales was investigated. Quantification of elements was made using powdered CRM NIST 1486 pressed into pellets. Laser ablation was applied as a line scan analysis of the HAP layer throughout the whole fish scale perpendicular to the growth rings encompassing the anterior and posterior part. Results showed different distributions, especially of some trace metals (Zn, Mn) but also matrix elements (Ca, P) and most common cation substituents (Mg, Sr) in both parts with increased contents in the posterior part. This pattern is attributed essentially to higher representation of the mineral phase which enables higher substitution and filling of vacancies. Some metal trace elements (Fe, Pb) were distributed symmetrically with a higher content near the edge of the scale reflecting most probably dietary changes or pollution. Behavior of the elemental distribution obtained by LA-ICP-MS was monitored by EMP analysis and ICP-MS solution analysis of different parts of fish scales.

LA-ICP-MS depth profiling was used for the first time in fish scales. The depth profiles showed homogenous incorporation of both matrix elements (Ca and P) and substituents (Mg and Sr) into

the external HAP layer with a decrease close to its boundary with a collagen layer. Accumulation of trace metal elements as Zn and Pb on the scale surface is well in accord with their assumed surface adsorption and complexation. The fact that the results of depth profiling are in good agreement both with EMP and PIXE results and with the assumed ways of incorporation of the studied elements in the HAP structure illustrates a good potential of this method for the study of changes in elemental concentrations within the fish scales.

Acknowledgement

This study was supported by the project MSM0021622412 (INCHEMBIOL).

References

[1] S.F. Durrant, J. Anal. At. Spectrom. 14 (1999) 1385–1403.
[2] D. Guenther, B. Hattendorf, Trends Anal. Chem. 24 (2005) 255–265.
[3] B. Fernandez, F. Claverie, C. Pecheyran, O.F.X. Donard, F. Claverie, Trends Anal. Chem. 26 (2007) 951–966.
[4] J.S. Becker, Spectrochim. Acta Part B 57 (2002) 1805–1820.
[5] N.S. Mokgalaka, J.L. Gardea-Torresdey, Appl. Spectrosc. 41 (2006) 131–150.
[6] A. Plotnikov, C. Vogt, V. Hoffmann, C. Teaschner, K. Wetzig, J. Anal. At. Spectrom. 16 (2001) 1290–1295.
[7] A. Plotnikov, C. Vogt, K. Wetzig, J. Anal. At. Spectrom. 17 (2002) 1114–1120.
[8] M.P. Mateo, J.M. Vadillo, J.J. Laterna, J. Anal. At. Spectrom. 16 (2001) 1317–1321.
[9] M. Sanborn, K. Telme, J. Anal. At. Spectrom. 18 (2003) 1231–1237.
[10] S.E. Campana, Mar. Freshwater Res. 56 (2005) 485–495.
[11] G.A. Begg, S.E. Campana, A.J. Fowler, I.M. Suthers, Mar. Freshwater Res. 56 (2005) 477–483.
[12] C.C. Coutant, C.H. Chen, Can. J. Fish. Aquat. Sci. 50 (1993) 1318–1323.
[13] B. Flem, V. Moen, A. Grimstvedt, Appl. Spectrosc. 59 (2005) 245–251.
[14] A.P. Farrell, A.H. Hodaly, S. Wang, Arch. Environ. Contam. Toxicol. 39 (2000) 515–522.
[15] C.C. Muhlfeld, B. Marotz, S.R. Thorrold, J.L. Fitzgerald, Trans. Am. Fish. Soc. 134 (2005) 945–959.
[16] J. Borcherding, C. Pickhardt, V. Hendrik, H.V. Winter, J.S. Becker, Aquat. Sci. 70 (2008) 47–56.
[17] B.K. Wells, B.E. Rieman, J.L. Clayton, D.L. Horan, C.M. Jones, Trans. Am. Fish. Soc. 132 (2003) 409–424.
[18] B.K. Wells, S.M. Thorrold, C.M. Jones, Trans. Am. Fish. Soc. 129 (2000) 889–900.
[19] M. Hola, J. Kalvoda, O. Babek, R. Brzobohaty, I. Holoubek, V. Kanicky, R. Skoda, Environ. Geol. 58 (2009) 141–151.
[20] J. Kalvoda, M. Novak, O. Babek, R. Brzobohaty, M. Hola, I. Holoubek, V. Kanicky, R. Skoda, Biogeochemistry 94 (2009) 197–215.
[21] B.M. Gillanders, U.S. Natl. Mar. Fish. Serv. Fish. Bull. 99 (2001) 410–419.
[22] B.K. Wells, G.E. Bath, S.M. Thorrold, C.M. Jones, Can. J. Fish. Aquat. Sci. 57 (2000) 2122–2129.
[23] L. Zylberberg, J. Bonaventure, L. Cohen-Solal, D.J. Hartmann, J. Bereiter-Hahn, J. Cell Sci. 103 (1992) 273–285.
[24] J.C. Schneider, P.W. Laarman, H. Gowing, Manual of Fisheries Survey Methods II: With Periodic Updates, Fisheries Special Report 25, Michigan Department of Natural Resources, Ann Argot, 2000 (Chapter 9).
[25] T. Ikoma, H. Kobayashi, J. Tanaka, D. Walsh, S. Mann, J. Struct. Biol. 142 (2003) 327–333.
[26] Y. Ohira, M. Shimizu, U. Kazuhiro, Y. Takali, Fish. Sci. 73 (2007) 46–54.
[27] H. Onozato, N. Satane, Cell Tissue Res. 201 (1979) 409–422.
[28] F.J. Meunier, Am. J. Zool. 24 (1984) 953–964.
[29] H.P. Schultze, Mesozoic Fishes Systematics and Paleoecology, Verlag Dr. F. Pfeil, München, 1996, pp. 83–93.
[30] L. Zylberberg, G. Nicolas, Cell Tissue Res. 223 (1982) 349–367.
[31] L. Zylberberg, J. Bereiter-Hahn, J.Y. Sire, Cell Tissue Res. 253 (1988) 597–607.
[32] A.A. Schönbörner, G. Boivin, C.A. Baud, Cell Tissue Res. 202 (1979) 203–212.
[33] J.Y. Sire, M.A. Akimenko, Int. J. Dev. Biol. 48 (2004) 223–247.
[34] W.T. Liu, Y. Zhang, G.Y. Li, Y.Q. Miao, X.H. Wu, J. Fish. Biol. 72 (2008) 1055–1067.
[35] L. Zylberberg, C. R. Palevol. 3 (2004) 591–604.
[36] M.M. Fouda, J. Fish. Biol. 15 (1979) 173–183.
[37] J.J. Hutchinson, C.N. Trueman, J. Fish. Biol. 69 (2006) 1874–1880.
[38] T. Leventouri, Biomaterials 27 (2006) 3339–3342.
[39] S.V. Dorozhkin, M. Apple, Angew. Chem. Int. Ed. 41 (2002) 3130–3146.
[40] S. Cazalbou, D. Eichert, C. Drobet, C. Combes, C. Rey, C. R. Palevol. 3 (2004) 563–572.
[41] J.M. Vadillo, J.J. Laterna, Spectrochim. Acta Part B 59 (2004) 147–161.
[42] A. Hrdlicka, V. Otruba, K. Novotný, D. Günther, V. Kanický, Spectrochim. Acta Part B 60 (2005) 307–318.
[43] J.L. Pouchou, F. Pichoir, Microbeam Analysis 20 (1985) 104–106.
[44] S.V. Dorozhkin, Biol. Med. Mater. 2 (2009) 399–498.
[45] Y. Pan, M.E. Fleet, Rev. Mineral. Geochem. 48 (2002) 13–49.
[46] M. Wakamura, K. Kandori, T. Ishikawa, Colloids Surf. A: Physicochem. Eng. Asp. 164 (2000) 297–305.
[47] T. Suzuki, T. Hatsushika, M. Miyake, J. Chem. Soc. Faraday Trans. I 78 (1982) 3605–3611.
[48] F.D. Pate, J.T. Hutton, K. Norrish, Appl. Geochem. 4 (1989) 303–316.
[49] A. Yasukawa, T. Yokoyama, K. Kandori, T. Ishikawa, Colloid Surf. A: Physicochem. Eng. Aspects 238 (2004) 133–139.
[50] A. Bigi, G. Falini, E. Foresti, M. Gazzano, A. Ripamonti, N. Roveri, Acta Crystallogr. 52 (1996) 87–92.
[51] J.C. Elliott, Rev. Mineral. Geochem. 48 (2002) 427–454.
[52] T. Suzuki, K. Ishigaki, M. Miyake, J. Chem. Soc. Faraday Trans. I 80 (1984) 3157–3165.
[53] X.B. Chen, J.V. Wright, J.L. Conca, L.M. Perrung, Water Air Soil Pollut. 98 (1997) 57–78.
[54] Q.Y. Ma, S.J. Traina, T.J. Logan, J.A. Ryan, Environ. Sci. Technol. 27 (1993) 1803–1810.
[55] W. Admassu, T. Breese, J. Hazard. Mater. 69 (1999) 187–196.
[56] H. Xu, L. Yang, P. Wang, Y. Liu, M. Peng, J. Mar. Sci. Technol. 23 (2007) 417–422.
[57] T. Moriguchi, S. Nakagawa, F. Kaji, Phosphorus Res. Bull. 22 (2008) 54–60.
[58] S.M. Tang, I. Orlic, K.N. Yu, J.L. Sanchez, P.S.P. Thong, F. Watt, H.W. Khoo, Nucl. Instrum. Methods B130 (2004) 396–402.
[59] N. Bury, P. Walker, C. Glover, J. Exp. Biol. 206 (2003) 11–23.
[60] O. Andersen, Fish Physiol. Biochem. 16 (1997) 223–231.
[61] T. Watanabe, V. Kiron, S. Satoh, Aquaculture 151 (1997) 185–207.
[62] G. Gregorovic, N. Kralj-Klobucar, N. Kopjar, J. Fish Biol. 72 (2008) 1841–1846.
[63] K. Matsunaga, H. Murata, T. Mizoguchi, A. Nakahira, Acta Biomater. 30 (2009) 2864–2872.
[64] R.D. Handy, E.B. Eddy, Water Res. 24 (1990) 521–527.
[65] S.M. Al-Weher, Jordan J. Biol. Sci. 1 (2008) 41–46.
[66] T. Yoshitomi, C. Nakayasu, S. Hasegawa, A. Iida, N. Okamoto, Chemosphere 36 (1998) 2305–2310.
[67] I. Bochenek, M. Protasowicki, E. Brucka-Jastrzebska, Arch. Pol. Fish. 16 (2008) 21–36.
[68] E.H. Park, S.H. Lee, Jpn. J. Ichtyol. 34 (1988) 476–482.

PAPER 3

Dual imaging of uranium ore by Laser Ablation Inductively Coupled Plasma Mass Spectrometry and Laser Induced Breakdown Spectroscopy

Holá, M., Novotný, K.*, Dobeš, J., Krempl, I., Wertich, V., Mozola, J., Kubeš, M., Faltusová, V., Leichmann, J., Kanický

Spectrochimica Acta Part B. 2021, 186, 106312. DOI 10.1016/j.sab.2021.106312

Contribution:

LA-ICP-MS design of experiments and measurements, data evaluation, graphic processing, manuscript writing.

Spectrochimica Acta Part B: Atomic Spectroscopy 186 (2021) 106312

Contents lists available at ScienceDirect

Spectrochimica Acta Part B: Atomic Spectroscopy

journal homepage: www.elsevier.com/locate/sab

Dual imaging of uranium ore by Laser Ablation Inductively Coupled Plasma Mass Spectrometry and Laser Induced Breakdown Spectroscopy

Markéta Holá [a], Karel Novotný [a,*], Jan Dobeš [a], Ivo Krempl [a], Vojtěch Wertich [b], Juraj Mozola [b], Martin Kubeš [b], Veronika Faltusová [a], Jaromír Leichmann [b], Viktor Kanický [a]

[a] Department of Chemistry, Faculty of Science, Masaryk University, Kotlářská 2, 61137 Brno, Czech Republic
[b] Department of Geological Sciences, Faculty of Science, Masaryk University, Kotlářská 2, 61137 Brno, Czech Republic

ARTICLE INFO

Keywords:
LA-ICP-MS
LIBS
Elemental imaging
Elemental mapping
Uranium ore
Geological samples

ABSTRACT

The great potential in combining two elemental imaging techniques - Laser Induced Breakdown Spectroscopy (LIBS) and Laser Ablation Inductively Coupled Plasma Mass Spectrometry (LA-ICP-MS) is demonstrated for uranium ore sample investigation. Dual imaging provides the advantages of both methods – high speed, large area imaging and additional evaluation of the whole spectrum for LIBS, and high resolution, low detection limits and isotopic imaging for LA-ICP-MS. Special software, ILAPS, was created for data processing to ensure the consistency of the resulting element images and the possibility of their combination. This new method for merging LIBS and LA-ICP-MS imaging data allows the display of detailed structures on the background of the overall sample image. Information contained in the detailed structures together with an overall view of the sample was displayed in one image to visualise the complete data from both methods. The effectiveness and usefulness of this new approach were demonstrated in identifying the structures responsible for elements migration in the uranium ore sample.

1. Introduction

The astonishing advancement of laser ablation-based techniques (namely LA-ICP-MS and LIBS) in recent years has increased their potential for many applications in different areas. This progress is remarkable especially in imaging techniques including applications in geological science. The LA-ICP-MS method is used for various geological applications, to which a suitable ablation mode is adapted. Recent literature mentions LA-ICP-MS analysis which can provide basic information regarding elements content in the selected area with a size of tens to thousands of μm^2. Detecting a change in the content of elements in the sample can be expressed by individual line scans [1] or a set of adjacent line scans covering a defined sample area (imaging) [2] which can be used to gain more complex information about the sample. The recent improvement of the LA-ICP-MS method was demonstrated in a number of articles [2–5] and this progress also provides great application in the field of geology [2,3,5–8].

The process of imaging using LA-ICP-MS requires the precise selection of an area for analysis which would be sufficient for the interpretation and on a time and cost effiecient basis. The setting of laser ablation parameters such as spot size or scan speed also depends on the total analysed area and the required resolution of the future image. The selection of isotopes and dwell times determines the data acquisition parameters which should be synchronised with the LA repetition rate [9]. The analysed area is scanned using adjacent parallel lines, if scanned horizontally, the resulting pixel size of the image is the product of dwell time and the scan speed on the x axis and the spot size on the y axis. The laser ablation process is followed by data generation and creation of element distribution images using special software, e.g. the software package "iolite" [2,10] based on compilation and processing data gained by LA-ICP-MS. The final images can be processed in two ways: qualitative, providing basic information about the relative changes of elements distribution in the sample, or quantitative, providing more complex information on the absolute content of elements in the imaged area.

The LIBS technique is based on the vaporisation of a small amount of the sample and generation of plasma directly by one laser pulse. Subsequently, plasma light emission is collected and analysed using an optical spectrometer [11,12]. Contrary to the LA-ICP-MS technique, a further excitation source is not needed; therefore, the instrumentation

* Corresponding author.
E-mail address: codl@sci.muni.cz (K. Novotný).

https://doi.org/10.1016/j.sab.2021.106312
Received 14 May 2021; Received in revised form 22 September 2021; Accepted 19 October 2021
Available online 22 October 2021

can be much simpler and cheaper. The response is generally faster compared to LA-ICP-MS where transport of the aerosol through relatively long tubes into the ICP is required. This feature is particularly crucial for the application of LIBS for fast elemental imaging [13,14]. LIBS imaging is based on the generation of a series of plasmas at different positions on the sample following a pre-programmed scan sequence. Consequently, step size must be set with respect to focusing of the laser spot and crater size [13]. Crater size is usually the object of careful optimisation and is influenced not only by the laser pulse parameters but also by the surrounding atmosphere and by the sample itself [15–17]. The applications of LIBS in analysis of various geological materials have already been reviewed in detail [18]. Detection of most of the elements of the periodic system with high spatial resolution is possible and the fast measurement allows imaging of a large sample area in a reasonable time. The capability of LIBS for two-dimensional multi-element mapping of mineral samples was demonstrated on different geological structures [19–22]. A multivariate approach and application of self-organising maps were used for LIBS chemical mapping of uranium in sandstone-hosted uranium ores [23,24].

The combination of both mentioned analytical techniques (LA-ICP-MS and LIBS) can enrich the results of analyses of only one method. There are efforts to connect both methods simultaneously not only for imaging but also for example, for multivariate classification of samples [25]. Elemental imaging by the simultaneous system can give rise to improvements in the quantification process for tissue analysis [26] or in studies of sample heterogeneity [27]. Concerning geological samples, simultaneous LIBS and LA-ICP-MS spatially resolved mapping of major and trace elements and isotopes within a Bastnaesite was demonstrated [28]. Such a combination of the two techniques provides complementary measurements for elements that are separately unattainable due to low sensitivity and/or strong interferences. However, it is worth mentioning that the utilisation of simultaneous systems is limited not only by available instrumentation but also by the need for compromised settings when neither method is operated under optimal conditions. In addition, it is impossible to acquire a quick overview of a large sample area by the LIBS method to select important regions and detailed examination of their fine structures by the LA ICP MS at the same time. On the other hand, the subsequent analysis allows the use of a simple (even mobile) LIBS system for preliminary sample investigation and sorting that is easy to operate without placement in a clean laboratory.

In this work, a developed combination of LIBS and LA-ICP-MS imaging technique was applied to a case study focused on a uranium ore sample. Such samples are important especially in connection with its utilisation in exploration, the mining and processing of uranium ore [29], "fingerprinting" of a uranium ore concentrates [30] and also in technologies used in nuclear waste repositories due to similarities in chemical composition between uraninite and spent nuclear fuel [31,32].

In this study, a new and comprehensive approach to imaging uranium ore was designed and implemented. Fast elemental imaging of the investigated sample by the LIBS serves for the preliminary view of the elemental distribution on a large area. Such an analysis was performed very quickly using relatively simple LIBS instrumentation. For a more detailed survey of selected areas, the LA-ICP-MS technique was used for a more detailed view and for the tracking of isotopes. Specially developed software ILAPS (Imaging of Laser ablation plasma spectrometry) [33] was used for both methods to evaluate the data and create images. Because the ILAPS allows the processing of different initial data into the same final form, it is also easy to compare, combine and merge images from both laser ablation-based methods in a uniform graphical form. Such a combination of LIBS and LA-ICP-MS offers new possibilities for 2D imaging of elements and isotopes in geological laboratories.

2. Experimental

2.1. Sample

The investigated geological sample represents U-mineralisation from a former deep uranium mine; Rožná (a part of the Rožná-Olší uranium ore field with a total mine production of 23,000 t U) situated 45 km NW of Brno [34]. On the thin-section scale, the analysed sample (BUK1B) is composed of three geochemically contrasting lithological types (Fig. 1A), represented in order from right to left by (1) massive uraninite vein (2) carbonate vein and (3) metasomatite. The relative time succession of individual types is as follows: the oldest part, hydrothermally altered host rock (metasomatite), was metasomatically overprinted due to interaction with hydrothermal fluids circulating through rock pores, along faults and/or fractures in which the carbonate along with uraninite subsequently crystallised.

The metasomatite, consisting mostly of calcite ($CaCO_3$), dolomite ($CaMg(CO_3)_2$), chloritised biotite to chlorite ($Mg_5Al(AlSi_3O_{10})(OH)_8$) with subordinate quartz (SiO_2), smectite ($(Na,Ca)_{0.33}(Al,Mg)_2(Si_4O_{10})(OH)_2.nH_2O$), and rare apatite ($Ca_5(PO_4)_3(OH,F,Cl)$), is typically red-coloured as a result of the presence of abundant Fe-oxides, particularly hematite (Fe_2O_3). The uraninite-bearing carbonate vein crosscut the host metasomatised rock and is predominantly built up by white-coloured calcite ($CaCO_3$) with macroscopically visible rhombohedral cleavage and a well-developed crystal shape. On the other hand, the vein-type U-mineralisation, occurring as uraninite (UO_2) closely associated with hydrothermal carbonate, typically forms colloform and spherulitic aggregates. Such a mineral texture is usually attributed to hydrothermal uraninites that crystallised under relatively low temperatures (150–170 °C for uraninite from the Rožná deposit) [34].

The ideal formula of uraninite, the most important uranium ore mineral, is UO_2, but in fact the formula is much more complex as the structure of uraninite has many defects caused mainly by oxidation of U^{4+} to U^{6+}, cationic substitution and radioactive decay [35]. Studying of oxidation states is crucial for both mineral deposit and environmental research because during oxidation of stable U^{4+}, U^{6+} ions are formed that are very mobile and can migrate for a long distance [36]. Cations with a similar ionic radius to U^{4+} (e.g. REE, Th, Y, Ca, Zr) can substitute for U if they are present in uranium ore forming fluids during uraninite crystallisation [37]. Radioactive decay of the most common ^{238}U leads to formation of the final decay product that is isotope ^{206}Pb. Moreover, some authors consider trace elements association in uraninites as a good tool for provenance analysis [29] or as a function of mineral deposit type [7,38].

2.2. LIBS

The experimental system for fast LIBS chemical mapping consists of Nd:YAG laser (Q-Smart, Quantel) with a fundamental wavelength of 1064 nm, a repetition rate of 20 Hz, a pulse duration of 5 ns and a laser pulse energy of 25 mJ. Although UV wavelength is preferred when spatial resolution is important, the NIR region of the fundamental Nd:YAG wavelength is sometimes more suitable due to simpler instrumentation (lower power laser, less expensive optics). For simple, preliminary and fast initial sample investigation, it is desirable that instrumentation should be as simple as possible, preferably as a compact tabletop or even a mobile device. Moreover NIR wavelength, when combined with ns pulse duration, usually gives the best sensitivity in LIBS measurements, due to strong plasma heating [39]. Therefore Nd:YAG fundamental wavelength of 1064 nm was used in our study.

Laser pulse was introduced on the sample surface by a series of mirrors and then focused by a 30 mm focal length glass dublet (Thorlabs, USA). The sample was placed on a lab-made sample holder which was fixed to x, y, z motorised translation stages (Standa, Lithuania). Collection optics focused the plasma radiation into a bundle of four fibres that transport radiation to a four-channel spectrometer (Avantes,

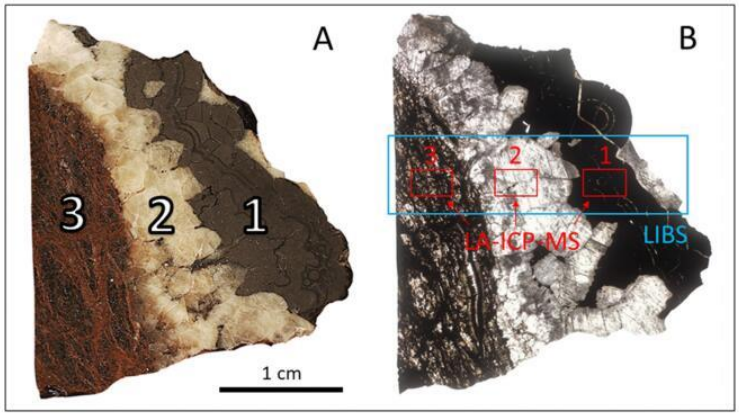

Fig. 1. A cross-section through (A) hand specimen and (B) polished thin section of U-mineralisation closely associated with metasomatite and carbonate vein (see text for detailed description) used for elemental distribution maps.

Netherlands) equipped with Avasoft software. Delay and integration time was set to 1 μs and 30 μs respectively. The mapped area was 4.0 × 23.2 mm (see Fig. 1B, blue region), which resulted in a chemical map of 51 × 290 locations (14,790 in total) with step 80 μm in both x and y axes. Net scanning time is approximately 13 min calculated from the laser repetition pulse rate and the number of image points. Taking into account the dead time of stages during movement between individual lines overall scanning time was approx. 20 min. Raw spectral data were processed in custom-made C++ software (CEITEC BUT Brno, Czech Republic) to background subtraction, selection of emission lines wavelength and to preparation of x, y image matrices.

2.3. LA-ICP-MS

The selected areas of fine structures mapped by LA-ICP-MS provided a detailed view with higher spatial resolution and higher sensitivity related to trace elements in different zones of the sample. Areas of 3 × 2 mm were analysed using an LA-ICP-MS system consisting of LSX 213 G2 laser ablation device (Teledyne Cetac Technologies, USA) and Agilent 7900 ICP MS analyser with a quadrupole analyser and an octopole reaction cell to attenuate polyatomic interferences (Agilent Technologies, Japan). The laser operates at a wavelength of 213 nm with a pulse duration of ~4 ns. Using helium as a carrier gas with a flow rate of 0.9 l min^{-1}, the aerosol was washed out by a 2-volume ablation cell (HelEx). The aerosol was then mixed with argon serving as a makeup gas with a flow rate of 1 l min^{-1} and transported through a FEP (Fluorinated Ethylene Propylene) tube (i.d. 2 mm, length 1 m) to the ICP-MS. Line scans with a spot size of 20 μm in diameter, 20 μm s^{-1} scan speed, 10 Hz and fluence of 10 J cm^{-2} were performed. 100 lines of 3 mm length with 20 μm spacing were performed to cover the area of 3 × 2 mm. The areas in the individual mineral zones are marked by red rectangles in the sample thin section within the Fig. 1B: (1) uraninite (2) carbonate, (3) metasomatite.

The mass spectrometer operated at the forwarded power of 1550 W with Ar gas flow rates of 15 (outer plasma gas), 0.7 (auxiliary), and Ar make-up gas of 0.6 l min^{-1}. Tuning of the instrument to maximize isotope intensities was performed using the NIST 610 glass standard. The following isotopes were monitored with a total integration time of 1 s: ^{43}Ca, ^{51}V, ^{56}Fe, ^{57}Fe, ^{204}Pb, ^{206}Pb, ^{207}Pb, ^{208}Pb, ^{235}U, ^{238}U. The pause between each line was 30 s, so the total measurement time was 5 h.

2.4. Software ILAPS for data evaluation

ILAPS (**I**maging of **L**aser **A**blation **P**lasma **S**pectrometry) is a python-based software tool specifically developed for data processing of laser ablation inductively coupled plasma mass spectrometry (LA-ICP-MS), found at https://github.com/nikadilli/Ilaps-v2/. So far it is possible to directly import data in different formats (.csv, .xlsx, .asc), primarily from ICP-MS instruments, however as an open-source software it is simple to add protocols for other formats or instruments, if necessary. ILAPS offers (I.) bulk analysis (II.) calculation of calibration curves (III.) elemental imaging from continuous time dependant data acquired in a single file. This is where ILAPS differs from most of the other accessible software; it uses ".iolite" files from Laser ablation systems to find the start of each ablation event and automatically segments the data stream into sections of signal and background.

Even though ILAPS is optimised for LA-ICP-MS, it can easily handle data from other instruments, such as laser induced breakdown spectroscopy (LIBS), just by a simple conversion of raw data to fit the importing format. In both cases the time resolved generated data stream is converted into a single matrix. After the segmentation of the signal and background, and subsequent background subtraction, the user needs to manually set the pixel size Δx and Δy. In LA-ICP-MS it is specified by scan speed × integration time vs. spot size (in cases where the spacing between parallel lines is equal to the spot size). In LIBS, the pixel size is given by the individual spot spacing in the direction of the x and y axes.

ILAPS also contains background correction as well as internal standard normalisation and total sum normalisation. Data can be visualised in different colour maps. A semi-interactive graph embedded directly in the user interface ensures proper control over the final appearance of the output image. Moreover, it is possible to scale, smooth, interpolate and quantify the data with instant response in the image. Ilaps offers multiple methods of interpolation (nearest, bilinear, bicubic, spline16, spline 36, quadratic, gaussian and Lanczos); bilinear interpolation was used for the image generation in this article. The calculated matrix for each measured element/isotope can be exported (and then imported back) into a single excel file, where each measured element is found on a separate spreadsheet. Even though ILAPS is optimised for LA-ICP-MS, it can easily handle data from other instruments such as laser-induced breakdown spectroscopy (LIBS) by a simple conversion of raw data to fit the importing format. This allows an easy comparison of elemental imaging by different methods, where the resulting images can be handled in the same way, using the same format and colours. ILAPS offers colour processing in 26 different colour palettes (e.g. jet, grey, binary or magma); all images in this article were prepared using jet palette. The scaling was adjusted individually for each image in order to make the necessary details visible and to unify the colours for both methods so that the images are unifiable. The z axis represents the intensity value of the analytical response of the element/isotope, so the

scale bar is in relative form and indicates only the colour range (blue minimum, red maximum).

3. Results and discussion

3.1. LIBS imaging

3.1.1. Emission lines selection

At first, several LIBS spectra were recorded in different sample locations and evaluated to optimise the conditions and set suitable measurement parameters, as well as to select suitable emission lines with sufficient sensitivity. These lines were selected also in respect of the presence of spectral interferents in individual mineralisation. Careful line selection was also done using the measurement of elemental standards which served for the precise setting of the emission line wavelength (spectrometer calibration) and for verification of spectral interferences. Primarily, interest has focused on calcium such as the matrix element of carbonate and because its presence can also be expected in metasomatic structures. On the other hand, calcium content in uraninite mineralisation is low. Emission lines Ca II 393.37 nm, Ca II 317.96 nm and Ca II 315.92 nm were selected as favourites. Line Ca II 393.37 nm represents a strong ion resonance line, while the less sensitive Ca II 315.92 nm line is more suitable for monitoring calcium at high contents (see Fig. 2).

As in the case of calcium in carbonate, the iron can represent hematite mineralisation in the metasomatite due to its high content in this phase. Therefore, imaging of iron can help reveal the structure and distribution of metasomatic mineralisation in the sample. The iron emission line 404.58 nm was chosen to respect this purpose and with negligible potential spectral interferences (Fig. 2B). Distribution maps of lead can help to elucidate uranium migration processes and selected parts can subsequently be subjected to LA-ICP-MS analysis for a more detailed view and to distinguish individual isotopes. The lead emission line Pb I 405.81 nm was chosen to respect sufficient sensitivity and low spectral interferences (Fig. 2).

It should be noted that the main purpose of this study is to contribute to the elucidation of the mechanisms of uranium migration in rocks. Although imaging of other elements is also important, a reliable technique for uranium distribution mapping is crucial. In the case of uranium, the selection of suitable emission lines was made according to previous experiences and data from the literature [23,24,40,41]. It was assumed that imaging of U II line and UO band can provide additional and valuable insight into uranium distribution and therefore the ionic line U II 367.007 nm and the molecular band UO 593.55 nm were selected (Fig. 2). Nevertheless, in this work, only detectability of these features was investigated for the construction of distribution maps. Whether stoichiometry of uranium and oxygen in uraninite corresponds to the ratio of UII and UO band intensities will be the subject of further study. It was found that the U II line and UO band provide sufficient intensities with low spectral interferences.

3.1.2. Settings of imaging area and parameters

LIBS is considered as the suitable technique for fast imaging of a large area for obtaining information which can help with initial acquaintance of the structure of the sample. While some approach for the quantification of signal or advanced chemometric methods have been published [23,24] this work is focused only on obtaining information about the spatial distribution of selected elements imaged in relative scale to reveal the basic structures of the sample. In this case, the main idea is to identify the structures which show or are responsible for uranium migration. For this reason, the rectangle chosen for LIBS imaging was placed approximately in the centre of the sample covering all structures (metasomatite, hydrothermal calcite and uraninite (U_3O_8) mineralisation) (Fig. 3).

The size of the chosen area was decisive for creating a suitable raster of spots with respect to the number of lines, the number of points, and the step size. All these parameters then define the spatial resolution, the volume of recorded data, and the time required for the measurement. However, the parameters cannot be set arbitrarily but must respect the limitations of the instrumentation. The most critical parameter is the maximum speed rate of the sample moving. In this case, at a laser pulse repetition frequency of 20 Hz, the translation stage allows the maximal distance between individual spots of 80 μm. However, this distance and a crater diameter of about 150 μm inevitably leads to overlapping craters, which has a number of undesirable effects. First of all, the deterioration of spatial resolution is determined by combining crater diameter and step size. Therefore, the spatial resolution is primarily limited by the crater diameter rather than by the step size in this case. Secondly,

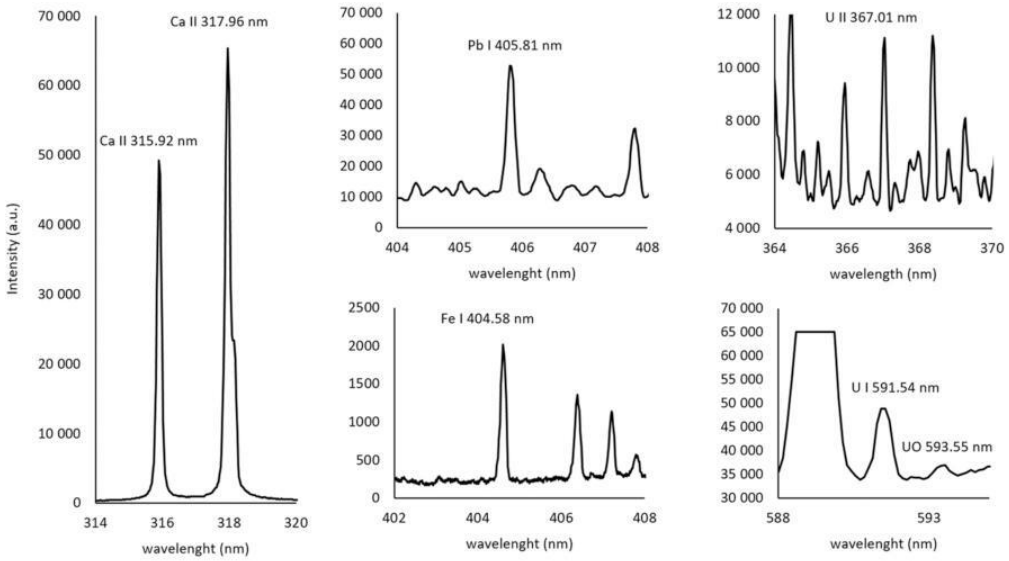

Fig. 2. Selected emission lines and band used for LIBS elemental imaging: calcium in spectrum of carbonate, iron in spectrum of metasomatite and lead and uranium in spectrum of uraninite.

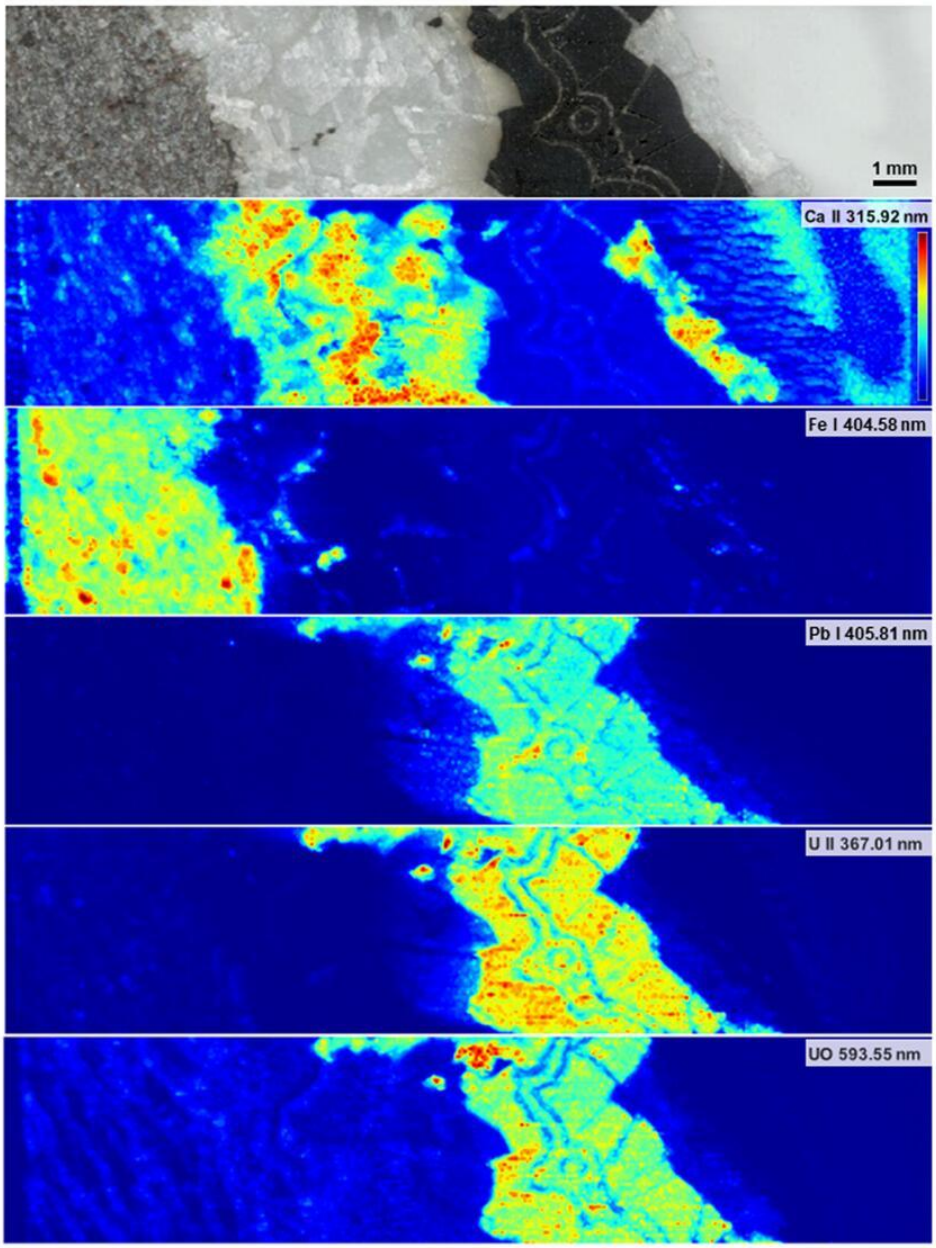

Fig. 3. Photography of analysed sample area and LIBS elemental distribution maps. LIBS emission on Ca II the 315.92 nm line was corrected by total LIBS emission; distribution maps of iron, lead and uranium are represented by intensities of emission lines (or eventually of band in the case of uranium) after background correction.

overlapping craters can result in material flushing between pulses and redeposition which can cause signal tailing [39]. Furthermore, different ablation mechanisms in carbonate and uraninite have resulted in different shape and size of ablation craters observed in BSE. In this context, it was no surprise that different ablation mechanisms in carbonate was also indicated by significantly lower total LIBS plasma emission. All these facts should be further taken into account when creating elemental images, as shown below.

3.1.3. Data processing and elemental images

After scanning the sample at the settings mentioned above, acquired spectral data for all channels of the Avantes spectrometer were exported and saved using the program Avasoft. Until now, the ILAPS program was not able to process raw spectral LIBS data because it was initially developed for processing data from LA-ICP-MS. The program extension is the subject of further work, and therefore, raw LIBS data were firstly processed by custom-made C++ software. After background subtraction, selection of emission lines wavelength and preparation of x, y image matrices followed the import of data into the ILAPS program for

the final elemental images creation. The data processing procedure by this program will be addressed in more detail below (see chap. 3.3.).

Because the obtained calcium elemental map showed a disproportionately high signal in uraninite compared to carbonate it is clear that a strong matrix effect occurs. In the next step, for the elimination of lower plasma emission in carbonate (see. 3.1.2), compensation using the total emission as a reference signal was chosen. The correction was done by dividing the emission of the line by the sum of the emission over the whole spectral interval of the spectrometer channel. The resulting map (Fig. 3) corresponded well to the real distribution of calcium in the sample, which was also verified by LA-ICP-MS.

On the obtained iron elemental map (Fig. 3), metasomatic structures, even some clusters extending into the carbonate phase, are clearly visible. On the other hand, it is evident that the iron content in uraninite mineralisation is relatively low. It was found that as in the case of calcium, using the total emission as a reference signal considerably improved the iron signal ratios between the individual phases. After this correction the signal better reflects the real iron content as verified by LA-ICP-MS.

Unfortunately, the LIBS technique does not allow identification of individual lead isotopes and therefore it is not possible to distinguish between radiogenic and non-radiogenic forms. Despite this fact, LIBS imaging can make it possible to obtain important information about the distribution of lead not only in the uraninite phase, but also in the interface and fine structures appearing in the carbonate or metasomatic. As was expected, the highest content of lead in uraninite is evident in the comparison of carbonate and metasomatite. Nevertheless, in fine structures locally increased content can also be observed in these phases (Fig. 3). These results were subsequently confirmed by LA-ICP-MS. Unlike iron and calcium, the total emission as a reference signal does not improve the lead signal ratios between the individual phases and therefore was not used. Although the maps obtained by both techniques were in good agreement, LIBS overlapping craters on the carbonate-uraninite interface probably result in material flushing between pulses and material redeposition. This effect which can cause signal tailing has also been observed to some degree and will be the subject of further investigation in the future.

The spatial distributions of the uranium as the main elements of interest were displayed by LIBS clearly and the results can serve as a quick initial characterisation of the sample. In the obtained images the main structures, the location of individual mineral phases, and also some fine structures and veins are clearly visible (Fig. 3). These images provide the first overview of the sample surface, but the experienced eye of a geologist can easily reveal interesting parts that deserve to be examined in more detail. Here it should be emphasised that the subsequent area selection for LA-ICP-MS imaging can therefore be made more reliable to save instrumental time and expense. Moreover, using a four-channel spectrometer, the whole emission spectra were saved and retrospective evaluation of other emission lines is possible.

3.2. LA-ICP-MS imaging

More detailed imaging of individual elements/isotopes was performed in separate mineral zones using the LA-ICP-MS method. Areas of 2×3 mm were analysed with parameters described in the experimental part, giving a spatial resolution of 20 μm. The scan speed of 20 μm s^{-1} was set so that the dwell time (1 s) and the shift time across the ablation crater diameter (20 μm) were identical. This ensured that the LA-ICP-MS signal did not blur in the x-axis direction. ILAPS software needs to separate individual scans within an imaged area to properly compose a record in time and space. To do this, the individual scans need to be separated by a sufficient time delay so that the isotope signal drops to units for up to tens of seconds in its background.

3.2.1. Uraninite

For uraninite vein imaging, a heterogeneous region was selected containing the spherulitic uranium aggregates overgrown and/or crosscut by hydrothermal calcite. The selection was set on characteristic structures clearly visible on the LIBS images. Most of the measured isotopes were concentrated in the region correlating with uranium represented by ^{235}U at Fig. 4. However, detailed imaging reveals differences in the distribution of elements and even isotopes. In some cases, individual zones of the aggregates seem to have different concentrations of major and trace elements, best visible on the distribution of ^{51}V. Diagonal hatching on the vanadium map is a consequence of the measurement artifact, so we must ignore it when interpreting the map. This artifact also occurred in the case of ^{238}U and its removal is one of the tasks needed to improve the imaging of the LA-ICP-MS method. Additional knowledge shows that this is a consequence of setting the parameters of the method, especially the combination of measured isotopes, their dwell times and the total integration time of the measurement [9]. Some very useful information for supplementing the elemental image of the LIBS method is the possibility of displaying individual isotopes by the LA-ICP-MS method. An example is the imaging of lead isotopes containing non-radiogenic ^{204}Pb and radiogenic ^{206}Pb, ^{207}Pb as the decay product of ^{238}U, ^{235}U and ^{208}Pb as radiogenic decay of ^{232}Th. Non-radiogenic lead is not related only to the structure of uraninite and also forms isolated clusters, probably as compounds with sulphur or selenium, while radiogenic isotopes of lead also copy their parent nuclides. Therefore, the most abundant and homogeneous is represented by the isotope ^{206}Pb as the decay product of the isotope ^{238}U (relative abundance of 99.274%), which is the main component of uraninite. Heterogenous distribution of ^{207}Pb and even more apparently ^{208}Pb within uraninite aggregates, considered to have originated in one-time period, is worth mentioning due to usage of lead isotope ratios for radiometric dating. In this context, intra-grain scale isotopic variations within fresh uraninite aggregates (Fig. 4), showing no visible effect of post-crystallisation alteration [42], demonstrate a possible utilisation of the LA-ICP-MS imaging for subsequent U/Pb dating of geological samples, precluding potential bias of isotopic systematics.

3.2.2. Carbonate

The LA-ICP-MS measurements of the carbonate vein show how important it is to create more detailed, high-resolution images. Here, the method allowed the visualisation of details of the carbonate vein, where a thin veinlet structure with elevated content of iron, lead (Fig. 5, left) as well as uranium (Fig. 6 C) can be observed (in consistence with the subtle hints of these structures in LIBS images). In addition to calcium as a matrix element of carbonate (calcite), all measured analytes appeared in the thin veinlet structure with the exception in distribution of ^{208}Pb, which also occurs in formations outside the vein, most probably as part of sulphide mineralisation. Uranium bound in the uraninite can became very mobile during redox changes (oxidation, indicated also by a presence of iron) and can migrate using the weakened parts of a surrounding carbonate vein as fissures or calcite grain boundaries. The discovered veinlet structure thus represented a possible migration path for uranium released from a massive uraninite vein during post crystallisation redox changes.

3.2.3. Metasomatite

Metasomatites in the Rožná uranium mine locally host impregnation style uranium mineralisation, mostly coffinites ($U(SiO_4)\cdot nH_2O$) that are considered to be formed by redistribution of uranium form older uraninite veins connected with reactivation during younger stages of the Alpine orogeny [34,43]. Both LA-ICP-MS and LIBS imaginig revealed poor uranium concentration of dissemination/impregnation style (Fig. 6 B) as well as iron rich clusters (Fig. 5, right) representing disseminated hematite (Fe_2O_3) mineralisation that indicate the above mentioned minerogenetic processes due to redox changes. Localisation and direction (Fig. 6) of the described thin veinlet structure in the carbonate vein suggests a possible connection between the uraninite vein and the metasomatite. Thus, it is possible that this veinlet structure was one of

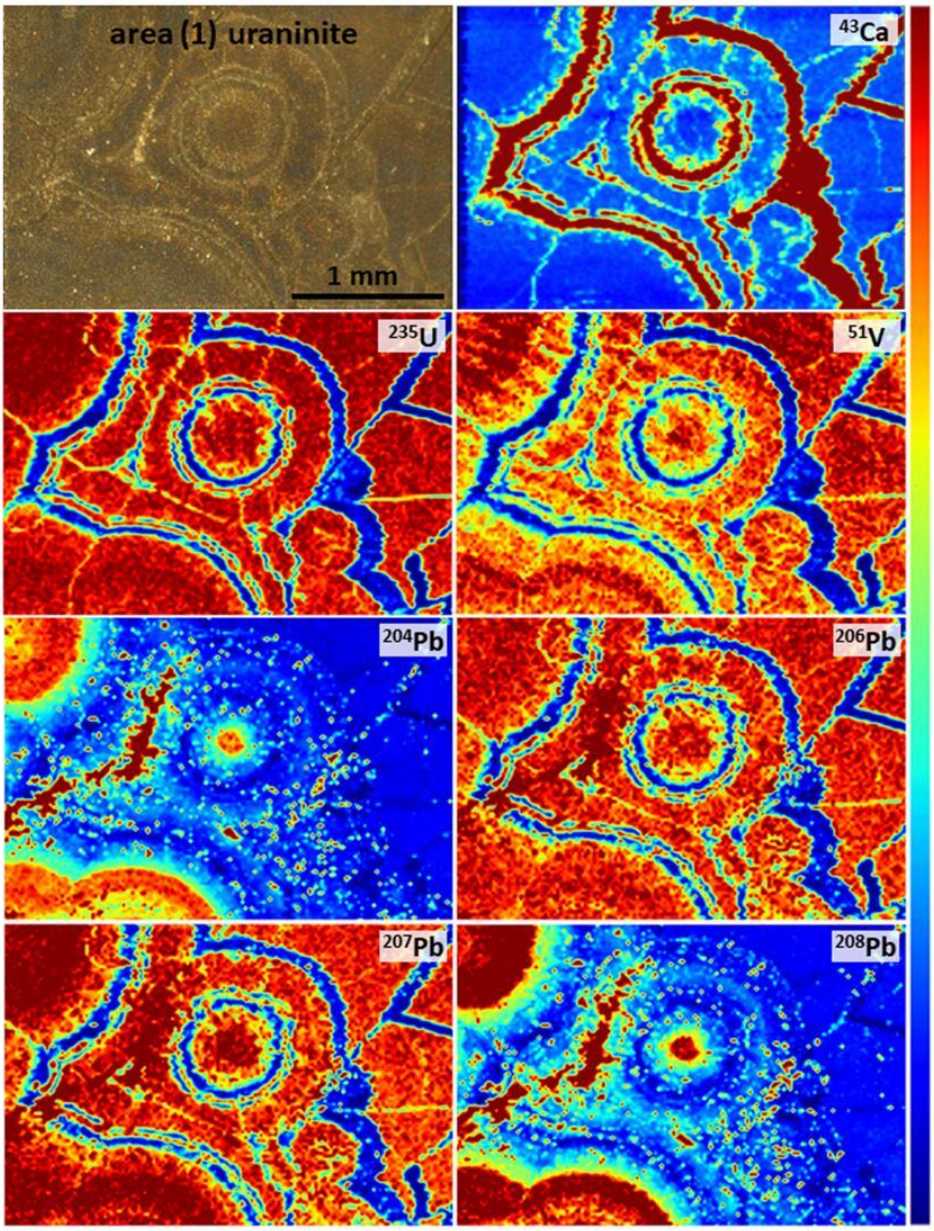

Fig. 4. Photography of analysed sample area (1) and distribution of selected isotopes in uraninite obtained by LA-ICP-MS. Normalised intensities in cps, blue colour as minimum, red as maximum. (For interpretation of the references to colour in this figure legend, the reader is referred to the web version of this article.)

the feeding channels allowing migration of uranium and as a consequence, the origin of a redistributed metasomatic uranium mineralisation.

3.3. Preparation of combined elemental images

Because LA-ICP-MS analysis is time-consuming and relatively expensive, choosing the right location on the sample is key to obtaining the necessary information about the distribution and behaviour of the elements in the sample. In the first step, LIBS provides a "rough" distribution image of a larger sample area, and then a smaller cut-out with higher resolution can be displayed in more detail using LA-ICP MS. Nevertheless, important information is not only contained in the detailed structures but is also important for the geologist to have an general view of the structure of the sample in terms of clarifying the overall context (e.g. positions of veins, the growth direction of structures, etc.). Therefore, it is desirable to preserve the data from both methods and combine it so that complete information can be displayed in one image.

Linking results of both analytical techniques enables the creation of merged elemental images. An example of such dual imaging shows the uranium distribution in Fig. 6. Cut-outs for laser ablation were chosen by

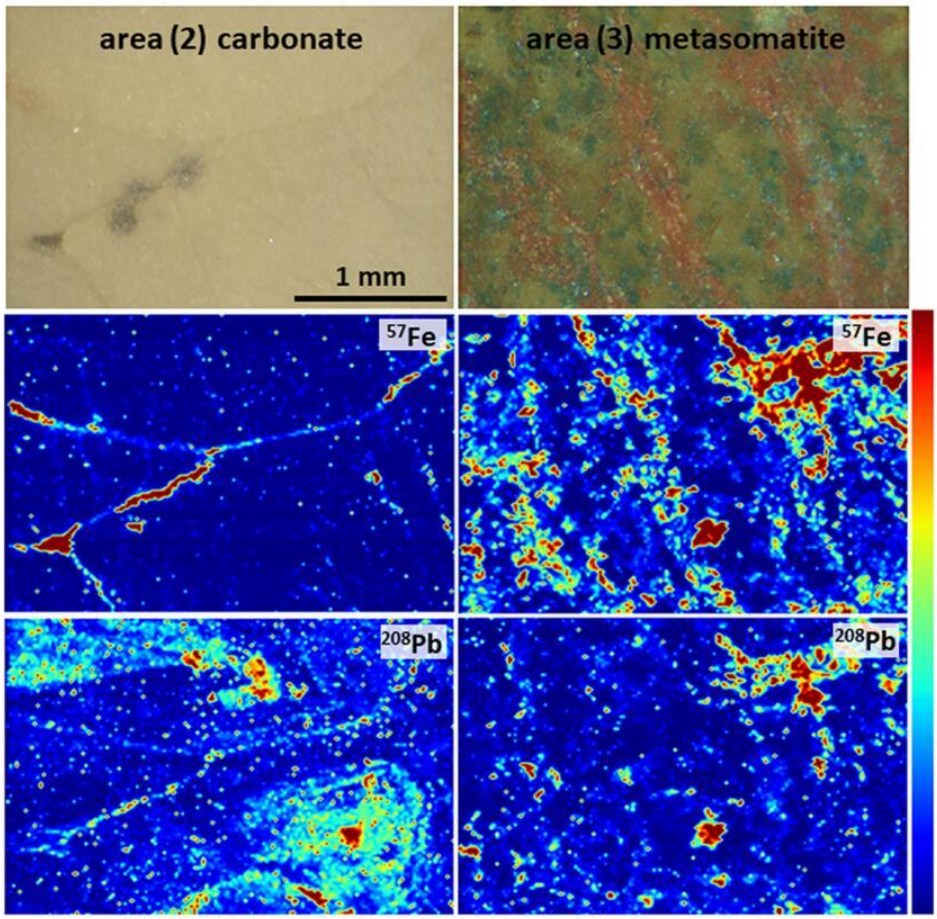

Fig. 5. Photography of analysed sample area (2 and 3) and distribution of selected isotopes in carbonate vein (left) and metasomatite (right) obtained by LA-ICP-MS. Normalised intensities in cps, blue colour as minimum, red as maximum. (For interpretation of the references to colour in this figure legend, the reader is referred to the web version of this article.)

taking interesting formations revealed by LIBS into consideration. The description of individual areas was already mentioned in Chapter 3.2.1–3. In addition, the LA-ICP-MS method allows the display of specific isotopes, which can be a significant extension of information regarding elemental distribution. For example, a comparison of radiogenic and non-radiogenic isotopes of elements may clarify the formation of a given structure, as mentioned in Chapter 3.2.1.

The main difficulty in creating an elemental distribution image can be in choosing the right intensity scale, especially if it is an image involving zones with extremely different content of the displayed element. Then it is necessary to choose which part of the sample is most important to see the details of and to adjust the scaling of that part. However, this usually means losing a more detailed distribution of the element in other zones.

The ILAPS software tool specially designed for processing the results for the imaging and formation of elemental images allows the arbitrary choice of scaling intensities, even if it is the output from various devices. Identical processing of differently measured data allows the creation of an image in the same way by interpolation and graphical processing. Thus, a result can be a combination of different distributions of the same graphics processing in one image, as shown in Fig. 7. Here, the detailed distribution of the ^{206}Pb isotope in the uraninite is inserted into the elemental distribution of lead measured by LIBS (left), and the ^{235}U veinlet structure is merged with uranium LIBS image in carbonate (right). The scaling of the LA-ICP-MS and LIBS images is unified so that the boundary between the merged images is almost imperceptible.

The exact procedure for creating images using ILAPS is as follows. In LA-ICP-MS the laser scans over the sample as a set of parallel lines, which are gathered into a single file as a continuous data stream of altering segments of background and analyte signal. This file is directly imported into the ILAPS software where the segments are automatically distinguished using timestamps of the laser activity from an .Iolite file exported from Chromium - the operating software of the laser. The lines are background corrected and rearranged into a matrix, which represents the intensities over the ablated area. The user needs to manually set the width and height of a pixel as Δx (integration time x scan speed) and Δy (y-offset of parallel lines) values. After the matrix is created for each measured element, the user can use the semi-interactive graph to adjust the image. This includes selecting the scale where the user can define the data range that the colourmap covers, using an interpolation method to smooth the image or selecting a colourmap.

These adjustments are necessary to be similar in the image processing of both methods, LA-ICP-MS and LIBS, to produce comparable images. Using one software for this purpose is the most straightforward method to achieve this. With a simple script, ILAPS can import an x,y matrix from LIBS, this script can be found at https://github.com/

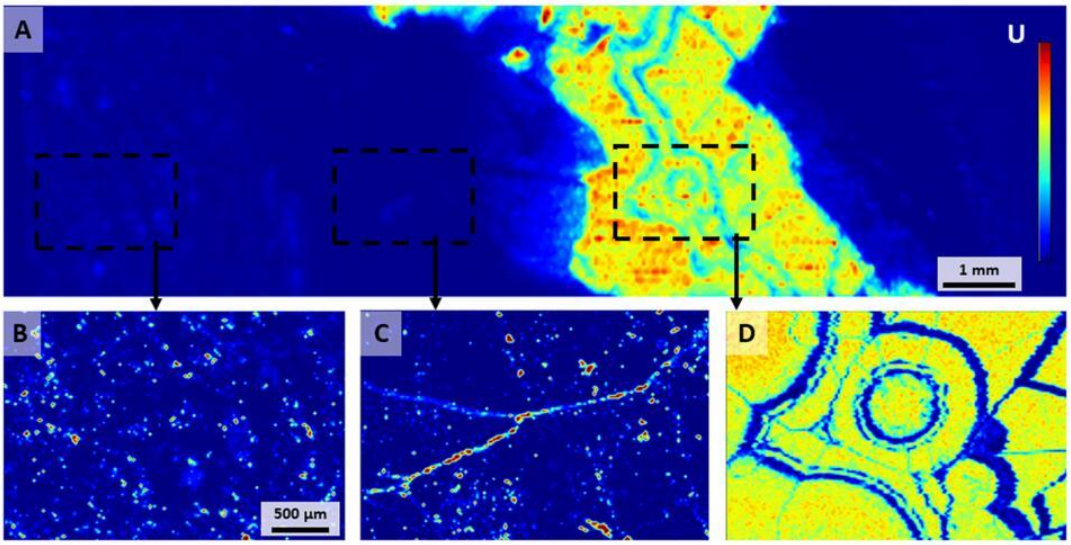

Fig. 6. Distribution of U in the sample: (A) LIBS U II 367.01 nm, (B—D) LA-ICP-MS sections ^{235}U.

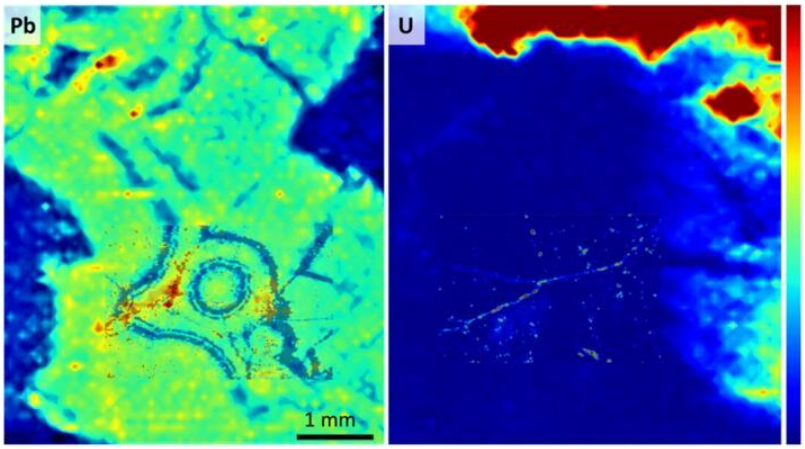

Fig. 7. Detailed views on combined parts of distribution maps obtained by two imaging techniques LIBS and LA-ICP-MS. Data merged and images overlaid by ILAPS software - lead in uraninite (left) and uranium in carbonate (right).

nikadilli/imageLIBS. The script simply rearranges the output matrix from the LIBS measurement (for the wavelength of the selected emission line) into the same format as the LA-ICP-MS matrix that is created by ILAPS. After creating this matrix, it can be imported into ILAPS and processed in the same manner as the matrix from LA-ICP-MS, ensuring the same colourmap, scale and interpolation. Subsequently, the matrices are combined, and the software makes it possible to determine the co-ordinates of specific places on the distribution image which were applied for translating different images on top of each other.

4. Conclusions

A method of dual imaging using a combination of two analytical techniques – LA-ICP-MS and LIBS was applied to create images revealing distribution and possible migration of elements and isotopes in a sample of uranium ore. Elemental/isotopic imaging can display presence and distribution of selected isotopes causing structural defects and thus can help to better understand the evolution of geological processes, and to identify the structures responsible for uranium migration. The images can also provide essential information for the provenance study of analysed uranium ore samples.

Fast LIBS scanning made it possible to perform an analysis across the entire width of the sample, containing three mineral phases (meta-somatite, carbonate vein, massive uraninite vein) in 20 min. The total mapped area was 4.0 × 23.2 mm, which resulted in a chemical map of 51 × 290 locations (80 µm resolution). Using four-channel spectrometer the entire emission spectrum was recorded and therefore suitable emission lines can be retrospectively evaluated and additional information on the sample composition can be obtained. After appropriate normalisation of selected emission lines, "rough" element images of the sample were created to identify interesting areas in individual minerals.

The LA-ICP-MS method focused in detail on interesting areas in individual minerals and created isotopic maps of 3 × 2 mm with a resolution of 20 µm (150 × 100 pixels), taking 5 h per map. The main advantage of LA-ICP-MS imaging is the high resolution of the resulting images together with the ability to display individual isotopes, which

provides another added value to elemental distribution. For the specific example given in the mapping of a uranium ore, conspicuous variations in radiogenic isotopes of lead in unaltered uraninite samples was revealed. Observed heterogeneous isotopic and elemental composition of natural uraninites suggest that any further analytical studies must take such isotopic variations into account, even in fresh samples, in order to prevent potential errors and bias in U/Pb age determinations of uranium mineralisation.

The aim of this work was to find a procedure for both methods of data processing so that the data can be displayed simultaneously in one image. From the geologist's point of view, such a picture will provide information about both the detailed structures and the overall view of the sample. Combination of large maps obtained by LIBS accompanied by highly detailed LA-ICP-MS imagining can serve as a very useful tool suitable for mineral deposit studies (mineral exploration and mining industry sector) as was demonstrated on the analysed sample where two different uranium mineralisation types and their possible genetic relationship were revealed.

ILAPS software specially developed for analytical data processing is presented for the creation of output distribution images of the same format for both LIBS and the LA-ICP-MS method. The same processing of different output data makes it possible to obtain a resulting 2D matrix of the same format, whether it represents the emission line signal intensity for LIBS or cps (counts per second) of isotopes in ICP-MS. The data in the form of a matrix is then inserted into the ILAPS software, which determines the final graphic form of the image. Another advantage is that the matrix makes it possible to determine the exact coordinates of a specific place on the distribution map, which can be applied when translating different maps on top of each other, as shown in this article. The plan for the future is to automate this process and create an application for directly combining maps of different sizes within the ILAPS system.

Author contribution statement

Markéta Holá, Karel Novotný conceived and designed the LA-ICP-MS and LIBS experiments; Jan Dobeš, Ivo Krempl performed the experiments; Vojtěch Wertich, Juraj Mozola, Martin Kubeš prepared sample, evaluated and interpreted the results from a geological point of view, Veronika Faltusová created and operated the ILAPS program, Jaromír Leichmann and Viktor Kanický supervised all steps.

Declaration of competing interest

There is no conflict of interest.

Acknowledgements

This research was carried out under the OP VVV project CZ.02.1.01/0.0/0.0/16_026/0008459 (GeoBarr) from the European Regional Development Fund with financial support from the Ministry of Education, Youth and Sports of the Czech Republic, and was supported also by the project MUNI/A/1390/2020 of Masaryk University.

References

[1] M. Hola, J. Kalvoda, H. Novakova, R. Skoda, V. Kanicky, Possibilities of LA-ICP-MS technique for the spatial elemental analysis of the recent fish scales: line scan vs. depth profiling, Appl. Surf. Sci. 257 (2011) 1932–1940.
[2] N. Cook, C.L. Ciobanu, L. George, Z.Y. Zhu, B. Wade, K. Ehrig, Trace element analysis of minerals in magmatic-hydrothermal ores by laser ablation inductively-coupled plasma mass spectrometry: approaches and opportunities, Minerals 6 (2016).
[3] T. Vaculovic, K. Breiter, Z. Korbelova, N. Venclova, K. Tomkova, S. Jonasova, V. Kanicky, Quantification of elemental mapping of heterogeneous geological sample by laser ablation inductively coupled plasma mass spectrometry, Microchem. J. 133 (2017) 200–207.
[4] T. Vaculovic, T. Warchilova, Z. Cadkova, J. Szakova, P. Tlustos, V. Otruba, V. Kanicky, Influence of laser ablation parameters on trueness of imaging, Appl. Surf. Sci. 351 (2015) 296–302.
[5] J. Xu, C.L. Ciobanu, N.J. Cook, Y.Y. Zheng, X. Sun, B.P. Wade, Skarn formation and trace elements in garnet and associated minerals from Zhibula copper deposit, Gangdese Belt, southern Tibet, Lithos 262 (2016) 213–231.
[6] R. Ismail, C.L. Ciobanu, N.J. Cook, G.S. Teale, D. Giles, A.S. Mumm, B. Wade, Rare earths and other trace elements in minerals from skarn assemblages, Hillside iron oxide-copper-gold deposit, Yorke Peninsula, South Australia, Lithos 184 (2014) 456–477.
[7] J. Mercadier, M. Cuney, P. Lach, M.C. Boiron, J. Bonhoure, A. Richard, M. Leisen, P. Kister, Origin of uranium deposits revealed by their rare earth element signature, Terra Nova 23 (2011) 264–269.
[8] J. Kalvoda, T. Kumpan, M. Hola, O. Babek, V. Kanicky, R. Skoda, Fine-scale LA-ICP-MS study of redox oscillations and REEY cycling during the latest Devonian Hangenberg crisis (Moravian karst, Czech Republic), Palaeogeogr. Palaeoclimatol. Palaeoecol. 493 (2018) 30–43.
[9] J.T. van Elteren, V.S. Selih, M. Sala, S.J.M. Van Malderen, F. Vanhaecke, Imaging artifacts in continuous scanning 2D LA-ICPMS imaging due to nonsynchronization issues, Anal. Chem. 90 (2018) 2896–2901.
[10] C. Paton, J. Hellstrom, B. Paul, J. Woodhead, J. Hergt, Iolite: freeware for the visualisation and processing of mass spectrometric data, J. Anal. At. Spectrom. 26 (2011) 2508–2518.
[11] D.A. Cremers, L.J. Radziemski, Handbook of Laser-Induced Breakdown Spectroscopy, 2nd edition, 2013, pp. 1–407.
[12] M.A. W, P. Vincenzo, S. Israel, Laser-Induced Breakdown Spectroscopy (LIBS), Cambridge University Press, 2006.
[13] D. Menut, P. Fichet, J.L. Lacour, A. Rivoallan, P. Mauchien, Micro-laser-induced breakdown spectroscopy technique: a powerful method for performing quantitative surface mapping on conductive and nonconductive samples, Appl. Opt. 42 (2003) 6063–6071.
[14] H. Bette, R. Noll, High speed laser-induced breakdown spectrometry for scanning microanalysis, J. Phys. D-Appl. Phys. 37 (2004) 1281–1288.
[15] K. Novotny, T. Vaculovic, M. Galiova, V. Otruba, V. Kanicky, J. Kaiser, M. Liska, O. Samek, R. Malina, K. Palenikova, The use of zinc and iron emission lines in the depth profile analysis of zinc-coated steel, Appl. Surf. Sci. 253 (2007) 3834–3842.
[16] L. Sancey, V. Motto-Ros, B. Busser, S. Kotb, J.M. Benoit, A. Piednoir, F. Lux, O. Tillement, G. Panczer, J. Yu, Laser spectrometry for multi-elemental imaging of biological tissues, Sci. Rep. 4 (2014).
[17] V. Pinon, M.P. Mateo, G. Nicolas, Laser-induced breakdown spectroscopy for chemical mapping of materials, Appl. Spectrosc. Rev. 48 (2013) 357–383.
[18] R.S. Harmon, R.E. Russo, R.R. Hark, Applications of laser-induced breakdown spectroscopy for geochemical and environmental analysis: a comprehensive review, Spectrochimica Acta Part B-Atomic Spectroscopy 87 (2013) 11–26.
[19] K. Novotny, J. Kaiser, M. Galiova, V. Konecna, J. Novotny, R. Malina, M. Liska, V. Kanicky, V. Otruba, Mapping of different structures on large area of granite sample using laser-ablation based analytical techniques, an exploratory study, Spectrochimica Acta Part B-Atomic Spectroscopy 63 (2008) 1139–1144.
[20] S. Romppanen, H. Hakkanen, S. Kaski, Singular value decomposition approach to the yttrium occurrence in mineral maps of rare earth element ores using laser-induced breakdown spectroscopy, Spectrochimica Acta Part B-Atomic Spectroscopy 134 (2017) 69–74.
[21] M. Wang, Q. Wang, M. Zhu, L. Sun, X. Peng, L. Liu, J. Qu, Ieee, Applying Stand-off LIBS to Paleoclimatic Research: A Case Study on Geochemical Content of Carbonate Rocks, 2015 Optoelectronics Global Conference (Ogc), 2015.
[22] C.D. Quarles, J.J. Gonzalez, L.J. East, J.H. Yoo, M. Morey, R.E. Russo, Fluorine analysis using laser induced breakdown spectroscopy (LIBS), J. Anal. At. Spectrom. 29 (2014) 1238–1242.
[23] J. Klus, P. Mikysek, D. Prochazka, P. Porizka, P. Prochazkova, J. Novotny, T. Trojek, K. Novotny, M. Slobodnik, J. Kaiser, Multivariate approach to the chemical mapping of uranium in sandstone-hosted uranium ores analyzed using double pulse laser-induced breakdown spectroscopy, Spectrochimica Acta Part B-Atomic Spectroscopy 123 (2016) 143–149.
[24] J. Klus, P. Porizka, D. Prochazka, P. Mikysek, J. Novotny, K. Novotny, M. Slobodnik, J. Kaiser, Application of self-organizing maps to the study of U-Zr-Ti-Nb distribution in sandstone-hosted uranium ores, Spectrochimica Acta Part B-Atomic Spectroscopy 131 (2017) 66–73.
[25] Y. Lee, S.H. Nam, K.S. Ham, J. Gonzalez, D. Oropeza, D. Quarles, J. Yoo, R. E. Russo, Multivariate classification of edible salts: simultaneous laser-induced breakdown spectroscopy and laser-ablation inductively coupled plasma mass spectrometry analysis, Spectrochimica Acta Part B-Atomic Spectroscopy 118 (2016) 102–111.
[26] M. Bonta, J.J. Gonzalez, C.D. Quarles, R.E. Russo, B. Hegedus, A. Limbeck, Elemental mapping of biological samples by the combined use of LIBS and LA-ICP-MS, J. Anal. At. Spectrom. 31 (2016) 252–258.
[27] C. Latkoczy, T. Ghislain, Simultaneous LIBS and LA-ICP-MS analysis of industrial samples, J. Anal. At. Spectrom. 21 (2006) 1152–1160.
[28] J.R. Chirinos, D.D. Oropeza, J.J. Gonzalez, H.M. Hou, M. Morey, V. Zorba, R. E. Russo, Simultaneous 3-dimensional elemental imaging with LIBS and LA-ICP-MS, J. Anal. At. Spectrom. 29 (2014) 1292–1298.
[29] H.E. Frimmel, S. Schedel, H. Bratz, Uraninite chemistry as forensic tool for provenance analysis, Appl. Geochem. 48 (2014) 104–121.
[30] T.L. Spano, A. Simonetti, E. Balboni, C. Dorais, P.C. Burns, Trace element and U isotope analysis of uraninite and ore concentrate: applications for nuclear forensic investigations, Appl. Geochem. 84 (2017) 277–285.

[31] J. Janeczek, R.C. Ewing, V.M. Oversby, L.O. Werme, Uraninite and UO2 in spent nuclear fuel: a comparison, J. Nucl. Mater. 238 (1996) 121–130.
[32] J. Bruno, R.C. Ewing, Spent nuclear fuel, Elements 2 (2006) 343–349.
[33] Ilaps. https://github.com/nikadilli/llaps-v2/.
[34] B. Kribek, K. Zak, P. Dobes, J. Leichmann, M. Pudilova, M. Rene, B. Scharm, M. Scharmova, A. Hajek, D. Holeczy, U.F. Hein, B. Lehmann, The Ro angstrom 3/4na uranium deposit (bohemian massif, Czech Republic): shear zone-hosted, late Variscan and post-Variscan hydrothermal mineralization, Mineral. Deposita 44 (2009) 99–128.
[35] J. Janeczek, R.C. Ewing, Structural formula of uraninite, J. Nucl. Mater. 190 (1992) 128–132.
[36] J. Plasil, Oxidation-hydration weathering of uraninite: the current state-of-knowledge, J. Geosci. 59 (2014) 99–114.
[37] R.D. Shannon, Revised effective ionic-radii and systematic studies of interatomic distances in halides and chalcogenides, Acta Crystallographica Section A 32 (1976) 751–767.
[38] P. Alexandre, K. Kyser, D. Layton-Matthews, B. Joy, Y. Uvarova, Chemical compositions of natural uraninite, Can. Mineral. 53 (2015) 595–622.
[39] A. Limbeck, L. Brunnbauer, H. Lohninger, P. Porizka, P. Modlitbova, J. Kaiser, P. Janovszky, A. Keri, G. Galbacs, Methodology and applications of elemental mapping by laser induced breakdown spectroscopy, Anal. Chim. Acta 1147 (2021) 72–98.
[40] B. Bhatt, K.H. Angeyo, A. Dehayem-Kamadjeu, LIBS development methodology for forensic nuclear materials analysis, Anal. Methods 10 (2018) 791–798.
[41] E.J. Kautz, P.J. Skrodzki, M. Burger, B.E. Bernacki, I. Jovanovic, M.C. Phillips, S. S. Harilal, Time-resolved imaging of atoms and molecules in laser-produced uranium plasmas, J. Anal. At. Spectrom. 34 (2019) 2236–2243.
[42] P. Martz, J. Mercadier, J. Perret, J. Villeneuve, E. Deloule, M. Cathelineau, D. Quirt, A. Doney, P. Ledru, Post-crystallization alteration of natural uraninites: implications for dating, tracing, and nuclear forensics, Geochim. Cosmochim. Acta 249 (2019) 138–159.
[43] F.J. Dahlkamp, Uranium Deposits of the World Europe, Springer-Verlag, Berlin Heidelberg, Berlin, 2016.

PAPER 4

Quantitative analysis of Fe-based samples using ultraviolet nanosecond and femtosecond laser ablation-ICP-MS

Možná, V., Pisonero, J.*, **Holá, M.**, Kanický, V., Günther, D.

Journal of Analytical Atomic Spectrometry. 2006, 21(11), 1194–1201. DOI 10.1039/b606988f

Contribution:

Student supervision, consultation (the work was developed at ETH Zurich).

Quantitative analysis of Fe-based samples using ultraviolet nanosecond and femtosecond laser ablation-ICP-MS

Veronika Možná,[ab] Jorge Pisonero,*[a] Markéta Holá,[b] Viktor Kanický[b] and Detlef Günther[a]

Received 17th May 2006, Accepted 28th September 2006
First published as an Advance Article on the web 9th October 2006
DOI: 10.1039/b606988f

The quantification capabilities of iron-based samples were investigated using three commercially available ultraviolet (UV) nanosecond (ns) and femtosecond (fs) laser ablation systems coupled to inductively coupled plasma mass spectrometry (LA-ICP-MS). A comparison of three pulsed laser ablation systems (ArF* excimer, Nd:YAG and Ti-sapphire) with different wavelengths and pulse time durations (15 ns, 4 ns and 150 fs, respectively) was performed. Minor and trace elements were determined using ^{57}Fe as internal standard element. Using similar spatial resolution for all laser systems and commonly applied operating conditions for each system, higher ion-signals (25–30%) and more stable elemental ratios (10% TRSD) were obtained for UV-fs-LA-ICP-MS. Scanning electron microscope images and particle size distributions measured for UV-ns-LA systems showed a bimodal distribution formed by nano-sized agglomerates and micro-sized molten spherical particles. In contrast, due to reduced thermal effects achieved using ultra-short pulses, the particle size distribution measured using UV-fs-LA showed a broad monomodal distribution (nano-sized agglomerates in the range of 50–250 nm). Matrix-matched (within metallic samples) and non-matrix matched calibrations were applied for the analysis of Fe-based samples, using a silicate glass (SRM NIST 610) as non-matrix matched calibration sample (glass-metals). Improved analytical results in terms of precision and accuracy were obtained using femtosecond laser ablation when using similar matrices for calibration. Moreover, non-matrix matched calibration used for quantification provides more accurate results (5–15%) in comparison with both UV-ns-LA-ICP-MS (5–30% using Nd:YAG laser and 15–60% using ArF* laser).

Introduction

Production control and quality assurance in steel and related industries are increasingly demanding the fast characterization of metallic samples with low limits of detection and high spatial resolution to reduce the required alloying material and to shorten the process control time. Laser ablation inductively coupled plasma mass spectrometry (LA-ICP-MS) allows direct elemental analysis of nearly all kind of sample matrices with low limits of detection (μg g^{-1}–ng g^{-1}), a lateral resolution of a few μm and a depth resolution of tens of nm.[1] Moreover, it is a fast and easy-to-use technique which requires, for such samples, little sample preparation. Sample material is ablated by a focused or imaged laser beam and transported as an aerosol by a carrier gas flow from an ablation cell into the ICP, where the aerosol is atomized and ionized for MS detection.

Today, the most commonly used nanosecond (ns)-LA-ICP-MS has not become a widely applied analytical technique for routine analysis of metallic samples in industry due to fractionation and matrix effects.[2–6] In this case, accurate analysis can only be assured using standard reference materials (SRM) of similar composition or morphology to the sample of interest. However, the lack of appropriate SRM is a serious restriction for most of the direct solid analysis techniques, including LA-ICP-MS.

All processes involved in LA-ICP-MS (ablation process, aerosol transport and conversion of the aerosol into ions within the ICP), may potentially alter the stoichiometric composition of the aerosol, resulting in unknown contributions to fractionation that still hinder a non-matrix matched calibration strategy.[7,8] Thus, one of the main aims of LA-ICP-MS research is the development of strategies to reduce fractionation. For instance, analytical performance of laser ablation using ICP-MS detection is significantly influenced by the particle size distribution of the generated aerosol.[9,10] Chemical composition, transport efficiency and decomposition of the aerosol within the ICP are closely related to the size of the aerosol particles. Full vaporization or ionization within the ICP cannot be achieved for particles bigger than a certain critical size which depends on the material.[5,6,11] Moreover, although it has been demonstrated that the overall aerosol composition represents the stoichiometry of the bulk sample,[12] the elemental composition of laser generated particles from different matrices (*e.g.*, glass and brass) was found to be strongly size dependent.[13,14] Therefore, to obtain a particle size distribution of the generated aerosol with appropriate small

[a] *Laboratory for Inorganic Chemistry, ETH Zurich, 8093 Zurich, Switzerland. E-mail: jorge.pisonero@inorg.chem.ethz.ch*
[b] *Laboratory of Atomic Spectrochemistry, Faculty of Science, Masaryk University, Kotlářská 2, Brno 611 37, Czech Republic*

particle sizes, different strategies depending on the sample material have been investigated, including the use of shorter ultraviolet wavelengths[15] or ultra-short (femtosecond) laser pulses.[16,17]

In the case of the analysis of metallic samples using LA-ICP-MS, it has been observed that the laser wavelength has only a small effect on the ablation characteristics, while the laser pulse duration (pulse width) appears to be the dominant parameter affecting the stoichiometry of the generated aerosol and the formation of molten material in and around the ablation spot.[5,18] The application of ns-LA has been found to produce a "heat affected zone" due to thermal diffusion into the target. As a result, preferential vaporization of the sample constituents from the melt of a metallic sample have been observed in brass.[12,19] Moreover, energy is partially dissipated into the formed laser-induced plasma affecting the composition of the aerosol particles formed during material expansion. In contrast, during femtosecond laser ablation (fs-LA) the pulse duration falls below the thermal relaxation time ($\sim$10 ps),[20] which is the time needed to transfer the absorbed pulse energy from heated electrons to the lattice, reducing the thermal effects and thus the preferential vaporization. In this sense, some preliminary results have highlighted the capabilities of fs-LA-ICP-MS for the analysis of silicates and metallic samples (brass and aluminium).[21–23] Furthermore, great progress in isotopic analysis (Fe) has been recently reported using a deep UV fs laser ablation system in combination with multi-collector (MC)-ICP-MS. It also needs to be mentioned that UV and deep UV laser ablation on silicates or oxides provides accurate results for a large number of elements when non-matrix matched calibration (similar matrix to the sample of interest) has been applied (mineral–glass).

In this work, a comparison of three commercially available pulsed laser ablation systems (ArF* excimer-based, Nd:YAG and Ti-sapphire) operating at different wavelengths and pulse time durations (15 ns, 4 ns and 150 fs, respectively) was performed for the LA-ICP-MS analysis of Fe-based samples. The major aim of this study was focused on the quantification capabilities of LA-ICP-MS using commercially available systems. An extreme case of non-matrix matched calibration between glass and metals was chosen. Since the pulse duration, fluence and wavelength play a major role in the ablation process, operating conditions reported in the literature as optimum parameters for a number of applications were selected. In addition, particle size distributions of the aerosols, as most significantly influencing parameter for the vaporization within the ICP, were measured online. Moreover, collected aerosol particles were analyzed by scanning electron microscope (SEM) in order to investigate particle size based fractionation and/or matrix effects. Pulse to pulse single hole drilling experiments were carried out to study the changes of the particle size distribution of the aerosol at increasing depths from the surface of the sample.

Experimental

Instrument

Laser sampling was performed using three different pulsed laser systems: an ArF* excimer laser (λ = 193 nm) with 15 ns pulse duration (GeoLas C, MicroLas, Göttingen, Germany), the 4th harmonic of a solid state Nd:YAG laser (λ = 266 nm) with 4 ns pulse duration (LSX 500, CETAC Technologies, Omaha, NB, USA), and the 3rd harmonic of a chirped pulse amplification (CPA)-type Ti-sapphire based laser system (λ = 265 nm) with 150 fs pulse duration (Legend, Coherent Inc., Santa Clara, CA, USA).[23]

Table 1 Detailed operating conditions of the lasers and ICP-MS instrument

Laser	ArF*	Nd:YAG	fs Ti-sapphire
Wavelength	193 nm	266 nm	265 nm
Pulse length	15 ns	4 ns	150 fs
Energy density	13 J cm^{-2}	8 J cm^{-2}	3 J cm^{-2}
Repetition rate	4 Hz	4 Hz	4 Hz
metal			
Spot size	95 μm	100 μm	95 μm
Ablation cell volume	$\sim$30 cm^3	$\sim$100 cm^3	$\sim$30 cm^3
ICP-MS			
Rf power	1400 W		
Sampling depth	4 mm		
Carrier He flow rate	1.00 L min^{-1}		
Make-up Ar flow rate	0.80 L min^{-1}		
Isotopes measured	^{27}Al, ^{29}Si, ^{31}P, ^{53}Cr, ^{55}Mn, ^{57}Fe, ^{60}Ni, ^{65}Cu, ^{95}Mo		

The solid samples were ablated in an airtight ablation cell and the laser induced aerosol was transported, *via* a He carrier gas (1 l min^{-1}), to the ICP-MS (Agilent 7500cs, Agilent Technologies, Waldbronn, Germany) using an approximately 1 m polyethylene transfer tube. Before entering the ICP, the aerosol was mixed with an Ar make-up gas (0.8 l min^{-1}). The ICP-MS was optimized prior to the analysis for the best compromise between high signal-to-noise ratio and low oxide formation. Detailed operating conditions of the lasers and the ICP-MS instrument are listed in Table 1.

The particle size distribution of the laser generated aerosol was measured using an optical particle counter (OPC). A 32-channel HSLAS instrument (Particle Measuring Systems, Denver, CO, USA) based on a 633 nm HeNe laser was used. The instrument covers the size range between 65 nm and 1 μm. The aerosol was diluted 250-fold in helium by a bucket wheel diluter (MD19-1i, Matter Engineering AG, Wohlen, Switzerland) before entering the HSLAS to avoid the saturation of any channel.[24] Additionally, the laser induced aerosol particles were collected on filters and analyzed using a scanning electron microscope (SEM, Leo 1530 Gemini, Zeiss, Oberkochen, Germany) in order to obtain information about particle size and structure.

Standard reference materials

A stainless steel (JK27A 66%Fe) and a pure iron (JK2D 98%) were used for matrix matched calibrations. Moreover, a silicate glass (SRM NIST 610) was used for non-matrix matched calibrations. Certified content values of selected elements are listed in Table 2.

Results and discussion

Ion-signal intensities and elemental ratios

Fig. 1 (a,b,c) illustrates the transient LA-ICP-MS ion-signals measured for an Fe-based sample using UV ns- and fs-LA

Table 2 Certified content values of the selected elements

	Composition/μg g^{-1}								
Matrix/element	Fe	Al	Si	P	Cr	Mn	Ni	Cu	Mo
Silicate glass (SRM NIST 610)	457	10 005	328 400	343	405	433	444	430	377
Stainless steel (SRM JK27A)	661 400	169	4110	222	167 600	15 890	120 400	1990	25 310
Pure iron (SRM JK2D)	983 800	249	2370	78	1540	7490	760	1540	180

systems. Background signals were acquired during the first 30 s. It can be seen that the ion-signal intensities measured with fs-LA were by 25–30% higher than those acquired using both ns-LA systems (Nd:YAG and ArF*), even using lower fluence ($\sim$3 J cm^{-2} *versus* $\sim$8–13 J cm^{-2}). Higher ion-signal intensities measured by fs-LA-ICP-MS could be related to improved vaporization of the aerosol particles within the ICP and to higher ablation rates on metallic samples due to the extreme power density ($\sim 10^{15}$ W cm^{-2}). Moreover, the comparison of the transient signal intensities obtained for ns-ArF* and fs-LA-ICP-MS using the same ablation cell shows that aerosol wash out time in the case of fs-LA is about twice as long ($\sim$35 s) as that of ns-LA. Differences in aerosol dispersion could be related to different particle kinetic energies, sizes and morphologies. These effects are being currently investigated in more detail.

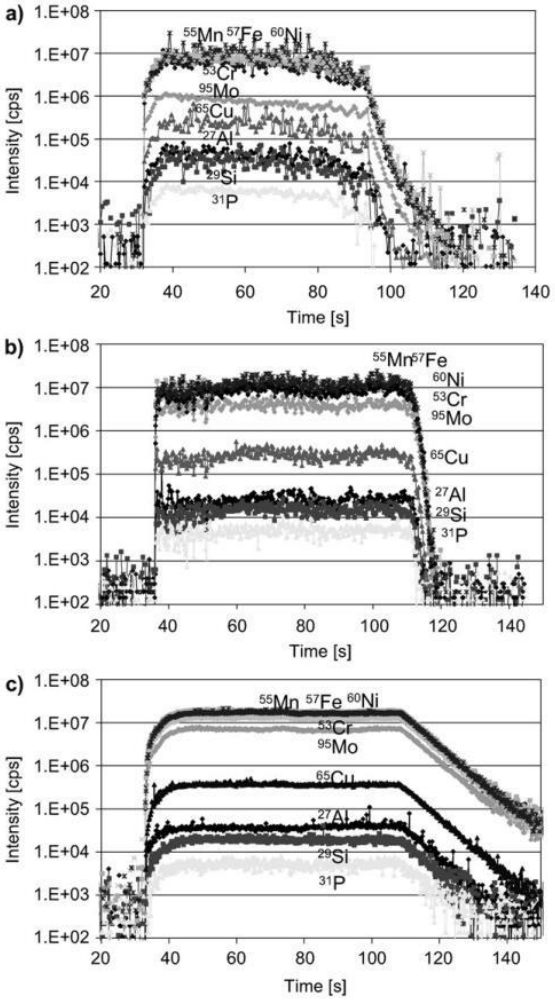

Fig. 1 Transient LA-ICP-MS ion-signals measured for SRM JK27A (Fe metal sample) using: (a) UV-ns-(ArF*)LA-ICP-MS; (b) UV-ns-(Nd:YAG)LA-ICP-MS; (c) UV-fs-(Ti-sapphire)LA-ICP-MS.

Table 3 lists the relative elemental fractionation indices (EFI) calculated according to Fryer *et al.*[25] ^{57}Fe was used as internal standard. It was observed that for all the selected elements, EFI was close to 1, indicating a negligible relative change of the average elemental ratios measured over time intervals of about 30 s. Fig. 2 (a,b,c) shows temporal profiles of elemental ratios relative to ^{57}Fe from an Fe-based sample, acquired using the UV ns- and fs-LA-ICP-MS systems. Significant amounts of spikes were observed in the measured transient signals using ns-LA, particularly using the 193 nm ArF* laser, indicating the presence of larger aerosol particles entering the ICP. In contrast, the transient signals measured using fs-LA show that these spikes were significantly reduced, thus improving the temporal relative standard deviation (TRSD) of the elemental ratios during the ablation time in comparison with ns-LA ($TRSD_{ArF}$ = 40%, $TRSD_{Nd:YAG}$ = 20%, $TRSD_{Ti\text{-}sapphire}$ = 10%). Moreover, the average values of the elemental ratios were observed to depend on the laser system. The elemental ratios measured by fs-Ti-sapphire and Nd:YAG were comparable but differed from the elemental ratios measured by ns-ArF*. For instance, ^{95}Mo/^{57}Fe increases from 0.15 (using ArF*) to about 0.5 (using Nd:YAG and fs-Ti-sapphire), while ^{31}P/^{57}Fe decreases from 1×10^{-3} (using ArF*) to about 5×10^{-4}(using Nd:YAG and fs-Ti-sapphire). These variations are not related to different tunings of the ICP and were consistently observed. Therefore, and in order to get further insights into the aerosol structure of the

Table 3 Relative elemental fractionation index (EFI) based on ^{57}Fe. EFI was calculated by dividing the relative elemental ratios measured during the last 30 s of ablation by the value obtained during the first 30 s. To show the small differences, figures are given without significance consideration

	Fractionation index $(X/^{57}Fe)_{(30\text{–}60\ s)}/(X/^{57}Fe)_{(0\text{–}30\ s)}$		
Isotope	ArF*	Nd:YAG	Ti-sapphire
^{27}Al	1.10	1.01	0.96
^{29}Si	1.07	1.04	1.01
^{31}P	0.99	1.08	1.00
^{53}Cr	1.04	1.06	1.01
^{55}Mn	1.08	1.12	1.03
^{60}Ni	1.04	0.99	0.99
^{65}Cu	1.05	1.03	0.99
^{95}Mo	0.99	0.91	1.00

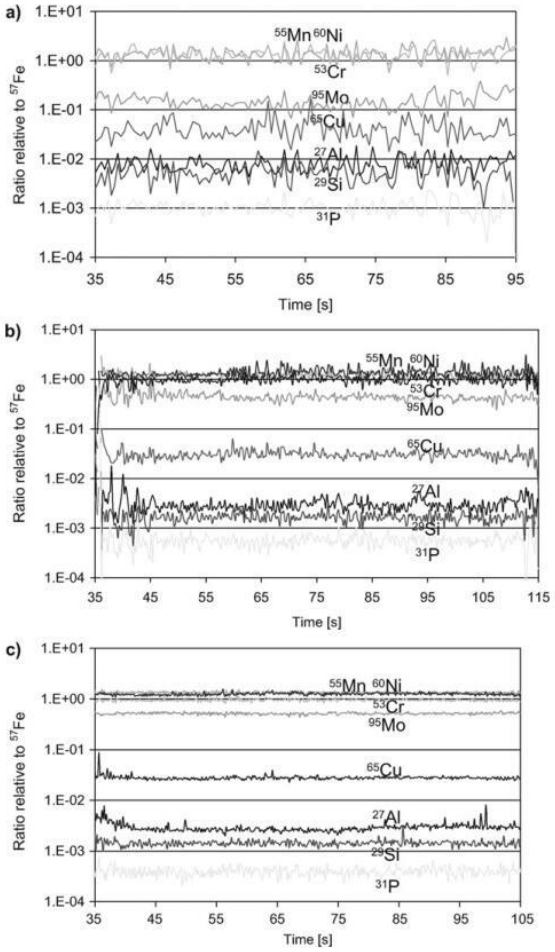

Fig. 2 Temporal profiles of elemental ratios relative to ^{57}Fe measured for SRM JK27A (Fe metal sample) using: (a) UV-ns-(ArF*)LA-ICP-MS; (b) UV-ns-(Nd:YAG)LA-ICP-MS; (c) UV-fs-(Ti-sapphire) LA-ICP-MS.

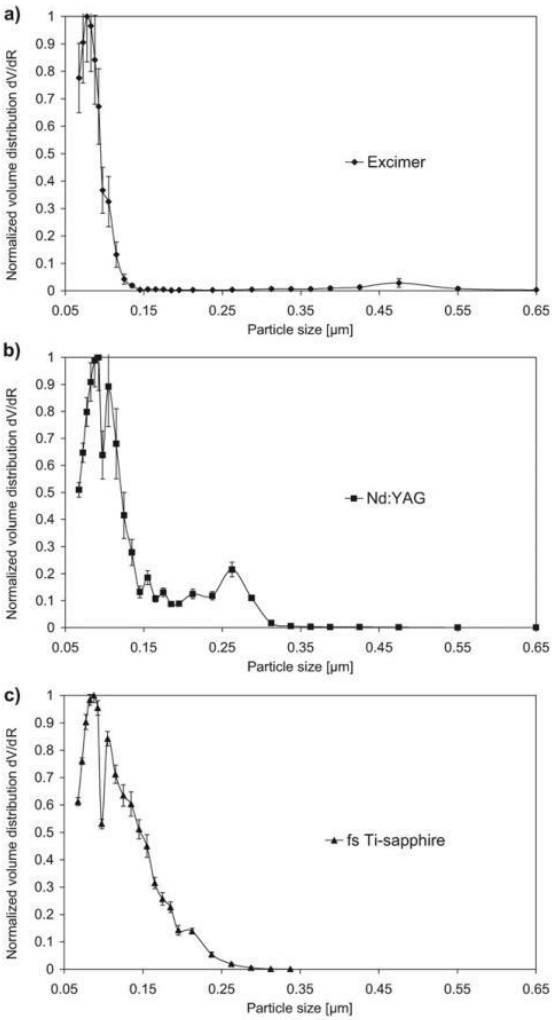

Fig. 3 Normalized particle size distribution of the generated aerosol measured after: (a) UV-ns-(ArF*)LA; (b) UV-ns-(Nd:YAG)LA; (c) UV-fs-(Ti-sapphire)LA.

laser-generated aerosols before entering the ICP-MS, the particle size distribution was studied in more detail.

Particle size distribution (PSD) of the transported aerosol

Fig. 3 (a,b,c) shows the normalized PSD of the aerosol generated from an Fe-based sample after UV ns- and fs-LA. Based on optical particle counter (OPC) experiments the volume distribution ($\mu m^3/\mu m$) was calculated and related to the particle diameter (µm). The volume distribution was normalized to its maximum to compare the relative PSD changes measured using the different lasers. The PSD obtained using both ns-LA systems produced a bimodal distribution, typically formed by agglomerates and melted spherical particles, which has been recently discussed by Hergenröder.[26,27] A first relative maximum of the PSD, representing the agglomerates, appeared at 75 nm (ArF*) and at 90 nm (Nd:YAG), while another maximum, representing the spherical molten particles, was determined at 475 nm and at 260 nm, respectively (further indications in Fig. 5). In contrast, the PSD measured using fs-LA showed a broad monomodal distribution. In this case, the aerosol predominantly consisted of agglomerates in the range of 50 up to 250 nm, with a maximum volume distribution at a particle size diameter of 90 nm. Incomplete vaporization of the large particles generated using UV-ns-LA within the ICP has been proposed to be responsible for elemental fractionation.[13,14] In order to reduce the number of large particles, it has been demonstrated that the aerosol can be filtered using a simple device. However, in good agreement with previous reports it was also observed (data not shown) that elements were not uniformly distributed within different particle size fractions after ablation of Fe-based samples using the Nd:YAG laser.

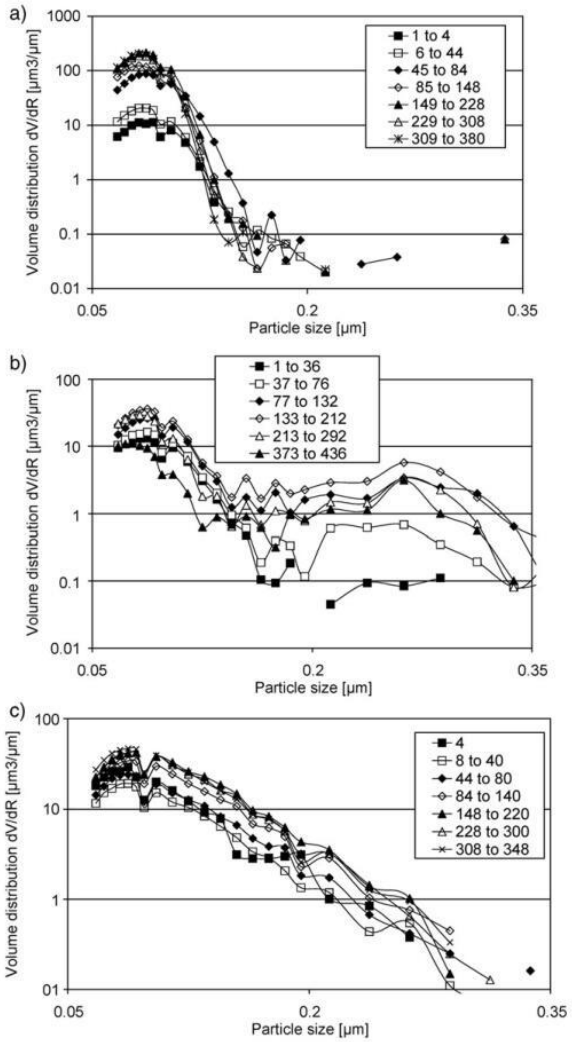

Fig. 4 Time-dependent variations of the particle size distribution (up to 350 nm), after different number of laser pulses obtained for an Fe metal sample using: (a) UV-ns-(ArF*)LA; (b) UV-ns-(Nd:YAG)LA; (c) UV-fs-(Ti-sapphire)LA.

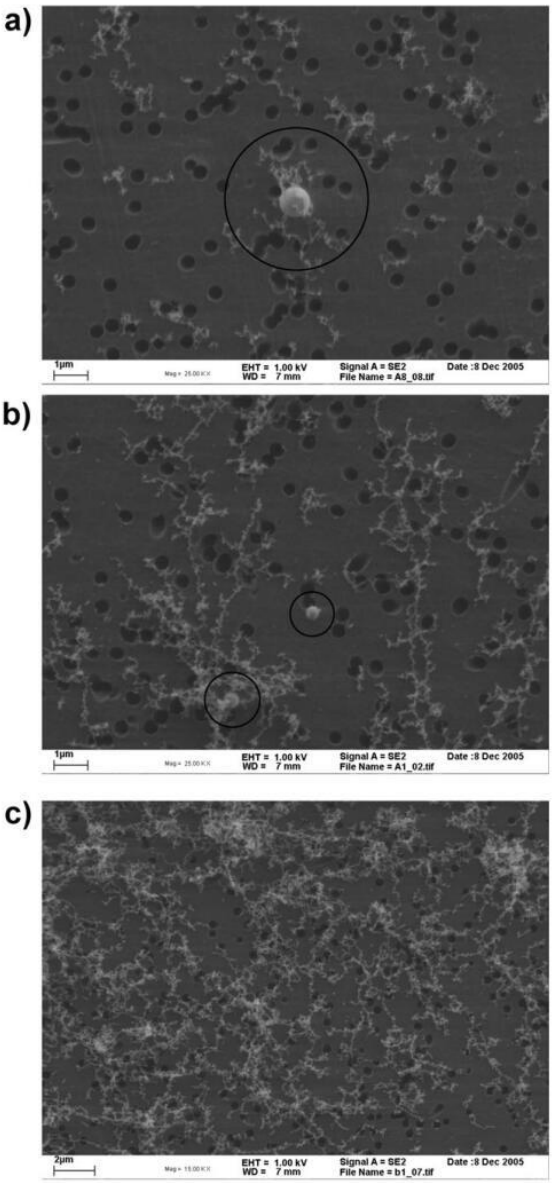

Fig. 5 Scanning electron microscope (SEM) images of the collected aerosol particles obtained for an Fe metal sample using: (a) UV-ns-(ArF*)LA; (b) UV-ns-(Nd:YAG)LA; (c) UV-fs-(Ti-sapphire)LA. These images show the different kinds of transported particles observed for each laser system but are not representative of the total transported mass.

Single hole drilling experiments

The PSD of the aerosol was studied at increasing crater depths using an Fe-based sample (increasing number of laser pulses). The ablation was stopped after 4 pulses and the PSD was determined based on OPC measurements. Fig. 4 (a,b,c) shows the time-dependent variations of the PSD at smaller particle sizes (up to 350 nm) obtained for an Fe-based sample using the ns- and fs-LA systems. Averaged values of increasing number of pulses were used to show the time-dependent variations in more detail.

It was observed that when using ns-ArF*LA the amount of transported material (related to the area below the PSD graph) increases by about 1 order of magnitude during the first 50 pulses. Small particles with a diameter <200 nm were predominant ($>99\%$). However, the small amount of larger particles reached sizes of up to $\varnothing$ 1 µm.

Temporal dependence of the PSD was different for the ns Nd:YAG laser. The amount of small (<200 nm) and big (200–400 nm) particles increased by a factor of 2 and by more than one order of magnitude, respectively, reaching a maximum after about 130 pulses. Small particles (<200 nm) were predominant ($>99\%$) during the first 40 pulses: afterwards the relative proportion of larger particles increased to about 10%.

At increasing number of pulses (>200 pulses) the amount of particles decreased and after 400 pulses the volume distribution was already half of the maximum. Using fs-LA, it was observed that the amount of transported material, formed only by particles smaller than 300 nm, slowly increased during the first 150 pulses to be constant afterwards. It can be seen that for the three laser systems the transported material (related to the ablated material of Fe-based samples) increased during the first laser pulses. Afterwards, the amount of transported material remained constant, except for the Nd:YAG laser, which showed a relative maximum of the volume distribution within the time interval studied.

Scanning electron microscope (SEM) analysis of the collected aerosol

In order to evaluate the size and morphology of the extracted aerosol particles, the generated aerosol was collected on filters and analyzed using a scanning electron microscope (SEM). The Fe-based sample was ablated at 4 Hz during 300 s using the ns- and fs-LA systems. The filters were placed in the transfer tube approximately 1 m behind the ablation cell to collect the aerosol particles and then placed on SEM-mounts using a conducting carbon tape. The accelerating voltage of the SEM electron gun was kept low (1 kV) to avoid charging effects on the uncoated filter. Fig. 5 (a,b,c) shows typical SEM images of the collected aerosol particles obtained for an Fe-based sample using the ns- and fs-LA systems. It was observed that using ns-ArF*LA, agglomerates and a few large molten spherical particles with diameters >400 nm were detected, which is in agreement with the PSD measurements. Moreover, using ns-Nd:YAG-LA the presence of agglomerates and molten spherical particles can be seen. However, their diameters were smaller in comparison with the particles collected at ablation with ArF* laser. In the case of fs-LA only agglomerates were observed, which compares well with the PSD measurements.

Therefore, aerosol structure, time dependent particle size measurements and the temporal EFI summarized in Table 3 indicate that an incomplete vaporization of particles for this type of matrix cannot be used as the argument for limited quantification capabilities.

Matrix and non-matrix matched quantitative analysis of Fe-based samples

To investigate the matrix and non-matrix matched calibration capabilities for the quantification of Fe-based samples, a stainless steel sample (SRM JK27A) was analyzed using a pure iron sample (SRM JK2D) and a silicate glass (SRM NIST 610) as calibration samples, respectively. Corrections for plasma instability and ablation yield were carried out by using ^{57}Fe as internal standard. Measured data were treated according to the protocol described by Longerich *et al.*[28] Data were acquired in runs of up to 20 analyses. Each run started and ended with two data acquisitions on a calibration material. Afterwards, LAMTRACE software was applied for data reduction and quantification. Table 4 (a,b,c) lists the reference and measured values of the elemental content, the relative standard deviations and the accuracy of the measured data obtained using the three pulsed laser ablation systems. Accuracy (%) was determined as the difference from the reference value.

Matrix matched calibration using a pure iron sample for the quantification of a stainless steel sample for both UV-ns-LA-ICP-MS (ArF* and Nd:YAG lasers) provided for most of the element deviations from the reference value of around 10%. Only some elements, such as Al or P, showed higher deviations from the reference values. Since all applied laser systems provide similar results, the RSD could be related to heterogeneous spatial distributions of these trace elements in the sample. Precision (RSD) was improved for the 4 ns Nd:YAG laser (2–10%) in comparison with the 15 ns ArF* laser (10–20%), with the exception of Al. At this point, it should be highlighted that when using UV-fs-LA-ICP-MS, the RSDs of all the elements were significantly reduced (1–4%) and the calculated concentrations deviated from the reference value by less than 2% (except for Al ~8%).

Non-matrix matched calibration for the quantification of a stainless steel sample was carried out using a silicate glass. This quantification approach represents one of the most extreme cases. The concentration of Fe in the stainless steel sample is about 661 400 μg g^{-1} (major element), while in the silicate glass is about 460 μg g^{-1} (trace element). Therefore, dual detector calibration was carried out to provide linearity between the pulse ($<10^6$ cps) and analog detection mode during data acquisition. Comparing the results obtained using matrix and non-matrix matched calibrations, similar RSDs were observed for the three laser systems. However, in the case of non-matrix matched calibration, the accuracy was significantly lower when using UV-ns-LA-ICP-MS. It was observed that using 15 ns ArF* laser the accuracy of the measured contents for all the elements decreased to values between 10–65%. The use of 4 ns Nd:YAG laser improved accuracy significantly to values in the order of 5–30%. Following this trend, it was demonstrated that the use of fs laser pulses allowed the non-matrix matched calibration analysis within (5–15%) of the reference values. Considering the particle size distribution generated on glass samples in comparison with the metal-like samples it becomes clear that two effects limit non-matrix matched calibration for quantitative analysis. The excimer laser (with the longest pulse duration) produces significantly smaller particles on the glass sample. Therefore, the calibration might represent the sample. However, due to the long pulse duration, the aerosol generated from the Fe based material has laser-induced alteration which leads to 10–60% deviations from the reference value. In contrast, the 266 nm Nd:YAG laser (6 ns) produces a broader particle size distribution during the glass ablation, which occurs most dominantly during the first seconds of ablation. Therefore, the calibration might be slightly biased. However, due to the shorter pulse duration the aerosol generated from the metal is less altered than that for the 15 ns laser and the overall deviation from the reference values is lower. This is in good agreement with results reported for both UV laser systems on brass. Finally, fs aerosol generation in glass is less wavelength dependent than is observed for a UV laser and produces also the most stoichiometric aerosols from metals. This combination leads finally to 5–15% deviation from the reference value.

Table 4 Elemental content values, relative standard deviations ($n = 6$) and accuracy values (bias from reference content) found for SRM JK27A using matrix and non-matrix matched calibration. (a) UV-ns (ArF*)-LA-ICP-MS; (b) UV-ns (Nd:YAG)-LA-ICP-MS; (c) UV-fs (Ti-sapphire)-LA-ICP-MS

(a)		ns-ArF* laser					
SRM JK27A		Matrix matched calibration with SRM JK2D			Non-matrix matched calibration with SRM NIST 610		
Element	Ref. content/μg g^{-1}	Content/μg g^{-1}	Precision RSD (%)	Accuracy (%)	Content/μg g^{-1}	Precision RSD (%)	Accuracy (%)
Al	169	171	16	1	274	13	62
Si	4110	4.23×10^3	9	3	6.56×10^3	10	60
P	222	167	21	25	252	18	13
Cr	167 600	1.77×10^5	7	6	2.25×10^5	8	34
Mn	15 890	1.67×10^4	12	5	2.58×10^4	11	62
Ni	120 400	1.09×10^5	9	10	1.42×10^5	11	18
Cu	1990	2.06×10^3	8	4	3.11×10^3	7	57
Mo	25 310	2.42×10^4	23	4	1.39×10^4	23	45

(b)		ns-Nd:YAG laser					
SRM JK27A		Matrix matched calibration with SRM JK2D			Non-matrix matched calibration with SRM NIST 610		
Element	Ref. content/μg g^{-1}	Content/μg g^{-1}	Precision RSD (%)	Accuracy (%)	Content/μg g^{-1}	Precision RSD (%)	Accuracy (%)
Al	169	195	20	15	217	21	28
Si	4110	4.34×10^3	5	6	4.99×10^3	3	21
P	222	259	6	17	234	10	6
Cr	167 600	1.65×10^5	2	1	1.89×10^5	8	13
Mn	15 890	1.52×10^4	3	4	2.04×10^4	7	29
Ni	120 400	1.18×10^5	3	2	1.19×10^5	2	1
Cu	1990	1.81×10^3	2	9	2.46×10^3	3	24
Mo	25 310	2.55×10^4	9	1	1.91×10^4	5	24

(c)		fs-Ti sapphire laser					
SRM JK27A		Matrix matched calibration with SRM JK2D			Non-matrix matched calibration with SRM NIST 610		
Element	Ref. content/μg g^{-1}	Content/μg g^{-1}	Precision RSD (%)	Accuracy (%)	Content/μg g^{-1}	Precision RSD (%)	Accuracy (%)
Al	169	156	2	8	188	12	11
Si	4110	4.10×10^3	2	0.2	4.35×10^3	2	6
P	222	220	4	1	212	2	5
Cr	167 600	1.66×10^5	2	1	1.60×10^5	3	4
Mn	15 890	1.59×10^4	1	0.4	1.52×10^4	3	4
Ni	120 400	1.20×10^5	3	0.1	1.14×10^5	3	5
Cu	1990	1.98×10^3	1	1	1.91×10^3	3	4
Mo	25 310	2.47×10^4	4	2	2.14×10^4	2	15

Therefore it could be well possible that deep UV-ns laser ablation with shorter pulse duration could provide very similar results to those obtained for fs laser ablation.

Conclusions

UV-ns-LA-ICP-MS (ArF* and Nd:YAG lasers) and UV-fs-LA-ICP-MS (Ti-sapphire laser) were investigated with the aim of describing their capabilities for quantitative analysis of Fe-based samples. It was observed that ablation of Fe-based samples using UV-ns-LA generated an aerosol with a bimodal distribution, formed by nano-sized agglomerates and micro-sized spherical molten particles. In the case of ns-ArF*-LA the proportion of larger particles was smaller but the sizes of these particles were up to 1 μm. In contrast, the aerosol generated by ultraviolet femtosecond laser ablation (UV-fs-LA) showed a broad monomodal particle size distribution (nano-sized agglomerates in the range of 50 up to 250 nm). Higher ion-signals and more stable elemental ratios were observed for UV-fs-LA-ICP-MS. Matrix and non-matrix matched quantitative analysis of Fe-based samples showed that the improved analytical performance in terms of precision and accuracy was achieved using shorter laser pulse durations. For instance, improved accuracy in non-matrix matched analysis was obtained for Nd:YAG-LA (4 ns) compared with ArF*-LA (15 ns) even at a lower fluence (8 *versus* 13 J cm^{-2}) and longer wavelength (266 *versus* 193 nm). However, this work shows that the pulse duration as provided by UV-fs-LA-ICP-MS and the reduced wavelength-dependence during glass ablation opens non-matrix matched calibration capabilities for the analysis of Fe-based samples by calibrating with SRM NIST 610 glass. However, and even more important, it also allows the use of other calibration materials containing elements which are currently limited (Ru, Rh, Pd, Ir, *etc.*) A promising result is that the determined concentrations deviate less than 10% from the reference value, which is, considering the differences in the concentrations of the internal standards, surprisingly good. However, a more detailed study on a variety

of matrices and better characterized materials will be necessary to validate and further improve the 10% bias from the reference values.

Acknowledgements

Financial support from Marie Curie Intra-European Fellowship (FP6-2004-Mobility 5) is greatly acknowledged. V. M. acknowledges the mobility program Erasmus/Socrates. V. K. and M. H. acknowledge the Ministry of Education, Youth and Sports of the Czech Republic for financial support through research plans MSM21622411 and MSM21622412. The authors thank Dr A. Bengtson for the supply of the samples.

References

1 B. Hattendorf, C. Latkoczy and D. Günther, *Anal. Chem.*, 2003, **75**(15), 341A–347A.
2 D. Günther and B. Hattendorf, *Trends Anal. Chem.*, 2005, **24**(3), 255–265.
3 G. C. Y. Chan, W. T. Chan, X. L. Mao and R. E. Russo, *Spectrochim. Acta, Part B*, 2001, **56**(1), 77–92.
4 R. E. Russo, X. L. Mao, O. V. Borisov and H. C. Liu, *J. Anal. At. Spectrom.*, 2000, **15**(9), 1115–1120.
5 H. R. Kuhn and D. Günther, *Anal. Chem.*, 2003, **75**(4), 747–753.
6 S. E. Jackson and D. Günther, *J. Anal. At. Spectrom.*, 2003, **18**(3), 205–212.
7 I. Rodushkin, M. D. Axelsson, D. Malinovsky and D. C. Baxter, *J. Anal. At. Spectrom.*, 2002, **17**(10), 1223–1230.
8 I. Rodushkin, M. D. Axelsson, D. Malinovsky and D. C. Baxter, *J. Anal. At. Spectrom.*, 2002, **17**(10), 1231–1239.
9 S. H. Jeong, O. V. Borisov, J. H. Yoo, X. L. Mao and R. E. Russo, *Anal. Chem.*, 1999, **71**(22), 5123–5130.
10 D. B. Aeschliman, S. J. Bajic, D. P. Baldwin and R. S. Houk, *J. Anal. At. Spectrom.*, 2003, **18**(9), 1008–1014.
11 M. Guillong and D. Günther, *J. Anal. At. Spectrom.*, 2002, **17**(8), 831–837.
12 J. Koch, A. von Bohlen, R. Hergenröder and K. Niemax, *J. Anal. At. Spectrom.*, 2004, **19**(2), 267–272.
13 H. R. Kuhn and D. Günther, *J. Anal. At. Spectrom.*, 2004, **19**(9), 1158–1164.
14 C. Y. Liu, X. L. Mao, J. Gonzalez and R. E. Russo, *J. Anal. At. Spectrom.*, 2005, **20**(3), 200–203.
15 M. Guillong, I. Horn and D. Günther, *J. Anal. At. Spectrom.*, 2003, **18**(10), 1224–1230.
16 V. Margetic, A. Pakulev, A. Stockhaus, M. Bolshov, K. Niemax and R. Hergenroder, *Spectrochim. Acta, Part B*, 2000, **55**(11), 1771–1785.
17 F. Poitrasson, X. L. Mao, S. S. Mao, R. Freydier and R. E. Russo, *Anal. Chem.*, 2003, **75**(22), 6184–6190.
18 C. Liu, X. L. Mao, S. S. Mao, X. Zeng, R. Greif and R. E. Russo, *Anal. Chem.*, 2004, **76**(2), 379–383.
19 R. E. Russo, X. L. Mao, J. J. Gonzalez and S. S. Mao, *J. Anal. At. Spectrom.*, 2002, **17**(9), 1072–1075.
20 B. N. Chichkov, C. Momma, S. Nolte, F. von Alvensleben and A. Tunnermann, *Appl. Phys. A: Mater. Sci. Process.*, 1996, **63**(2), 109–115.
21 Q. Z. Bian, J. Koch, H. Lindner, H. Berndt, R. Hergenröder and K. Niemax, *J. Anal. At. Spectrom.*, 2005, **20**(8), 736–740.
22 Q. Z. Bian, C. C. Garcia, J. Koch and K. Niemax, *J. Anal. At. Spectrom.*, 2006, **21**(2), 187–191.
23 J. Koch, M. Wälle, J. Pisonero and D. Günther, *J. Anal. At. Spectrom.*, 2006, **21**, 932–940.
24 H. R. Kuhn, J. Koch, R. Hergenröder, K. Niemax, M. Kalberer and D. Günther, *J. Anal. At. Spectrom.*, 2005, **20**(9), 894–900.
25 B. J. Fryer, S. E. Jackson and H. P. Longerich, *Can. Mineral.*, 1995, **33**, 303–312.
26 R. Hergenröder, *J. Anal. At. Spectrom.*, 2006, **21**, 505–516.
27 R. Hergenröder, *Spectrochim. Acta, Part B*, 2006, **61**, 284–300.
28 H. P. Longerich, S. E. Jackson and D. Günther, *J. Anal. At. Spectrom.*, 1996, **11**(9), 899–904.

PAPER 5

Feasibility of Nanoparticle-Enhanced Laser Ablation Inductively Coupled Plasma Mass Spectrometry

Holá, M., Salajková, Z., Hrdlička, A., Pořízka, P., Novotný, K., Čelko, L., Šperka, P., Prochazka, D., Novotný, J., Modlitbová, P., Kanický, Kaiser, J.

Analytical Chemistry. 2018, 90(20), 11820–11826. DOI 10.1021/acs.analchem.8b01197

Contribution:

Design of experiments, LA-ICP-MS measurements, data evaluation, manuscript writing.

analytical chemistry

Article

Cite This: *Anal. Chem.* 2018, 90, 11820−11826

pubs.acs.org/ac

Feasibility of Nanoparticle-Enhanced Laser Ablation Inductively Coupled Plasma Mass Spectrometry

Markéta Holá,[†,‡] Zita Salajková,[§] Aleš Hrdlička,*[,†,‡] Pavel Pořízka,[§] Karel Novotný,[†,‡] Ladislav Čelko,[§] Petr Šperka,[∥] David Prochazka,[§] Jan Novotný,[§] Pavlína Modlitbová,[§] Viktor Kanický,[†,‡] and Jozef Kaiser[§]

[†]Department of Chemistry, Faculty of Science, Masaryk University, Kotlářská 267/2, 611 37 Brno, Czech Republic

[‡]Central European Institute of Technology (CEITEC), Masaryk University, Kamenice 753/5, 625 00 Brno, Czech Republic

[§]Central European Institute of Technology, Brno University of Technology, Purkyňova 656/123, 612 00 Brno, Czech Republic

[∥]Institute of Machine and Industrial Design, Faculty of Mechanical Engineering, Brno University of Technology, Technická 2896/2, 616 69 Brno, Czech Republic

ABSTRACT: Nanoparticles (NPs) applied to the surface of some solids can increase signals in inductively coupled plasma mass spectrometry (ICPMS). Drops containing 20 and/or 40 nm nanoparticles of Ag and/or Au were deposited on metallic and ceramic/glass samples, and after being dried, both the samples treated with NPs and plain targets were ablated by one pulse per spot. The laser ablation ICPMS (LA-ICPMS) signals were enhanced for metallic samples modified with NPs in comparison to signals produced at the plain, untreated surface. Maps of LA-ICPMS signals recorded for several laser fluences show that the NP-induced signal enhancement exceeds even 2 orders of magnitude for metallic samples. No enhancement was achieved for nonconductive samples. This enhancement is limited to the peripheral annular region of the dried droplet area where NPs are concentrated due to the "coffee stain" effect. Ablation crater profilometric inspection revealed a more uniform material rearrangement over the NP-treated surface compared with the ablated plain target. However, besides a smoother crater bottom, no other evidence of an NP-enhancing effect was noticed, although an increased ablation rate was anticipated. Limits of detection dropped by 1 order of magnitude for the minor elements in the presence of NPs. Observed phenomena depend only on the NP surface concentration but not on the material or size of the NPs. An electron microprobe study of the collected ablation aerosol has shown that aerosol particles consisting of target material are aggregated around the NPs. The hypothesis is that such aggregates exhibit better transport/vaporization efficiency, thus enhancing signals for metallic samples. A detailed study of the suggested mechanism will be continued in ongoing work.

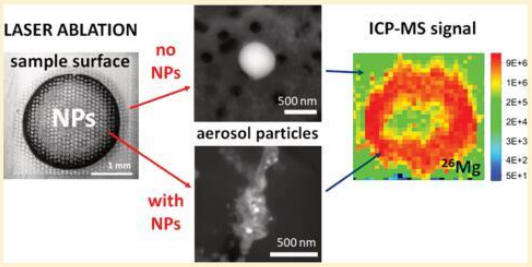

Laser ablation (LA) became an effective and widespread sampling technique for analysis of mainly solid samples. Numerous modifications have been developed during the past four decades. Laser beam interaction with a target causes release of material in a form of vapor and liquid or solid particles, finally creating dry aerosol, which is introduced into an inductively coupled plasma source for mass or optical emission spectrometry (ICPMS or ICPOES).[1] Another laser−sample interaction effect is microplasma formation, which in situ atomizes and ionizes the sample. This principle is the basis for laser-induced breakdown spectroscopy (LIBS).[2] Apart from the discussion about the pros and cons of both methods, which can be found reviewed elsewhere,[3−5] it is necessary to emphasize a permanent effort to improve the sensitivity and limits of detection (LODs). Each analytical method can be subjected to a certain optimization for achieving better sensitivity and LOD; nevertheless, the best yielded values are limited by a particular instrumentation and physical limits. Namely, the level of the collected useful radiation presented as a signal-to-background ratio is lowered by the presence of a strong radiation continuum such as Bremsstrahlung for LIBS, ICPOES, and other OES techniques. On the other hand, the MS detection is disturbed practically only by the detector noise and nonanalyte particles (flying in the inner space) or energetic particles (coming from the outer space of the mass spectrometer). The latter must not be confused with interference of different ions with similar or the same m/z.

Signal enhancement in the presence of nanoparticles (NPs) has been observed and used for many years in surface-enhanced Raman spectroscopy (SERS). The main effect is supposed to be an intensification of the local electric field induced by incident photons on edges, tips, NPs, and other nanostructures on the surface, which could even be amplified by a surface plasmon resonance.[6−9] In any case, a strong electric field is formed in the gap between the NP and the

Received: March 16, 2018
Accepted: August 21, 2018
Published: August 21, 2018

DOI: 10.1021/acs.analchem.8b01197
Anal. Chem. 2018, 90, 11820−11826

substrate plain,[10] enhancing the emission of seed electrons. It was also found that NPs are fragmented into smaller ones under laser irradiation on a 0.1 ns time scale for gold and on a femtosecond time scale for TiO_2 NPs. This change of their dimensions influences the resulting signal amplification.[11] Moreover, another effect of the ion signal enhancement has been observed and used in laser desorption ionization (LDI) techniques. Thermal mechanisms are more dominant for low irradiances in LDI than for high irradiances (10^9 W cm^{-2}) in LA. Very important is the heat transfer influenced by the thermal conductivity of the NPs.[12]

Efforts to obtain signal enhancement have led to the use of NPs also in the field of LIBS. The first study presented a signal increase by the presence of NPs on the sample surface in LIBS of nondesiccated plant leaves.[13] Without NPs, the yielded LODs were inferior compared to those for ICP. Later, the following two aspects were theoretically suggested and experimentally confirmed with nansecond Nd:YAG lasers: the ablation threshold is significantly lowered on metallic materials,[14] and the magnitude of signal amplification induced by the presence of NPs depends on the diameter of the NPs, distances between the NPs, the incident laser wavelength, and the irradiance.[15−17] However, the 2-fold amplification for the lines Cu(I) 510.6, 515.32, 521.86, and 578.29 nm was also observed on a copper target using a 50 fs laser.[18] An intensification of the molecular bands of the AlO $B^2\Sigma^+ \rightarrow X^+\Sigma^+$ band system was also observed while using AgNPs.[19] The amplification of the band emission at longer gate delays—around 50 μs—was due to the higher primary concentrations of Al atoms enhanced by the NP surface effects mentioned above. The LIBS sensitivity and LODs in analysis of solutions were substantially enhanced by two effects: the preconcentration effect of drying a solution drop on a substrate and the NP effect, when NPs were deposited onto the substrate prior to the sample drop.[20] A recent study on the effect of AgNPs with combination of lowered pressure in air showed the best NP-induced signal enhancement at a pressure of 400 mbar for the Pb(I) 405.78 nm line.[21] Among the other parameters, such as the gate delay and the pulse energy, it was only the ambient pressure which dominantly influenced the signal enhancement by NPs.

An optimization of the LA process, namely, part of a laser−sample interaction, lies in the elimination or substantial suppression of matrix effects, the production of regular craters (best smooth cylinder without any melting and cracks), and the best level of the analytical signal. To fulfill these requirements, short laser pulses, short lasing wavelengths, and a sufficiently high irradiation are recommended. This is because of a shorter penetrating depth and a shorter heat propagation path in the sample body. Nonthermal ablation is thus required to reduce selective evaporation.[5,22,23] These items are mostly valid for both LIBS and LA-ICPOES/ICPMS techniques. While the irradiation could be relatively easily controlled and optimized, the laser wavelength depends on the quality of a particular laboratory's equipment. Furthermore, the LA process should ideally produce an aerosol. Its particles' elemental composition should fully reflect the elemental composition of the original sample, i.e., a stoichiometric representation of the sample.[5] This requirement applies mainly to LA-ICPOES/ICPMS. To fulfill this requirement, the particle size distribution of the aerosol must allow the complete evaporation of the particles in ICP. Also, the ablation cell flushing and transport tubing should not change the particle transport efficiency by their size and composition.[22] The particles' sizes and their size distribution are strongly influenced by the laser parameters, the sample properties, and the ablation atmosphere (gas, pressure).[5] There are also fluctuations in the arrival time and the size of individual ablated particles transported to the ICP.[24]

Surface phenomena in LA-ICPMS have been studied in terms of aerosol redeposition around the ablation crater.[25] The redeposition is efficiently reduced by the use of a helium atmosphere instead of an argon one. Also, the sensitivity of the LA-ICPMS analysis increases. The difference between the ablation yielded from the first pulse on the fresh surface and the one yielded from other pulses may not be as critical as in the case of LIBS. The reason is that the aerosol formation, its flush out of the interaction cell, and its dispersion in the tubing between this cell and ICP lead mostly to a mix of material from several pulses. Besides, the sample surface is often pretreated to obtain a smooth area. However, monitoring the signal peaks from individual pulses (i.e., mapping the sample surface) at a low repetition rate is possible.[26]

Although NPs in solution are nowadays routinely analyzed with ICPMS (so NPs are the analyte), their effects on the ablation of the sample surface have not been investigated yet. Therefore, our work aims to demonstrate the effect of silver and gold NPs on the measured LA-ICPMS signal of elements which are constituents of smoothed reference aluminum alloy, brass, glass, and glaze samples.

EXPERIMENTAL SECTION

The used equipment consisted of an Agilent 7500ce (Agilent Technologies, United States) ICP mass spectrometer with a quadrupole analyzer and an octopole reaction cell. This instrument was operated at the forwarded power of 1500 W, Ar gas flow rates of 15 (outer plasma gas) and 0.7 (auxiliary) L min^{-1}, He carrier flow rate of 1.0 L min^{-1}, and Ar makeup gas flow rate of 0.6 L min^{-1}. The ablated material was transported through a polyurethane tube (i.d. 4 mm, length 1 m) to the ICPMS system. For minor elements (isotopes ^{208}Pb, ^{63}Cu, ^{26}Mg, and ^{57}Fe), the dwell time per isotope was adjusted to 0.1 s and for major elements (isotopes ^{27}Al and ^{107}Ag) to 0.01 s. The total length of one cycle was then 0.246 s. Laser ablation was performed with a New Wave UP 213 system (New Wave Research, Fremont, CA) equipped with a frequency-quintupled pulsed Nd:YAG laser emitting a wavelength of 213 nm at a pulse duration of 4.2 ns fwhm with a flat-top beam profile and a helium-flushed *xyz* movable supercell. We chose an ablation spot of 100 μm diameter to ensure a sufficient isotopic signal and a representative area containing NPs on the sample surface. The line scan was performed, with an ablation speed of 0.5 mm s^{-1} at a repetition rate of 5 Hz, i.e., a chain of adjacent 100 μm ablation spots was produced, and the NP area was crossed by about 25−32 ablation spots close to the equator. The applied pulse energy was varied corresponding to the needs of the experiment so that the fluences were 4.5, 3.7, 3, 2, 1, 0.4, 0.3, and 0.2 J cm^{-2}.

The shape, structure, and composition of laser-generated particles were studied after their collection on a polycarbonate membrane filter (25 mm in diameter and 0.2 μm pores, Cyclopore, Whatman) using scanning electron microscopy (SEM; Mira 3, Tescan Orsay Holding, Tescan Brno, Czech Republic; 10 kV, backscattered electron mode).

DOI: 10.1021/acs.analchem.8b01197
Anal. Chem. 2018, 90, 11820−11826

The shapes and profiles of ablation craters were studied with an optical 3D microscope (Contour GT-X8, Bruker, United States).

Aluminum alloy AW 2030 was used as a model sample. The composition was (wt %) Al (92), Cu (3.9), Pb (1.2), Mg (0.8), Mn (0.6), and Fe (0.1). The sample surface was carefully polished (FEPA 800, 1000, 4000, diamond pastes 3 and 1 μm, cleaned with IPA) prior to the application of drops containing NPs. A drop corresponded to 5 μL of a water suspension containing spherical NPs and was freely dried in the open air onto the sample surface. Typically, the created drop was shaped in an almost circular area with a diameter of about 2.7–3 mm.

Other materials has been tested to study the effects of the physical properties on the signal enhancement: alloy AW 6082, Al (97 wt %), Cu (<0.1 wt %), Pb (<0.003 wt %), Mg (0.9 wt %), Mn (0.7 wt %), Si (1.0 wt %), and Fe (0.1 wt %); brass MBH, Cu (62.1 wt %), Zn (35.3 wt %), Pb (1.3 wt %), Al (0.4 wt %), Fe (0.3 wt %), and Ni (0.3 wt %); certified glass standard reference material (SRM) NIST 610 as commonly used material for LA-ICPMS calibration; ceramic glaze tile L600 (Keramika HOB in Horni Briza, Czech Republic, as a subsidiary of Lasselsberger Co.).[27]

Two types of spherical nanoparticles (Ag and Au) in two sizes (20 and 40 nm) were used (citrate, NanoXact, Nanocomposix, United States; mass concentration for Ag ~30 ng mL^{-1} and for Au ~50 ng mL^{-1}).

RESULTS AND DISCUSSION

The investigation of the NPs' influence on laser ablation brings numerous questions. In the present study, we aim to launch basic information regarding a possible influence of NPs on the LA-ICPMS signal. In other words, we investigate whether the presence of NPs on the surface of the sample changes the measured intensities of the isotopes and whether NPs eventually alter the laser sampling process.

The experimental approach is best illustrated by Figure 1. A rectangular matrix of ablation spots was created so that the matrix covered the NP area. The measured time signal sections of the isotopes were assigned to the particular ablation spots.

Each elemental color map (deep red as maximum, dark blue as minimum, or black as zero) is also accompanied by the numerical scale to compare the absolute isotopic intensities of the elements.

The signal enhancement of individual analytes was observed only for metallic samples (Al alloys and brass). The NP layer did not bring any improvement for LA-ICPMS of non-conductive materials such as glass or ceramics. As a model example for the experiment, aluminum alloy AW 2030 was used. The influence of the nanoparticle type (composition and size) and the laser fluence is discussed below.

Four kinds of NPs were investigated (40 nm Ag, 20 nm Ag, 40 nm Au, and 20 nm Au), but the yielded results are very uniform. Therefore, we demonstrate the analysis of the NPs' influence on the aluminum alloy sample with 40 nm AgNPs.

The droplet photo and the distribution of the Ag intensity show that the NP distribution is more uniform than the distribution of any other element intensity. It can be clearly seen (Figures 1 and 2) that the highest intensities correspond to the highest NP concentration in the droplet peripheral parts (due to the coffee stain effect). Regardless of the fluence, the central part of the droplet provides substantially lower element signals than the droplet ring. The signal enhancement is thus a

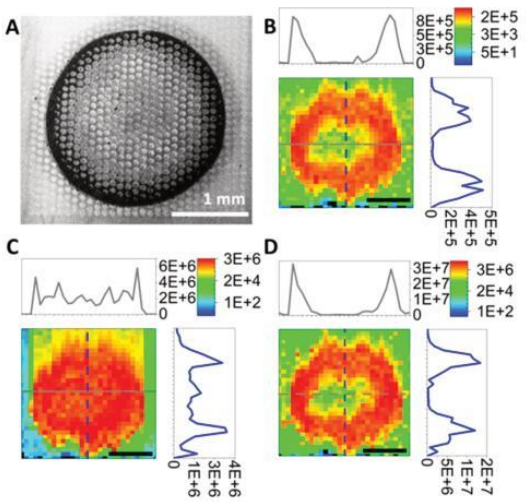

Figure 1. Photograph of the ablated area with a dried drop of 40 nm AgNPs and craters on the aluminum alloy (AW 2030) sample for a fluence of 4.5 J cm^{-2} (A) and intensity maps with *xy* cross-sections for Mg (B), Ag (C), and Pb (D).

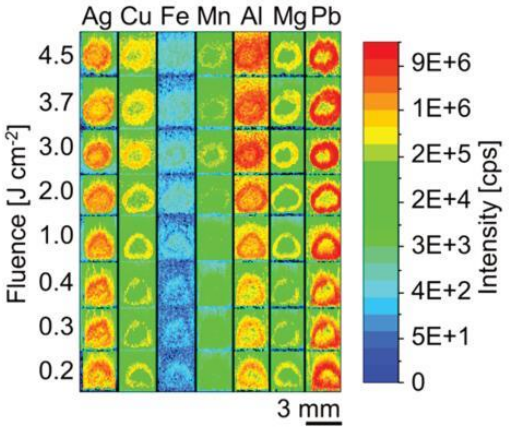

Figure 2. LA-ICPMS intensity maps of the selected elements for the droplet with 40 nm AgNPs and its rectangular vicinity for fluences of 0.2–4.5 J cm^{-2} on the aluminum alloy (AW 2030).

nonlinear function of the Ag NP concentration. The enhancement amplitude can exceed 2 orders of magnitude in the ring with the highest NP concentration.

The threshold NP concentration from which the element signals are enhanced can be simply estimated by visual inspection of the analyte element signal (Pb, Mg, Cu, ...) and Ag or Au signals (cps) in the 2D maps and selected cross-sections from the maps (examples of the maps and cross-sections can be seen in Figure 1). First, it is necessary to recalculate the Ag or Au cps signal to the local concentration of NPs. On the basis of the knowledge of the total NP number in the deposited droplet, which is merely equal to the product of the pipetted droplet volume and the NP concentration declared by the manufacturer, the single NP-related intensity of the Ag or Au signal was obtained by dividing the sum of all measured Ag intensities (cps) over the dried droplet area by

DOI: 10.1021/acs.analchem.8b01197
Anal. Chem. 2018, 90, 11820–11826

the total number of NPs in this droplet. Now we know "how many cps's correspond to one NP". Supposing a linear dependence of the Ag or Au signal (cps) on the number of AgNPs or AuNPs (may not be completely fulfilled for a high cps), the Ag or Au 2D intensity map of the dried droplet can be converted to the concentration of NPs, c(AgNPs or AuNPs). It follows from the experiment that 0.3 NP corresponds to 1 cps. Finally, the moment of the sudden increase of the analyte element signal in the cross-section profile can be read as well as the corresponding Ag or Au signal. This moment corresponds to $(3-4.5) \times 10^5$ NPs per analyzed 0.1×0.1 mm^2 square. The threshold density is then $(3-4.5) \times 10^7$ NPs mm^{-2}. However, the yielded value suffers from considerable uncertainty. We are currently not able to responsively present precise data to provide differences among various elements, fluences, and materials. More accurate results could be obtained from a set of new special experiments with a much better defined surface concentration of NPs and a larger ablated area with a constant c(NPs) for better statistics.

Ablation craters are clearly distinct at fluences exceeding about 3 J cm^{-2}. The limit of crater observation is at a fluence of 1 J cm^{-2}. Craters are very poorly recognizable at fluences of 0.4–0.2 J cm^{-2}. The craters were measured with a scanning electron microscope in the backscattered electron (BSE) mode (Figures 3 and 4) and an optical profilometer (Figure 5) to find the differences in their structure, which could eventually be dependent on the presence of NPs. At fluences of 1 J cm^{-2} and less, the profiles were not measurable. At fluences of 3–4.5 J cm^{-2}, it could be stated that the ablation with NPs on the surface created more regular and smoother crater profiles than the one without NPs present (depicted for 4.5 J cm^{-2} in Figures 3–5). For a fluence of 1 J cm^{-2}, the crater profile is nearly not resolvable from the surrounding untouched surface without NPs. The crater SEM picture in Figure 3A shows the single pulse ablated surface on the aluminum sample without NPs (A) and with NPs (B) and details of the craters without NPs (C) and with NPs (D). The situation on the drop boundary is illustrated by Figure 4. The crater area consists of two strictly separated parts. The splashed area is without NPs, and the smooth area is with NPs. These results from SEM-BSE are supported by optical profilometry (Figure 5). The black line marks the scanning path for the surface without NPs (A) and with NPs (B) at a fluence of 4.5 J cm^{-2}. Craters and the

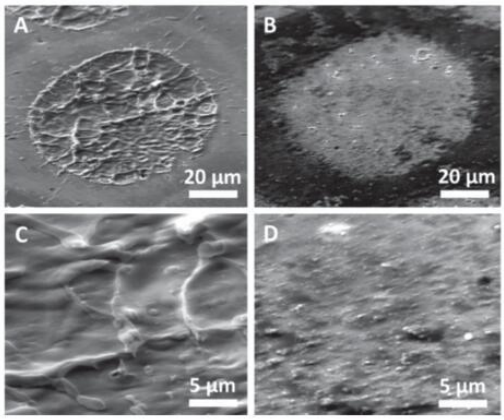

Figure 3. Crater images by SEM-BSE for a fluence of 4.5 J cm^{-2} without NPs (A) and with AgNPs (B) and crater detail without NPs (C) and with AgNPs (D).

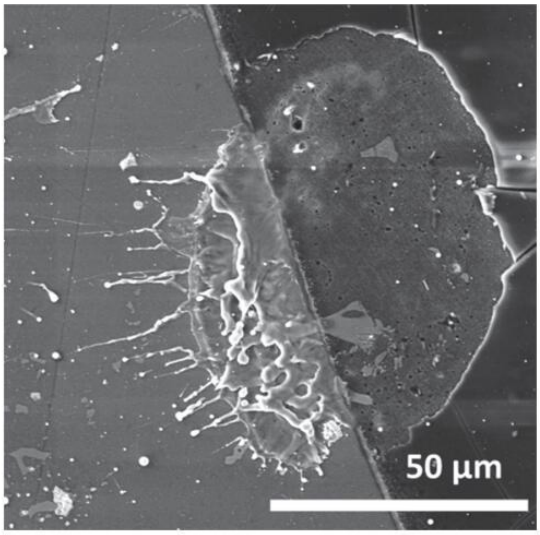

Figure 4. Crater images by SEM-BSE for a fluence of 4.5 J cm^{-2} on the interface of the droplet with 40 nm AgNPs (right) and the surface without NPs (left).

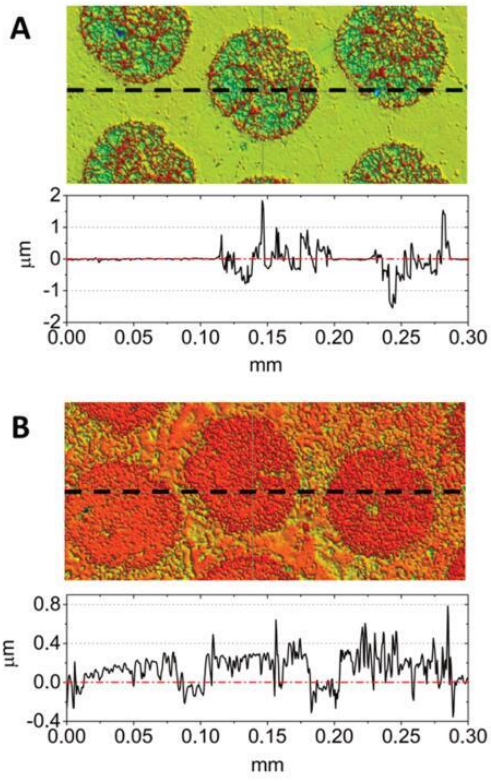

Figure 5. Crater images and sections of the sample AW 2030 by optical profilometry for a fluence of 4.5 J cm^{-2} without NPs (A) and with 40 nm AgNPs (B).

DOI: 10.1021/acs.analchem.8b01197
Anal. Chem. 2018, 90, 11820–11826

adjacent surface morphology are better visible in Figure 5, which demonstrates that the presence of NPs apparently makes the craters a little bit smoother and the material is less splashed.

Once more, it can be said that the material rearrangement is substantially more uniform thanks to the presence of NPs. A question remains about the exact mechanism involved. Some mechanisms are reviewed in the Introduction. However, these mechanisms were described in the frame of immediate laser–material interaction. Such interaction demonstrates itself in LIBS, but LA-ICPMS measurement reflects changes of the transported aerosol.

The second step in the investigation of the NPs' influence on LA-ICPMS is thus calculation of the LOD. Also, in this aspect, we can infer that the ablation through NPs also has a very positive effect not only on the measured isotopic intensities but also on the LOD for the minor elements in the alloys. This can be a very useful finding in the determination of minor and trace elements. The calculated 3σ values are presented in Table 1. The presented values are

Table 1. LODs ($\mu g\ g^{-1}$) for Different Fluences (J cm^{-2}) without and with 40 nm AgNPs (Sample AW 2030)

fluence	Mg	Mn	Fe	Cu	Pb
		Without NPs			
0.2	120	440	1300	5400	4.9
0.3	110	360	970	4800	4.0
0.4	50	190	730	2500	2.2
1.0	42	87	440	1100	1.5
2.0	51	51	450	580	2.5
3.0	60	35	350	450	2.1
3.7	30	26	250	340	1.7
4.5	46	23	270	280	3.0
		With 40 nm AgNPs			
0.2	3.3	73	750	250	0.15
0.3	5.5	77	610	430	0.29
0.4	5.2	60	490	370	0.27
1.0	2.8	30	280	220	0.15
2.0	2.9	20	170	160	0.16
3.0	1.7	11	120	84	0.10
3.7	1.9	14	140	110	0.11
4.5	1.9	12	130	98	0.12

calculated for all the minor elements in the aluminum alloy (AW 2030) sample with 40 nm AgNPs for brevity, but very similar results were also obtained for other NPs and the brass MBH sample. The calculation of the LOD with NPs is based on the average intensity of the particular isotope in the ring of maximum intensities (Figure 1B–D). Although the LOD is generally influenced by a big error, the yielded differences between the surfaces without and with NPs mostly exceed 1 order of magnitude. There is no doubt that the observed LODs are statistically significant. The absolute values of the LOD both with and without NPs are relatively high, but it should be taken into account that the measurement was done by the system of one pulse per fresh spot. The material intake was thus very limited. However, the resulting structure is very clear and expectable. The LODs also decrease with increasing fluence.

The third step of our work aims to explain the observed phenomena on the microscopic scale. To do this, an additional SEM analysis was performed to explain some experimental facts (Figure 6). The structure of the aerosol generated by the laser ablation of a sample with/without 20 nm AgNPs was

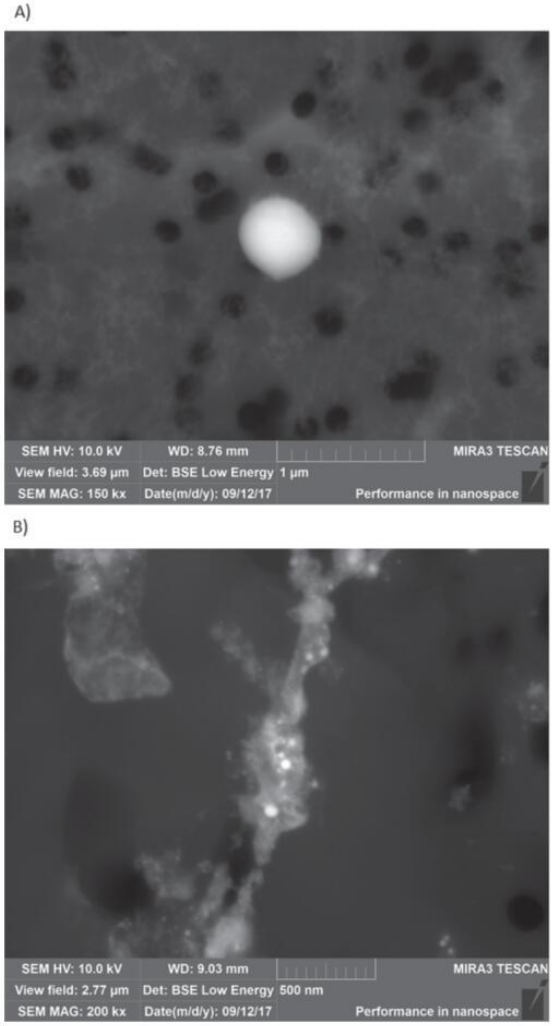

Figure 6. Images of aerosol particles captured on the filter at a fluence of 1 J cm^{-2} (A) without and (B) with NPs on the surface (sample AW 2030).

studied by SEM and energy-dispersive spectroscopy (EDS) after having done a particle collection on filters. A fluence of 1 J cm^{-2} was used to collect a sufficient amount of particles after 20 min of ablation. Two different particle generation mechanisms are typical for a nanosecond laser ablation: first, a condensation of small particles (tens of nanometers) from the vapor and, second, a direct ejection of droplets.[26,28] The condensed aerosol particles create clusters with a size typically up to 300 nm.[29] This statement is proved by Figure 6A (concerning the ablation of a sample without NPs). The aerosol contains condensed small particles creating agglomerates and large spherical particles (up to micrometers in diameter) arisen from droplet solidification. The EDS analysis showed a fractionation effect typical for nanosecond ablation:

DOI: 10.1021/acs.analchem.8b01197
Anal. Chem. 2018, 90, 11820–11826

volatile elements are preferentially vaporized and condensed to primary small particles (Pb, Mg) that agglomerate together. Large spherical particles arose directly from the melted material enriched with low-volatility elements (Cu), as shown in Table 1. Al, which was the main component of the alloy (92 wt %), was distributed homogeneously in both types of particles. The investigation of aerosol formed by laser ablation of the alloy covered by Ag nanoparticles proved a different mechanism of laser−sample interaction.

The aerosol was comprised of two types of particles, but the structure and composition were different compared to those from the ablation of a plain alloy surface. The spherical particles were also present, but they were much smaller; the dominant size was a diameter of around 20 nm (Figure 6B). The size corresponded to the original size of AgNPs in the solution, so it could be considered as a direct release of the NPs (or their part) from the surface without evaporation and without any following condensation process. The spherical particles were surrounded by agglomerated particles, creating compact clouds on the filter. The EDS analyses of different particle structures done for aerosol proved a higher content of Ag in the spherical particles. All results of EDS analysis are summarized in Table 2. The ratios were calculated from five

Table 2. Ratios of Element Content (Spherical Particles per Nanoparticle Conglomerate) (Sample AW 2030)

alloy composition and boiling points of the elements			spherical/agglomerated particle mass ratio of each element	
element	element content (wt %)	BP (°C)	no NPs	with NPs
Ag	–	2162	–	1.8 ± 0.5
Al	92	2519	1.0 ± 0.4	0.58 ± 0.19
Cu	3.9	2562	7.5 ± 2.4	0.19 ± 0.12
Mg	0.9	1091	0.8 ± 0.3	1.1 ± 0.5
Pb	1.2	1749	0.24 ± 0.14	1.1 ± 0.4

average values (five points on different particles of the same type); the uncertainty values are caused by high relative standard deviations (up to 40%) of the measurements due to the irregular sample surface. Consequently, the accumulation of Ag in this type of particle was conclusive even though the results were influenced by the surrounding agglomerates. The results may indicate the theory that the spherical particles mainly composed of the AgNPs in their original form serve as a condensation core for other compounds.

Comparing the role of the individual components/elements in the particle formation is very hard because the properties and composition of the alloy surface layer change with the application of NPs (so we analyze different samples, comparing them to the original). However, the EDS analysis shows more volatile elements (Mg, Pb) distributed homogeneously in all particles, while the incidence of low-volatility compounds (Cu, Al) is mainly detectable in agglomerates (Table 2). This indicates some connection between nanoparticles and more volatile compounds, which probably supports ICPMS signal enhancement, as we observe the best results for Pb (see Figure 2 or Table 1. On the other hand, the enhancement works also for higher volatility elements (Cu). This can be attributed to the better evaporation efficiency of smaller particles in ICP that are enriched mainly of Cu, while during plain sample surface ablation Cu accumulates mainly in the large spherical particles not completely vaporized in ICP. This implies that signal enhancement is individual for each sample compound and is dependent on its physical properties (influences aerosol formation), definitely fractionation during particle transport and in ICP.

In any case, it was shown that the character of the aerosol is altered by the presence of NPs on the sample surface. We suppose that NPs change the element fractionation because each isotope shows a different enhancement. The observed absolute differences in the signal enhancement are greater for lower fluences (in this case, only the fluence of 4.5 J cm^{-2} approaches the irradiation of 1 GW cm^{-2}). This fact is in accordance with the known theory which states that non-stoichiometric ablation has greater effect at lower irradiances.

■ CONCLUSION

It was experimentally proved that, regardless of the NP material (Ag, Au) and size (20 or 40 nm), NPs on the used aluminum and brass sample surfaces are capable of causing a substantial signal enhancement during an LA-ICPMS analysis. This phenomenon was shown on ^{208}Pb, ^{63}Cu, ^{26}Mgn and ^{57}Fe signals. The signal enhancement is conditioned by the conductivity of the sample as it has not been observed for nonconductive materials such as glass or ceramics. For the given lasing wavelength of 213 nm, the best signal enhancement exceeds 2 orders of magnitude in the peripheral annular region of the dried droplet area where the highest NP concentration occurs. These positive results on metallic targets may indicate some involvement of the surface plasmon resonance and intensification of the electric field between the NPs and the surface. On the other hand, the ICPMS signal increases with the surface NP concentration monotonously, which is not typical for the surface plasmon resonance, where emission decreases over a critical NP concentration.[15−17] The corresponding 3σ LODs are decreased by about 1 order of magnitude in the presence of NPs. Crater formation and the character of the aerosol particles found by profilometric and SEM measurements indicate that there is no evidence of enhanced material removal in the presence of NPs but the ablation single-pulse crater is smoother on the surface with NPs. It also proves that aerosol particles of the metallic target probably condense/aggregate on the NPs as cores. In such a way, aggregated particles exhibit better transport/vaporization efficiency and thus give rise to signal enhancement. The particular phases of the aerosol formation in the presence of NPs will be the subject of ongoing works together with the study of the mechanism. The observed facts drawn from our preliminary experiment confirm that the NP-induced signal enhancement should be taken into account for LA-ICPMS analysis as a possible means of sensitivity improvement. The limitation of this approach consists in a single-pulse ablation per spot which indicates that a larger affordable area is required on the sample. The practical advantage of application of NPs for LA-ICPMS analysis consists in lesser damage of metallic samples (such as metallic foils, thin layers, and objects of cultural heritage) when applying lower laser fluence while necessary sensitivity is preserved. This finding represents a substantial contribution to establishing LA-ICPMS as a nondestructive analytical method.

■ AUTHOR INFORMATION

Corresponding Author

*E-mail: ahrdlicka@chemi.muni.cz. Fax: +420 54949 2494.

DOI: 10.1021/acs.analchem.8b01197
Anal. Chem. 2018, 90, 11820−11826

ORCID

Aleš Hrdlička: 0000-0002-5732-1134

Notes

The authors declare no competing financial interest.

■ ACKNOWLEDGMENTS

This work was financially supported by the Ministry of Education, Youth and Sports of the Czech Republic under the project CEITEC 2020 (LQ1601) under the National Sustainability Programme II. Z.S. acknowledges the support of CEITEC, Brno University of Technology, in the frame of Grant STI-J-18-5419. This work was also carried out with the support of the CEITEC Nano Research Infrastructure (MEYS CR, 2016–2019).

■ REFERENCES

(1) Cremers, D. A.; Radziemski, L. J. *Laser Induced Breakdown Spectroscopy*; Wiley: Chichester, U.K., 2006.
(2) Montaser, A., Golightly, D. W., Eds. *Inductively Coupled Plasmas in Analytical Atomic Spectrometry*, 2nd ed.; Wiley: New York, 1992.
(3) Hahn, D.; Omenetto, N. *Appl. Spectrosc.* **2010**, *64*, 335A–366A.
(4) Hahn, D.; Omenetto, N. *Appl. Spectrosc.* **2012**, *66*, 347–419.
(5) Russo, R. E.; Mao, X.; Gonzalez, J. J.; Zorba, V.; Yoo, J. *Anal. Chem.* **2013**, *85*, 6162–6177.
(6) Zeng, S.; Baillargeat, D.; Ho, H.-P.; Yong, K.-T. *Chem. Soc. Rev.* **2014**, *43*, 3426–3452.
(7) Li, M.; Cushing, S. K.; Wu, N. *Analyst* **2015**, *140*, 386–406.
(8) Li, W.; Zhao, X.; Yi, Z.; Glushenkov, A. M.; Kong, L. *Anal. Chim. Acta* **2017**, *984*, 19–41.
(9) Cailletaud, J.; De Bleye, C.; Dumont, E.; Sacré, P.-Y.; Netchacovitch, L.; Gut, Y.; Boiret, M.; Ginot, Y.-M.; Hubert, Ph.; Ziemons, E. *J. Pharm. Biomed. Anal.* **2018**, *147*, 458–472.
(10) Schertz, F.; Schmelzeisen, M.; Kreiter, M.; Elmers, H.-J.; Schönhense, G. *Phys. Rev. Lett.* **2012**, *108*, 237602.
(11) El Sherbini, A. M.; Abdel Galil, A.; Allam, S. H.; El Sherbini, Th. M. *J. Phys.: Conf. Ser.* **2014**, *548*, 012031.
(12) Picca, R. A.; Calvano, C. D.; Cioffi, N.; Palmisano, F. *Nanomaterials* **2017**, *7*, 75.
(13) Ohta, T.; Ito, M.; Kotani, T.; Hattori, T. *Appl. Spectrosc.* **2009**, *63*, 555–558.
(14) De Giacomo, A.; Gaudiuso, R.; Koral, C.; Dell'Aglio, M.; De Pascale, O. *Anal. Chem.* **2013**, *85*, 10180–10187.
(15) De Giacomo, A.; Gaudiuso, R.; Koral, C.; Dell'Aglio, M.; De Pascale, O. *Spectrochim. Acta, Part B* **2014**, *98*, 19–27.
(16) De Giacomo, A.; Dell'Aglio, M.; Gaudiuso, R.; Koral, C.; Valenza, G. *J. Anal. At. Spectrom.* **2016**, *31*, 1566–1573.
(17) De Giacomo, A.; Koral, C.; Gaudiuso, R.; Dell'Aglio, M. *Anal. Chem.* **2016**, *88*, 9871–9872.
(18) Kalam, S. A.; Murthy, N. L.; Krishna, J. R.; Srikanth, V. V. S. S.; Rao, S. V. Nanoparticle Enhanced Laser Induced Breakdown Spectroscopy with Femtosecond Pulses. *13th International Conference on Fiber Optics and Photonics, OSA Technical Digest* [Online]; Optical Society of America: Washington, DC, 2016; Paper Th3A.89.
(19) Koral, C.; De Giacomo, A.; Mao, X.; Zorba, V.; Russo, R. E. *Spectrochim. Acta, Part B* **2016**, *125*, 11–17.
(20) De Giacomo, A.; Koral, C.; Valenza, G.; Gaudiuso, R.; Dell'Aglio, M. *Anal. Chem.* **2016**, *88*, 5251–5257.
(21) Sládková, L.; Prochazka, D.; Pořízka, P.; Škarková, P.; Remešová, M.; Hrdlička, A.; Novotný, K.; Čelko, L.; Kaiser, J. *Spectrochim. Acta, Part B* **2017**, *127*, 48–55.
(22) Günther, D.; Hattendorf, B. *TrAC, Trends Anal. Chem.* **2005**, *24*, 255–265.
(23) Russo, R. E.; Mao, X.; Mao, S. S. *Anal. Chem.* **2002**, *74*, 70A–77A.
(24) Cromwell, E. F.; Arrowsmith, P. *Anal. Chem.* **1995**, *67*, 131–138.
(25) Eggins, S. M.; Kinsley, L. P. J.; Shelley, J. M. G. *Appl. Surf. Sci.* **1998**, *127–129*, 278–286.
(26) Kuhn, H.-R.; Gunther, D. *Anal. Bioanal. Chem.* **2005**, *383*, 434–441.
(27) Zaorálková, L.; Hrdlička, A.; Otruba, V.; Sulovský, P.; Gilon, N.; Günther, D.; Kanický, V. *Chem. Pap.* **2011**, *65*, 769–781.
(28) Holá, M.; Konečná, V.; Mikuška, P.; Kaiser, J.; Páleníková, K.; Pruša, S.; Hanzlíková, R.; Kanický, V. *J. Anal. At. Spectrom.* **2008**, *23*, 1341–1349.
(29) Nováková, H.; Holá, M.; Vojtíšek-Lom, M.; Ondráček, J.; Kanický, V. *Spectrochim. Acta, Part B* **2016**, *125*, 52–60.

DOI: 10.1021/acs.analchem.8b01197
Anal. Chem. 2018, 90, 11820–11826

PAPER 6

Influence of sample surface topography on laser ablation process

Salajková, Z.*, **Holá, M.**, Prochazka, D., Ondráček, J., Pavliňák, D., Čelko, L., Gregar, F., Šperka, P., Pořízka, P., Kanický, De Giacomo, A., Kaiser, J.

Talanta 222 (2021) 121512, DOI 10.1016/j.talanta.2020.121512

Contribution:

LA-ICP-MS design of experiments and measurements, data evaluation, manuscript writing.

Talanta 222 (2021) 121512

Contents lists available at ScienceDirect

Talanta

journal homepage: www.elsevier.com/locate/talanta

Short communication

Influence of sample surface topography on laser ablation process

Zita Salajková [a,b,*], Markéta Holá [c], David Prochazka [a,d], Jakub Ondráček [e], David Pavliňák [f], Ladislav Čelko [a], Filip Gregar [c], Petr Šperka [g], Pavel Pořízka [a], Viktor Kanický [c], Alessandro De Giacomo [b], Jozef Kaiser [a,d]

[a] Materials Characterization and Advanced Coatings, Central European Institute of Technology, Purkyňova 656/123, Brno, Czech Republic
[b] Department of Chemistry, University of Bari, Via Orabona 4, 70126, Bari, Italy
[c] Department of Chemistry, Masaryk University, Faculty of Science, Kamenice 735/5, 625 00, Brno, Czech Republic
[d] Faculty of Mechanical Engineering, Brno University of Technology, Technická 2, Brno, Czech Republic
[e] Department of Aerosol Chemistry and Physics, Institute of Chemical Process Fundamentals of the ASCR, Rozvojová 135, 165 00, Prague, Czech Republic
[f] Department of Physical Electronics, Faculty of Science, Masaryk University, Kotlářská 267/2, 611 37, Brno, Czech Republic
[g] Institute of Machine and Industrial Design, Faculty of Mechanical Engineering, Brno University of Technology, Technická2896/29, 616 69, Brno, Czech Republic

ARTICLE INFO

Keywords:
Laser ablation
LA-ICP-MS
Surface analysis
Surface topography
Fractionation

ABSTRACT

In this work we discuss how sample surface topography can significantly influence the laser ablation (LA) process and, in turn, the analytical response of the LA Inductively Coupled Plasma Mass Spectrometry (LA-ICP-MS) method. Six different surface topographies were prepared on a certified aluminium alloy sample BAM 311 and SRM NIST 610 to investigate the phenomenon. All the samples were repetitively measured by LA-ICP-MS using a spot by spot analysis. The effect of laser fluence in the range of 1–13 J/cm^2 was studied. For majority of measured isotopes, the ICP-MS signal was amplified with roughening of the sample surface. A stronger effect was observed on the Al alloy sample, where the more than sixty-time enhancement was achieved in comparison to the polished surface of the sample. Since the effect of surface topography is different for each analyte, it can be stated that surface properties affect not only the ICP-MS response, but also elemental fractionation in LA. The presented results show that different surface topographies may lead to misleading data interpretation because even when applying ablation preshots, the signal of individual elements changes. The utmost care must be taken when preparing the surface for single shot analysis or chemical mapping. On the other hand, by roughening the sample surface, it is possible to significantly increase the sensitivity of the method for individual analytes and supress a matrix effect.

1. Introduction

Laser ablation is a simple and straightforward process of material sampling prior to qualitative and quantitative elemental analysis [1,2]. The high-efficiency laser beam focused on a sample surface converts a small portion of the sample into its vapor phase constituents (vapor and particles). The vapor can then be analyzed either by acquiring the spectral emission in laser-induced breakdown spectroscopy (LIBS) or by transporting to another measurement system in inductively coupled plasma optical emission spectrometry or mass spectrometry (LA-ICP-OES/MS). There are no sample type or size requirements, there is no need for tedious sample preparation and it is possible to perform spatially resolved measurements (lateral and depth). Chemical analysis by laser ablation is considered semi-destructive since it requires typically less than a few micrograms of the sample and the ablation crater diameter is in the range from units to hundreds of micrometres [3]. Despite analytical methods based on laser ablation, such as LIBS and LA-ICP-MS, are well established, the complex process of laser-matter interaction is not fully understood. Understanding fundamental laser ablation mechanisms is important in order to efficiently couple the laser beam into the sample, ablate a reproducible quantity of mass, control fractionation and plasma ignition [2]. In the first stage of laser-matter interaction, the laser interacts with the sample's surface, therefore the surface properties directly influence all mentioned mechanism.

In the case of LIBS, irradiances well above the breakdown threshold are used. Then, the surface morphology affects the emission signal in the same way for each element. However, in the case of LA-ICP-MS, the situation can be more complex because the analytical response is related

* Corresponding author. Materials Characterization and Advanced Coatings, Central European Institute of Technology, Purkyňova 656/123, Brno, Czech Republic.
E-mail address: zita.salajkova@ceitec.vutbr.cz (Z. Salajková).

https://doi.org/10.1016/j.talanta.2020.121512
Received 30 March 2020; Received in revised form 31 July 2020; Accepted 3 August 2020
Available online 13 August 2020

to the aerosol formation and consequent particle composition rather than to the plasma composition. The aerosol quality is influenced by loss of aerosol due to particle size, which affects the transport to the ICP as well as its vaporization in the torch, and by unrepresentative composition with respect to the sample bulk [2]. Thus, quantitative analysis typically requires matrix-matched calibration standards which might be difficult to obtain or fabricate in some cases. In addition, for chemical mapping and single pulse analysis, differences in the matrix can cause a misinterpretation of the obtained data [4]. Utilization of laser ablation in analytical chemistry including a discussion about calibration, optimization and fractionation is described in detail in Ref. [2,5–7].

The amount of ablated mass and its composition are highly dependent on the laser and sample properties. For samples containing constituents with different melting-points, fractionation can occur [8,9]. Quantitative evaluation of elemental fractionation can be done in terms of fractionation index (FI). The FI describes a change in the intensity ratios of elements in particles generated by LA. In the study [10], the FI of thirty-four elements in NIST 610 were determined. As a result, the elements were divided into two groups according to their temperature of boiling and melting point. Elements with a high melting point, such as Mn, Ni, Al, Cr, and Mg, have an FI close to 1. For the second group of elements with a low melting point, such as Pb and Bi, the FI increased to values higher than 1.5. The same effect of the fractionation process was also demonstrated on aluminium alloys [9], where lead is captured in small clusters (contrary to the homogenous NIST 610 sample). It has been shown that those lead-contained clusters are ablated preferentially and the volcano-like features at the crater's bottom are created at those points. This effect decreases with an increasing laser pulse fluence. The effect of laser pulse fluence on fractionation was studied also in Ref. [11] where the ICP-MS intensity of elements with a high FI (Pb and Bi) in NIST 610 decreased with an increasing fluence. For other elements, the intensity naturally increased together with fluence. Thus, the measured ratios between the elements can change rapidly depending on the fluence used.

With increasing fluence, all components of the sample material are more likely to melt. Bigger particles are produced during the melting process. It has been shown that the elements are not uniformly distributed within different particle size fractions [12]. For example, enrichment of Cu, Zn, Ag, Tl, Pb and Bi was observed in the aerosol particle fraction bellow 125 nm in comparison to larger particles in a glass sample. On the other hand, larger particles are not fully vaporized, atomized and ionized completely in the ICP. Thus, they also contribute to elemental fractionation effects. Consequently, a fluence which is too high can shift the size distribution of the aerosol in an undesirable direction. Moreover, the sample surface properties also play a significant role in the laser-matter interaction and ablation process. The influence of sample surface properties on LA is well demonstrated by depositing nanoparticles on the sample surface [13,14]. It is expected that the topography of the sample surface is another factor that influences the fractionation. Based on observations, the non-symmetrical vortex ring appears when ablation occurs close to the edge of the sample. The origin of the vortex ring results from the inward flow of the background gas from the edge to the low pressure region around the laser spot. This vortex ring improves the heat transfer and cooling rate of the vapor plume and thus influences the results observed by the ICP-MS system [15].

The effect of surface topography in the generation of chemical maps has already been studied by LIBS [16]. Five samples with a different surface topography were measured and it was concluded that surfaces with higher roughness values yield higher optical emission signal intensities despite the same composition. The influence of steel surface topography on the optical emission signal of laser induced plasma was studied in Ref. [17]. Conclusions of both studies are in good agreement. In addition, the authors determined that the influence of the surface topography had been diminished by higher laser irradiances. In Refs. [18], the roughness effect of the sample surface on the hydrogen signal was studied by LIBS in a Mars-like atmosphere. The authors observed that for targets with obvious roughness, the hydrogen spectral line intensity had increased significantly with the increasing exposure of the target surface to the laser induced plasma.

One of the goals of the LA-ICP-MS method development is to increase the spatial resolution of the analyses, which is accompanied by a reduction in the ablation crater (area) and the number of pulses (depth) [19], which can even lead to analysis from a single shot (SS-LA-ICP-MS). This method is known e.g. in geochronology [20,21]. The reduction of the number of pulses per analysis is performed also if the minimum destruction of the sample is required [22]. Generally, LA-ICP-MS is considered a method linking compromise between low destructiveness of samples and the analytical assumptions of the method, allowing the determination of trace amounts of most elements together with isotope ratios. If the emphasis is on the non-destructiveness of the sample, for example in archaeological research or the analysis of cultural heritage samples, the ridges are usually analyzed without prior surface treatment [23–28]. Despite this growing trend in LA-ICP-MS analysis, no study has been focused on the examination of surface topography influence on this technique's performance. Therefore, the aim of this work is to determine the effect of the surface topography on the process of laser ablation and on the ICP-MS response. For this purpose, six samples with different surface roughness were prepared from aluminium standard with a well-defined concertation of minor elements and from SRM NIST 610. The surface topography for each sample was measured with an optical 3D microscope. Afterwards, the analytical response of selected isotopes was measured by LA-ICP-MS and the elemental fractionation for samples with different surface roughness was discussed.

2. Experimental

2.1. Samples

Certified glass standard reference material (SRM) NIST 610 and aluminium alloy standard BAM 311 (BAM, Germany) samples were utilized throughout the whole experiment. The composition of the NIST 610 and the alloy is guaranteed by the supplier, for the BAM 311 see Table 1. As for the NIST 610, the matrix components are 72% SiO_2, 14% Na_2O, 12% CaO and 2% Al_2O_3. The nominal mass fractions of 61 elements added to the glass matrix are in the range of 100 mg/kg to 500 mg/kg [29]. For purpose of experiment were used 6 pieces of NIST 610 samples embedded in 1 inch diameter resin molds. The aluminium alloy standard was delivered in a form of a block from which the six samples with dimensions of 15 × 15 mm in size and 10 mm in thickness were produced using high precision metallographic saw Secotom-50 (Struers, Germany) with diamond cutting wheel.

The different samples surface roughness was produced by wet grinding or polishing using different silicon carbide papers (from #80 up to #2000) or 3 μm and 1 μm diamond pastes. An automatic, microprocessor-controlled machine Tegramin 30 (Struers, Germany) and pre-set up the lowest force of 5 N for each sample was used for wet grinding and/or polishing procedure with the aim to avoid 1) the unwanted changes in the alloy surface microstructure, i.e. to supress any kind of a phase transformation, to minimize the probability on intermetallic phase particles pull out and to neglect the mechanical deformation provided by the contact force between sample and grinding media, and 2) the foreign particles introduction onto the specimen's surface, i.e. to minimize wear of the sand paper(s) and release of the grinding media. For this purpose, were the samples after each 5 min sequence removed from the grinding/polishing machine, washed with acetone in an ultrasonic cleaner and dried by compressed air. A final set contained 6 samples with different roughness (the roughest sample was grinded with paper #80; the smoothest sample went through a complete polishing process) for further investigation were manufactured.

The final surface roughness of samples was measured with an optical 3D microscope (Contour GT-X8, Bruker, USA) within the area of 2 mm^2,

Table 1
Chemical composition of aluminium alloy standard BAM 311 in nominal content in mass concentration percentages (Figures in bold type are certified, figures in small italic type are only approximate.).

REF NO.	Description									
BAM 311	Aluminium Alloy AlCuMg2	Li 0.00053	Be 0.00052	Na *0.0018*	Mg 1.567	Al Bal.	Si 0.204	Ca 0.00056	Ti 0.056	V 0.0240
		Cr 0.104 Sn 0.0127	Mn 0.694 Pb 0.0504	Fe 0.310 Bi 0.0500	Ni 0.052	Cu 4.653	Zn 0.200	Ga 0.0159	Zr 0.140	Cd 0.0013

Table 2.

2.2. LA-ICP-MS

The analytical equipment consisted of an excimer laser ablation system Analyte G2 (Photo Machines Inc., WA, USA) and an ICP-MS Agilent 7900 (Agilent Technologies, Japan) with a quadrupole analyser and an octopole reaction cell to attenuate polyatomic interferences. This instrument was operated at the forwarded power of 1500 W, with Ar gas flow rates of 15 (outer plasma gas) and 0.7 (auxiliary), He carrier of 0.65 and Ar make-up gas of 0.6 l/min. The ablated material was transported through a FEP (Fluorinated Ethylene Propylene) tubing (i.d. 2 mm, length 1 m) to ICP-MS. The laser operated at a wavelength of 193 nm with a pulse duration of $\leq$4 ns, using a 2-vol ablation cell (HelEx, Photon Machines Inc., WA, USA). An ablation spot of 110 μm in diameter was applied in order to assure a sufficient ICP-MS signal and homogenous sampling from the sample surface. The line scan "pulse by pulse" was performed with ablation speed of 0.5 mm/s at the repetition rate of 5 Hz. This implies that each shot irradiates fresh surface acting as a single shot measurement. One line scan length was 15 mm which means 150 shots in 30 s (27x integration time). The applied pulse energy was adjusted so that it corresponded with the need of the experiment. Consequently, the fluences were: 1, 3, 5, 10 and 13 J/cm^2. The following isotopes were monitored during the LA-ICP-MS measurement, the dwell time is given in parentheses is seconds for each isotope: ^{24}Mg (0.1), ^{27}Al (0.05), ^{29}Si (0.05), ^{43}Ca (0.1), ^{47}Ti (0.05), ^{51}V (0.05), ^{52}Cr (0.05), ^{55}Mn (0.05), ^{57}Fe (0.1), ^{60}Ni (0.05), ^{63}Cu (0.05), ^{66}Zn (0.05), ^{71}Ga (0.1), ^{90}Zr (0.05), ^{118}Sn (0.05), ^{208}Pb (0.05), ^{209}Bi (0.05) with a total integration time of 1.1 s.

2.3. SEM and EDX

Images of the surfaces/particles were made by a scanning electron microscope (SEM) MIRA3 (Tescan, Czech Republic). If not specified otherwise, all samples were measured using secondary emission mode (in-beam detector) at 15 kV, and a depth regime and working distance of 7 mm. Elemental analysis was provided by Energy-dispersive X-ray spectroscopy (EDX), with a working distance of 15 mm, visualized with a BSE detector and a 50 mm SDD detector (Oxford Instruments, UK). Data were evaluated using Aztec software ver. 3.1 (Oxford Instruments, UK).

The laser-generated particles were studied after their collection on a polycarbonate membrane filter (25 mm in diameter and 0.2 μm pores, Cyclopore, Whatman) using SEM described above. Ablation was performed 20 min to obtain a sufficient amount of particles. To prevent charging, the filters were covered with a carbon layer as the same as the glass NIST samples themselves. BAM samples did not require any plating.

Table 2
Surface roughness measured by an optical 3D microscope for samples with different grinding set up.

Ra [nm]	#80	#220	#500	#1200	#2000	polished
BAM 311	2717.3	875.7	335.0	190.0	73.0	14.0
NIST 610	2601.8	514.5	136.8	24.2	8.1	1.2

2.4. DustTrak DrX monitor

The DustTrak™ DrX Aerosol Monitor (TSI, USA) is a light-scattering laser photometer that provides real-time mass concentration readings for aerosols in the range of 0.1–15 μm. It allows for measurements of size-segregated mass fractions including PM1, PM2.5, respirable, PM10 and Total PM. It utilizes a real-time 90° light-scattering signal from the passing particles in order to separate the particles into size fractions and to estimate their mass.

The original inlet from the DustTrak DrX was removed and the pump was disconnected so that the DustTrak would be suitable for LA-ICP-MS purposes. The sampling line leading from LA was directly connected into the DustTrak DrX. The flow rate was different from the original DustTrak flow, but since only Total PM concentration was taken into account, the results should be within calibration limits.

2.5. Reflectance measurement

The reflectance measurements were performed by fiber optic reflection probe (Ocean Optics, USA), Deuterium-Halogen lamp (DH-2000, OceanOptics, USA) and Czerny-Turner spectrometer (Freedom UV-VIS, Ibsen Photonics, DK). The set up used made it possible at a wavelength of 266 nm in 90° arrangement. 100 values of reflectivity were recorded for each sample from different spots. The detector exposition time was selected at 100 ms. The probe distance from the sample surface was set at 1 mm.

3. Results and discussion

The influence of sample surface topography on the LA process was investigated on aluminium alloy (BAM 311) and glass standard (NIST 610). Six samples with different surface roughness were prepared from both materials, discussed in detail in section 2.1. Although the elemental distribution of both selected materials is globally homogenous, their microstructure is strongly different. The glass material was prepared in rod form and then sliced into wafers. Considerable effort was invested in the manufacturing of the material to ensure sufficient homogeneity to yield a $\leq$2% relative repeatability of measurement when an entire wafer is used [29]. The elemental distribution in this alloy was verified by EDX. From Fig. 1 we assume that the alloy exhibits a dendritic structure that was created during the unidirectional solidification process. Due to different melting points and solidification ratios of elements, the dendrites are enriched with Cu, Bi and Pb. This dendritic structure is globally homogenous, thus the spot size utilized in this work (>100 μm) affects a sufficiently large area. The distribution of all elements in area 9500 μm^2 is uniform.

The LA-ICP-MS response of measured isotopes was studied for different fluences (1, 3, 5, 10 and 13 J/cm^2). Each measurement was performed as a "spot by spot" line scan of 5 mm length and 10 repetitions. The average value of counts per second (cps) for each isotope was calculated together with the standard deviation (SD). The values were then compared for each isotope and changing fluence. The ratio between cps of samples with specific roughness and the cps of polished samples enabled an estimation of the changes in signal response. Since this ratio was greater than one in most cases, we will call it an "enhancement".

The enhancement as a function of surface roughness is presented in

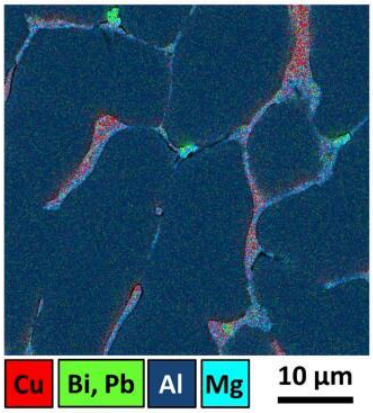

Fig. 1. The image of a polished BAM 311 surface: EDX map of elemental distribution. Cu (red) and Mg (turquoise) form dendrites. Bi and Pb (green) are captured together in small inclusions within dendrites. Al (blue) is mainly contained in the space between them. (For interpretation of the references to colour in this figure legend, the reader is referred to the Web version of this article.)

the graphs in Fig. 2. To improve readability, enhancement at fluence 5 J/cm^2 was chosen to also represent 3 and 10 J/cm^2 as the behaviour was very similar within this range for both materials.

The trend of signal enhancement of Al alloy is similar for most elements, in Fig. 2a representing by Mg, Al, Cr, Mn, Fe, Ni and Cu and grows with increasing surface roughness. However, the maximum value of enhancement varies for individual elements (from 10 to 60). In general, for this group of elements, a greater enhancement was obtained for sample #220 (surface roughness 875.7) using lower fluence values. Applying fluence 10 J/cm ^{2} and more caused mostly a suppression of the surface topography effect. Different behaviour was observed for Pb and Bi. For these two elements, the intensity decreased with growing surface roughness in comparison to the polished sample. Therefore, in the case of alloy, we could expect a different fractionation of elements depending on the surface topography.

In the case of NIST 610 (Fig. 2b) the trend of signal enhancement is more or less similar for all measured elements and grows with surface roughness with the maximum enhancement varying slightly between 3 and 4. Some differences are seen for Mg and Cu, where irregular enhancement trend occurs. The used fluences show only little impact on the enhancement.

Since the enhancement effect is not equally strong for all analytes, changes in the proportions of individual elements also occur with the surface treatment. This means that the fractionation differs compare to ablation of the polished sample surface. The fractionation of alloy was studied from the isotope intensities representing each element. The signal intensities were converted to 100% isotopic abundance, the sum of these values is the sum of all elements present in the sample. The individual converted intensities were then expressed as a percentage of the sum. Fig. 3 shows a percentage of ICP-MS response of measured elements in Al alloy for different surface roughness and fluences.

It was confirmed that elemental representation of the sample composition strongly varies depending on the surface roughness. Generally, the mass percentage of the major elements increases with growing fluence and surface roughness. In the case of Pb and Bi, the opposite dependence was observed. This phenomenon can be explained by two facts. First, different physical properties of elements: Pb and Bi represent volatile components with the lowest melting point of the sample [30]. Second, their distribution in the matrix differs from the other elements, Fig. 1. It was already found that in some cases, an element can segregate from a solid matrix into a pure liquid phase when the temperature rises above the melting point of the element. This is the case of Pb in Al alloy, as described previously [9]. This effect is most pronounced at low fluences where selective melting of low melting point elements occurs, in our case Pb and Bi. Moreover, the micro-heterogeneity of the sample itself, forming regions with different melting and boiling points or optical parameters, can be a source of fractionation. This implies that, when the ablation parameters are changed, the greatest changes in the analytical response will occur just with the elements from the inclusions. That also explain why the fractionation effect is minor for NIST sample, as it will be discussed later.

When studying NIST 610 (not all of its components were measured), fractionation was expressed by plotting isotope/^{43}Ca ratios [12]. Fig. 4 shows the relative change of the isotope/^{43}Ca ratios for sample with various surface roughness related to the polished sample using fluence 5 J/cm^2. Most analytes show a relative increase with increasing surface roughness, 3 isotopes behave anomalous. Mg and Zn show highest relative signal increase but not for the maximal surface roughness but for #500 and #1200, respectively. Their different behaviour is probably related to lower boiling points compared to other analytes (1090 °C for Mg and 907 °C for Zn). The opposite extreme is Zr, with the highest boiling point (4409 °C) showing a relative attenuation of intensity for all sample roughnesses.

It is clear that the change in the analytical response for variously treated surfaces is significant, especially for the Al alloy. Therefore, the topic of the importance of fluence value will be discussed for this material. When the same material with different surface treatment is ablated, the most significant changes in analytical results are observed at low fluences. To explore the ablation process, SEM images of ablation craters were made after laser ablation of polished surfaces with fluence of 1 J/cm^2, see Fig. 5. The preferential ablation of the inclusions containing Pb and Bi, and those that create local volcano features was observed. The fact of segregation of elements with a low melting point from the solid was confirmed. The volcano features are formed by an ejection of molten material which is also preferentially vaporized. Pb and Bi have a rather low ablation threshold, thus those clusters are more likely ablated during low fluence LA. With increasing fluence, energy starts to overcome the ablation threshold of all the elements, and the mass percentage of elements changes, as presented in Fig. 3.

Besides the effect of fluence, a significant impact of surface roughness on the enhancement and mass percentage of elements was shown. Higher analytical ICP-MS signals of measured isotopes implicated that more ions had been produced from the aerosol in ICP. The aerosol was transported from the ablation cell. The reason may be a large amount of transported aerosol or its different structure. To determine the total mass produced by LA, a DustTrack DrX monitor was used. The aerosol mass produced by LA of a polished sample and a sample with the roughness #220 (highest enhancement) was measured for various fluencies (1, 3, 5, 10 and 13 J/cm^2) for both materials. More than ten times higher mass production was found for the Al alloy sample #220 compared to the polished sample, NIST 610 #220 provided increased aerosol production in the order of units (Table 3). These values are roughly in agreement with the signal enhancement for both materials, so this confirmed the formation of larger mass of aerosol particles for samples with higher surface roughness. Table 3 also shows degree of relative reflectivity for #220 BAM and NIST 610, if we estimate that polished sample has a reflectivity of 100%. The decrease of reflectivity increases the amount of radiation absorbed by the sample surface. The results of reflectance measurements showed 44% resp. 60% of rel. reflectivity for sample #220 BAM, resp. NIST 610.

Further information about the ablation process was obtained by SEM images of aerosol and ablation craters; see Fig. 6. SEM images of Al alloy aerosol captured on a filter confirmed that the aerosol's structure preserve, and together with crater image demonstrate that the material melted more with growing surface roughness resulting in a formation of a higher quantity of particles. One reason of the formation of larger mass of aerosol particles for samples with higher surface roughness may be

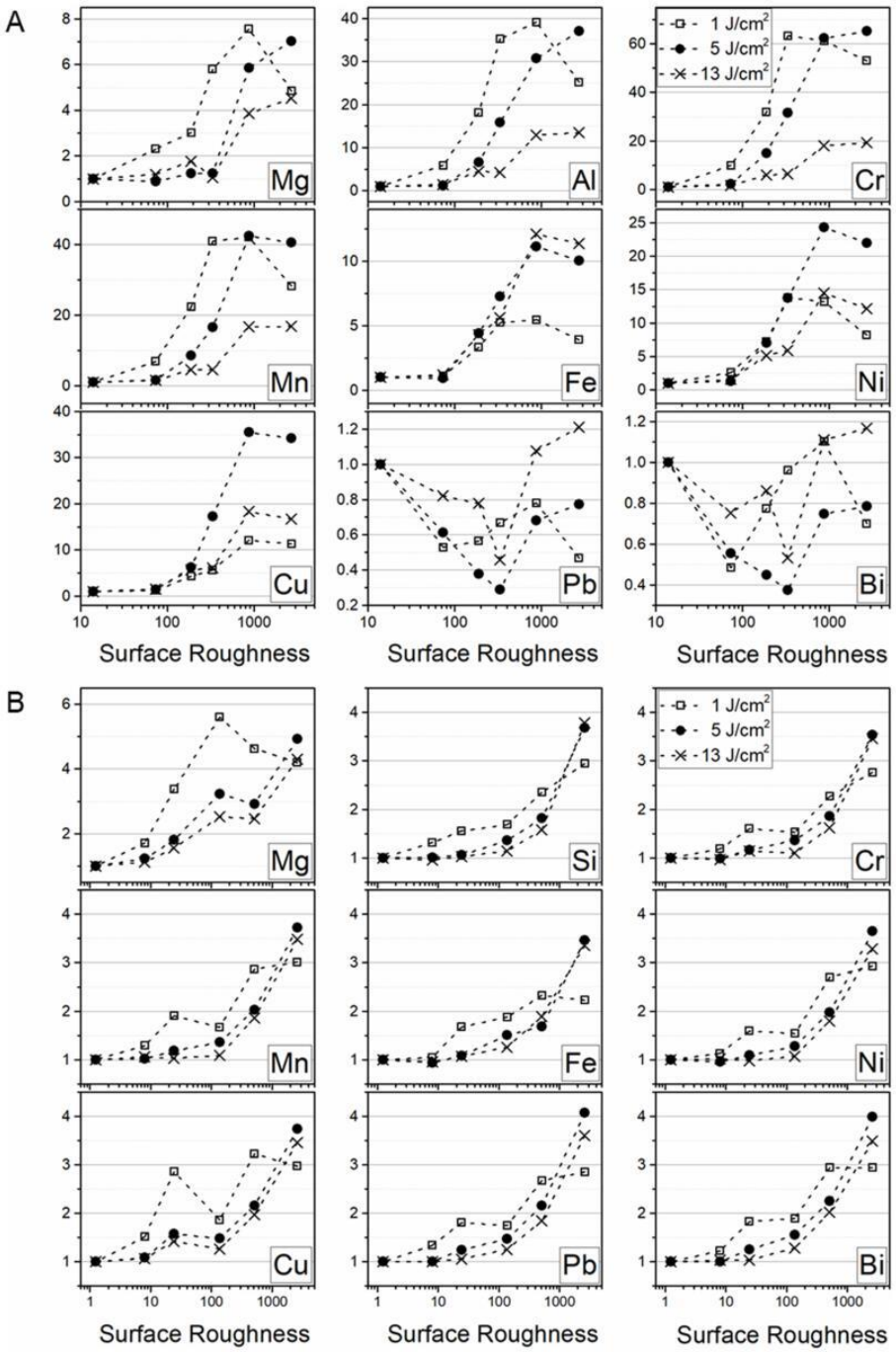

Fig. 2. The ratio between cps of samples with specific surface roughness and the cps of polished samples for selected isotopes as a function of surface roughness (A) BAM 311 (B) NIST 610.

caused by its reduced reflectivity, Table 3.

The changes were not only in the aerosol mass but also in its elemental composition (ICP-MS response). It is assumed that with a surface roughness increase, the laser radiation is better coupled with the sample surface and more energy is captured. This energy starts to accumulate in the apexes, where the ratio of surface irradiated by laser and mass is higher. Ablation of the apex occurs with a higher probability. With increasing surface roughness this phenomenon starts to be dominant over the preferential ablation of elements with a low melting point. As a result, more mass is ablated and preferential ablation is supressed (as an example of Pb and Bi in Al alloy). It has been proved that a lower fluence and a smoother sample surface facilitate the

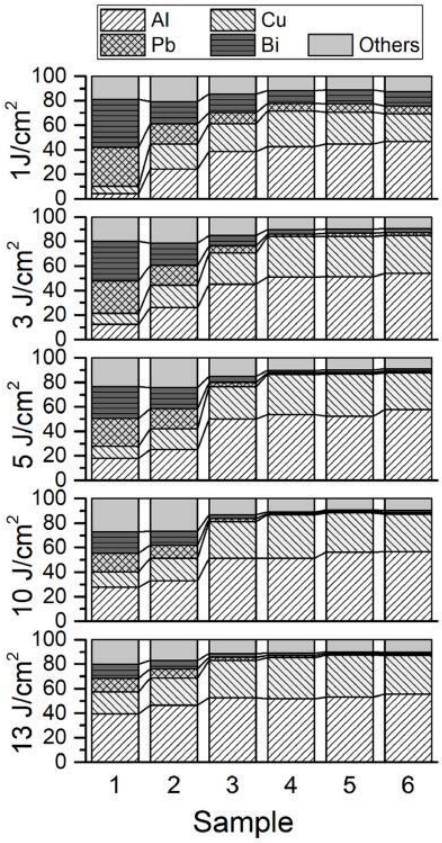

Fig. 3. The total elemental representation (expressed as a percentage of sum of signal intensities) for BAM 311 sample with different surface roughness: 1 polished (14.0), 2 #2000 (73.0), 3 #1200 (190.0), 4 #500 (335.0), 5 #220 (875.7) and 6 #80 (2717.3).

preferential ablation of Pb and Bi in this sample. Therefore, their representation seems higher than it really is. A higher laser energy transfer achieved by using higher fluence or accumulation in surface irregularities will suppress preferential ablation of components differing by their physical properties from the rest of the bulk.

Performing the surface trace analysis by laser ablation, the procedure is usually pre-treated applying one or more ablation preshots of low fluence to clean the surface [31]. For this reason, the influence of preshot number on the analytical signal was studied on variously treated surfaces. Results represent Fig. 7. Five ablation preshots are shown for Si, Al and Ca and three fluences. The effect of the surface diversity can be visible even after the fifth shot to the same place, especially using low

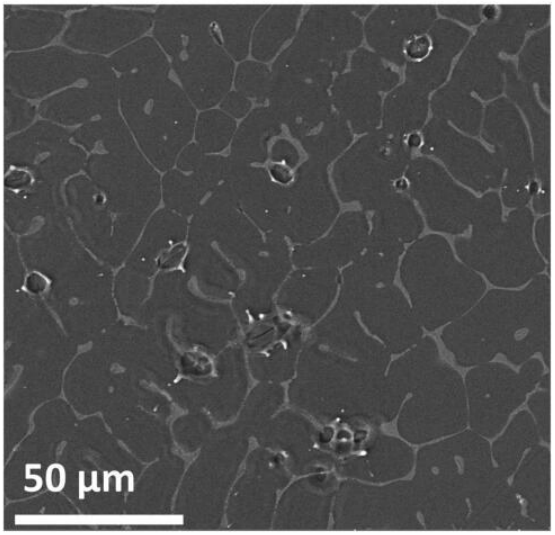

Fig. 5. SEM image of the polished BAM 311 sample surface ablated by 1 J/cm2 spot by spot of 110 µm diameter.

Table 3
Ablated mass [mg/m3] during laser ablation with various fluencies (1, 3, 5, 10 and 13 J/cm2) and reflectivity of polished sample and sample #220 (with the highest enhancement in case of alloy).

[J/cm2]	NIST 610 [mg/m^3]		BAM 311 [mg/m^3]	
	Polished	220	Polished	220
1	0.020	0.136	0.007	0.093
3	0.033	0.167	0.005	0.211
5	0.045	0.143	0.005	0.234
10	0.053	0.147	0.005	0.275
13	0.058	0.146	0.008	0.295
Reflectivity	100%	60%	100%	44%

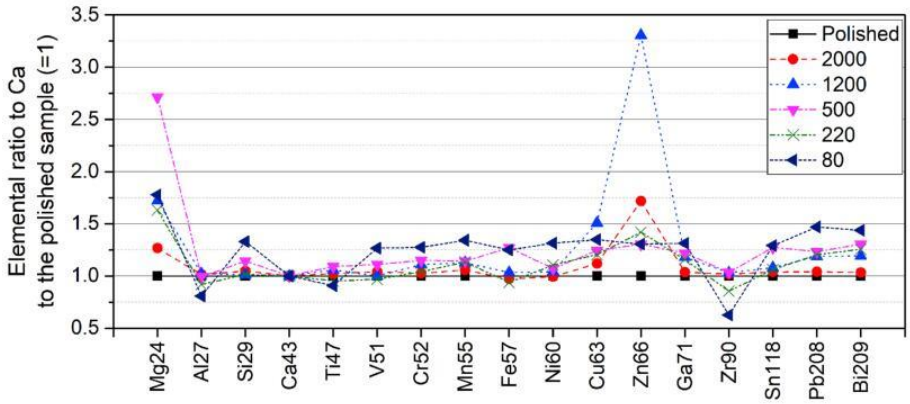

Fig. 4. The change of elemental/Ca ratio of NIST 610 sample with various surface rougness related to the polished sample (=1). Presented analysis was performed with fluence 5 J/cm2.

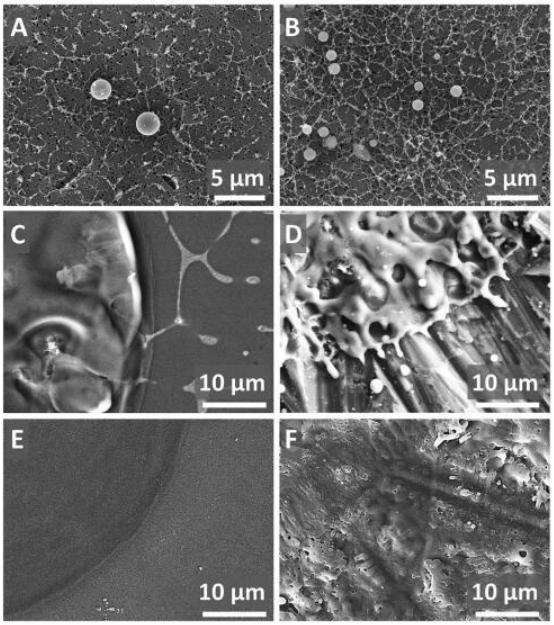

Fig. 6. The SEM image of aerosol on filter from alloy (A) polished (B) #220 and crater detail made by laser fluence 5 J/cm2 on the alloy with roughness (C) polished (D) #220 and on the NIST (E) polished (F) #220.

fluence. For Al alloy material, the effect is more pronounced than for glass. The degree of material melting will be crucial here, for easily melting material, such as metal, there may be a permanent change in the constantly remelting surface. Therefore, the same surface preparation should always be performed for the sample and the external standard when performing surface spot analysis or surface imaging. Particularly in the case of untreated metal samples, such as archaeological ones, a different surface of the standard plays a significant role in the accuracy of the LA-ICP-MS analysis.

4. Conclusion

This work studies the effect of sample surface treatment on the analytical response of the LA-ICP-MS method while performing surface analysis. "Spot by spot" analysis of a homogeneous Al alloy sample BAM 311 and glass SRM NIST 610, both with six different surface roughness values was applied using fluence in the range from 1 to 13 J/cm^2. The ICP-MS signal enhancement was observed for most of the analytes for samples with higher surface roughness. A greater enhancement effect was achieved in the case of Al alloy samples with the two highest surface roughness (#220, #80), where the analyte signal increased more than sixty times compared to the polished sample surface. On the other hand, two elements (Bi and Pb) showed no signal enhancement. Glass samples provided a maximum about five times enhancement and in general the results were more uniform for different elements.

A more detailed study was performed on polished samples and samples with a roughness #220 (significant enhancement for both materials). The total mass of generated aerosol by laser ablation was estimated using an aerosol monitor. More than ten times higher mass production was found for the Al alloy sample #220 compared to the polished sample. NIST 610 #220 provided increased aerosol production in the order of units, which roughly corresponds to the signal enhancement of the isotopes. Thus, this experiment demonstrated that roughening the material surface increases aerosol production and thus the analytical response of most isotopes. One reason could be in the different material reflectivity, which regulates the amount of radiation absorbed by the sample surface. The results of reflectance measurements showed 44% resp. 60% of rel. reflectivity for sample #220 BAM, resp. NIST 610, if we estimate that polished sample has a reflectivity of 100%. The other reason should be in variously intense energy transfer through surface spikes and a flat surface. The different ablation crater structure suggested a more efficient energy transfer across the apexes of the roughened surface of the sample. More material melting occurred causing a higher particle production. Different energy transfer is further

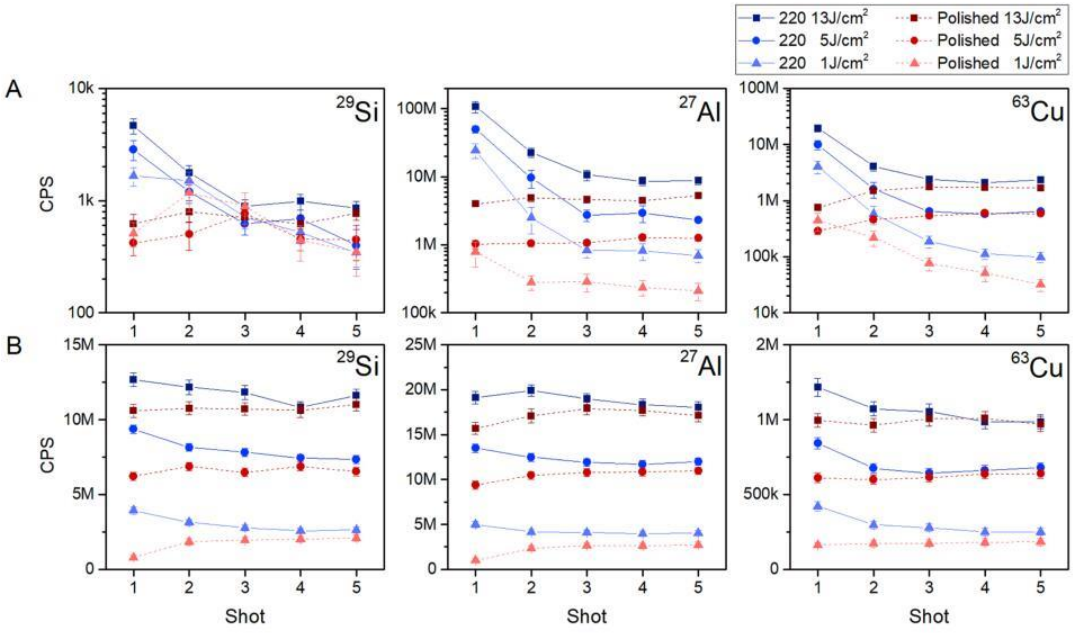

Fig. 7. LA-ICP-MS intensity (CPS) from shot 1–5 for (A) BAM 311 and (B) NIST 610 (polished vs #220).

associated with different aerosol generation mechanisms. These explanations correspond to the greater enhancement effect for the metal sample compared to glass. In the case of glass, the reflectance is not reduced to such an extent as in the case of metal. Also, the lower thermal conductivity of glass does not allow such an energy transfer [32], which is also visible from the ablation craters.

The finding that the enhancement does not work for all elements equally certainly is also related to changed fractionation process when ablating sample with uneven surface. Thus, this has a noticeable effect on the response of individual analytes resulting in a different ratio of analytical signals representing the sample composition. This is more evident on Al alloy; where it has been found that surface roughening suppresses the preferential evaporation of the volatile components. In this way, an increase in surface roughness can reduce the matrix effect.

Furthermore, the laser fluence value is a critical parameter for the analytical result. First, it influences the effect of signal enhancement - the effect is mostly suppressed by higher fluences. Second, the final representation of individual elements in the sample varies based on the laser fluence used. Using higher fluences reduces preferential vaporization of volatile components, which was demonstrated on the Al alloy sample. The change in the response of the measured analytes persists even after the application of several preshots, in the case of metallic materials where there is extreme melting of the sample, the composition may change permanently by surface re-melting, especially for lower fluences.

The work demonstrates that sample surface treatment may be an important parameter to be controlled during surface elemental mapping or single spot analysis, even if the pre-cleaning shots are used. In this view the use of standards with similar surface roughness is strongly suggested in any calibration strategy. Therefore we can conclude that it may be advantageous in terms of reproducibility and accuracy to suitably treat the sample surface before mapping or single spot analysis, when quantitative or semi-quantitative analysis is required. In addition, by roughening the sample surface, it is possible to significantly increase the sensitivity of the method for individual analytes and to supress the matrix effect.

Credit author statement

Zita Salajková: Conceptualization, Methodology, Validation, Writing - Original Draft, Visualization, Writing - review & editing. Markéta Holá: Conceptualization, Validation, Investigation, Writing - Original Draft, Writing - review & editing. Prochazka David: Conceptualization, Formal analysis, Writing - Original Draft, Data Curation. Jakub Ondráček: Investigation. David Pavliňák: Investigation. Ladislav Čelko: Investigation. Filip Gregar: Formal analysis, Investigation. Petr Šperka: Investigation. Pavel Pořízka: Resources, Supervision. Viktor Kanický: Resources, Supervision. Alessandro De Giacomo: Supervision. Jozef Kaiser: Resources, Supervision.

Declaration of competing interest

The authors declare that they have no known competing financial interests or personal relationships that could have appeared to influence the work reported in this paper.

Acknowledgement

This research has been financially supported by the Ministry of Education, Youth and Sports of the Czech Republic under the project CEITEC 2020 (LQ1601). Also, this work was carried out with the support of CEITEC Nano Research Infrastructure (MEYS CR, 2016–2019) and CEITEC Nano + project, ID CZ.02.1.01/0.0/0.0/16_013/0001728.

References

[1] J. Koch, D. Günther, Review of the state-of-the-art of laser ablation inductively coupled plasma mass spectrometry, Appl. Spectrosc. 65 (2011) 155–162, https://doi.org/10.1366/11-06255.
[2] R.E. Russo, X. Mao, J.J. Gonzalez, et al., Laser ablation in analytical chemistry, Anal. Chem. 85 (2013) 6162–6177, https://doi.org/10.1021/ac4005327.
[3] A. Raith, R.C. Hutton, I.D. Abell, J. Crighton, Non-destructive sampling method of metals and alloys for laser ablation-inductively coupled plasma mass spectrometry, J Anal At Spectrom 10 (1995) 591–594, https://doi.org/10.1039/ja9951000591.
[4] N. Miliszkiewicz, S. Walas, A. Tobiasz, Current approaches to calibration of LA-ICP-MS analysis, J. Anal. At. Spectrom. 30 (2015) 327–338.
[5] R.E. Russo, X. Mao, H. Liu, et al., Laser ablation in analytical chemistry - a review, Talanta 57 (2002) 425–451.
[6] R.E. Russo, Laser ablation, Appl. Spectrosc. 49 (1995) 14A–28A, https://doi.org/10.1366/0003702953965399.
[7] R.E. Russo, X. Mao, O.V. Borisov, Laser ablation sampling, in: TrAC - Trends in Analytical Chemistry, 1998, pp. 461–469.
[8] P.M. Outridge, W. Doherty, D.C. Gregoire, Ablative and transport fractionation of trace elements during laser sampling of glass and copper, Spectrochim. Acta Part B At. Spectrosc. 52 (1997) 2093–2102, https://doi.org/10.1016/S0584-8547(97)00112-2.
[9] E.F. Cromwell, P. Arrowsmith, Fractionation effects in laser ablation inductively coupled plasma mass spectrometry, Appl. Spectrosc. 49 (1995) 1652–1660, https://doi.org/10.1366/0003702953965713.
[10] R. Machida, T. Nakazawa, N. Furuta, Temporal changes of fractionation index caused by changes in the large size of ablated particles in laser ablation-inductively coupled plasma mass spectrometry, Anal. Sci. 31 (2015) 345–355, https://doi.org/10.2116/analsci.31.345.
[11] P.M. Outridge, W. Doherty, D.C. Gregoire, The formation of trace element-enriched particulates during laser ablation of refractory materials, Spectrochim. Acta Part B At. Spectrosc. 51 (1996) 1451–1462, https://doi.org/10.1016/0584-8547(96)01542-X.
[12] H.R. Kuhn, D. Gunther, Laser ablation-ICP-MS: particle size dependent elemental composition studies on filter-collected and online measured aerosols from glass, in: Journal of Analytical Atomic Spectrometry, 2004, pp. 1158–1164.
[13] M. Holá, Z. Salajková, A. Hrdlička, et al., Feasibility of nanoparticle-enhanced laser ablation inductively coupled plasma mass spectrometry, Anal. Chem. 90 (2018) 11820–11826, https://doi.org/10.1021/acs.analchem.8b01197.
[14] A. De Giacomo, R. Gaudiuso, C. Koral, et al., Nanoparticle-enhanced laser-induced breakdown spectroscopy of metallic samples, Anal. Chem. 85 (2013) 10180–10187, https://doi.org/10.1021/ac4016165.
[15] S.B. Wen, X. Mao, R. Greif, R.E. Russo, Experimental and theoretical studies of particle generation after laser ablation of copper with a background gas at atmospheric pressure, J. Appl. Phys. 101 (2007), https://doi.org/10.1063/1.2748635.
[16] I. Lopez-Quintas, V. Piñon, M.P. Mateo, G. Nicolas, Effect of surface topography in the generation of chemical maps by laser-induced plasma spectroscopy, in: Applied Surface Science, Elsevier B.V., 2012, pp. 9432–9436.
[17] L.M. Cabalín, D. Romero, J.M. Baena, J.J. Laserna, Effect of surface topography in the characterization of stainless steel using laser-induced breakdown spectrometry, Surf. Interface Anal. 27 (1999) 805–810, https://doi.org/10.1002/(SICI)1096-9918(199909)27:9<805::AID-SIA576>3.0.CO;2-K.
[18] W. Rapin, B. Bousquet, J. Lasue, et al., Roughness effects on the hydrogen signal in laser-induced breakdown spectroscopy, Spectrochim. Acta Part B At. Spectrosc. 137 (2017) 13–22, https://doi.org/10.1016/j.sab.2017.09.003.
[19] E.P. Corbett, A. Simonetti, P. Shaw, et al., Shallow sampling by multi-shot laser ablation and its application within U-Pb zircon geochronology, Chem. Geol. 544 (2020), 119568, https://doi.org/10.1016/j.chemgeo.2020.119568.
[20] J.M. Cottle, M.S.A. Horstwood, R.R. Parrish, A new approach to single shot laser ablation analysis and its application to in situ Pb/U geochronology, J Anal At Spectrom 24 (2009) 1355–1363, https://doi.org/10.1039/b821899d.
[21] J.M. Cottle, A.R. Kylander-Clark, J.C. Vrijmoed, U-Th/Pb geochronology of detrital zircon and monazite by single shot laser ablation inductively coupled plasma mass spectrometry (SS-LA-ICPMS), Chem Geol 332–333 (2012) 136–147, https://doi.org/10.1016/j.chemgeo.2012.09.035.
[22] P. Degryse, F. Vanhaecke, Status and prospects for quasi-non-destructive analysis of ancient artefacts via LA-ICP-MS, Elements 12 (2016) 341–346, https://doi.org/10.2113/gselements.12.5.341.
[23] R. Borges, L. Alves, R.J.C. Silva, et al., Investigation of surface silver enrichment in ancient high silver alloys by PIXE, EDXRF, LA-ICP-MS and SEM-EDS, Microchem. J. 131 (2017) 103–111, https://doi.org/10.1016/j.microc.2016.12.002.
[24] L. Gentelli, Enhancing understanding of the emergence of global trade: analysis of 17th- to 19th-century Spanish coins recovered from western Australian shipwrecks using laser ablation – inductively coupled plasma – mass spectrometry (LA–ICP–MS), Archaeometry 61 (2019) 701–719, https://doi.org/10.1111/arcm.12444.
[25] T. Trejos, J.R. Almirall, Sampling strategies for the analysis of glass fragments by LA-ICP-MS: Part I. Micro-homogeneity study of glass and its application to the interpretation of forensic evidence, Talanta 67 (2005) 388–395, https://doi.org/10.1016/j.talanta.2005.01.042.
[26] A.M. De Francesco, D. Barca, M. Bocci, et al., Provenance of obsidian artifacts from the Natural Protected Area Laguna del Diamante (Mendoza, Province Argentina) and upper Maipo valley (Chile) by LA-ICP-MS method, Quat. Int. 468 (2018) 134–140, https://doi.org/10.1016/j.quaint.2017.10.004.

[27] E. Vaníčková, M. Holá, K. Rapouch, et al., LA-ICP-MS analysis of metal layers on samples of cultural heritage, Chem. Pap. 73 (2019) 2923–2936, https://doi.org/10.1007/s11696-019-00745-6.
[28] C. Gauert, M. Schannor, L. Hecht, et al., A comparison of *in situ* analytical methods for trace element measurement in gold samples from various South African gold deposits, Geostand. Geoanal. Res. 40 (2016) 267–289, https://doi.org/10.1111/j.1751-908X.2015.00362.x.
[29] NIST - SRM order request system. https://www-s.nist.gov/srmors/view_cert.cfm?srm=610. (Accessed 27 July 2020).
[30] A.M. James, M. Arthur, M.P. Lord, Macmillan's Chemical and Physical Data, Macmillan, 1992.
[31] L. Dussubieux, P. Robertshaw, M.D. Glascock, LA-ICP-MS analysis of African glass beads: laboratory inter-comparison with an emphasis on the impact of corrosion on data interpretation, Int. J. Mass Spectrom. 284 (2009) 152–161, https://doi.org/10.1016/J.IJMS.2008.11.003.
[32] M. Holá, V. Konečná, P. Mikuška, et al., Influence of physical properties and chemical composition of sample on formation of aerosol particles generated by nanosecond laser ablation at 213 nm, Spectrochim. Acta Part B At. Spectrosc. 65 (2010) 51–60, https://doi.org/10.1016/j.sab.2009.11.003.

PAPER 7

Online monitoring of nanoparticles formed during nanosecond laser ablation

Nováková, H., **Holá, M.***, Vojtíšek-Lom, M., Ondráček, J., Kanický, V.

Spectrochimica Acta Part B. 2016, 125, 52–60. DOI 10.1016/j.sab.2016.09.017

Contribution:

LA-ICP-MS and aerosol design of experiments and measurements, data evaluation, studying of ablation craters and the particle structure, manuscript writing, corresponding author.

Spectrochimica Acta Part B 125 (2016) 52–60

Contents lists available at ScienceDirect

Spectrochimica Acta Part B

journal homepage: www.elsevier.com/locate/sab

Online monitoring of nanoparticles formed during nanosecond laser ablation

Hana Nováková [a], Markéta Holá [a,*], Michal Vojtíšek-Lom [b], Jakub Ondráček [c], Viktor Kanický [a,d]

[a] Central European Institute of Technology (CEITEC), Masaryk University, Kamenice 5, 62500 Brno, Czech Republic
[b] Faculty of Mechanical Engineering, Czech Technical University of Prague, Zikova 4, 16000 Prague, Czech Republic
[c] Institute of Chemical Process Fundamentals of the ASCR, Rozvojová 135, 16500 Prague, Czech Republic
[d] Department of Chemistry, Faculty of Science, Masaryk University, Kotlářská 2, 61137 Brno, Czech Republic

ARTICLE INFO

Article history:
Received 9 November 2015
Received in revised form 20 September 2016
Accepted 20 September 2016
Available online 21 September 2016

Keywords:
Laser ablation
Inductively coupled plasma mass spectrometry
Fast mobility particle sizer
Particle size distribution

ABSTRACT

The particle size distribution of dry aerosol originating from laser ablation of glass material was monitored simultaneously with Laser Ablation – Inductively Coupled Plasma Mass Spectrometry (LA-ICP-MS) analysis and two aerosol spectrometers – Fast Mobility Particle Sizer (FMPS) and Aerodynamic Particle Sizer (APS). The unique combination of LA-ICP-MS and FMPS offers the possibility of measuring the particle size distribution every 1 s of the ablation process in the size range of 5.6–560 nm. APS extends the information about particle concentration in the size range 0.54–17 μm. Online monitoring of the dry aerosol was performed for two ablation modes (spot and line with a duration of 80 s) with a 193 nm excimer laser system, using the glass reference material NIST 610 as a sample. Different sizes of laser spot for spot ablation and different scan speeds for line ablation were tested. It was found that the FMPS device is capable of detecting changes in particle size distribution at the first pulses of spot laser ablation and is suitable for laser ablation control simultaneously with LA-ICP-MS analysis. The studied parameters of laser ablation have an influence on the resulting particle size distribution. The line mode of laser ablation produces larger particles during the whole ablation process, while spot ablation produces larger particles only at the beginning, during the ablation of the intact layer of the ablated material. Moreover, spot ablation produces more primary nano-particles (in ultrafine mode size range <100 nm) than line ablation. This effect is most probably caused by a reduced amount of large particles released from the spot ablation crater. The larger particles scavenge the ultrafine particles during the line ablation mode.

1. Introduction

Laser ablation (LA) sampling, together with inductively coupled plasma mass spectrometry (ICP-MS) as a detection system, has become a routine method for the direct analysis of various solid samples. The product of laser ablation contains a mixture of vapour, droplets and solid particles. All components are finally transported to a plasma by a carrier gas as a dry aerosol including mainly agglomerates of nanoparticles. In general, the characterisation of aerosols by their particle size distribution (PSD) represents an indispensable tool for fundamental studies of the interaction of laser radiation with materials. Many works have studied PSD of dry aerosol for different samples [1–3] and different ablation conditions such as wavelength [1,3–5], pulse duration [3,6–8], repetition rate [9], pulse energy [6] or carrier gas type [10] and flow rate [9]. Another field of research is the influence of particle size on the ICP-MS signal and elemental fractionation [11–19].

Dry aerosol can be studied by different offline or online techniques. Offline methods include particle collection on special filters, grids or discs and their subsequent analysis. The sample collection can be improved by enhancing the collection efficiency either by using an electrostatic sampler [7] or by separating and depositing particles on substrates according to their size, based on their aerodynamic diameter, e.g. a cascade impactor [20,21]. The offline methods enable not only the visual determination of the particle shapes and size through various microscopic methods (Scanning Electron Microscopy (SEM), Transmission Electron Microscopy (TEM), Electron Microprobe Analysis (EMPA), etc.) but also the study of particle composition by a subsequent chemical analysis (ICP-MS, Particle-induced X-ray Emission (PIXE), etc.) of collected samples [2,7,20,22–24]. The stoichiometry of the ablation can be checked by bulk analyses of all particles using a dissolution method. Furthermore, Energy Dispersive X-ray spectroscopy (EDX) allows the acquisition of the composition of specific particles on the filter, which is very useful for clarification of the fractionation processes [7,23–27]. Nevertheless, the main disadvantage of the offline methods are the lack of time resolution. All the gathered samples include the mass collected during the whole sampling period. In other words, it

* Corresponding author.
E-mail address: mhola@sci.muni.cz (M. Holá).

http://dx.doi.org/10.1016/j.sab.2016.09.017
0584-8547/

means that the offline methods do not bring any information about particle dynamics (the evolution of particle sizes and concentration over time). If such information is required, the use of online sampling methods becomes necessary.

The online monitoring of the particle size distribution can be performed by different types of aerosol analysers. Several different techniques using different physical principles are used to detect the airborne particle concentration (number or mass) – such as Condensation Particle Counters (CPC), photometers such as Optical Particle Sizer (OPS) or Optical Particle Counter (OPC) or electrometers. With regard to particle size, two main principles are used – sizing particles according to their mobility in an electrostatic field (Differential Mobility Analyser (DMA)) and sizing particles according to their aerodynamic behaviour in an accelerated flow (Aerodynamic Particle Sizer (APS)). By combining the particle counters and sizers, a complex aerosol spectrometer can be obtained. The most frequently used for laser-generated aerosol analysis is the Scanning Mobility Particle Sizer (SMPS) system in the submicrometre size range of particle diameters (units of nanometres to 1 μm) [28–30] and APS systems measuring in the size range of 0.5–20 μm. For the processes which involve quick changes in particle concentration, the Fast Mobility Particle Sizer (FMPS) is a very efficient solution, combining principles of the sizing of particle diameters according to their mobility in an electrostatic field along with the detection of their concentration by a set of electrometers. Furthermore, the FMPS system has not been used in combination with the LA-ICP-MS method before.

It is necessary to point out that different methods for PSD estimation provide complementary data based on measuring different physical characteristics of particles. As an example, by comparing the offline impactor technique together with DMA (SMPS) and OPC, the different interpretations of the agglomerated nano-particles in the laser-generated aerosol are revealed. DMA yields physical diameters of particles (based on their mobility in an electrostatic field), which are larger than their volume-equivalent diameter in the case of porous particles and therefore, the mass of the particles cannot be determined accurately compared to the mass-correct impactor measurement. On the other hand, OPC provides particle diameter values, based on the optical equivalent particle diameter, which is strongly dependent on the optical properties of measured particles (scattering coefficient). If the optical properties of measured material are different from particles used during the calibration of the optical instrument (usually polystyrene latex spheres) then the results can significantly differ, usually strongly underestimating the diameter of particles compared to the real sizes [21].

The particle size distribution of laser generated particles is strongly dependent on the ablation conditions (laser parameters, atmosphere…) [10,31–33]. This knowledge is used not only for ICP spectrometry but also for nanoparticle formation [34–37] or pulsed laser deposition methods because different ablation conditions such as laser wavelength, pulse width and energy lead to different morphology, structure and composition of the deposited film [38].

This study deals with the 193 nm ns laser ablation of certified glass standard reference material (SRM) NIST 610. Some studies using SRM NIST 610 as a sample and 193 nm ablation systems were already published and all describe two the main processes used in particle formation. The first process involves condensation of nano-particles (in the 10 nm range) and their coagulation to clusters [5,7,39,40]. The second process includes direct ejection of melted material and the subsequent solidification to spherical particles. The SEM observation refers to spherical particles with a maximum diameter of 200 nm [39]. The characterisation of the clusters' size as non-spherical particles depends on the used particle determination technique and can vary by as much as one order of magnitude [21]. Therefore findings about cluster size differ (depending on the different particle size measuring techniques and different ablation conditions) in various works. Kuhn, Gunther [40] presents particle volume distribution up to 700 nm of particle diameter (spot size 40 μm, repetition rate of 10 Hz, fluence of 18 J cm^{-2}), Kroslakova, Gunther [5] refers to the connection between the spot size and the particle size distribution, 500 nm as a maximum particle size was observed for the 30 μm spot size and particles up to 1 μm occurred for 120 μm spot size (repetition rate 10 Hz, fluence of 28 J cm^{-2}). Guillong et al. [4] state that no particles larger than 400 nm were observed (spot size 60 μm, repetition 4 Hz, fluence of 4.2 J cm^{-2}).

In our study, FMPS and APS aerosol spectrometers were used together with LA-ICP-MS. The FMPS spectrometer offers the possibility of obtaining particle size distribution in quite a wide size range with high time resolution (about 1 s per scan) at the same time. This work is unique in terms of the instrumentation set-up; Laser ablation coupled with the FMPS spectrometer allows for online monitoring of particle physical properties during the ablation process with a high time resolution.

Quantitative LA-ICP-MS analysis traditionally requires parallel measurements of internal standard in order to account for the effects of particle properties on the response of the instrument. Thus, parallel use of FMPS data was also investigated as a potential supplement or alternative to internal standardisation.

2. Experimental

2.1. Sample

The study of the size and concentration of particles formed during laser ablation was carried out on the certified glass standard reference material (SRM) NIST 610. The sample surface was polished and cleaned with ethanol. This transparent glass is one of the most frequently used standards in laser ablation coupled with inductively coupled plasma mass spectrometry.

2.2. Experimental set-up

The particles produced by laser ablation of NIST 610 were analysed by ICP-MS and aerosol spectrometers FMPS and APS giving information about the physical properties of generated particulates.

2.2.1. LA-ICP-MS

The instrumentation consisted of an excimer laser ablation system Analyte G2 (Photo Machines Inc., Redmond, WA, USA) and ICP-MS with a quadrupole analyser Agilent 7500ce and a collision-reaction cell (Agilent, Japan). The laser operates at a wavelength of 193 nm with a pulse duration ≤4 ns. Using helium as a carrier gas with a flow rate of 0.65 l min^{-1}, the aerosol was washed out from the chamber (HelEx) and transported through a polyurethane tube (i.d. 4 mm) to the aerosol spectrometers and ICP-MS. Two ablation modes - spot and line scan - were performed. Spot ablation with different spot sizes and line scan ablation using 85 μm spot size and different scan speeds were compared. The experimental conditions are summarised in Table 1 together with the important parameters of ICP-MS. Selected isotopes were monitored with the total integration time of 1 s which was similar to the FMPS scanning rate.

2.2.2. Fast Mobility Particle Sizer (FMPS)

The FMPS spectrometer is an aerosol instrument measuring number size distribution in a fixed particle size range of 5.6–560 nm with a high time resolution (down to 1 s per sample). The FMPS sizes the particles according to their mobility in an electrostatic field and counts their number using a set of 22 electrometers.

After passing the two unipolar diffusion chargers, the aerosol particles gain a positive charge and continue to the DMA where they are sized according to their mobility in an electrostatic field. In this case, the central rod of the DMA is separated into 4 sections, each having constant positive voltage (0, 85, 470 and 1200 V) throughout the whole scan. The entering aerosol particles are repelled from the central rod, depending on their electrical mobility, and hit one of the electrometers positioned along the outer cylinder of the DMA. The current induced by

Table 1
Experimental parameters and conditions used for LA-ICP-MS.

Experimental parameters for LA ICP-MS	
Laser ablation system	Analyte G2
Wavelength/pulse duration	193 nm/≤4 ns
Fluence	7.8 J cm^{-2}
Repetition rate	10 Hz
Sampling mode	Single spot, line scan
Spot size (single spot)	30, 50, 85, 110, 150 μm (circle)
Spot size (line scan)	85 μm (circle)
Line scan speed	5, 10, 20, 40, 60 μm·s^{-1}
Duration of analysis	80 s
ICP-MS	Agilent 7500ce
RF power	1500 W
Carrier gas	0.65 l min^{-1} He + 0.6 l min^{-1} Ar
Outer plasma gas	15 l min^{-1} Ar
Isotopes analysed	^{7}Li, ^{23}Na, ^{27}Al, ^{28}Si, ^{42}Ca, ^{43}Ca, ^{44}Ca, ^{88}Sr, ^{89}Y, ^{137}Ba, ^{139}La, ^{140}Ce, ^{151}Eu, ^{153}Eu, ^{172}Yb, ^{206}Pb, ^{207}Pb, ^{208}Pb, ^{232}Th, ^{238}U
Sample	
Silicate glass	SRM NIST 610

the particles is then measured and, based on the calibration of the instrument, recalculated to provide the number of particles.

The number of particles in individual size bins (16 channels per decade) is then obtained, resulting in a complete particle number size distribution. The FMPS measures the entire size distribution at once allowing for a substantial reduction in the sampling time. The FMPS spectrometer enables us to obtain particle number size distribution with a fast time resolution, but on the other hand the resolution with regard to particle size is limited to a total of 32 channels (fixed) and the concentration range is limited to about four orders of magnitude, with a lower detection limit slightly below urban background aerosol concentration levels.

The Engine Exhaust Particle Sizer (EEPS, Model 3090, TSI) was used in this work and is functionally similar to the FMPS (Model 3091, TSI). The measurement size range is spread between 5.6 and 560 nm and the scanning rate was set to 1 s per sample.

2.2.3. Aerodynamic Particle Sizer (APS)

The APS is an optical aerosol spectrometer measuring particle number size distribution in the range 0.54–17 μm. The size of the particles in the APS spectrometer is based on their inertial behaviour. At the inlet of the instrument, the stream of the air containing aerosol particles is accelerated in the nozzle. After being accelerated, the aerosol particles pass two parallel laser beams (approximately 100 μm apart from each other) perpendicular to the airflow and the time of the passage of aerosol particles between the two beams is measured. The measured time, after the calibration of the instrument, is directly proportional to the particle size. The APS spectrometer separates the measured particles into 52 size channels with maximum time resolution in orders of seconds. The APS spectrometer represents a useful extension of FMPS measurement range allowing us to measure the number size distribution of aerosol particles in the merged size range from units of nanometres up to 17 μm.

2.3. Sampling procedure

The experimental set-up of the measurement is described in Fig. 1. The particles produced by laser ablation were sampled by two aerosol spectrometers (FMPS and APS).

In order to achieve correct and representative data from the laser ablation process, the following sampling procedure was adopted (see Fig. 1): Two flow splitters were added into the sample transfer line between the LA and ICP-MS about 24 cm apart. In the first one, 1.65 l min^{-1} of Ar was metered by a mass flow controller. From the second one, 1.65 l min^{-1} of diluted sample (with a dilution ratio of 3.5:1) was extracted through an aerosol charge neutraliser (^{85}Kr, 370 MBq, 10 mCi) by an ejector diluter (DI-1000, Dekati) for analysis. This allowed a sample to be taken for external instruments without substantially altering the flow from LA and into ICP-MS. The ejector diluter was also fed by 40.0 l min^{-1} of dried and filtered compressed air, resulting in a dilution ratio of approximately 25:1. Moreover, it allowed the use of aerosol spectrometers without any additional changes in evaluation procedures due to the use of gases with different physical properties than air (for which all the instruments are calibrated). The outlet of the ejector was equipped with a flow splitter, allowing correct isokinetic subsampling, feeding online instruments for particle analysis (FMPS and APS).

2.4. Scanning electron microscope

The shape and structure of the laser-generated particles were studied only on the sample with the ablation craters. Particles deposited on the walls, bottom or surroundings of the ablation crater were investigated using a Scanning Electron Microscope (SEM) MIRA3. It is a FEG SEM (Field Emission Gun Scanning Electron Microscope) with a high

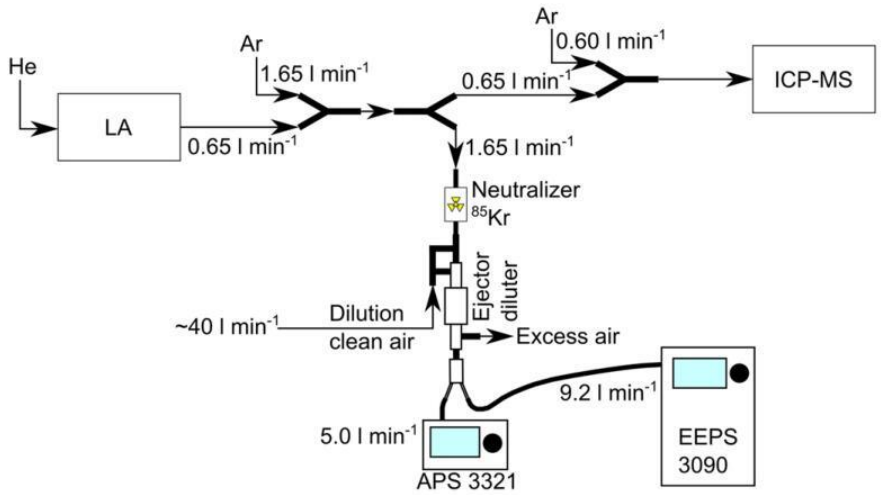

Fig. 1. Schematics of measurement set-up for laser ablation coupled with ICP Mass Spectrometer, Fast Mobility Particle Sizer (EEPS) and Aerodynamic Particle Sizer (APS).

brightness Schottky emitter. FEG SEM microscope has an extraordinary resolution with powerful optional In-Beam SE (Secondary Electron) Detector (1 nm or 2 nm at 30 kV), which is useful for observation of small particles. The sample surface was covered with 10 nm of gold using the accelerating voltage 30 kV prior to SEM analysis in order to increase conductivity of the surface.

2.5. 3D measuring laser microscope

The depth and volume of the ablation craters were estimated by 3D measuring laser microscope LEXT OLS4000 (Olympus). The Olympus LEXT OLS4000 is a confocal microscope capable of taking high-resolution 3D images. The magnification (Optical and Digital) of this microscope ranges from 108×–17,280×. It is capable of resolving features 10 nm in size in the z direction (sample height) and 120 nm in the x-y plane. The system is capable of performing a variety of metrology measurements. Step height, surface/line roughness, and area/volume measurements are some of the more commonly used metrology measurements.

3. Results and discussion

3.1. Temporal behaviour of particle size during spot and line scan ablation

The particle size distribution (PSD) was monitored using the FMPS simultaneously with ICP-MS signal for the spot and line ablation, using the parameters described in the experimental section. The FMPS device was permanently connected to measure the signal (the plasma was on continuously during the experiment).

The FMPS records particle size distribution for each second of the entire ablation process using 32 size channels. To show some specific dynamic features of spot and line ablation and to demonstrate the high scan time of the FMPS device, maps representing the change in PSD over time were created for spot and line scan ablation (Figs. 2, 3). The increase of the signal at the beginning and the decrease at the end of

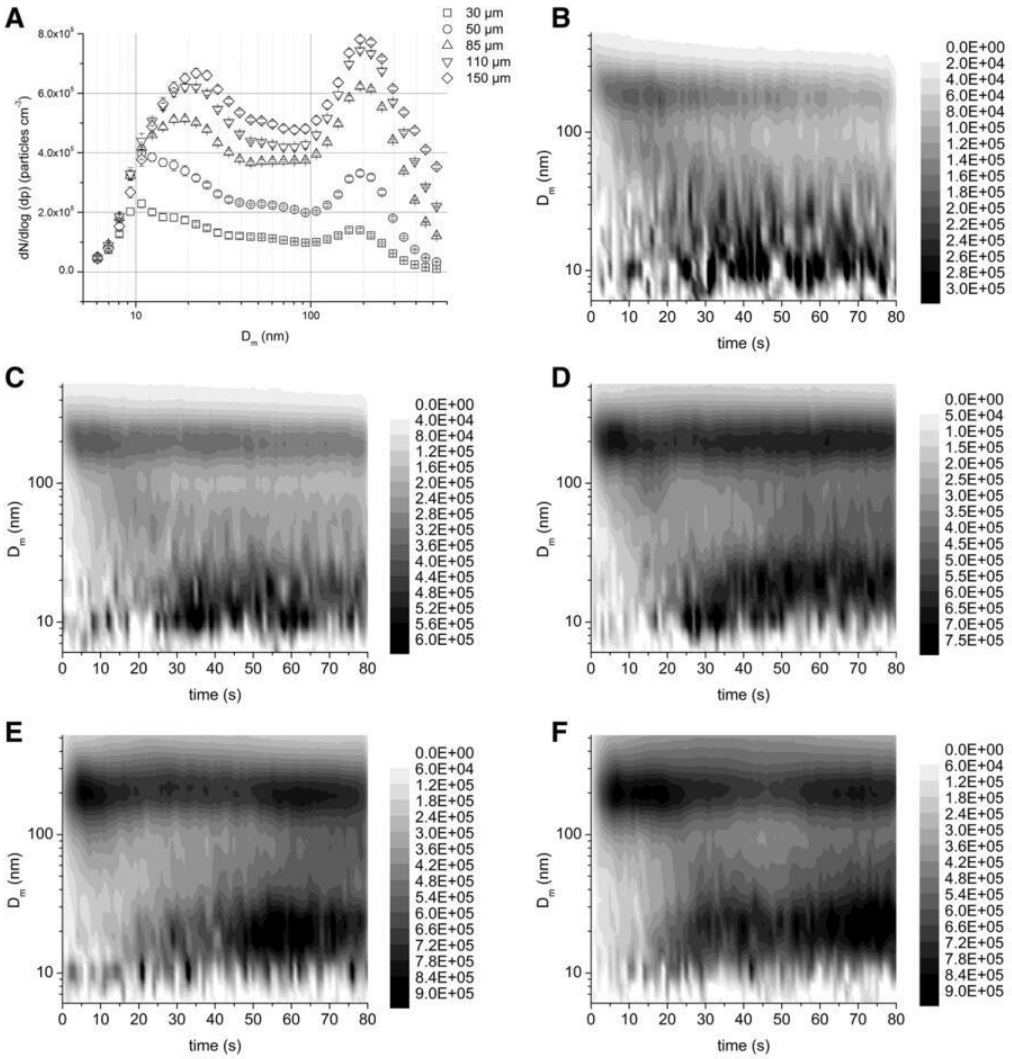

Fig. 2. Particle size distribution graphs (average of 80 s spot ablation) for different spot sizes (2a), the error bars indicate standard deviation of 5 measurements; distribution maps for temporal behaviour of particle number concentration in individual size channels for spot size of 30 µm (2b), 50 µm (2c), 85 µm (2d), 110 µm (2e), 150 µm (2f). The particle concentration scale is shown to the right of each graph dN/dlog(dp) (particles cm^{-3}).

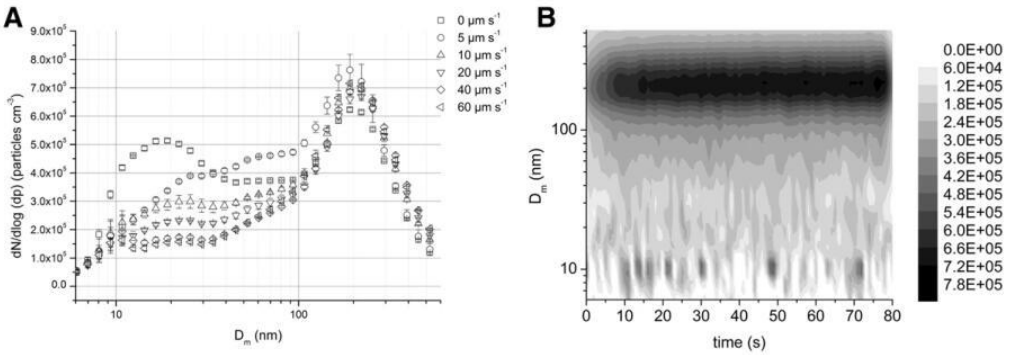

Fig. 3. Particle size distribution graphs (average of 80 s spot ablation) for different scan speeds (3a), the error bars indicate standard deviation of 5 measurements; distribution map for temporal behaviour of particle number concentration in individual size channels for scan speed of 40 μm s^{-1} (3b). The particle concentration scale is shown to the right of each graph $dN/dlog(d_p)$ (particles cm^{-3}).

ablation were excluded from the maps. We decided not to average the repeated measurements in order to preserve the dynamic changes during ablation, which might be different for each measurement. For that reason, only one record for each mode (from the five repetitions of spot and line ablation) is shown below (Figs. 2, 3).

In general, the spot nanosecond laser ablation is characterised by a non-stable temporal response of analytical signals (ICP, laser induced breakdown spectrometry, etc.), attributed to the changes in particle production due to the increasing depth of the ablation crater [41]. Even if the width and depth of the ablation crater is kept at an appropriate ratio, we have to expect a fractionation effect during the sample drilling [42].

The particle size distribution maps (time on x-axis, size of particles (D_m) on y-axis and the concentrations represented by different darkness) are depicted for spot (Fig. 2) and line (Fig. 3) scan of laser ablation. Fig. 2a shows average size distributions for different spot sizes (30, 50, 85, 110 and 150 μm). All the size distributions are bimodal with the first mode in nucleation size range (10–22 nm) and the second mode in fine size range (190 nm). The smaller particles represent the primary particles produced by laser ablation, the larger particles are most probably a product of coagulation/agglomeration of primary nanoparticles or particles originated from the droplets' solidification. The nucleation mode is moving towards larger particle sizes with increasing spot size, which is given by an increased amount of evaporated material. The concentration in the whole size distribution increases as well with increasing spot size, again corresponding to more material being dispersed. In Figs. 2b–2f we can observe temporal changes in the PSD for the spot ablation mode with different spot sizes. Increased production of particles (D_m ~ 190 nm) was observed during single hole drilling within the first 10 s of laser ablation. The production of primary nanoparticles starts approximately 20 s after the start of ablation, which corresponds to a deeper crater. Furthermore, the number concentration of particles with D_m < 50 nm rises with increasing crater depth. Such behaviour at the beginning of the surface layer ablation confirms the theory of nanoparticles being scavenged by larger particles of the standard material. When the crater becomes deeper, the production of larger particles is diminished and the relative concentration of smaller nanoparticles thus increases. Generally, the spot ablation is dynamically changing during the ablation process.

Fig. 3 displays size distributions for different line scan speeds (0, 5, 10, 20, 40 and 60 μm s^{-1}) and particle size distribution evolution in time (map) for the scan speed of 40 μm s^{-1} as an example. Fig. 3a shows averaged size distributions for different scan speeds. All the size distributions are bimodal similar to spot scans. The main difference from spot ablation is diminishing of the nanoparticle mode with increasing line scan speed. This effect is connected with increasing ratio of fresh surface being ablated with faster speed producing primarily larger particles scavenging the nanoparticles. The maximum of the mode for agglomerated particles is fixed for all speeds at 190 nm as in the case of spot ablation. Fig. 3b proves that the ablation process is steadier for the line scan mode compared to spot scan mode. The scan ablation is stabilized after initial 10 s (see Fig. 3b for the scan speed of 40 μm s^{-1}).

3.2. Particles with diameter >540 nm

3.2.1. APS particle size distribution

APS was used to extend the measurement range of FMPS in order to confirm or reject the hypothesis of supermicrometre particle production during laser ablation. Fig. 4 displays comparison of average size distributions from spot (85 μm in diameter) and line scan (scan speed of 40 μm s^{-1}) ablation processes. It has to be pointed out that the agglomerate nature of larger particles, having higher porosity and thus much lower effective density, results in higher acceleration of these particles inside APS than standard compact spherical particles. This effect causes a shift of measured sizes towards smaller particles resulting in a shift of sampled particles out of the APS measurement range, which inflicts also much lower concentrations of the large particles compared to the corresponding end of FMPS particle size distribution being even two orders of magnitude higher. Nevertheless, even the measurement burdened by such an artefact in the measurement principle shows that the line

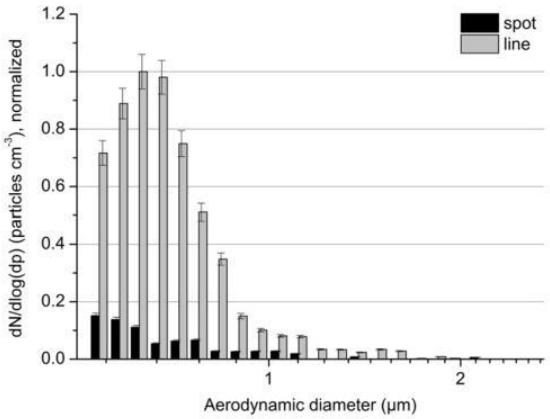

Fig. 4. Particle size distribution by Aerodynamic Particle Sizer for spot ablation mode (85 μm) and line scan (40 μm s^{-1}); the error bars indicate standard deviation of 5 measurements.

scan produces almost 10× higher concentration of particles >540 nm with visible shift towards larger particles.

3.2.2. Crater volume and LA-ICP-MS signal

The presence of particles larger than 0.5 μm in diameter during laser ablation of NIST610 is also discussed in the following chapters. The temporal changes of LA-ICP-MS signal indicate that large particles (>0.5 μm) form mostly at the beginning of spot ablation (first 20 s), while they are produced constantly during line ablation (see Section 3.3, Fig. 5). The volumes of ablation craters estimated by 3D measuring laser microscope indicate 2× more material volume released during line ablation (crater of 1100 000 ± 28,000 μm^3 with the depth of 9 μm for 40 μm s^{-1}) than in the case of ablation into one spot (510,000 ± 11,000 μm^3 with the depth of 87 μm). Because the FMPS results do not support this finding (approximately the same particle volume for spot and line) we can expect a higher production of particles >0.5 μm for line scan which was confirmed by APS measurements.

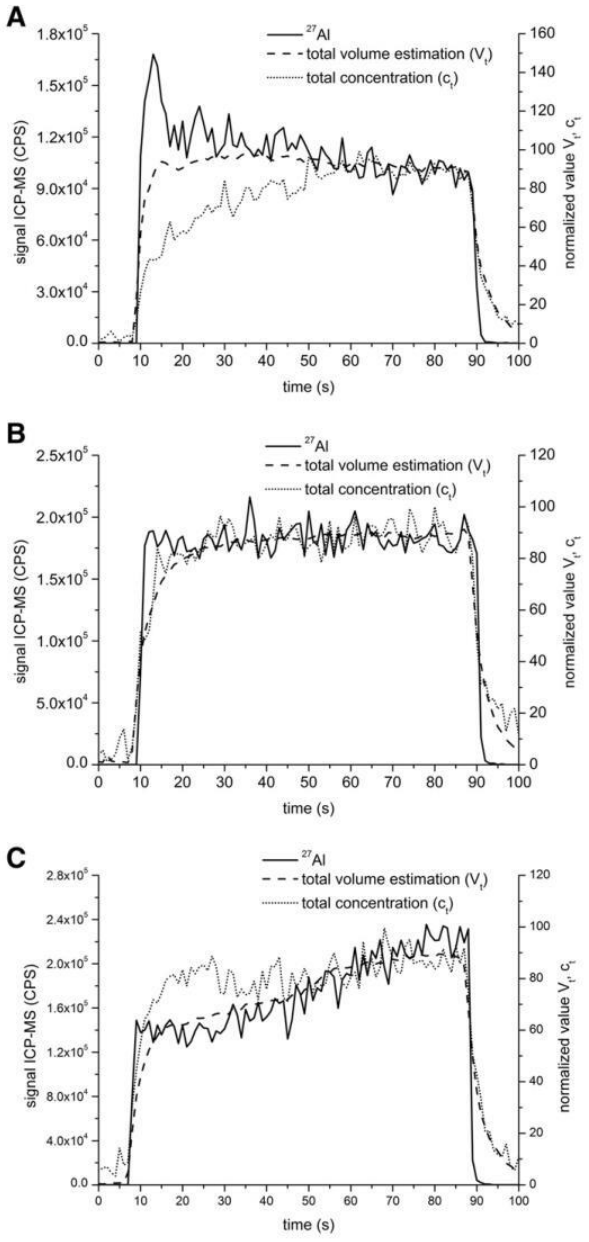

Fig. 5. Temporal behaviour of total particle concentration by FMPS, total particle volume by FMPS and LA-ICP-MS signal for ^{27}Al; a spot ablation, b stable line scan, c non-stable line scan.

Generally, the LA-ICP-MS response gave 1.8× higher signal intensity of selected isotopes for the line ablation mode compared to single hole ablation (see Fig. 5). Several experiments confirmed the presence of particles with diameter >560 nm (out of FMPS range), which contribute to the LA-ICP-MS signal, although they are probably not completely vapourized and ionized in the ICP plasma [14,17]. The imperfect vapourization could be the reason for the reduced LA-ICP-MS signal for the line scan when comparing line/spot ratios of crater volumes (2:1) to signal ratios (1.8:1), if we expect increased contribution of large particles for the line scan mode. This is in good agreement with the theory published previously, which reported that during the contact of a laser beam with an intact sample surface (e.g. the first pulses of spot ablation), the size of the particles is larger than during ablation of a surface already transformed by a laser beam interaction [17]. In the case of line ablation, each pulse hits the ablated area together with the intact area and the ratio of the areas depends on the velocity of the line scan.

3.3. LA-ICP-MS signal vs particle formation

The capability of any particle spectrometer to detect online temporal changes in particle formation (particle concentration, volume or mass) could be applied instead of the internal standardisation for LA-ICP-MS quantitative analysis. Even if the FMPS does not cover the whole particle size range the correlation between the LA-ICP-MS signal and the total particle concentration (sum of particle concentrations in all size bins) was tested. Because the LA-ICP-MS response should correspond to the volume of material entering the plasma we decided to work with a rough estimate of the total particle volume (calculated as spherical particle shape) from FMPS as well.

The results are represented by three examples in Fig. 5. The first – spot ablation (diameter of 85 μm, Fig. 5a) shows that the particle number concentration copies the ICP-MS signal (represented by ^{27}Al) only at the end of ablation (55–80 s) when the production of large particles is reduced and the concentration of nanoparticles and clusters is almost stable (see PSD in Fig. 2d). Using the particle volumetric concentration led to an obvious improvement in correlation with LA-ICP-MS dependence during the whole ablation analysis. A detailed study of Fig. 5a points out that the LA-ICP-MS signal exceeded the particle volume during the first 20 s of spot ablation. This can be explained by volume released from particles with D_m larger than 560 nm that are also present in the sample, especially at the start of a single hole drilling and that also partially contributes to the LA-ICP-MS signal [17].

Fig. 5b demonstrates uniform laser ablation stabilized in ICP-MS signal and in particle formation using line mode (40 μm s^{-1}; temporal PSD is shown in Fig. 3b). In this case the particle number concentration temporal record is closely following the fluctuations during LA-ICP-MS analysis (after the initial 10 s when the particle formation is stabilized as it was presented by the distribution map in Fig. 3b). This behaviour agrees well with the previously discussed constant formation of larger particles, keeping the ration between the large and nanoparticles constant during the whole line scan. And thus also the volumetric concentration does not exhibit any significant deviation from the ICP-MS signal pattern. Even if a stable LA-ICP-MS signal is expected, signal fluctuation can occur during analysis as in the case of line ablation in Fig. 5c. We simulated nonstable ablation signal by strangling the transport tube at the beginning of ablation which caused a reduction of the LA-ICP-MS signal. After 30 s the tubing was unfastened and the signal started to increase. The volumetric concentration is able to copy the ^{27}Al signal changes whereas the total particle concentration is almost stable

throughout the scan pointing to the variable large/nano particle ratio during this particular scan.

In this study only a rough particle volume estimation was employed. In the case of porous particle aggregates produced from laser ablation, the estimation of precise particle volume is highly complicated for several reasons. First, FMPS covers only particles up to the size of 560 nm in diameter and second, the FMPS measurement principle use neither correction to non-spherical shape of particles nor correction for particle aggregates. Nevertheless, we can see the potential in using the volumetric particle concentration as control of signal fluctuations during LA-ICP-MS analysis based on the obtained results.

3.4. Structure of the particles

The knowledge of the particle shape and structure should be an essential part of an aerosol study improving the information about particle formation. Traditionally, particles are collected on a filter for subsequent analysis. Using this method raises a question regarding the origin of the clusters on the filter, where they usually form "fibres". In previous works it has been proved that although the particles agglomerate already in the ablation cell [39] the "fibre" clusters form on the filter due to the high particle concentration in specific filter areas [23].

To avoid another supplemental discussion about the cluster origin the particles were observed by SEM directly on the sample – as deposited particles on the ablation craters or surrounding the ablation craters. Two different particle generation mechanisms were expected – condensation of nanoparticles from the vapour and direct ejection of droplets [39]. Fig. 6 shows SEM observations. Laser ablation crater after spot laser ablation (Fig. 6a; spot diameter of 85 μm) proved the presence of condensed nanoparticles creating agglomerates (Fig. 6b) as well as mostly spherical particles created from droplet solidification. The later mentioned particles mostly did not exceed the diameter of 100 nm. The size of the clusters formed due to coagulation of vapour-condensed particles is not evident but we can suppose it from the particle size distribution graphs (Fig.2). The initial vapour-condensed particles (about

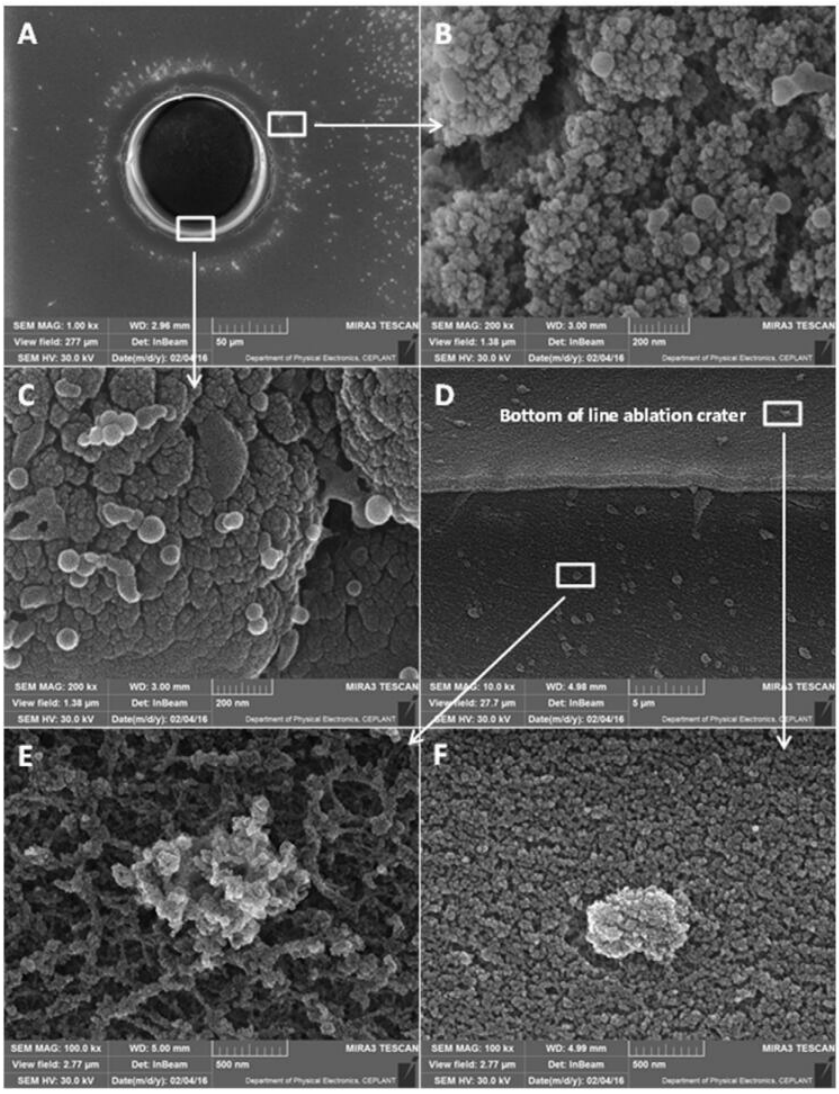

Fig. 6. SEM image of laser-generated particles deposited in the ablation craters or their near proximity. A) spot laser ablation crater, B) detail of spherical particles caught on spot crater wall, C) detail of spot crater surroundings, D) part of line ablation crater, E) detail of particle cluster surrounding line crater, F) detail of particle cluster from the line crater bottom.

20 nm of diameter as shown) coagulate to clusters with the diameter mostly about 200 nm (as shown in Fig. 2).

Observing line ablation craters (Fig. 6d; scan speed 20 μm s^{-1}) some differences were found compared to spot ablation. No spherical particles originating from the droplets were found. A possible explanation could be due to the reduction of thermal effect during line scan ablation. On the other hand, clusters with obviously larger diameters were observed at the bottom of the ablation crater, the same as the ones surrounding the crater. The size of the "large clusters" mostly exceeds the upper limit of FMPS (560 nm) and so we can assume their PSD was obtained by APS with the distribution maximum around 650 nm (Fig. 4). APS determined a concentration 10× higher of "large clusters" for the line scan than for spot mode. Therefore, a link between intact sample surface-laser interaction and "large cluster" formation is presumed.

The SEM together with APS results can lead to the finding that an increased amount of clusters >500 nm is produced using the line ablation mode. The structure of the clusters is irregular, probably composed of vapour-condensed primary nanoparticles. The cluster size leads to incomplete vapourization and ionization in ICP and so only to partial contribution to the ICP-MS signal. [13,14].

4. Conclusions

In this study, a novel approach of using a fast-response particle size classifier has been examined. The suitability of high time resolution FMPS for online size characterisation of dry aerosol was tested during LA-ICP-MS analysis of SRM NIST 610. Single spot and line scan ablation was performed using different spot sizes for spot ablation and different scan speeds for line ablation. This enabled the determination of the capability of aerosol spectrometers to monitor changes in particle size distribution caused by different ablation modes.

At first, the modal structure of particle number size distribution was studied for each ablation mode in the FMPS measurement range (5.6–560 nm). All size distributions are bimodal with the first mode in nucleation size range (10–22 nm) and the second mode in fine size range (190 nm). The smaller particles represent the primary particles produced by laser ablation, the larger particles are most probably a product of coagulation/agglomeration of primary nanoparticles or droplet solidification particles. Using spot ablation, the nucleation mode moves towards larger particle sizes with increasing spot size, which is given by an increased amount of evaporated material. In the case of line scan, the main difference from spot ablation is diminishing of the nanoparticle mode with increasing line scan speed. This effect is probably connected with increasing the ratio of fresh surface being ablated with faster scan speeds producing primarily larger particles consequently scavenging the nanoparticles.

Temporal changes of PSD with the time resolution of 1 s were examined. Increased production of particles (D_m ~ 190 nm) were observed during single hole drilling within the first 10 s of laser ablation. The production of primary nanoparticles starts approximately 20 s after the start of the ablation process, which corresponds to a deeper crater. Temporal behaviour of laser ablation proves that the ablation process is steadier for the line scan mode compared to the spot scan mode.

The structure of the particles was studied by SEM. For spot ablation, agglomerates with irregular shape were observed together with mostly spherical particles with a maximum diameter of 100 nm originating from droplet solidification. In the case of line ablation, the solidified droplets were missing but large clusters mostly exceeding the upper limit of FMPS (560 nm) were observed. The size of the large clusters were estimated by APS. The APS PSD proved the presence of supermicrometre particles up to 2 μm with 10× higher concentration for line ablation mode compared to spot ablation mode.

LA-ICP-MS signals of selected isotopes gave approximately 1.8× higher response for the line mode than for the spot ablation. Confocal microscopy showed 2× higher volume for line ablation craters. The reduced LA-ICP-MS signal for the line scan can be caused by incomplete evaporation and ionization of larger particles (present in higher concentrations during ablation of intact surface) in the plasma source. All findings point to much higher particle production using line scan ablation. From the particle size distribution measurements we can claim that nearly half of the released material volume (for the line scan) is created by clusters with a diameter of 0.5–2 μm.

This detailed study of online monitoring of particles produced by laser ablation simultaneously with the ICP-MS signal shows the variations in particle concentration and analytical signal during different ablation modes with various laser conditions. FMPS results give a promise for the future use of an aerosol spectrometer to compensate the signal fluctuations instead of the internal standard. Although much work is needed to ensure proper understanding of the signals and calibration for the respective instruments, this work suggests that the particle size distribution is not constant, neither throughout the laser ablation process nor with respect to the geometric pattern of the ablation process and that online monitoring of particle size distribution may be valuable as complementary information aiding the interpretation and derivation of quantitative data from the LA-ICP-MS signal.

Acknowledgements

The results of this research have been acquired within CEITEC 2020 (LQ1601) project with financial contribution made by the Ministry of Education, Youths and Sports of the Czech Republic within special support paid from the National Programme for Sustainability II funds. V.K. acknowledges the Czech Science Foundation for a grant to support the project S 14-13600S. H.N. and V.K. acknowledge support of the project MUNI/A/1492/2015 from Masaryk University Specific Research Programme. J. O. acknowledges Czech Science Foundation for grant P503/12/G147. M.V. acknowledges Czech Ministry of Education, Youth and Sports programme NPU I (LO), project LO1311. The authors would like to thank Dr. Jurmanova for SEM micrographs supported by the project CZ.1.05/2.1.00/03.0086 funded by European Regional Development Fund and project LO1411 (NPU I) funded by Ministry of Education Youth and Sports of Czech Republic. All authors thank Dr. Michael Cusack for his language corrections of the manuscript.

References

[1] D.W. Lee, M.D. Cheng, Particle generation by laser ablation during surface decontamination, J. Aerosol Sci. 35 (2004) 1527–1540.
[2] M. Hola, V. Konecna, P. Mikuska, J. Kaiser, V. Kanicky, Influence of physical properties and chemical composition of sample on formation of aerosol particles generated by nanosecond laser ablation at 213 nm, Spectrochim. Acta B At. Spectrosc. 65 (2010) 51–60.
[3] M. Ohata, D. Tabersky, R. Glaus, J. Koch, B. Hattendorf, D. Gunther, Comparison of 795 nm and 265 nm femtosecond and 193 nm nanosecond laser ablation inductively coupled plasma mass spectrometry for the quantitative multi-element analysis of glass materials, J. Anal. At. Spectrom. 29 (2014) 1345–1353.
[4] M. Guillong, I. Horn, D. Gunther, A comparison of 266 nm, 213 nm and 193 nm produced from a single solid state Nd: YAG laser for laser ablation ICP-MS, J. Anal. At. Spectrom. 18 (2003) 1224–1230.
[5] I. Kroslakova, D. Gunther, Elemental fractionation in laser ablation-inductively coupled plasma-mass spectrometry: evidence for mass load induced matrix effects in the ICP during ablation of a silicate glass, J. Anal. At. Spectrom. 22 (2007) 51–62.
[6] P.K. Diwakar, S.S. Harilal, N.L. LaHaye, A. Hassanein, P. Kulkarni, The influence of laser pulse duration and energy on ICP-MS signal intensity, elemental fractionation, and particle size distribution in NIR fs-LA-ICP-MS, J. Anal. At. Spectrom. 28 (2013) 1420–1429.
[7] R. Glaus, R. Kaegi, F. Krumeich, D. Gunther, Phenomenological studies on structure and elemental composition of nanosecond and femtosecond laser-generated aerosols with implications on laser ablation inductively coupled plasma mass spectrometry, Spectrochim. Acta B At. Spectrosc. 65 (2010) 812–822.
[8] J. Koch, A. von Bohlen, R. Hergenroder, K. Niemax, Particle size distributions and compositions of aerosols produced by near-IR femto- and nanosecond laser ablation of brass, J. Anal. At. Spectrom. 19 (2004) 267–272.
[9] J.J. Gonzalez, A. Fernandez, D. Oropeza, X. Mao, R.E. Russo, Femtosecond laser ablation: experimental study of the repetition rate influence on inductively coupled plasma mass spectrometry performance, Spectrochim. Acta B At. Spectrosc. 63 (2008) 277–286.
[10] I. Horn, D. Gunther, The influence of ablation carrier gasses Ar, He and Ne on the particle size distribution and transport efficiencies of laser ablation-induced aerosols: implications for LA-ICP-MS, Appl. Surf. Sci. 207 (2003) 144–157.

[11] D.C. Perdian, S.J. Bajic, D.P. Baldwin, R.S. Houk, Time-resolved studies of particle effects in laser ablation inductively coupled plasma-mass spectrometry, J. Anal. At. Spectrom. 23 (2008) 325–335.
[12] S.H. Jeong, O.V. Borisov, J.H. Yoo, X.L. Mao, R.E. Russo, Effects of particle size distribution on inductively coupled plasma mass spectrometry signal intensity during laser ablation of glass samples, Anal. Chem. 71 (1999) 5123–5130.
[13] M. Guillong, D. Gunther, Effect of particle size distribution on ICP-induced elemental fractionation in laser ablation-inductively coupled plasma-mass spectrometry, J. Anal. At. Spectrom. 17 (2002) 831–837.
[14] M. Guillong, H.R. Kuhn, D. Gunther, Application of a particle separation device to reduce inductively coupled plasma-enhanced elemental fractionation in laser ablation-inductively coupled plasma-mass spectrometry, Spectrochim. Acta B At. Spectrosc. 58 (2003) 211–220.
[15] H.R. Kuhn, D. Gunther, Elemental fractionation studies in laser ablation inductively coupled plasma mass spectrometry on laser-induced brass aerosols, Anal. Chem. 75 (2003) 747–753.
[16] H.R. Kuhn, N.J. Pearson, S.E. Jackson, The influence of the laser ablation process on isotopic fractionation of copper in LA-MC-ICP-MS, J. Anal. At. Spectrom. 22 (2007) 547–552.
[17] H.R. Kuhn, D. Gunther, Laser ablation-ICP-MS: particle size dependent elemental composition studies on filter-collected and online measured aerosols from glass, J. Anal. At. Spectrom. 19 (2004) 1158–1164.
[18] H.R. Kuhn, M. Guillong, D. Gunther, Size-related vaporisation and ionisation of laser-induced glass particles in the inductively coupled plasma, Anal. Bioanal. Chem. 378 (2004) 1069–1074.
[19] P. Weis, H. Beck, D. Gunther, Characterizing ablation and aerosol generation during elemental fractionation on absorption modified lithium tetraborate glasses using LA-ICP-MS, Anal. Bioanal. Chem. 381 (2005) 212–224.
[20] R. Jaworski, E. Hoffmann, H. Stephanowitz, Collection and separation of particles by size from laser ablated material, Int. J. Mass Spectrom. 219 (2002) 373–379.
[21] H.R. Kuhn, J. Koch, R. Hargenroder, K. Niemax, M. Kalberer, D. Gunther, Evaluation of different techniques for particle size distribution measurements on laser-generated aerosols, J. Anal. At. Spectrom. 20 (2005) 894–900.
[22] E.C. Hathorne, R.H. James, P. Savage, O. Alard, Physical and chemical characteristics of particles produced by laser ablation of biogenic calcium carbonate, J. Anal. At. Spectrom. 23 (2008) 240–243.
[23] M. Hola, V. Konecna, P. Mikuska, J. Kaiser, K. Palenikova, S. Prusa, R. Hanzlikova, V. Kanicky, Study of aerosols generated by 213 nm laser ablation of cobalt-cemented hard metals, J. Anal. At. Spectrom. 23 (2008) 1341–1349.
[24] J. Kosler, M. Wiedenbeck, R. Wirth, J. Hovorka, P. Sylvester, J. Mikova, Chemical and phase composition of particles produced by laser ablation of silicate glass and zircon — implications for elemental fractionation during ICP-MS analysis, J. Anal. At. Spectrom. 20 (2005) 402–409.
[25] G. Alloncle, N. Gilon, C. Legens, C.P. Lienemann, B. Rebours, L. Sorbier, S. Morin, R. Revel, Following the evolution of morphology, composition and crystallography of alumina based catalysts after laser ablation: implications for analysis by LA-ICP-AES, Appl. Surf. Sci. 255 (2009) 8978–8985.
[26] D. Fliegel, M. Klementova, J. Kosler, Phase and composition changes of titanite during laser ablation inductively coupled plasma mass spectrometry analysis, Anal. Chem. 82 (2010) 4272–4277.
[27] M. Hola, P. Mikuska, R. Hanzlikova, J. Kaiser, V. Kanicky, Tungsten carbide precursors as an example for influence of a binder on the particle formation in the nanosecond laser ablation of powdered materials, Talanta 80 (2010) 1862–1867.
[28] J.H. Choi, D. Lucas, C.P. Koshland, Laser ablation of nanoscale pairticles with 193 nm right, 8th International Conference on Laser Ablation, Iop Publishing Ltd., Banff, Canada 2005, pp. 54–59.
[29] D.W. Lee, M.D. Cheng, Particle generation by ultraviolet-laser ablation during surface decontamination, J. Air Waste Manage. Assoc. 56 (2006) 1591–1598.
[30] Z. Marton, L. Landstrom, M. Boman, P. Heszler, A comparative study of size distribution of nanoparticles generated by laser ablation of graphite and tungsten, Mater. Sci. Eng. C Biomim. Supramol. Syst. 23 (2003) 225–228.
[31] V. Dudoitis, V. Ulevicius, G. Raciukaitis, N. Spirkauskaite, K. Plauskaite, Generation of metal nanoparticles by laser ablation, Lith. J. Phys. 51 (2011) 248–259.
[32] N.L. LaHaye, S.S. Harilal, P.K. Diwakar, A. Hassanein, P. Kulkarni, The effect of ultrafast laser wavelength on ablation properties and implications on sample introduction in inductively coupled plasma mass spectrometry, J. Appl. Phys. 114 (2013).
[33] N.J. Saetveit, S.J. Bajic, D.P. Baldwin, R.S. Houk, Influence of particle size on fractionation with nanosecond and femtosecond laser ablation in brass by online differential mobility analysis and inductively coupled plasma mass spectrometry, J. Anal. At. Spectrom. 23 (2008) 54–61.
[34] H. Cai, N. Chaudhary, J. Lee, M.F. Becker, J.R. Brock, J.W. Keto, Generation of metal nanoparticles by laser ablation of microspheres, J. Aerosol Sci. 29 (1998) 627–636.
[35] C.B. Juang, H. Cai, M.F. Becker, J.W. Keto, J.R. Brock, Synthesis of nanometer glass particles by pulsed-laser ablation of microspheres, Appl. Phys. Lett. 65 (1994) 40–42.
[36] M. Ullmann, S.K. Friedlander, A. Schmidt-Ott, Nanoparticle formation by laser ablation, J. Nanopart. Res. 4 (2002) 499–509.
[37] P.S. Waraich, B. Tan, K. Venkatakrishnan, Laser ablation of microparticles for nanostructure generation, J. Nanopart. Res. 13 (2011) 5251–5256.
[38] J. Perriere, C. Boulmer-Leborgne, R. Benzerga, S. Tricot, Nanoparticle formation by femtosecond laser ablation, J. Phys. D Appl. Phys. 40 (2007) 7069–7076.
[39] H.R. Kuhn, D. Gunther, The agglomeration state of nanosecond laser-generated aerosol particles entering the ICP, Anal. Bioanal. Chem. 383 (2005) 434–441.
[40] H.R. Kuhn, D. Gunther, A quantification strategy in laser ablation ICP-MS based on the transported aerosol particle volume determined by optical particle size measurement, J. Anal. At. Spectrom. 21 (2006) 1209–1213.
[41] V. Mozna, J. Pisonero, M. Hola, V. Kanicky, D. Guenther, Quantitative analysis of Fe-based samples using ultraviolet nanosecond and femtosecond laser ablation-ICP-MS, J. Anal. At. Spectrom. 21 (2006) 1194–1201.
[42] S.M. Eggins, L.P.J. Kinsley, J.M.G. Shelley, Deposition and element fractionation processes during atmospheric pressure laser sampling for analysis by ICP-MS, Appl. Surf. Sci. 127 (1998) 278–286.

PAPER 8

The influence of material properties on highly time resolved particle formation for nanosecond laser ablation

Holá, M.*, Ondráček, J., Nováková, H., Vojtíšek-Lom, M., Hadravová, R., Kanický, V.

Spectrochimica Acta Part B. 2018, 148, 193–204, DOI 10.1016/j.sab.2018.07.001

Contribution:

LA-ICP-MS and aerosol design of experiments and measurements, data evaluation, studying of ablation craters and the particle structure, manuscript writing, corresponding author.

Spectrochimica Acta Part B 148 (2018) 193–204

Contents lists available at ScienceDirect

Spectrochimica Acta Part B

journal homepage: www.elsevier.com/locate/sab

The influence of material properties on highly time resolved particle formation for nanosecond laser ablation

Markéta Holá[a,b,*], Jakub Ondráček[c], Hana Nováková[a,b], Michal Vojtíšek-Lom[d], Romana Hadravová[e], Viktor Kanický[a,b]

[a] Central European Institute of Technology (CEITEC), Masaryk University, Kamenice 5, 62500 Brno, Czech Republic
[b] Department of Chemistry, Faculty of Science, Masaryk University, Žerotínovo náměstí 9, 60200 Brno, Czech Republic
[c] Institute of Chemical Process Fundamentals of the CAS, Rozvojová 135, 16500 Prague, Czech Republic
[d] Faculty of Mechanical Engineering, Czech Technical University of Prague, Zikova 4, 16000 Prague, Czech Republic
[e] Institute of Organic Chemistry and Biochemistry of the CAS, Flemingovo náměstí 2, 16610 Prague, Czech Republic

A B S T R A C T

The dynamics of aerosol particles formed during nanosecond laser ablation of glass and steel samples was studied in the Laser Ablation – Inductively Coupled Plasma Mass Spectrometry (LA-ICP-MS) system. In order to follow the evolution of particle size distribution with high time resolution during the laser ablation process, two fast response aerosol spectrometers were used. Engine Exhaust Particle Sizer (EEPS) together with Optical Particle Sizer (OPS) provided Particle Size Distribution (PSD) in the range 5.6 nm – 10 μm with the integration time of 1 s. To obtain additional information about the PSD of larger particles (0.5–10 μm) in more detail, an Aerodynamic Particle Sizer (APS) recorded average PSD of each ablation (80 s). To investigate the effect of the sample matrix on aerosol dynamics and composition, glass NIST 610 and steel F4 samples were studied. Spot and line ablation mode was applied to compare the behavior of both ablation modes in time. The degree of thermal effect and fractionation was studied from the structure and size of ablation craters, the structure of particles and the LA-ICP-MS signal. The ablation process was influenced mostly by the material itself even if the ablation mode also plays an important role on the formation of aerosol. A significant correlation of ICP-MS signal with a concentration of particles > 300 nm was observed.

1. Introduction

Laser Ablation Inductively Coupled Plasma Mass Spectrometry (LA-ICP-MS) is a method widely used in analytical chemistry for the direct elemental analysis of solid samples. In this connection, laser ablation means the process of removing material from the sample surface under the action of laser light. The released material is then transported to ICP where it is vaporized and ionized. Finally, a mass spectrometer is used to separate and quantify those ions. Laser ablation should ensure representative sampling to ICP, so the course of laser ablation is critical for the usability of the analytical method.

The laser beam-sample interaction is a complex process depending on both the laser ablation conditions (pulse duration, wavelength, repetition rate, pulse energy, spot size) and the samples physical and chemical properties [1–6]. Generally, the process of laser ablation can interact with the material in two basic ways – *thermal* (photothermal) and *non-thermal* (photochemical) [7–10]. For longer laser pulses (nanosecond ablation) heat conduction, melting, evaporation and plasma formation are the dominant processes. The energy of the laser pulse is absorbed by the sample surface and form a temperature field due the heat conduction. Depending on the achieved temperature the material is molten up, evaporates or is transferred to a plasma state. The parameters of the laser ablation especially pulse duration, and pulse energy influence the proportionality of evaporation and melt sputtering as main processes for nanosecond laser ablation [11]. The physical and chemical properties of the sample can significantly influence the laser energy absorption (absorption coefficient for the specific wavelength) the heat transfer (thermal conductivity) [12] and degree of plasma shielding (attenuation of the incoming laser radiation by plasma). On the other hand the sample heating by the laser irradiation modifies the optical and thermo-physical properties significantly, such as surface reflectivity, electrical and thermal conductivity, surface tension, latent heat of vaporization [13].

Longer laser pulses in particular (nanoseconds, picoseconds) raise the ratio of thermal effects causing non-stoichiometric ablation (preferential vaporization of volatile components) [14–19]. The heat transfer during longer pulses causes material melting. The mechanical liquid-plasma interaction is a source of large particles present in the aerosol due to the hydrodynamic sputtering. The extent of the hydrodynamic sputtering is dependent on the melt thickness creating the upper layer of the ablation crater surface. Generally, higher heat diffusion and lower fluences increase the melt thickness and thus the

* Corresponding author at: Central European Institute of Technology (CEITEC), Masaryk University, Kamenice 5, 62500 Brno, Czech Republic.
E-mail address: mhola@sci.muni.cz (M. Holá).

https://doi.org/10.1016/j.sab.2018.07.001
Received 28 November 2017; Received in revised form 26 June 2018; Accepted 2 July 2018
Available online 10 July 2018
0584-8547/

solidification time which increases fractionated evaporation and hydrodynamic sputtering. Very different thermal diffusivity of samples such as metal and glass can result in a layer about one order thicker for metal using fluences < 10 J cm^{-2} [20]. The generated droplet amount and size is dependent on the melt layer thickness and models of the hydrodynamic sputtering were created for different ablation conditions [21].

The other part of the aerosol is formed by gas-to-particle formation process, for smaller size fractions. Several works have tried to explain the process of nanoparticle formation in the laser induced plume during the cooling stage based on visualization techniques performed directly in the ablation cell (e.g. the scattering images of the laser plume) [22] or based on theoretical modeling [23–26]. Other works are interested in the nanoparticles as a "product" of the sampling process and use an aerosol analyser to characterize their size in the gas flow [27]. All studies confirm that nanoparticles produced by nucleation of the vapor are smaller than 100 nm (depending on the laser and sample parameters) before cluster agglomeration starts [28]. The detailed observation of nanoparticle formation is difficult thanks to the fact that the nanoparticles create clusters with irregular shapes and undefined density. These cluster properties make it impossible to accurately determine their size using aerosol spectrometers that usually work with a model for spherical particles with uniform density and optical properties. This can lead to significantly different results of the cluster's size (as much as one order of magnitude) if a different determination technique is used [29]. The visualization of nanoparticles and the clusters is also problematic. Because the commonly used methods such as Scanning Electron Microscopy (SEM) or Transmission Electron Microscopy (TEM) work with "static" samples it is necessary to fix the particles from the gas flow to the proper substrate. This causes additional formation of larger clusters and to differentiate them from the original is almost impossible [19, 27]. However, comparison of the images of the particles formed under different conditions can be very helpful [30, 31].

Generally, the estimation of the proportion of thermal effects during laser/sample interaction is simply achieved from the study of ablation craters or a detailed study of ICP-MS signal for each isotope [32–34]. More detailed research determines the particle size distribution of the laser generated aerosol [1, 35–37]. The properties of aerosol produced by laser ablation can be monitored on-line simultaneously with LA-ICP-MS analysis using aerosol spectrometers [38]. The choice of aerosol spectrometer is usually dependent on the measured size range of the particles, but the detection principle of aerosol spectrometer must also be considered to avoid a wrong interpretation of the results, especially for non-spherical clusters [29].

Different techniques for the analysis of physical properties of aerosol particles produced during the laser ablation process are commercially available. These include electrostatic classifiers combined with particle detectors (such as condensation particle counters or electrometers), various photometric devices and cascade impactors for offline analysis. All the instruments offer some advantages in their measurement principles, but most of them are also burdened with some limitation.

For example, the Scanning Mobility Particle Sizer (SMPS) offers excellent resolution in regards to particle sizing, but it is limited in time resolution [39, 40]. Fast Mobility Particle Sizers (FMPS or EEPS) have great time resolution, but fewer particle size bins and rely on calibration due to initial unipolar electrical charging of the particles in the sample [41]. Photometric devices are simple instruments, easy to use, but their measurement is strongly dependent on the optical properties (scattering coefficient, surface morphology) of the sampled aerosol [42]. The cascade impactors [43, 44] can be taken as a standard method (gravimetric analysis), but they give limited size resolution and offer only integral values in time (offline analysis). Generally, when using any of the aerosol instruments, we have to be aware of the measurement method used and take its advantages and limitations into account when interpreting the measured data.

In this study, two fast response aerosol spectrometers were used (EEPS and OPS) in order to follow the fast process of particle formation and the consecutive processes changing the particle size and morphology (e.g. coagulation and agglomeration).

This study follows the previous research on NIST 610 [38]. Beside the laser ablation conditions such as fluence, spot size or ablation mode, the sample properties are another important parameter that influences the particle formation. The measurement of highly time resolved PSD of aerosol particles produced by laser ablation of two standard materials with different composition and physical properties can reveal the differences in particle formation, coagulation and agglomeration. The influence of the ablation mode on particle formation and fractionation is shown on spot and line scan ablation mode.

2. Experimental

2.1. Studied materials

Experiments were performed on two samples for which a different course of laser ablation was expected. NIST 610 as a certified reference glass represents non-conductive material with low thermal conductivity (0.7 W m^{-1} K^{-1} at 25 °C) and a density of 2.5 g cm^{-3}. F4 is a chrome nickel steel, representing conductive material with thermal conductivity of 20 W m^{-1} K^{-1} at 25 °C and a density of 7.5 g cm^{-3}. The chemical composition of F4 together with the boiling and melting points of each element is given in Table 1. The surfaces of both samples were polished and cleaned with ethanol prior to the analysis.

2.2. Experimental set-up

A combination of conventional analytical method of laser ablation coupled with ICP-MS and a set of aerosol spectrometers (Table 2) was utilized within this study. A detailed description of the methods and instruments is listed in the following paragraphs. The analysis of particle size distribution and time evolution was performed using three different aerosol instruments. The Engine Exhaust Particle Sizer enables highly time resolved measurements of particles below 500 nm. The Aerodynamic Particle Sizer allows for detailed size distribution (particles > 500 nm) and its measurement principle is independent of the materials properties but it has limited time resolution (one averaged size distribution per laser ablation). On the other hand the Optical Particle Sizer (particles > 300 nm) has high time resolution (1 s scans), but it has only 16 size bins and is strongly dependent on the optical properties of sampled particles (scattering coefficient and morphology).

2.2.1. LA-ICP-MS

The LA-ICP-MS system utilized within this study consists of an Analyte G2 LA system (Photon Machines Inc., Redmond, WA, USA) and an Agilent 7500ce ICP-MS analyser (Agilent Technologies, Japan). The LA system operates at a wavelength of 193 nm with a pulse duration of 4 ns using helium as a carrier gas with a 2-volume ablation cell (HelEx). The ablation parameters can be changed in the following ranges: spot

Table 1
Chemical composition of steel sample F4 and the melting and boiling points of each element.

Chemical composition of steel sample F4								
Element	Fe	Si	Mn	Ni	Cr	Mo	W	Cu
wt%	61.6	0.19	0.46	7.4	25.5	3.5	0.63	0.58
Melting point °C	1538	1414	1246	1455	1907	2623	3422	1085
Boiling point °C	2861	2900	2061	2913	2671	4639	5555	2567

Table 2
Parameters of aerosol spectrometers used in the study.

Aerosol spectrometers used in the study			
	EEPS	OPS	APS
Size range	5.6–560 nm	0.3–10 μm	0.5–20 μm
Size resolution	16 channels/decade (32 total)	16 channels (user adjustable)	32 channels/decade (52 total)
Equivalent diameter	electrical mobility	optical	aerodynamic
Time resolution	1 s	10 s	80 s (one ablation)

Table 3
Experimental parameters and conditions used for LA-ICP-MS.

Experimental parameters for LA ICP-MS	
Laser ablation system	Analyte G2
Wavelength/pulse duration	193 nm/4 ns
Fluence	8 J cm^{-2}
Repetition rate	10 Hz
Sampling mode	Single spot, line scan
Spot size	110 μm (circle)
Line scan speed	20 μm.s^{-1}
Duration of analysis	80 s
ICP-MS	Agilent 7500ce
RF power	1500 W
Carrier gas	0.65 l min^{-1} He + 0.6 l min^{-1} Ar
Outer plasma gas	15 l min^{-1} Ar
Isotopes analysed*	
SRM NIST 610	^{7}Li, ^{23}Na, ^{26}Mg, ^{27}Al, ^{28}Si, ^{43}Ca, ^{53}Cr, ^{55}Mn, ^{56}Fe, ^{88}Sr, ^{89}Y, ^{92}Zr, ^{139}La, ^{140}Ce, ^{153}Eu, ^{208}Pb, ^{232}Th, ^{238}U
Steel F4	^{53}Cr, ^{55}Mn, ^{56}Fe, ^{57}Fe, ^{60}Ni, ^{63}Cu, ^{95}Mo, ^{182}W

* Integration time for each group of isotopes was 1 s.

size 1–400 μm, repetition rate 1–500 Hz, fluence up to 30 J cm^{-2}. The ICP-MS system is a quadrupole analyser with collision-reaction cell. The aerosol is transported from the ablation cell to ICP-MS by polyurethane tubing (i. d. 4 mm) using He as a carrier gas (0.65 l min^{-1}). For the purposes of this study, two ablation modes (spot and line ablation) were chosen for comparison of different ablation conditions. The detailed description of the experimental conditions used for the experiments in this study is summarised in Table 3.

2.2.2. Engine exhaust particle sizer (EEPS)

The Engine Exhaust Particle Sizer (EEPS 3090, TSI) represents a version of the Fast Mobility Particle Sizer (FMPS) with a fast sampling rate and additional analog outputs. EEPS is an aerosol spectrometer allowing the measurement of number size distribution in a fixed particle size range of 5.6–560 nm with a high time resolution (down to 1 s per sample). The EEPS separates the particles according to their mobility in an electrostatic field and their number is subsequently counted using a set of electrometers. The aerosol sample is drawn into the instrument, where first the aerosol is electrically charged. A set of two unipolar diffusion chargers is used in the EEPS. The first, negative charger, puts negative net charge on the aerosol particles to reduce the number of highly positive charged particles and to prevent overcharging in the second charger. The second, positive charger, puts a predictable net positive charge on aerosol particles. The charged particles then continue to the measurement (sizing) column. The measurement column consists of a central rod with 4 electrically separated sections (having also different column diameters), where different constant positive voltages are applied and an outer cylinder which accommodates a set of 22 electrometers along the column height. The charged aerosol enters the measurement column in the axis and it is uniformly distributed around the central rod. The outer cylinder is protected by particle free air – the sheath flow. The two flows (the aerosol and the sheath flow) are merged to form laminar co-current flow. Positive voltages (4 sections) are applied to the central rod and as the particles flow next to it, the electrostatic field repels particles with the same charge polarity. When the particles travelling through the sheath flow due to electrical force hit one of the electrometers, the elemental charge carried by the particle is measured by this electrometer. The position of electrometers corresponds to particle having certain mobility in the electrostatic field, which is proportional to applied voltage, particle mobility diameter, geometric arrangement of the measurement column and the sheath flow. In this way the whole size distribution is measured simultaneously (using the signals from all 22 electrometers). The number of particles in individual size bins (16 channels/decade) is then obtained resulting in a whole particle number size distribution. Compared to SMPS spectrometers used more traditionally, the EEPS measures the whole size distribution at once allowing for substantially reduced sampling times. The EEPS spectrometer enables one to obtain particle number size distribution with high time resolution (1 s), but on the other hand the resolution in regards to particle size is limited to a total of 32 channels (fixed) and the measurement range is limited to about four orders of magnitude, with a detection limit slightly below urban background aerosol concentration levels. Other limitation of EEPS lies in the measurement principle – namely the use of unipolar charging and electrometers to measure number of particles. Multiply charged particles can be counted as many particles corresponding to number of charges on these particles (multiple charging is handled in instrument's kernel matrix based on calibration of the instrument).

2.2.3. Aerodynamic particle sizer (APS)

The Aerodynamic Particle Sizer (APS 3321, TSI) is an aerosol spectrometer measuring particle number size distribution in the aerodynamic size range 0.5–20 μm. The size of the particles in the APS spectrometer is determined from their inertial behaviour. The APS measures the time-of-flight of aerosol particles (velocity of particles) in an accelerating flow through a nozzle. The entering aerosol sample is split into two flows – aerosol and sheath flow. The sheath flow is filtered and serves for accelerating the aerosol flow which is confined to the center in the nozzle. Once the particles are accelerated (approximately 150 m s^{-1}) they pass through two broadly focused laser beams and scattered light from each laser beam is detected. The electronic timing between the peaks of the two pulses allows the calculation of the velocity of each individual particle. The velocity of the particles is then proportional to their aerodynamic diameter. The APS spectrometer separates the measured particles into 52 size channels with maximum time resolution in orders of seconds. APS spectrometer represents a useful extension of the EEPS measurement range allowing one to measure number size distribution of aerosol particles in the merged size range from units of nanometers up to 20 μm. The time resolution of APS spectrometer was 80 s. The time resolution can be set higher up to 1 s, but in this case the statistics for individual channels might be poor. The other limitation of APS is in the density of particles. If the density is outside the range of 0.9–1.1 g cm^{-3} (outside the Stokes regime), the particles can be incorrectly sized. The instrument uses correction for different densities, but if the density inserted does not correspond to the density of the particles the results may deviate slightly. This is the case for particles with complex shapes, agglomerates, porous particles, where it would be more applicable to use equivalent density. But this quantity is in most of the cases very difficult to estimate.

2.2.4. Optical particle sizer (OPS)

The Optical Particle Sizer (OPS 3330, TSI) is an optical photometer measuring particle number size distribution in the range 0.3–10 μm separating particles into 16 size channels. Determination of the size of the particles in the OPS spectrometer is based on the intensity of light being scattered by the particles. The OPS has an advantage in high time resolution and independence on carrier gas type, but at the same time is

burdened with uncertainty in particle size when the optical properties of measured aerosol differ from the calibration particles. The time resolution was set to 1 s. The limitation of OPS is in the optical properties of the particles being sampled (shape and index of refraction). For known samples, the index of refraction can be entered and the instrument should be working properly. But for unknown samples having complex composition of aerosol particles, the difference from refractive index of calibration particles (standard polystyrene latex spheres) can cause deviations in sizing of particles.

2.2.5. Nanometer aerosol sampler (NAS)

Nanometer Aerosol Sampler (NAS 3089, TSI) consists of a grounded cylindrical sampling chamber with an electrode at the bottom of the chamber. The NAS uses the electrode to attract particles of opposite polarity (positively charged). The sampling grid is attached on the electrode to collect the particles for further analysis. The instrument samples particles using electrostatic field with efficiency > 10% for particles < 150 nm (having the sample flow at 1 l min^{-1}). The smaller particles are sampled with higher efficiency, while for the larger particles the sampling efficiency goes down. The NAS was connected directly to LA via aerosol neutralizer (Kr^{85}, 10 mCi). In this case the aerosol neutralizer was used in order to charge the particles to be collected on the TEM grid.

2.3. Sampling procedure

The laser ablation system was connected to an ICP-MS instrument and to three aerosol spectrometers (EEPS, APS, OPS). The flow of carrier gas with particles created by laser ablation was split into two branches – one leading to the ICP-MS and the other to aerosol spectrometers. In order to preserve the proper flow rate of the carrier gas with particles into the ICP-MS, an additional flow of Ar (1.65 l min^{-1}) was added before the split into the measurement devices (see Fig. 1). The flow leading to the aerosol spectrometers was first led through a bipolar aerosol neutralizer (Kr^{85}, 10 mCi) in order to prevent excessive losses of particles due to electrostatic deposition and to ensure correct charge distribution for the aerosol spectrometers. After neutralization the aerosol was diluted using ejector diluter to lower the high aerosol concentration and to maintain sufficient flow into the aerosol spectrometers. The ejector diluter ensures proper dilution with minimal losses of the particles and homogenization of the sample. The diluted aerosol was than split using isokinetic flow splitters in order to assure representative aerosol sampling to all aerosol spectrometers.

2.4. Scanning electron microscope (SEM) and laser microscope

The structure, shape and size (depth) of the ablation craters were studied by Scanning Electron Microscope and 3D Measuring Laser Microscope. The pictures of the craters were made by FEG SEM (Field Emission Gun Scanning Electron Microscope) MIRA3 with a high brightness Schottky emitter. The FEG SEM microscope has an extraordinary resolution with powerful optional In-Beam SE (Secondary Electron) Detector (1 nm or 2 nm at 30 kV), which is useful for observation of small particles. The sample surface was covered with 10 nm of gold using a rotary-pumped sputter prior to SEM analysis in order to increase conductivity of the surface.

Additionally, the depth of the ablation craters was estimated by 3D Measuring Laser Microscope LEXT OLS4000 (Olympus). The Olympus LEXT OLS4000 is a confocal microscope capable of taking high-resolution 3D images. The magnification (Optical and Digital) of this microscope ranges from 108×–17,280×. It is capable of resolving features of 10 nm in size in the z direction (sample height) and 120 nm in the x-y plane. The system is capable of performing a variety of metrology measurements. Step height, surface/line roughness, and area/volume measurements are some of the more commonly used metrology measurements.

2.5. Transmission electron microscope (TEM)

The post-situ off-line measurements were made by Transmission Electron Microscope (JEOL JEM 1011) operated at 80 kV. The particles were collected on grids for TEM analysis using Nano Aerosol Sampler (TSI).

3. Results and discussion

The nanosecond laser ablation mechanism for glass and metal material was studied on-line during LA-ICP-MS analysis with high time

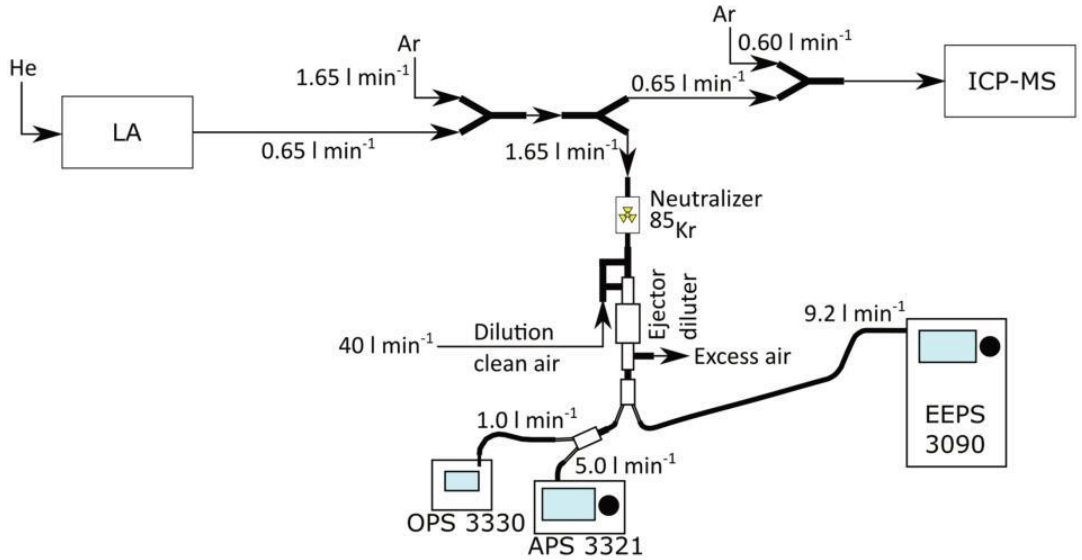

Fig. 1. Schematics of measurement set-up for laser ablation system coupled with ICP-MS and aerosol spectrometers, Engine Exhaust Particle Sizer (EEPS), Aerodynamic particle sizer (APS) and Optical Particle Sizer (OPS).

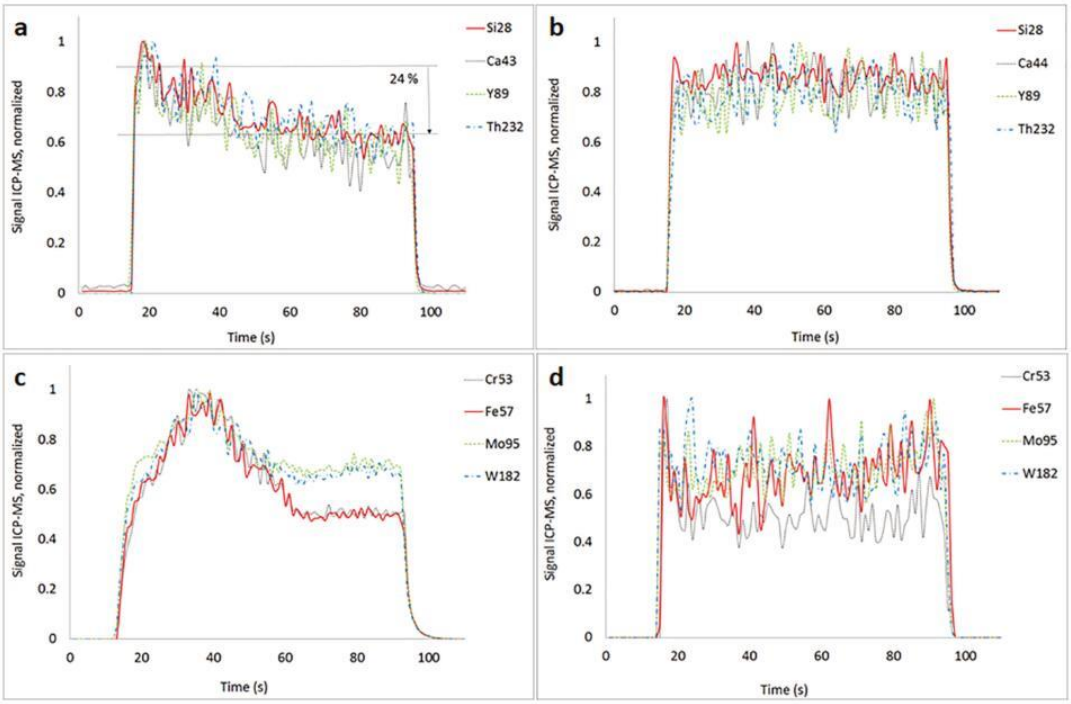

Fig. 2. Time evolution of ICP-MS signal for different isotopes during spot ablation of a) NIST 610, c) F4, and line ablation b) NIST 610, d) F4.

resolution and post-situ off-line. On-line techniques included PSD measurements, off-line particle visualization and estimation of the crater parameters.

3.1. ICP-MS signal behaviour vs crater formation

The temporal behaviour of the ICP-MS signal will be discussed for spot and line ablation on two samples with different matrices. It is known that different ablation modes give different material mass sampled into ICP, different aerosol composition [38] and so influences the analytical results. The line scan ablation provides a particle size distribution stable in time that brings also steady analytical response [45].

The signals of selected isotopes for NIST 610 display Fig. 2a and 2b. In the case of spot ablation the intensities decrease over the ablation time (Fig. 2a). The continual signal decline reflects the hole drilling and is therefore dependent on the crater depth. One factor can be incomplete washing of the material from deeper crater, the other factor is decreasing ablation rate with pulse count. Average ablation rate for the first 100 pulses was 195 nm per pulse while for 700–800 pulses only 145 nm per pulse which indicates descent of the ablation rate in time (Fig. 3e). The line ablation provides a relatively stable signal in time (Fig. 2b), the partial fluctuations are most likely due to heterogeneity of the aerosol and variation of aerosol particle size distribution in time. The isotope signals registered for the steel sample show different behavior especially for spot ablation mode (Fig. 2c). First the signals grow, all measured isotopes reach the maximal intensity after 250 pulses (25 s), then decrease and stabilise after 500 pulses (50 s). The line scan ablation can be regarded as more fluctuating than in the case of glass but with no clear trend in time (Fig. 2d).

One way of helping to characterize the ablation process is the observation of the ablation craters and an estimation of the crater parameters (width, depth and ablation rate). The crater growth during spot laser ablation was studied after each 100 pulses using SEM and confocal microscope. Different crater development can be evident for different materials as shown in Fig. 3 where SEM pictures of the craters after 100 pulses are presented together with dependence of crater depth on the number of pulses (with 100 pulses steps).

Spot laser ablation of NIST 610 produces precise cylinder-shaped ablation craters with minimal sign of material melting (Fig. 3a). The particles surrounding the crater and covering the bottom suggest new particle formation (material evaporation followed by condensation) and consecutive agglomeration of these primary particles into clusters. The detailed structure of the clusters shows Fig. 3c. The even distribution of the agglomerates around the crater and on the crater bottom indicates the particle deposition due the gravitational settling independent on the sample melting. Release of considerable amounts of melted material is evident during spot ablation of metal samples (Fig. 3b). This causes a high ablation rim around the crater as well as a significant amount of splashed material deposited around it. The coarse particles are covered with nanoparticles as visible in Fig. 3d. As a result, we can assume the scavenging of nanoparticle particles by the coarse particles.

The ablation rate differs significantly for both materials. The NIST 610 ablation crater depth grows linearly with number of pulses. The rim is negligible even with an increasing number of pulses (Fig. 3e). In the case of steel, the height of the rim is evidence of the material melting where the recoil plasma pressure pushes the melt out of the crater. The depth of the ablation crater as well as the rim increase is more or less linear up to 500 pulses after which the height of the rim is stabilised (at 40 µm) and the progress of the ablation crater is slower (Fig. 3f).

If the LA-ICP-MS response is put into context with the crater observations, the connection is evident. In the case of NIST 610 the signal decreases more or less constantly while the crater depth constantly grows (Fig. 2a and 3e). The signal decrease during the 800 pulses reached 24 ± 4% on average for all isotopes. The decrease was calculated as a difference between the average intensity of first and last 20

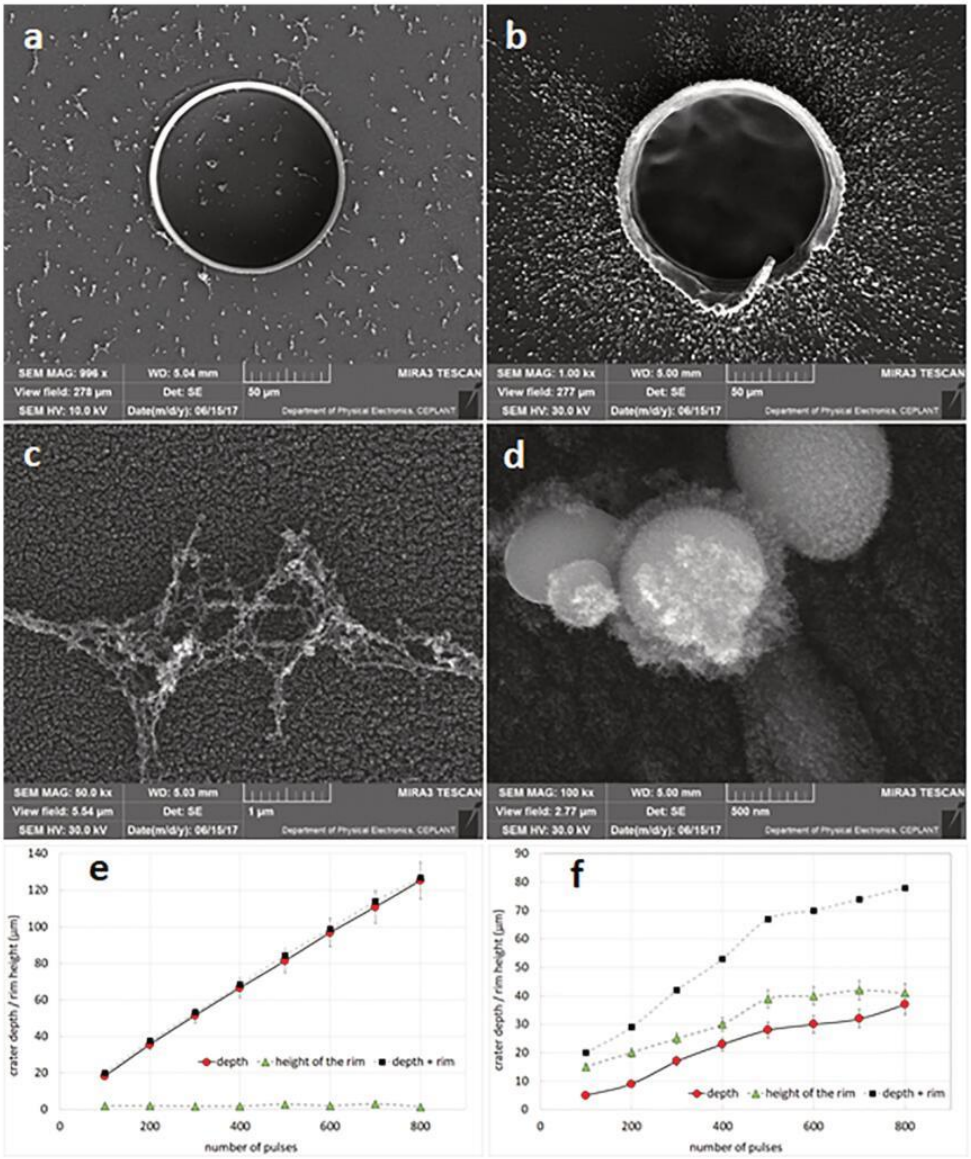

Fig. 3. SEM of the ablation craters after 100 pulses a) NIST 610, b) steel F4 and detail of deposited particles c) NIST 610, d) steel F4; Depth and rim height of the ablation craters after a definite number of pulses e) NIST 610, f) steel F4.

values of the whole signal record (Fig. 2a). Theoretical value of the crater depth was 156 µm (19.5 µm × 8) if we calculate that the ablation rate remain constant during the whole 60 s ablation. The real depth was found to be only 125 µm which means 20 ± 2% reduction of the crater depth due to the decreasing of the ablation rate in time. The remaining 4% of signal loss is attributed to incomplete aerosol washing from deeper crater. The unsteady signal of the steel sample also reflects the creation of the crater. We can observe that the signal stabilises after 500 pulses; the crater rim stops growing and the depth does not change as dramatically as during the first 500 pulses (Fig. 2c and 3f).

Because the fractionation effect influences each nanosecond laser ablation [31], the stability of the isotopes signal was studied for both ablation modes. Taking into account the irregular analytical response of spot steel ablation the fractionation index (FI) was calculated based on two unevenly long time parts, 0–50 s and 50–80 s using following equation (Eq. 1):

$$FI = \frac{\sum \text{cps}\,(M_{50-80s}) / \sum \text{cps}\,(X_{50-80s})}{\sum \text{cps}\,(M_{0-50s}) / \sum \text{cps}\,(X_{0-50s})} \quad (1)$$

where M is measured isotope, X is ^{43}Ca for NIST 610 and ^{57}Fe for steel F4 (absence of Ca in steel); the subscript is the time period observed.

FI of measured isotopes in NIST 610 shows minimal fractionation changes during line ablation, FI calculated for spot ablation slightly fluctuated, mostly towards values < 1 which indicates a relative depletion of these elements with increasing time of analysis (Fig. 4a). FI of components in the steel sample point to fractionation in time more clearly. During line scan the LA-ICP-MS response shows enrichment of Ni and Cu relatively to Fe as the main part of the sample. Spot ablation FI reports about significant enrichment of mainly refractory elements such as Mo and W in the second part of the analysis (50–80 s). This is

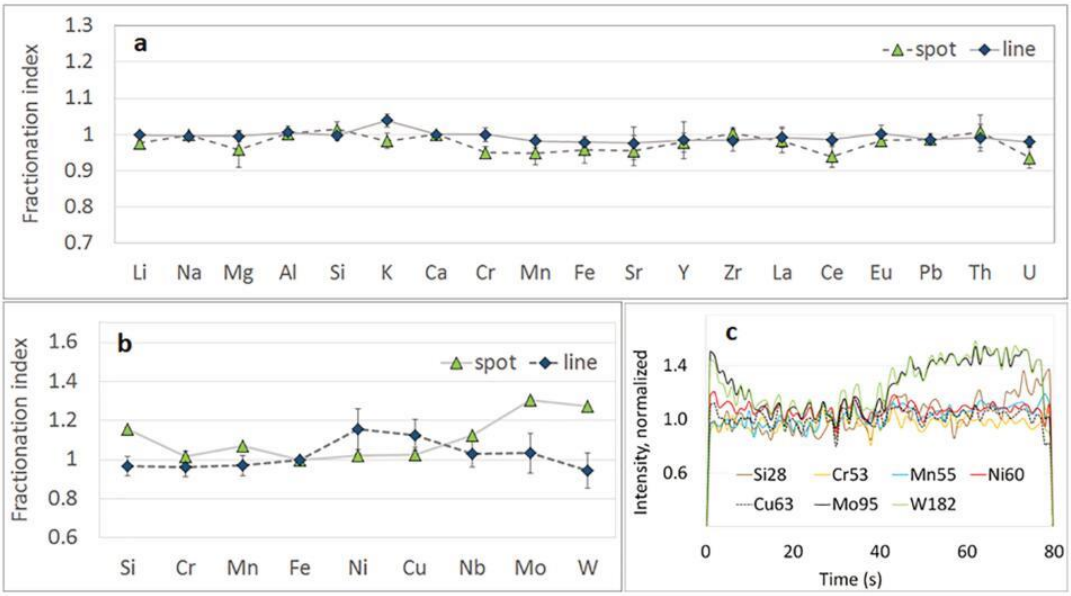

Fig. 4. Fractionation index for 80 s spot laser ablation a) NIST 610, normalized to Ca, b) F4, normalized to Fe; c) Signal normalized to ^{57}Fe.

against the expectation that the refractory elements accumulate in the melted sample. The explanation can be more clear after normalization of the isotope temporal signal records to the main component represented by isotope ^{57}Fe (Fig. 4c). Mo and W signals strongly decrease relatively to Fe in the first 20 s. During the period 20–40 s the intensity ratios of all isotope are more or less stable and after 40 s the signals rise back to their initial value. Although FI points to temporal fractionation of Mo and W, the effect of their enrichment in the end of ablation is false. The temporal signals point to instability of Mo/Fe and W/Fe the same as all isotope signals in first 50 s (compare Fig. 4c and Fig. 2c). During this time period visible fractionation occurs in a form of refractory element depletion due to higher thermal effect inducing extreme material melting and crater rim growth (see Fig. 3f). After 500 pulses the ablation becomes stable with no more crater rim growth and a stable analytical signal.

This finding is consistent with the temporal behavior of particle formation mainly in the size range of 0.3–1 μm as can be seen from OPS data evolution in time as discussed in Chapter 3.3.2.

3.2. Particles < 560 nm

3.2.1. EEPS – Particle size distribution

The size distributions were averaged for the duration of the whole laser ablation process (80 s) and through repeated laser ablations with the same conditions. The average size distributions show very similar multimodal shape for both materials and both ablation modes (see Fig. 5). The origin of particles was previously discussed in [38]. Particles < 30 nm represent the primary particles produced by laser ablation, particles > 50 nm are most probably a product of coagulation/agglomeration of primary nanoparticles or particles originating from the droplets' solidification. The spot ablation mode of both materials produces higher concentrations of primary particles and a lower concentration of the largest particles compared to the line ablation mode. This behavior is more pronounced in the case of NIST 610 material. The position of the primary particle mode for spot ablation mode is similar for the ablation of both materials.

The other modes of the size distributions (visible between 20 and 100 nm) for both materials and both ablation modes are secondary particles formed by coagulation and aggregation of primary particles and the larger particles released from melted material by laser pulses as splashes.

For the line ablation mode, the concentration of the largest particles is much higher than the concentration of primary particles for both materials (again more pronounced for NIST 610 material). This is most probably given by the ablation of a fresh surface producing larger particles throughout the whole ablation process, while in the case of spot ablation these particles are produced only at the very beginning of the ablation process [38].

In the case of NIST 610 material, the last mode (accumulation) of PSD is shifted to larger sizes (200 and 220 nm for spot and line ablation respectively) compared to F4 material (120 and 160 nm for spot and line ablation respectively) for both ablation modes. Moreover, the whole size distribution exhibits lower concentrations for ablation of F4 material. This shift is most probably caused by differences in material properties – stronger fractionation effect and/or production of coarse mode particles (in μm size range). This corresponds to a shallower crater and higher rim of splashed material around the crater edge in the case of spot ablation of F4 material (see chapter 3.1.). During spot ablation of F4 material the sample heats up and easily creates a pool of melted components, which can result in splashes of the melt. Such behavior can be attributed mainly to higher thermal conductivity of F4 material compared to NIST 610 (almost 30 times).

However, the EEPS spectrometer is burdened with measurement error at the end of its measurement range, especially in the large particle end of the size distribution. The measurement principle relying on the predictable distribution of charges on particles is more complex in the case of the large particles close to the measurement range edge and thus can be causing larger deviations in estimation of particle number concentration than in the rest of the measured size distribution. Moreover, the shape of the particles is also very important for charge distribution on the particles.

The structure of particles with a diameter below 150 nm (with the collection efficiency above 10%) was studied using TEM. This size region should include mainly primary nanoparticles created from gas-to-particle conversion process and also smaller agglomerates. The NIST 610 shows more affinity for clustering than F4 (compare 6a and 6c). NIST 610 also shows the presence of only one type of particle clustering together but F4 produces two different types of particles as evident

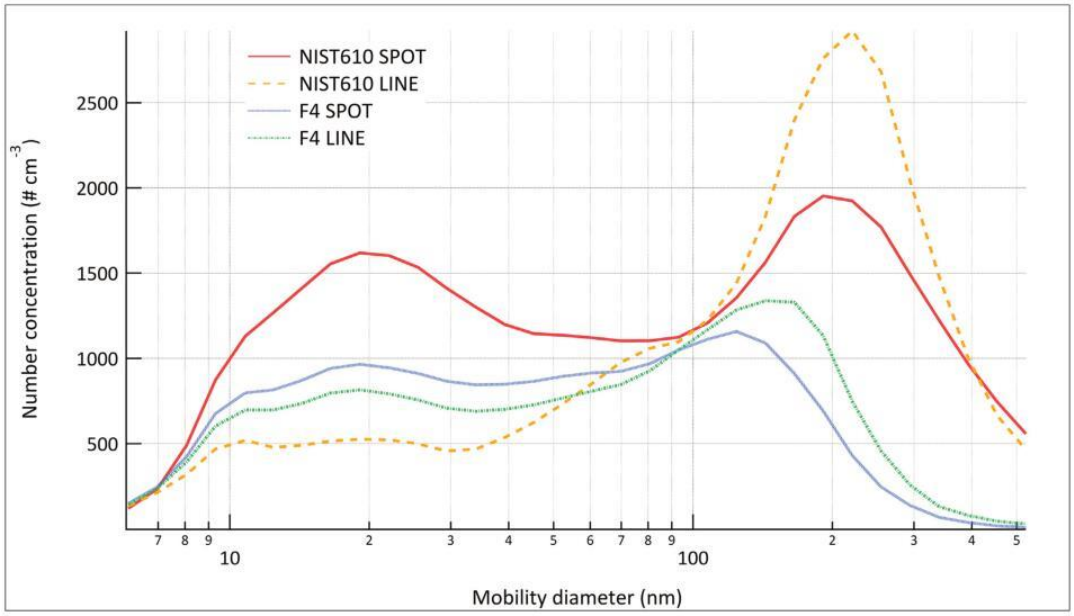

Fig. 5. Average PSD for laser ablation of different materials and different ablation modes (measured by EEPS).

from Fig. 6d. The origin of large spheres should be from the hydrodynamic sputtering of liquid layer and their size can reach units of microns [27].

3.2.2. EEPS – Formation of nanoparticles in time

The measurements from EEPS spectrometer were taken during the period of the whole laser ablation process with a time resolution of 1 s. To show the different trends of particle formation process for different particle sizes, the time resolved signal of particle number concentration for five size intervals was pictured into graphs (Fig. 7). The time evolution of particle number size distribution during spot ablation of NIST 610 material shows delayed increased concentration of primary particles, while the accumulation particles are visible from the beginning of LA. This means that the primary nanoparticles are mainly produced when the ablation crater reaches a certain depth (for shallow crater) – less material for the condensation process is released and production of larger particles is stable. The primary particles are slowly growing by accumulation of the evaporated material and coagulation with other particles during the ablation process. In the case of line ablation of NIST 610, all the particle sizes seem to be produced from the beginning of the LA process with erratic primary particle production during the ablation process. The difference between primary and accumulation mode particle concentration is large, favouring the concentration of accumulation mode particles.

However, in the case of F4 material the primary particles are produced from the beginning of the LA process again with erratic particle production for line ablation. The accumulation mode particles are also produced from the beginning of the LA process. The line ablation of F4 shows loss of agglomerated particles throughout the whole ablation process comparing to NIST 610. This can be explained by scavenging of nanoparticles by the coarse particles as discussed in Chapter 3.1.

3.3. Particles with diameter > 540 nm

3.3.1. APS – Size distribution

The time resolution of the APS spectrometer was 80 s, so there was one APS scan per laser ablation. The particle size distributions were averaged through successive ablation processes having the same conditions.

The larger particles (> 0.5 μm) are produced more for F4 than NIST 610 material and this effect is more pronounced for spot ablation mode (see Fig. 8). This behavior is connected again with the thermal properties of the materials. The NIST 610 has a thermal conductivity almost 30 times lower than F4 resulting in overheating of the F4 sample and formation of a melt pool, where the large particles are splashed out by laser pulses. This effect is more pronounced for SPOT ablation probably due to laser radiation on a larger area of deeper crater, causing a larger melt layer surface. It has to be mentioned that in the case of APS, not all the particles might be characterized in a proper size bin. If the chain-like clusters or agglomerates are oriented parallel to the flow inside the optical cell of the instrument, then they might be excluded from the analysis by evaluation routines in the APS as having too long response or they might be sized based on their diameter and not the length. The coarse particles can also scavenge smaller particles, especially the primary nanoparticles, thus causing lower concentrations of nanoparticles (see Fig. 5). Moreover, the results obtained from the APS spectrometer are also density dependent. The results obtained from the LA scans were corrected using the real density of the materials (2.5 g cm^{-3} for NIST610 and 7.5 g cm^{-3} for F4). If such correction is applied, the whole size distribution shifts towards smaller particles, moving some of the measured size bins outside of the measurement range. Unfortunately, the real density is much smaller, because of the complex nature of the particles generated by LA, where they create highly porous aggregates or chain-like particles, where estimation of the real or effective density is very difficult. If the real density is applied (most probably even < 1 g cm^{-3}) the size distribution measured by APS would shift towards larger particles. And this effect would be larger for F4, because of larger difference between the effective density of the particles formed by LA and the real of the ablated material. Nevertheless, the results still show, that for F4 more of the micron size particles are produced compared to the NIST610 and this difference would be even larger if the effective density would be known and applied to the results.

3.3.2. OPS – Size distribution spectra (evolution in time)

The time resolution for OPS spectrometer was set to 10 s in order to have a statistically significant number of particles counted. The OPS

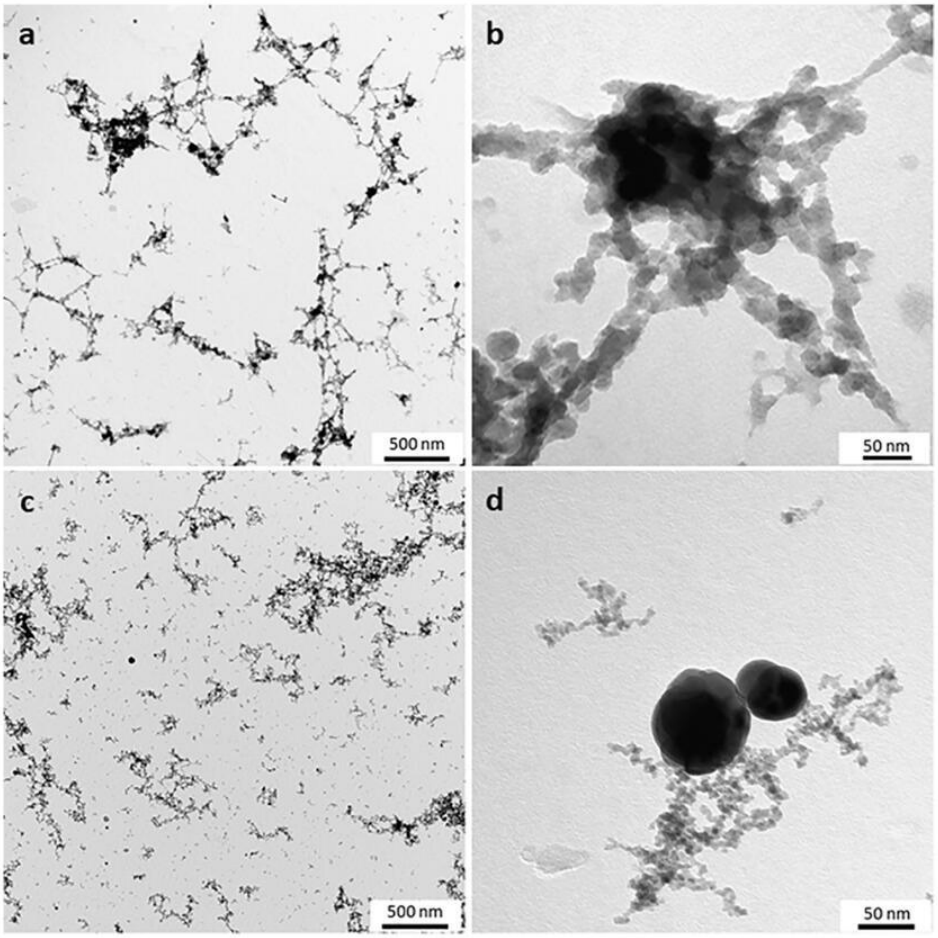

Fig. 6. TEM NIST spot (a, b), F4 (steel) spot (c, d).

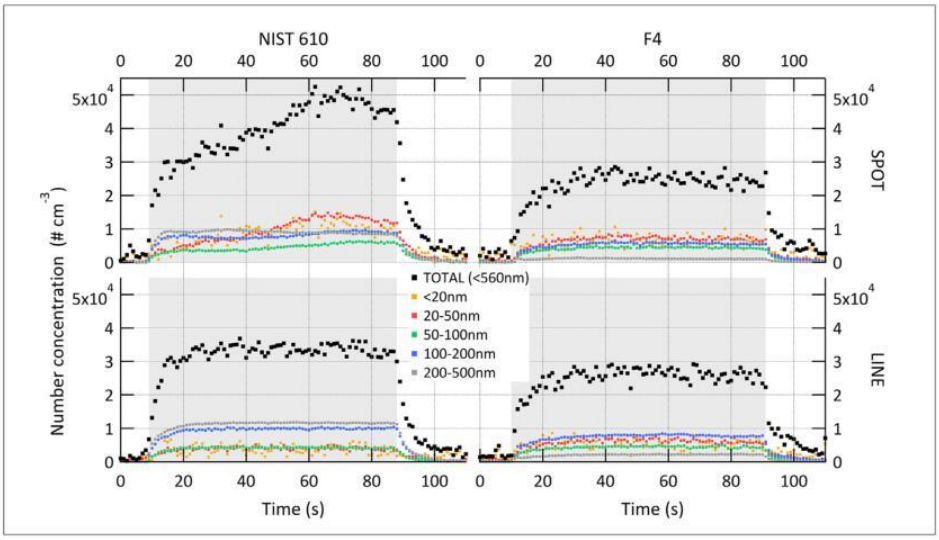

Fig. 7. Time evolution of individual size fractions for different materials and different ablation modes (measured by EEPS), the grayed area denotes the duration of LA scan.

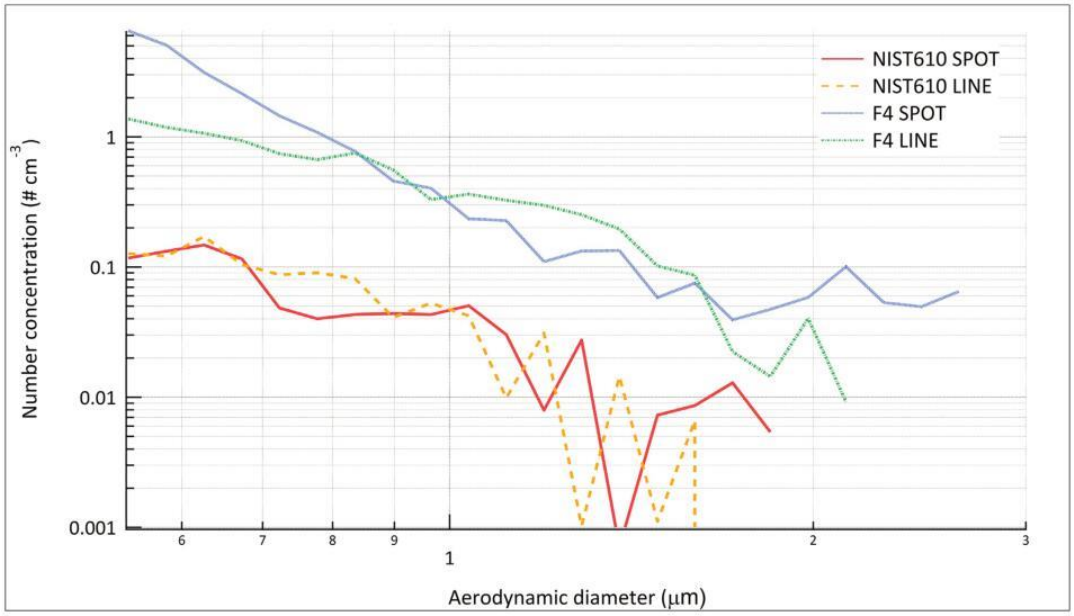

Fig. 8. Average PSD for laser ablation of different materials and different ablation modes (measured by APS).

uses a different technique for particle analysis than the EEPS and APS spectrometers and therefore the data from the OPS spectrometer was also included in this study. Moreover, the OPS offers higher time resolution than APS for highly time resolved analysis of the laser ablation. The data from OPS were separated into four larger size intervals (out of original 16) for easier reading of graphs. The main emphasis was given to particles bellow 1 µm, because larger particles are not fully evaporated in ICP and therefore only partially influencing the MS signal. The dynamic behavior of accumulation mode particles < 1 µm is very similar for both materials and differs by the type of laser ablation process (spot versus line ablation).

In the case of spot ablation mode, most of the particles were emitted during the first half of the ablation process. The difference between spot ablation NIST 610 and F4 is in the second half of the laser ablation process – for NIST 610 the concentration goes gradually down, while for F4 the concentration stabilises after 50 s. This difference can be attributed again to the different thermal properties of the two materials. For spot ablation of both materials most of the total concentration measured by OPS consists of the particles from the smallest size bin (0.30–0.47 µm). Only at the beginning of the laser ablation process is there a small contribution of larger particles (0.47–0.72 µm) which can be attributed to creation from the intact surface of the ablated material.

The difference between behavior of particles in the overlapping region of EEPS (200–500 nm, Fig. 7) and OPS (300–500 nm, Fig. 9) is given by the different measurement principles of both instruments. The EEPS signal depends only on electrical properties and transferred elemental charges, while the OPS signal depends on the size of the particles and their optical properties. In this specific case the OPS better reflects the ICP-MS signal, because both rely on the particle interaction with light – scattering/light absorption.

For line ablation mode the production of accumulation mode particles is constant during ablation for both materials. The time evolution of the particle number size distribution corresponds to the ICP-MS signal of both materials as shown in Fig. 2 for the spot ablation which points to the fact that the ICP-MS signal is mainly influenced by the accumulation mode or larger particles.

4. Conclusions

The SEM images revealed significant release of melted material during ablation of steel F4 material, which resulted in a high rim around the ablation crater and a large amount of deposited material around the crater due to the hydrodynamic sputtering. In the case of glass NIST 610, the rim height is negligible and the amount of the material dispersed around the ablation crater is less significant than in the case of F4.

The analysis of particle structure using TEM shows a larger tendency of NIST 610 to create clusters than F4. In the case of F4, two distinct types of particles can be found – the small primary nanoparticles available for clustering and large spherical particles released directly from melted material.

Primary mode particle size is influenced mainly by ablation mode (smaller sizes for line ablation) and independent of the ablated material. This can be explained by the fact that primary particles are formed by the same mechanism for both materials – evaporation and following condensation of the vapours, whereas the conditions for this process are given by the setup of laser ablation (laser settings, the carrier gas, etc.). On the other hand, the size of accumulation mode particles is governed by material type (larger sizes for NIST 610).

Particles larger than 500 nm are produced mainly by hydrodynamic sputtering which is dependent on material properties such as thermal diffusivity. The melted layer thickness is more significant for metals compared to glass so higher concentration of large particles was detected for steel. The spot ablation mode supports material sputtering of metals.

The ICP-MS signal seems to be strongly correlated with a concentration of particles larger than 300 nm for both reference materials.

It has to be mentioned that the results obtained by individual aerosol spectrometers can be burdened with measurement artifact especially for longer chains or agglomerates. In this case especially for OPS and APS spectrometers the result depends on the orientation of such elongated cluster of particles in the measurement volume. In case of APS it may lead to discarding of such particle into category of non-valid measurement, because of exceeding the longest allowed time period between reaching from one laser light or the other. The APS

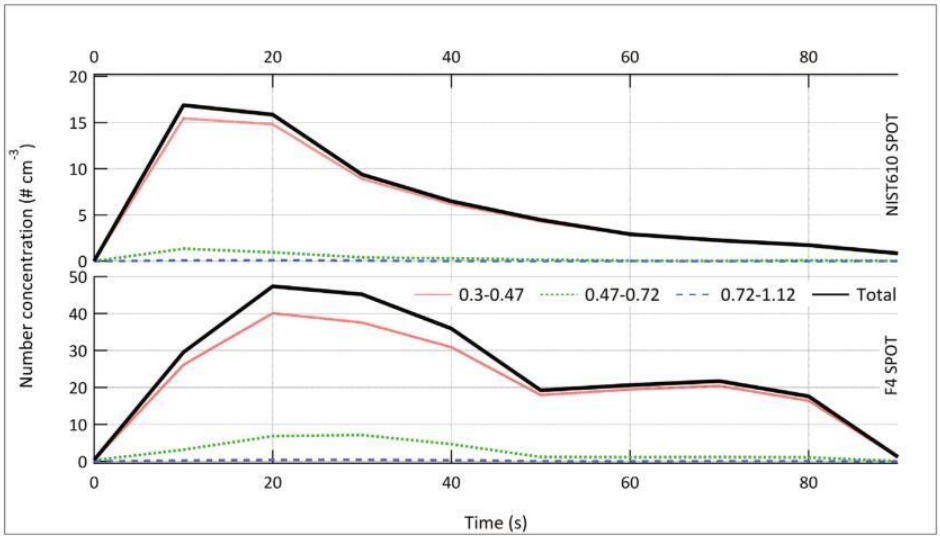

Fig. 9. OPS particle size distribution time evolution for spot ablation a) NIST 610, b) steel F4.

sizing principle – acceleration of the particles in the flow field, also depends on the particle density. If the density of measured particles deviates from the standard density (1 g cm^{-3}), the results can change substantially and the size distribution can be shifted towards larger (density $<$ 1 g cm^{-3}) or smaller particles (density $>$ 1 g cm^{-3}). This can be solved by estimation of the effective density of the particles or even a density function, but unfortunately in most of the cases this is not feasible. In the case of OPS it may cause scattering of the laser light from the diameter of the chain-like structure, omitting the long dimension, which does not necessarily mean wrong sizing, but it may influence the overall results. In both cases it leads to underestimating or even neglecting the concentration of the micrometer sized particles or to wrong sizing in the smaller size bins, which were detected and visible on the SEM and TEM images. The EEPS can be burdened by larger measurement errors close to its upper measurement range (the particles close to 500 nm) due to complex characterization of charge distribution on larger particles. It means that the direct intercomparison of results in the overlapping regions of the aerosol spectrometers based on different physical principles is usually very difficult and sometimes even impossible without additional information (e.g. the average effective density of the particles or even the density function for different particle sizes if the discussed LA artifacts – non-stoichiometric composition of the particles is taken into account). Nevertheless, it does not mean that the results obtained by aerosol spectrometers cannot be used. The users of such instruments, just has to be careful about the data treatment and the following data interpretation.

Acknowledgements

The results of this research have been acquired within the CEITEC 2020 (LQ1601) project with financial contributions made by the Ministry of Education, Youths and Sports of the Czech Republic with special support grant aid from the National Sustainability Programme II (NPU II) funds. V.K. acknowledges the Czech Science Foundation for a grant to support the project GA14-13600S. H.N. and V.K. acknowledge support of the project MUNI/A/0886/2016 from Masaryk University Specific Research Programme. J. O. acknowledges Czech Science Foundation for grant P503/12/G147. M.V. acknowledges Czech Ministry of Education, Youth and Sports of the Czech Republic for support within the National Sustainability Programme I, NPU I (LO), project LO1311. R.H. acknowledges NPU project LO1302 from Ministry of Education of the Czech Republic.

References

[1] M. Hola, P. Mikuska, R. Hanzlikova, J. Kaiser, V. Kanicky, Tungsten carbide precursors as an example for influence of a binder on the particle formation in the nanosecond laser ablation of powdered materials, Talanta 80 (2010) 1862–1867.
[2] H.R. Kuhn, D. Gunther, A quantification strategy in laser ablation ICP-MS based on the transported aerosol particle volume determined by optical particle size measurement, J. Anal. At. Spectrom. 21 (2006) 1209–1213.
[3] D.W. Lee, M.D. Cheng, Particle generation by laser ablation during surface decontamination, J. Aerosol Sci. 35 (2004) 1527–1540.
[4] M. Hola, V. Konecna, P. Mikuska, J. Kaiser, V. Kanicky, Influence of physical properties and chemical composition of sample on formation of aerosol particles generated by nanosecond laser ablation at 213 nm, Spectrochim. Acta, Part B 65 (2010) 51–60.
[5] M. Ohata, D. Tabersky, R. Glaus, J. Koch, B. Hattendorf, D. Gunther, Comparison of 795 nm and 265 nm femtosecond and 193 nm nanosecond laser ablation inductively coupled plasma mass spectrometry for the quantitative multi-element analysis of glass materials, J. Anal. At. Spectrom. 29 (2014) 1345–1353.
[6] A.A. Tseng, Y.T. Chen, K.J. Ma, Fabrication of high-aspect-ratio microstructures using excimer laser, Opt. Lasers Eng. 41 (2004) 827–847.
[7] D. Bäuerle, Laser Processing and Chemistry, (2011).
[8] R.E. Russo, X.L. Mao, H.C. Liu, J. Gonzalez, S.S. Mao, Laser ablation in analytical chemistry - a review, Talanta 57 (2002) 425–451.
[9] S.S. Mao, X.L. Mao, R. Greif, R.E. Russo, Simulation of a picosecond laser ablation plasma, Appl. Phys. Lett. 76 (2000) 3370–3372.
[10] S.S. Mao, X. Mao, R. Greif, R.E. Russo, Initiation of an early-stage plasma during picosecond laser ablation of solids, Appl. Phys. Lett. 77 (2000) 2464–2466.
[11] K.H. Leitz, B. Redlingshofer, Y. Reg, A. Otto, M. Schmidt, Metal ablation with short and ultrashort laser pulses, lasers in manufacturing 2011: proceedings of the sixth international Wlt conference on lasers in manufacturing, 12 (Pt B) (2011) 230–238.
[12] P.M. Outridge, W. Doherty, D.C. Gregoire, Ablative and transport fractionation of trace elements during laser sampling of glass and copper, Spectrochim. Acta, Part B 52 (1997) 2093–2102.
[13] D. Marla, U.V. Bhandarkar, S.S. Joshi, A model of laser ablation with temperature-dependent material properties, vaporization, phase explosion and plasma shielding, Appl. Phys. A Mater. Sci. Process. 116 (2014) 273–285.
[14] C. Liu, X.L. Mao, S.S. Mao, X. Zeng, R. Greif, R.E. Russo, Nanosecond and ferntosecond laser ablation of brass: particulate and ICPMS measurements, Anal. Chem. 76 (2004) 379–383.
[15] H.R. Kuhn, D. Gunther, Elemental fractionation studies in laser ablation inductively coupled plasma mass spectrometry on laser-induced brass aerosols, Anal. Chem. 75 (2003) 747–753.
[16] N. Miliszkiewicz, S. Walas, A. Tobiasz, Current approaches to calibration of LA-ICP-MS analysis, J. Anal. At. Spectrom. 30 (2015) 327–338.
[17] S.D. Zhang, M.H. He, Z.B. Yin, E.Y. Zhu, W. Hang, B.L. Huang, Elemental fractionation and matrix effects in laser sampling based spectrometry, J. Anal. At. Spectrom. 31 (2016) 358–382.
[18] I. Kroslakova, D. Gunther, Elemental fractionation in laser ablation-inductively coupled plasma-mass spectrometry: evidence for mass load induced matrix effects in the ICP during ablation of a silicate glass, J. Anal. At. Spectrom. 22 (2007) 51–62.

[19] M. Hola, V. Konecna, P. Mikuska, J. Kaiser, K. Palenikova, S. Prusa, R. Hanzlikova, V. Kanicky, Study of aerosols generated by 213 nm laser ablation of cobalt-cemented hard metals, J. Anal. At. Spectrom. 23 (2008) 1341–1349.
[20] R. Hergenroder, A model of non-congruent laser ablation as a source of fractionation effects in LA-ICP-MS, J. Anal. At. Spectrom. 21 (2006) 505–516.
[21] R. Hergenroder, Hydrodynamic sputtering as a possible source for fractionation in LA-ICP-MS, J. Anal. At. Spectrom. 21 (2006) 517–524.
[22] S.B. Wen, X.L. Mao, R. Greif, R.E. Russo, Experimental and theoretical studies of particle generation after laser ablation of copper with a background gas at atmospheric pressure, J. Appl. Phys. 101 (2007) 15.
[23] S.B. Wen, X.L. Mao, R. Greif, R.E. Russo, Expansion of the laser ablation vapor plume into a background gas. I. Analysis, J. Appl. Physiol. 101 (2007) 13.
[24] R. Hergenroder, A model for the generation of small particles in laser ablation ICP-MS, J. Anal. At. Spectrom. 21 (2006) 1016–1026.
[25] L.V. Zhigilei, Dynamics of the plume formation and parameters of the ejected clusters in short-pulse laser ablation, Appl. Phys. A Mater. Sci. Process. 76 (2003) 339–350.
[26] A.A. Morozov, A.B. Evtushenko, A.V. Bulgakov, Gas-dynamic acceleration of laser-ablation plumes: hyperthermal particle energies under thermal vaporization, Appl. Phys. Lett. 106 (2015).
[27] H.R. Kuhn, D. Gunther, The agglomeration state of nanosecond laser-generated aerosol particles entering the ICP, Anal. Bioanal. Chem. 383 (2005) 434–441.
[28] T. Ohkubo, M. Kuwata, B. Luk'yanchuk, T. Yabe, Numerical analysis of nanocluster formation within ns-laser ablation plume, Appl. Phys. A Mater. Sci. Process. 77 (2003) 271–275.
[29] H.R. Kuhn, J. Koch, R. Hargenroder, K. Niemax, M. Kalberer, D. Gunther, Evaluation of different techniques for particle size distribution measurements on laser-generated aerosols, J. Anal. At. Spectrom. 20 (2005) 894–900.
[30] F.X. D'Abzac, A.M. Seydoux-Guillaume, J. Chmeleff, L. Datas, F. Poitrasson, In situ characterization of infra-red femtosecond laser ablation in geological samples. Part B: the laser induced particles, J. Anal. At. Spectrom. 27 (2012) 108–119.
[31] R. Glaus, R. Kaegi, F. Krumeich, D. Gunther, Phenomenological studies on structure and elemental composition of nanosecond and femtosecond laser-generated aerosols with implications on laser ablation inductively coupled plasma mass spectrometry, Spectrochim. Acta, Part B 65 (2010) 812–822.
[32] B.N. Chichkov, C. Momma, S. Nolte, F. von Alvensleben, A. Tunnermann, Femtosecond, picosecond and nanosecond laser ablation of solids, Appl. Phys. A Mater. Sci. Process. 63 (1996) 109–115.
[33] C. Geertsen, A. Briand, F. Chartier, J.L. Lacour, P. Mauchien, S. Sjostrom, J.M. Mermet, Comparison between infrared and ultraviolet-laser ablation at atmospheric-pressure - implications for solid sampling inductively-coupled plasma spectrometry, J. Anal. At. Spectrom. 9 (1994) 17–22.
[34] D. Gunther, C.A. Heinrich, Comparison of the ablation behaviour of 266 nm Nd: YAG and 193 nm ArF excimer lasers for LA-ICP-MS analysis, J. Anal. At. Spectrom. 14 (1999) 1369–1374.
[35] J. Koch, A. von Bohlen, R. Hergenroder, K. Niemax, Particle size distributions and compositions of aerosols produced by near-IR femto- and nanosecond laser ablation of brass, J. Anal. At. Spectrom. 19 (2004) 267–272.
[36] P.K. Diwakar, S.S. Harilal, N.L. Lahaye, A. Hassanein, P. Kulkarni, The influence of laser pulse duration and energy on ICP-MS signal intensity, elemental fractionation, and particle size distribution in NIR fs-LA-ICP-MS, J. Anal. At. Spectrom. 28 (2013) 1420–1429.
[37] H.R. Kuhn, D. Gunther, Laser ablation-ICP-MS: particle size dependent elemental composition studies on filter-collected and online measured aerosols from glass, J. Anal. At. Spectrom. 19 (2004) 1158–1164.
[38] H. Novakova, M. Hola, M. Vojtisek-Lom, J. Ondracek, V. Kanicky, Online monitoring of nanoparticles formed during nanosecond laser ablation, Spectrochim. Acta, Part B 125 (2016) 52–60.
[39] E.O. Knutson, K.T. Whitby, Aerosol classification by electric mobility: apparatus, theory, and applications, Journal of Aerosol Science, 1975, pp. 443–451.
[40] A. Wiedensohler, A. Wiesner, K. Weinhold, W. Birmili, M. Hermann, M. Merkel, T. Muller, S. Pfeifer, A. Schmidt, T. Tuch, F. Velarde, P. Quincey, S. Seeger, A. Nowak, Mobility particle size spectrometers: calibration procedures and measurement uncertainties, Aerosol Sci. Technol. 52 (2018) 146–164.
[41] H. Tammet, A. Mirme, E. Tamm, Electrical aerosol spectrometer of Tartu University, Atmos. Res. 62 (2002) 315–324.
[42] W.W. Szymanski, A. Nagy, A. Czitrovszky, Optical particle spectrometry-problems and prospects, J. Quant. Spectrosc. Radiat. Transf. 110 (2009) 918–929.
[43] A. Berner, C. Lurzer, F. Pohl, O. Preining, P. Wagner, Size distribution of the URBAN aerosol in VIENNA, Sci. Total Environ. 13 (1979) 245–261.
[44] R.E. Hillamo, E.I. Kauppinen, On the performance of the berner low-pressure impactor, Aerosol Sci. Technol. 14 (1991) 33–47.
[45] M. Guillong, D. Gunther, Effect of particle size distribution on ICP-induced elemental fractionation in laser ablation-inductively coupled plasma-mass spectrometry, J. Anal. At. Spectrom. 17 (2002) 831–837.

PAPER 9

Influence of physical properties and chemical composition of sample on formation of aerosol particles generated by nanosecond laser ablation at 213 nm

Holá, M.*, Konečná, V., Mikuška, P., Kaiser, J., Kanický, V.

Spectrochimica Acta Part B. 2010, 65(1), 51–60. DOI 10.1016/j.sab.2009.11.003

Contribution:

LA-ICP-MS and aerosol design of experiments and measurements, data evaluation, studying of ablation craters and the particle structure, manuscript writing, corresponding author.

Spectrochimica Acta Part B 65 (2010) 51–60

Contents lists available at ScienceDirect

Spectrochimica Acta Part B

journal homepage: www.elsevier.com/locate/sab

Influence of physical properties and chemical composition of sample on formation of aerosol particles generated by nanosecond laser ablation at 213 nm

Markéta Holá [a,*], Veronika Konečná [a], Pavel Mikuška [b], Jozef Kaiser [c], Viktor Kanický [a]

[a] Department of Chemistry, Faculty of Science, Masaryk University, Kotlářská 2, 611 37 Brno, Czech Republic
[b] Institute of Analytical Chemistry, Academy of Sciences of the Czech Republic v.v.i., Veveří 97, 602 00 Brno, Czech Republic
[c] Institute of Physical Engineering, Faculty of Mechanical Engineering, Brno University of Technology, Technická 2896/2, 616 69 Brno, Czech Republic

ARTICLE INFO

Article history:
Received 28 January 2009
Accepted 8 November 2009
Available online 14 November 2009

Keywords:
213 nm laser ablation
Sample properties
Aerosol particles
Composition

ABSTRACT

The influence of sample properties and composition on the size and concentration of aerosol particles generated by nanosecond Nd:YAG laser ablation at 213 nm was investigated for three sets of different materials, each containing five specimens with a similar matrix (Co-cemented carbides with a variable content of W and Co, steel samples with minor differences in elemental content and silica glasses with various colors). The concentration of ablated particles (particle number concentration, PNC) was measured in two size ranges (10–250 nm and 0.25–17 μm) using an optical aerosol spectrometer. The shapes and volumes of the ablation craters were obtained by Scanning Electron Microscopy (SEM) and by an optical profilometer, respectively. Additionally, the structure of the laser-generated particles was studied after their collection on a filter using SEM.

The results of particle concentration measurements showed a significant dominance of particles smaller than 250 nm in comparison with larger particles, irrespective of the kind of material. Even if the number of particles larger than 0.25 μm is negligible (up to 0.1%), the volume of large particles that left the ablation cell can reach 50% of the whole particle volume depending on the material.

Study of the ablation craters and the laser-generated particles showed a various number of particles produced by different ablation mechanisms (particle splashing or condensation), but the similar character of released particles for all materials was observed by SEM after particle collection on the membrane filter. The created aerosol always consisted of two main structures — spherical particles with diameters from tenths to units of micrometers originally ejected from the molten surface layer and μm-sized "fibres" composed of primary agglomerates with diameters in the range between tens and hundreds of nanometers.

The shape and structure of ablation craters were in good agreement with particle concentration measurements. Samples with a high crater rim and melted bottom produced the highest number of large spherical particles. The mass values of all produced aerosols were calculated from the measured ablation crater volumes and sample densities.

1. Introduction

Over the last decade laser ablation has become a groove technique in analytical chemistry widely used for the sampling of solid material into an inductively coupled plasma mass/optical spectrometer (LA-ICP-MS/OES) or into other plasma assisted methods such as Laser Induced Breakdown Spectrometry (LIBS). These techniques are applied for qualitative and quantitative elemental analysis in the fields of geology, biology, the environment, metallurgy and in other scientific or industrial sectors [1–8]. The main problem of the LA-ICP-MS method still remains the creation of a suitable calibration strategy for each specific quantitative analysis [2]. Various ablation mechanisms of materials with different matrices called "matrix effect" cause changes in volume and composition of the generated particles during the laser beam interaction with the different sample surfaces. This fact points to the importance of a suitable calibration strategy, such as matrix matched calibration, as the most common quantification technique for LA-ICP-MS, relying on a certified reference material (CRM) with the same matrix. The problems associated with matrix matched calibration are still a frequent topic of research connected with laser ablation methods [2,9]. Nowadays many different CRMs exist for a wide range of applications, mainly in geological research. However, for many of them, only a few or no CRMs with certified values of analytes are available. In that case, laboratory standards are prepared from the mixture of an appropriate matrix and analytes with a given concentration using different procedures such as simple powder pressing, fusing or sintering [2,10–12]. For those standards requiring a high degree of homogeneity, utilization of a sol–gel method has been described [13,14].

* Corresponding author.
E-mail address: mhola@sci.muni.cz (M. Holá).

0584-8547/$ – see front matter © 2009 Elsevier B.V. All rights reserved.
doi:10.1016/j.sab.2009.11.003

Table 1
Composition of Co-cemented tungsten carbide samples (wt.%).

Sample	Density g cm^{-3}	C	Co	Ti	Ta	Nb	W
1457HF3	15.0	6.13	3.33	–	1.03	0.42	89.09
3648K	14.8	5.62	6.55	0.28	0.16	0.07	87.32
554S30	12.5	6.85	8.17	6.25	3.93	1.58	73.22
2286S10	10.5	7.85	9.11	14.07	7.82	3.1	58.05
1520GH25	13.1	4.59	25.1	–	–	–	70.31

Investigation of the laser ablation behavior of samples differing from their matrices is important not only to understand some general rules in the ablation mechanism of similar types of materials (e.g. metal, glass, …), but also to help when considering the suitability of materials as calibration standards. The importance of suitable calibration standards is proved e.g. in [15], where a particle formation study together with LA-ICP-MS quantification analysis of iron based samples using matrix matched and non-matrix matched calibration with different laser systems is described. The particle formation mechanism and several particle parameters (size distribution and chemical composition) originating from the laser beam–sample interaction have been intensively studied for various types of material and different laser ablation conditions. The connection between laser parameters such as laser wavelength [16–20] pulse duration [15,21–24] or energy density [25–27] and particle formation mechanism was unambiguously confirmed.

Recently, for metals the most popular material for research is a binary brass containing two main constituents with a significant difference in physical properties [28–32]. For geological materials glass is the calibration material of choice, so glass is also a frequent topic for the ablation process studies [33]. The experiments using different methods for the specification of particle size, concentration, structure and composition suggested several mechanisms to be responsible for the production of different particles during laser ablation.

Particle formation studies are often focused on various glass samples, frequently to CRMs, which are used as calibration standards in laser ablation assisted analytical methods because of their proper homogeneity and multi-elemental composition [34–36]. The determination of particle size, concentration and composition is not the only topic of research for glass ablation principles. An example of further parameters which have been studied is the ablation crater depths of glasses which did not show any direct correlation between the ablation rate and the glass absorbance. This means that the optical properties are not the only parameters to be considered as influencing the UV ablation mechanism [37]. However, the laser wavelength is one of the most important parameters for glass ablation due to the different absorptions at various wavelengths. The UV region was found to be suitable for the ablation of glass materials because of the absorption of light for samples with different colors [36].

This work deals with the study of aerosol particles produced by 213 nm laser interaction with solid samples composed of different matrices such as Co-cemented tungsten carbide hardmetals (metal–ceramic), steel (Fe-based metal) and glass (non-metal) using the optical aerosol spectrometer and the scanning electron microscopy. The ablation craters were additionally studied with the SEM and the optical profilometer.

2. Studied materials

2.1. Co-cemented tungsten carbides

Cemented carbide, or hardmetal as it is often called, is a material containing a ceramic non-conductive constituent – tungsten carbide (WC) – and metal cobalt which plays the role of a binder during the sintering process, so the physical properties of both main constituents are very different (WC m.p. 2870 °C, b.p. 6000 °C; Co m.p. 1495 °C, b.p. 2877 °C). To obtain a hardmetal with specific properties, other constituents such as Ti, Ta, Nb or V are added in the form of carbides before sintering.

Five samples with a varied content of their main constituent were selected as being representative of a larger set of miscellaneous tungsten carbide hardmetal products obtained from a powder metallurgy plant — Pramet Tools, L.L.C., Šumperk, Czech Republic, a subsidiary company of Seco Tools AB, Fagersta, Sweden. Their properties were expected to vary over the whole sample collection. Samples were routinely analysed using XRF spectrometry in the laboratory of the Research Institute of Inorganic Chemistry, J.S.C., (VÚAnCh) Ústí nad Labem, Czech Republic. The composition of the studied Co-cemented tungsten carbide samples is shown in Table 1.

The samples were in the form of blocks with a target area of about 1.5 cm^2 and a thickness of 7 mm. The sample preparation consisted of embedding the blocks into a polymethylmetacrylate (PMM) using a rounded mould to obtain an easily manipulated cast disc with a diameter of 3.5 cm. The sample surface of the disc was additionally rubbed down and polished.

2.2. Steel

Steel represents a conductive material with iron as the main component so the physical properties of Fe provide the characteristics of steel materials (m.p. 1535 °C and b.p. 3070 °C). To obtain specific properties depending on the steel utilization, other constituents are added during steel production. Steel samples were obtained from Královopolská a.s., Brno, Czech Republic, which is focusing on the supply of steel for machinery manufacturing. Five samples representing ferritic steel with an advanced corrosion resistance were in the form of a roller piece with a diameter of 3 cm. The sample preparation consisted only in the rollers being cut into 2 mm thick slices. The density of the samples did not differ significantly (7.6–7.8 g cm^{-3}). The hardness was obtained by the Vickers test. Physical properties with the sample elemental composition are described in Table 2. The content of the different phases in each sample was measured by Mössbauer analysis. The results show a pure ferritic phase for sample no. 54666, content of austenite up to 9% for sample nos. 24195, 43181 and 43182 and 27% of carbidic phase for sample no. 43164 (see Table 3).

Table 2
Physical properties and composition of steel samples (mg kg^{-1}).

Sample	Density g cm^{-3}	Hardness HV 1	25 °C[a] W/m K	Fe	Al	Si	P	Cr	Mn	Ni	Cu	Mo
24195	7.70	468	42	97.8%	310	3 300	200	500	14 000	400	400	200
43164	7.71	420	44	98.3%	220	3 400	130	1 100	10 700	800	600	200
43181	7.64	555	38	91.9%	140	10 000	160	48 900	3 500	1 500	1 100	11 500
43182	7.83	266	44	97.6%	160	2 500	110	9 100	5 200	1 000	900	4 100
54666	7.79	300	50	98.8%	2 700	2 400	100	1 300	4 500	1 000	1 100	300

[a] Thermal conductivity at 25 °C.

Table 3
Results of Mössbauer phase analysis for steel samples. The phase content is given as atomic fraction of iron atoms.

Sample	Ferite	Carbides	Austenite
24195	0.98		0.02
43164	0.73	0.27	
43181	0.91		0.09
43182	0.98		0.02
54666	1.00		

2.3. Glass

Glass is a non-conductive material with SiO_2 (m.p. 1800 °C and b.p. 2230 °C) as its main component. Commercial standards for X-ray fluorescence spectrometry — silica glass (2 THETA Co. Ltd., Český Těšín, Czech Republic) with different colors and visible transparency were used for the laser ablation experiments. Even if some of the glasses were classified as transparent to visible light, all studied glass samples absorbed strongly at 213 nm (A>2.4) so the optical properties for the laser working wavelength can be declared as nearly identical. The list of glass samples with their specifications and chemical composition is presented in Table 4.

2.4. Representative samples

For measurements describing the comparison between the mentioned materials, such as temporal behavior of particle formation (Chapter 4.3), *off-line* study of the generated particles (Chapter 4.4) and formation of ablation craters (Chapter 4.5), the following samples were chosen to represent each group of materials: sample no. 3648 K for Co-cemented tungsten carbides, sample no. 54666 for steels and U12 as a representative sample for glass. The sample selection was based on two criteria. The particle number concentration as the first one — on the base of PNC measurements, samples with extremely low or high PNC were edged out (Fig. 1A–C) and a selection was made from the rest of the samples. The sample composition as the second criterion — representative samples contain all the important elements and the content of matrix elements as the same as sample density of samples do not reach extreme values (see Tables 1, 2, and 4).

3. Experimental

3.1. Laser ablation system

The laser ablation was undertaken using a pulsed Nd:YAG laser operating at a wavelength of 213 nm with a pulse duration of 4.2 ns (UP 213, New Wave Research, Inc., Fremont, CA, USA). In order to generate a sufficient number of particles within the whole particle size range studied for all examined sample types, several optimization experiments were undertaken. Based on these experiments, the following parameters of the ablation laser system were employed: A laser spot diameter of 100 µm, a laser pulse repetition rate of 10 Hz and a fluence of 13 J cm^{-2}. The 33 cm^3 sample chamber (SuperCell, New Wave Research, USA) of the ablation system has been specifically designed to enable rapid eluting of the aerosol in a large format cell. Using helium as a carrier gas under normal operating conditions with a flow rate of 1.0 l min^{-1}, the ablation-generated aerosol was transported from the chamber through a 0.5-m long polyurethane transport tube (i.d. 4 mm) to an aerosol spectrometer.

3.2. Optical aerosol spectrometer for particle classification

The particle size and concentration of the produced aerosol particles were measured and evaluated *on-line* with the optical Aerosol Spectrometer Welas® 3000 Series (WhitE Light Aerosol Spectrometer, Palas GmbH, Karlsruhe, Germany). The Welas® operates on the principle of the single particle scattering of white light. The intensity of the scattered-light detected at an angle of 90° is the measure of the particle size. The number of scattered-light impulses measured per time unit determines the particle concentration. Welas® sensor 2200 provides a direct measurement of size distribution of particles in the size range 0.25−17 µm (particles in this size range are called "large" particles in this paper) with a maximum concentration of 10^4 particles cm^{-3}. The large particles are classified into 60 size channels on the basis of polystyrene-latex-equivalent diameters. Particles smaller than 250 nm are below the size limit for the direct detection by the Welas® sensors. To detect these small particles their size is first increased, by condensing 2-propanol vapour onto all present particles in the Condensation Nucleus Counter (CNC), to µm-sized particles that are on-line detected with the Welas® sensor 2100. However, as a result of 2-propanol condensation, the former size distribution of all particles is lost and we can only count the total concentration of all particles larger than 10 nm up to 17 µm with a maximum concentration of up to 10^5 particles cm^{-3}. The concentration of small particles (the size range 0.01–0.25 µm) was calculated as the difference between the total concentration of all particles (measured with sensor 2100 as a result of 2-propanol condensation in the CNC; the size range 0.01–17 µm) and the concentration of large particles (measured with sensor 2200; the size range 0.25–17 µm).

During interpretation of the results from the Welas® as well as from other optical particle counters, it is necessary to take into account that the intensity of the scattered-light does not depend only on the particle size, but also on the shape, orientation and especially on the refractive index of the particle [38–41]. The difference between the refractive index of the analysed particle and the refractive index of a latex particle that is used for Welas calibration can consequently lead to an incorrect indication of measured particle size [42,43]. As a result, the indicated particulate diameter can be shifted to a higher or smaller diameter in comparison with the true size of the particle in question. On the other hand, the difference between the refractive index of the analysed particle and the refractive index of a latex particle has no effect on the determination of the particle concentration in the Welas® because it counts all particles passing through the sensing volume regardless their refractive index.

3.3. Scanning electron microscopy

The structure of the laser-generated particles was studied off-line after their collection on a polycarbonate membrane filter (25 mm

Table 4
Composition of glass samples (wt.%).

Sample	Description	Density g cm^{-3}	SiO_2	Al_2O_3	BaO	CaO	Fe_2O_3	K_2O	MgO	Na_2O	PbO	SrO	ZnO
U8	Colorless, clear	2.79	60.9	2.0	11.2	0.94	0.05	7.4	0.57	7.9	1.95	4.97	
U12	White, opaque	2.47	69.9	7.0		4.5	0.02	2.5	0.05	14.0			2.0
U35	Red, clear	2.63	60.5	1.2		0.75	0.05	5.3	0.02	13.5			14.5
U37	Dark blue, clear	2.48	73.0	1.9		8.0	0.05	2.5	0.05	12.0			1.0
U42	Colorless, clear	2.48	67.8	3.9		4.0	0.05	4.0	2.1	10.0			

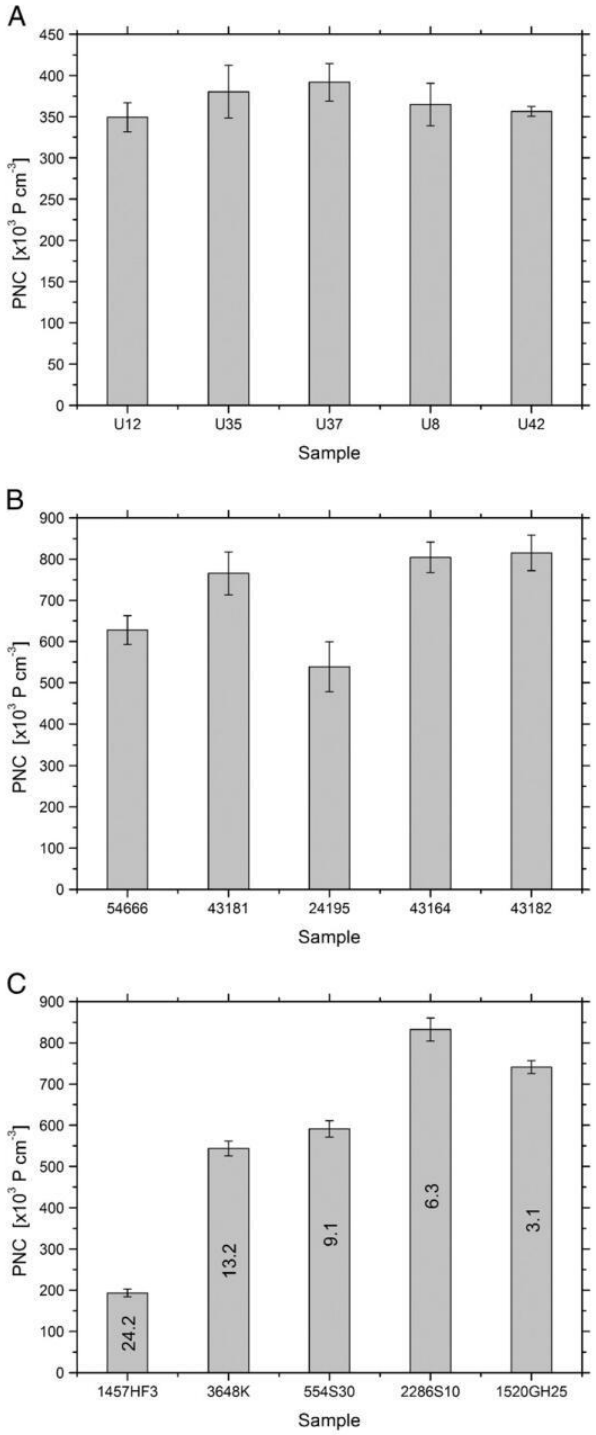

Fig. 1. Particle number concentration (PNC) of small particles (10–250 nm) generated by ablation of different samples: A) glasses, B) steels and C) Co-cemented tungsten carbides. The numbers on bars of C) indicate the W/Co ratio in the sample.

diameter and 0.2 μm pores, Cyclopore, Whatman). To collect a sufficient number of particles, the ablation was performed over a 5 minute time period. The filter was placed behind the ablation cell at a distance equal to the ablated particle measurements conducted on the Welas® (0.5 m). The particles collected on the filter as well as the laser ablated craters were imaged using the Scanning Electron Microscopy SEM (Vega, TESCAN, s.r.o., Brno, Czech Republic) equipped with a tungsten heated cathode electron source. The SEM Vega operates at a base pressure lower than 8.0×10^{-3} Pa. The SEM pictures were recorded in the resolution imaging mode with a resolution in the order of tens of nm. The standard secondary electron detector was used during image collection. The electron beam acceleration voltage was kept constant at 30 kV for all presented pictures.

3.4. Optical profilometry

An optical profilometer MicroProf (FRT, Germany) was used for the measurements of the ablation crater shape and volume with 1-μm lateral and 3-nm vertical resolution. The operational principle of this equipment has been described elsewhere [44,45]. In this device white light from a halogen lamp passes through the CHR 150 N lens with a high chromatic aberration. Different monochromatic light components are focused at different heights from a reference plane at the output of the optical fibre. The same optical fibre collects scattered-light from the surface under study. This light is analysed by means of a spectrometer. The spectral intensity distribution of the light processed by the spectrometer has a maximum at the wavelength of the monochromatic component exactly focused on the surface. The height of the surface irregularities is deduced by means of a calibration table from the wavelength of the spectral intensity distribution maximum.

4. Results and discussion

4.1. Particle concentration and particle size distribution measurements

Three sets of samples, each having five specimens of material, were studied to obtain information about particle formation both for the samples with a similar matrix (within each set) and for different materials. The concentration both for small (size range of 10–250 nm) and large (size range of 0.25–17 μm) particles was measured using ablation parameters presented in Chapter 3.0 (Experimental). The results showed a significant dominance of small particles in comparison with the large particles, irrespective of the kind of material. Although the steel samples produced the highest concentration of large particles, the overall number of large particles produced forms only 0.1% of the total number of all generated particles (size range of 10 nm–17 μm). For the carbides, the contribution of the large particles varies from 0.01% to 0.1% due to the different sample composition [44]. In the case of glass samples, the occurrence of the large particles was even lower (<0.01%). The results indicate diverse amounts of large particles in aerosols generated from glass samples compared to other materials (especially steel) and are in good agreement with the ablation crater observations (see Chapter 4.5). It points to minimal glass melting during the ablation process which is understandable if we take into consideration that the molten surface layer serves as the source of large particle formation. This problem is discussed in detail in Chapter 4.2.

To characterize the laser ablation behavior of each sample, we compared the concentration of small particles as a major part of the generated material. To define the variation in the particle concentration of samples within each material, relative standard deviation (RSD) was calculated. RSD was obtained for each material from the values of particle concentrations of all related samples. Fig. 1 presents the total concentration of small particles for all 15 specimens.

4.1.1. Glass samples

In the case of the glass samples (Fig. 1A), the total concentration of all small particles is in very good agreement for all samples (RSD 5%). That probably results from the similar chemical composition and physical properties of studied glass in spite of the different colors. A

very important parameter is the similar strong absorption of 213 nm of all samples (A>2.4).

4.1.2. Steel samples

The five steel samples showed increased diversity in small particle production (Fig. 1B). The RSD value of 17% indicates the respective importance of the sample melting that occurs during the ablation process for each steel sample, resulting from the difference in chemical composition, structure and physical properties. The lowest value of small particle production was found for sample no. 24195. A possible reason for the difference from the other samples can be found in the material structure connected with the sample composition. Sample no. 24195 contained the least amounts of Cr, Ni and Mo — elements creating precipitates in ferritic steels. Moreover these precipitates are formed along the ferritic grain border whereas precipitates in other samples are spread independently of the grain structure. These observations were made by optical microscopy (metallography microscope NEOPHOT32 Carl Zeiss). An example of different structures is given in Fig. 2. Sample no. 24195 with the least content of Cr, Ni and Mo and sample no. 43181 with the highest content of these elements (both samples with ferritic structures with a small content of austenite structure) are compared. Different percent occurrence of precipitates being the same as their location is obvious.

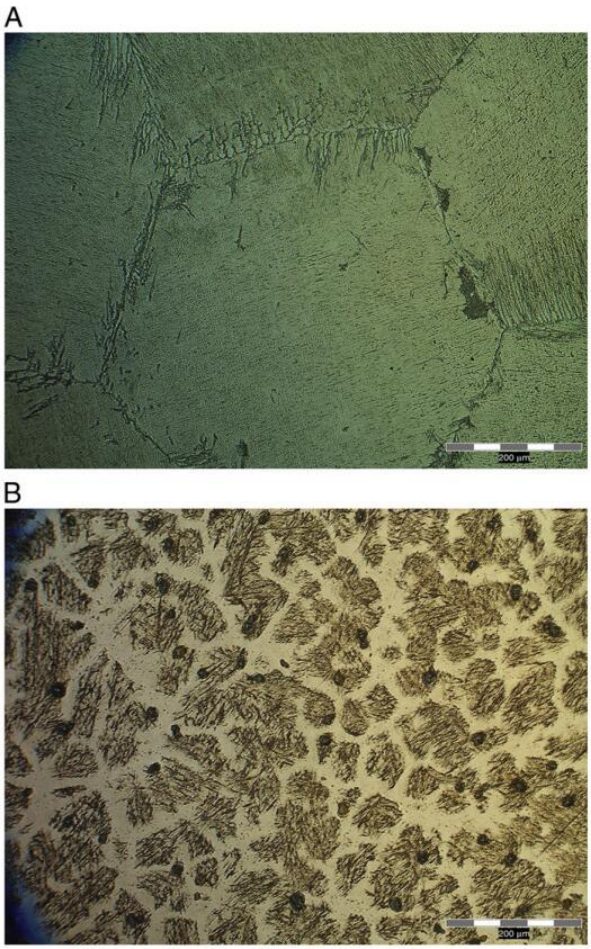

Fig. 2. Microstructure of ferritic steels, optical microscopy in reflected light A) sample no. 24195 (2% of austenite), B) sample no. 43181 (9% of austenite).

Steel samples can give a good example of the material structure impact on the laser ablation. Even if the sample composition seems to be very similar (e.g. all samples contain 97–99% Fe) the structure influenced by the minor element content or fabrication procedure can be different and plays an important role in the laser ablation mechanism.

4.1.3. Co-tungsten carbide samples

The most significant differences in the concentration for both large and small particles were observed for Co-cemented ceramic samples. The RSD for small particles of five ceramic samples reached a value of 42% (Fig. 1C). Evaluation of the relationship between the particle concentration and the composition of the ceramic samples revealed the production of a high number of small particles for the samples with a small ratio of W/Co while an increase in the W/Co ratio induced a decrease in the formation of small and an increase in the formation of large particles. Samples with a lower content of Co (higher W/Co ratio) provided a higher concentration of large particles and a lower concentration of small particles. Recently, we reported that the small particles are enriched with Co while large particles are enriched with tungsten [44], which is in good agreement with theories describing particle formation — small particles are enriched with more volatile elements while large particles show a significant enrichment of elements with a high melting point [29]. The W/Co values are mentioned together with the PNC of small particles in Fig. 1C.

Other research was focused on a detailed study of the concentration of large spherical particles. Even if the contribution from large particles is very low, the results indicate an increased occurrence of the large particles for samples with a dominant rim around the ablation crater (see Chapter 4.5). This is understandable if we presume that the ablation rim increases with the more intensive melting of the sample surface.

4.2. Size distribution and total volume of large spherical particles

The number of generated particles larger than 250 nm is negligible in comparison with the total concentration of all generated particles for all samples (<0.1%) but the question is: what is the total volume of these large particles. The volume of generated spherical particles larger than 250 nm was calculated from the particle size distribution graphs that were created using the data from the Welas® measurements. The distribution graphs (Fig. 3) correspond to 60 s laser ablations and show a similar behavior for all types of tested materials differing mainly in the absolute value of particle concentration. The particle size distribution diagrams are displayed across the whole

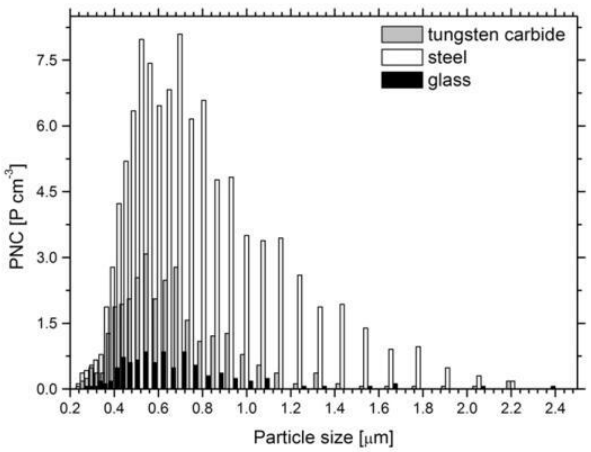

Fig. 3. Particle size distribution graph for large spherical particles (Co-cemented tungsten carbide sample no. 3648 K, steel no. 54666, and glass no. U12).

range that covers the increase and the decrease of the particle concentration within the particle diameters. On the basis of these graphs we can categorize the single spherical particles by their diameters in the size range of 0.25–3 μm with the mode diameter around 0.6 μm. Only a negligible number of particles larger than 3 μm in diameter were detected. By SEM we can observe structures – "fibres" – larger than 3 μm on the filter (Fig. 6, Chapter 4.4). Because no particles with such a large diameter were detected by optical spectrometer we can deduce the creation of the "fibre" structures by impaction and coagulation only during the particle's collection on the filter surface. Consequently, it follows that particles taking part in the formation of "fibres" on the filter are transported either as single particles or in clusters smaller than 250 nm in diameter.

The calculation of large particle volume presumes that the particles are spherical in shape. The results show that a substantial part of the large particle volume comes from steel samples (9–50%) and tungsten carbides (6–23%). For the glass samples the total volume of large particles does not exceed 0.2%. Calculating backwards using the volume of the ablation craters gave the following average for particle diameters smaller than 250 nm (during this calculation, a production of monodisperse particles was assumed but, in reality, polydisperse particles are generated): 70 nm for steels, 100 nm for tungsten carbides and 150 nm for glasses. These results are comparable with values published for UV ns laser ablation of metal and glass samples [46,47].

4.3. Temporal behavior of particle formation

To obtain information about particle formation during the laser ablation process, the temporal evolution of the ablation process during the single spot drilling was monitored by means of the Welas®. One sample from each group of materials (i.e., carbides, steels and glasses) was studied (see Chapter 2.4). The number of particles produced was monitored over 5 second intervals during a 400 second laser ablation period using the laser conditions described in Chapter 3.1 (Experimental). Measurements for the selected sample of each material were repeated three times both for small (size range of 10–250 nm) and large particles (size range of 0.25–17 μm). The temporal evolution of small-particle formation was similar for all investigated materials. The only difference was in the total concentration of small particles obtained (Fig. 4). The highest concentration of small particles was observed during the first 100 s of ablation with a maximum around 45 s from the start of the ablation process.

The temporal evolution of the large-particle formation showed a different behavior for each material studied (Fig. 5). The steel sample

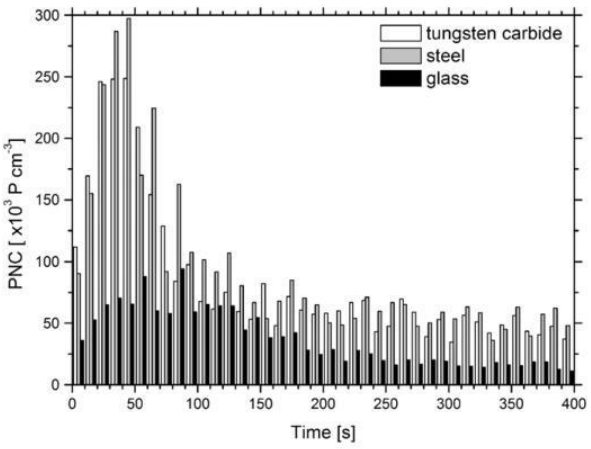

Fig. 4. Temporal behavior of particle formation during 400 s of laser ablation for particles in the size range 10–250 nm; PNC — particle number concentration.

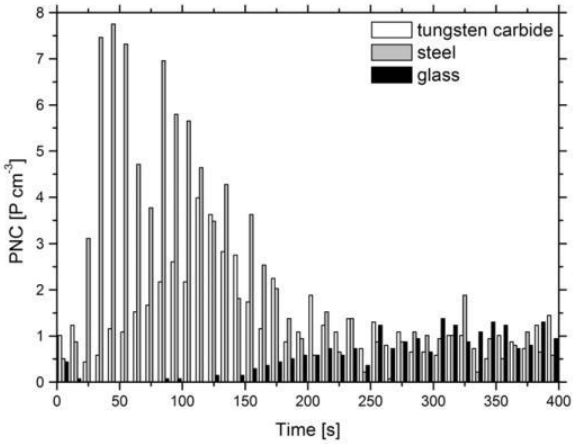

Fig. 5. Temporal behavior of particle formation during 400 s of laser ablation for particles in the size range 0.25–17 μm; PNC — particle number concentration.

produced the highest concentration of large particles with a maximum around 40 s after the laser ablation started. The maximum concentration of large particles generated during the ablation of Co-cemented carbide was shifted towards a later time (i.e., 100 s after the ablation started) and the total concentration of large particles produced is lower in comparison with the steel sample. The glass sample showed a completely different behavior. The production of a more significant number of particles in the size range 0.25–17 μm only started after 100 s from the beginning of the ablation and then their concentration increased with time without any obvious maximum. The time delay can be explained by the different mechanism of the laser–glass interaction. As it has been reported [37], the first few laser shots cause only minimal production of large particle, because the glass samples are, for these initial shots, more transparent. However, these shots create defects in the glass surface and progress in the formation of these defects strengthens the ablation process and consequently enhances the production of large particles.

Fig. 5 indicates that, if only during the first ~300 s, the temporal behavior of large particle formation for all three samples is different. After this time interval the ablation processes are stabilized and from that time onwards the concentration of large particles produced is comparable for all materials.

4.4. Off-line study of the generated particles

A more detailed study of the shape and structure of laser-generated particles was performed off-line after the collection of particles on the polycarbonate membrane filter. SEM observations provided a similar picture for all materials which independently proved the same mechanism of particle formation on physical or chemical sample properties of the sample. The SEM images indicate a polydisperse particle size distribution that is typical for ns laser ablation and is in good agreement with other published studies [13–15,34]. Spherical particles with the diameters from tenths to units of micrometers are surrounded by a net of "fibres" composed of particles with diameters in the range of tens to hundreds of nanometers. The origin of the "fibres" is discussed in [44], and is attributed to several processes (condensation, coagulation, collision–coalescence process, hard and soft agglomeration) inside the ablation cell (clusters composed of several nanoparticles are formed) and on the filter. As a representative example, Fig. 6 shows the structures of particles described above collected on filters from the steel sample. Very

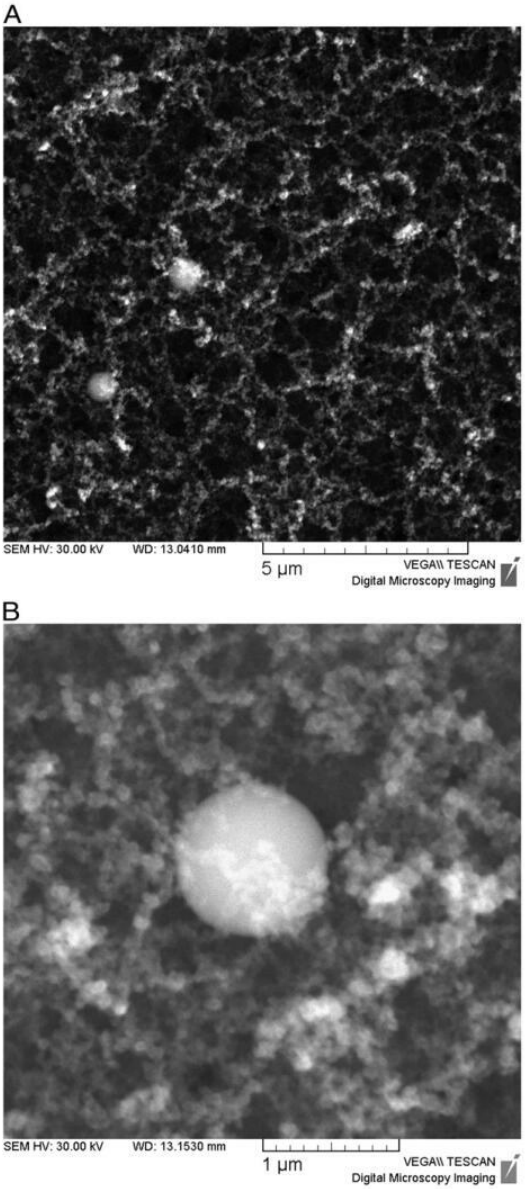

Fig. 6. SEM images of laser-generated particles from steel sample no. 54666 (A, B) after their collection on a polycarbonate membrane filter; A) overall view to the net of "fibres" composed of primary clusters with diameters ranging from tens to hundreds of nanometers surrounding the large spherical structures, B) detailed view with a large spherical particle and surrounding clusters.

similar structures were observed for Co-cemented carbides and glass samples too.

4.5. Formation of ablation craters

The shape, structure and volume of an ablation crater can be a clue to the ablation process behavior. The ablation rate, the degree of sample melting or the degree of reverse condensation of evaporated material can be estimated. The amount of material lifted during laser ablation can be specified from the ablation crater volume with regard to the amount of material remaining around the crater as a rim. The height of the crater rim and the amount of material deposited around the craters for each material were studied using both the SEM and the optical profilometer. The SEM images of ablation craters after 600 pulses for each material, together with the optical micrographs and selected cross-section, are presented in Fig. 7A, B, and C.

Steel is a material with the most visible melting during laser ablation. As an example, steel sample no. 54666 (Fig. 7A) provided a 40 µm deep ablation crater with a high crater rim (40 µm) and the crater bottom with a shape indicating the presence of a liquid phase during ablation. Although only contributing a negligible concentration of large particles compared to the total concentration of all particles (see Chapter 4.2), there is an evident correlation between the PNC (in the size range 0.25–17 µm) and the height of the ablation rim. The biggest difference was found between sample no. 43164 (as the only sample containing carbide) with a minimal crater rim (5 µm) and sample no. 43182 with the ablation rim of up to 40 µm and a three times higher PNC value which indicates a higher occurrence of sample melting during the nanosecond ablation. In general the height of the crater rim grows with an increase in the concentrations of large particles produced. The crater rims of all steel samples reached heights from 5 to 40 µm with an RSD of 55%.

A melted bottom was also observed in the crater of the Co-cemented carbide sample (Fig. 7B). The presence of the crater rim was not so obvious as in the case of steels. The rim heights reached values of 2–8 µm with an RSD of 40%.

From Fig. 7C we can conclude that glass samples provided ablation craters with the least evidence of thermal effects when crater rims of less than 5 µm with an RSD of 16% were observed. Smaller thermal effects in comparison with metal or ceramic samples are explainable by the lower thermal conductivity of glass. The absence of larger deposited particles (tenths–units of microns) corresponds with the fact that a very small production of large particles was observed in comparison with steel or tungsten carbide samples during Welas® measurements (Chapter 4.2).

The size and geometry of the ablation craters for all materials were obtained from ten cross-sections placed at regular angles across each ablation crater. The depth of the ablation craters differed very significantly for each material which indicates diverse ablation rates (after 600 pulses): Co-cemented carbide 20 µm, steel 40 µm and glass 100 µm; as well as the height of the rim as discussed above. With regard to the geometry of the craters, the volume of carbide and steel craters reached the values of 120,000–160,000 μm^3 and 230,000–260,000 μm^3, respectively. Utilizing the same laser ablation conditions, the ablation craters for glass show the release of significantly higher volumes of material (680,000–700,000 μm^3).

4.6. Total mass of the particles

The material mass corresponding to the ablated volume was calculated using the sample density (Chapter 2.0). The volume of material finally flushed away from the sample was used — the melted layer on the crater rim was subtracted from the crater volume. The calculation does not consider the fractionation that must occur during ns 213 laser ablation. The following ranges of mass per ablation were obtained from the samples: Co-cemented tungsten carbides 1.8–2.1 µg with 8% RSD, steels 1.6–1.9 µg with 5% RSD and glass 1.7–1.9 µg with an RSD of 9%. The RSD values can be caused by different matrices of specimens within each sample set or by the estimation of ablation crater volumes that was probably not perfectly precise due the irregular shape of the craters. Comparing the average mass of each material, the lowest value came from the steel samples (1.7 µg). This is probably caused by the extreme deposition of melted material in the form of the crater rim (large numbers of particles remain around of the crater instead of evaporating). The glass samples provided a lower mass (1.8 µg) compared to the Co-cemented tungsten carbides (2.0 µg) and this is probably due to the different optical and mechanical properties. We can also take into account the inaccuracy

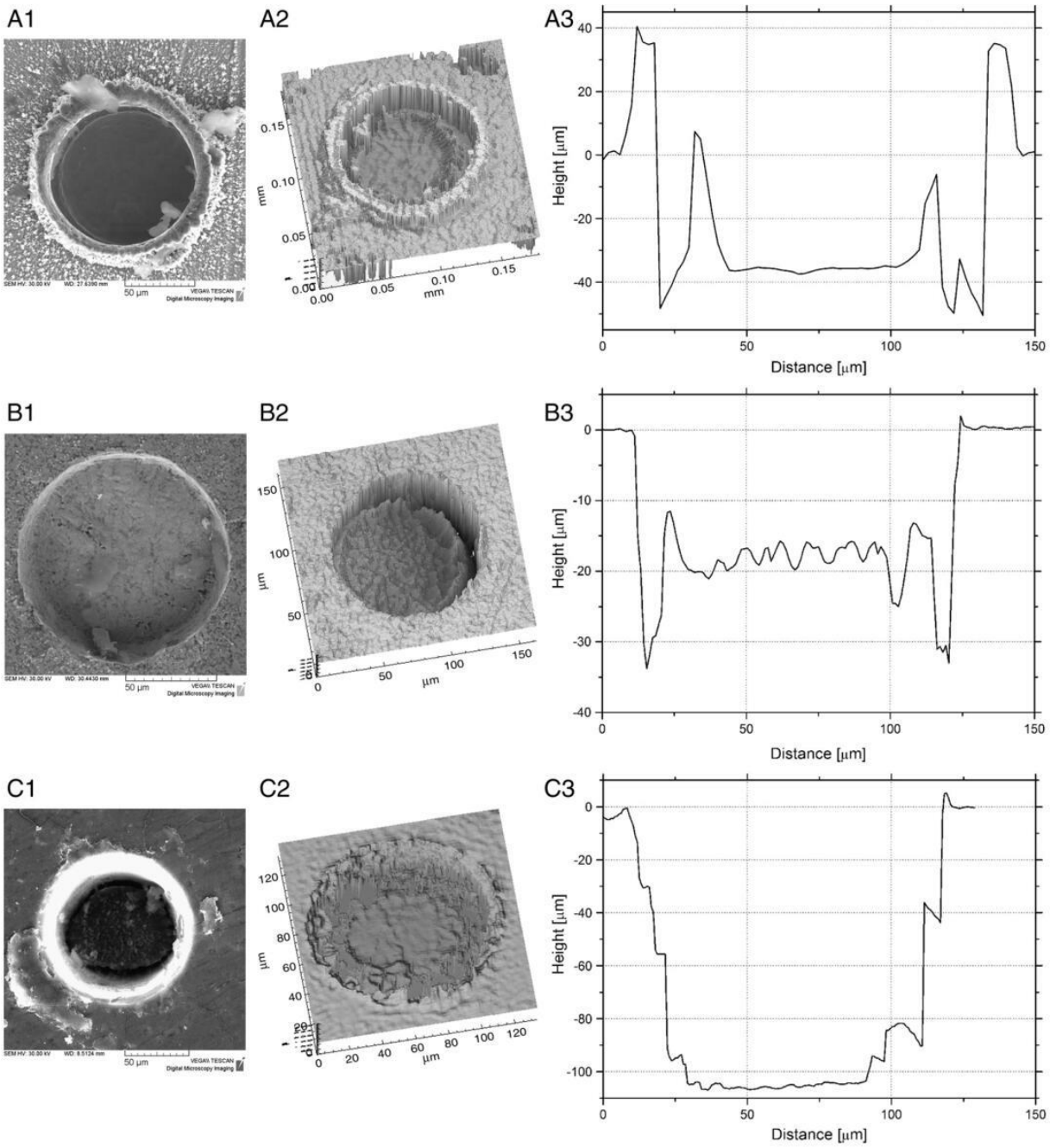

Fig. 7. SEM and optical micrograph of the ablation crater together with a representative cross-section on A) steel sample no. 54666, B) Co-cemented carbide sample no. 3648K, C) glass sample no. U12.

of the calculation caused by the different densities of ablated samples and particles formed during the ablation.

5. Conclusion

The nanosecond 213 nm laser ablation of samples with different matrices, chemical composition and physical properties was studied using the optical aerosol spectrometer, the SEM and the optical profilometer. Metal (steel), metal–ceramic (Co-cemented tungsten carbide hardmetals) and non-metal (glass) samples were chosen to represent materials with significantly different characteristics. Each material was represented by five specimens. The optical measurements, allowing the determination of particle concentrations at two size ranges (small particles with diameters ranged from 10–250 nm and large particles with diameters in the size range of 0.25–17 μm) revealed different temporal behavior of large particle formation as well as diverse amounts of large particles in the aerosol during glass, steel and metal–ceramic sample ablation.

The dependence of the production of particles smaller than 250 nm on the composition and structure of the single specimens is unquestionable for metal and metal–ceramic samples. A connection between Co content and particle production was found in the case of tungsten carbides. The explanation for the steel samples is more complicated due to the multicomponent composition and different physical properties of each sample. The different behavior of laser ablation can be accredited to the various sample structures.

Even if the number of generated particles larger than 250 nm is slight (<0.1%) in comparison with the total concentration of all generated particles for all samples, the volume of large particles is negligible only for glass (<0.2%). In the case of steel samples it can reach up to 50%. This is attributed to the reduced melting of glass samples during the ablation whereas the melting surface serves as a source for the ejection of particles reaching diameters up to several micrometers.

The structure of the ablation craters also points to a higher participation of the melting processes in the case of metal/metal–ceramic samples in comparison with glass. Ablation craters with a minimal deposit on the crater rim and minimal melted bottom were observed on the glass samples in contrast to e.g. craters on metal samples where the material has been evidently melted. A smaller thermal effect in comparison with metal or ceramic samples is explainable by the lower thermal conductivity of glass. The results of the particle concentration and particle size distribution measurements together with the off-line study of collected particles by SEM suggest the same ablation products for all studied samples, independent of the sample matrix. Particles generated during the laser ablation contain two main structures. First, spherical particles with a diameter range of 0.25–3 μm with the mode diameter around 0.6 μm formed by ejection from a liquid surface layer due to hydrodynamic instability. Second, clusters reaching sizes of tens to hundreds of nanometers that are visible by SEM as construction units of "fibres" with a length of several micrometers forming explicitly on the filter surface.

The total mass of the particles obtained from the crater volume and sample density provided lowest values for steel samples (1.7 μg in average) probably because of the high number of particles remaining around the rim of the crater instead of evaporating. The mass reached values 1.8 and 2.0 μg for glass and Co-cemented tungsten carbides, respectively. Consideration should be given to the fact that the calculation does not consider the fractionation that must occur during ns 213 laser ablation.

Acknowledgements

M.H. gratefully acknowledges the Czech Science Foundation for bestowing the project 203/07/P439. M.H. and V.K. acknowledge the Ministry of Education, Youth and Sports of the Czech Republic for the research projects MSM0021622412 and MSM0021622410, respectively. P.M. acknowledges an institutional research plan of the Institute of Analytical Chemistry of the Academy of Sciences of the Czech Republic No. AV0 Z40310501. J.K. acknowledges the Ministry of Education, Youth and Sports of the Czech Republic for the research project MSM 0021630508.

Special acknowledgement belongs to Oldrich Schneeweiss from the Institute of Physics of Materials, Academy of Sciences of the Czech Republic for the Mössbauer analysis, optical microscopy and hardness testing of steels.

References

[1] D. Günther, S.E. Jackson, H.P. Longerich, Laser ablation and arc/spark solid sample introduction into inductively coupled plasma mass spectrometers, Spectrochim. Acta Part B 54 (1999) 381–409.
[2] S.F. Durrant, Laser ablation inductively coupled plasma mass spectrometry: achievements, problems, prospects, J. Anal. At. Spectrom. 14 (1999) 1385–1403.
[3] J.D. Winefordner, I.B. Gornushkin, D. Pallas, O.I. Matveev, B.W. Smith, Novel uses of lasers in atomic spectroscopy. Plenary Lecture, J. Anal. At. Spectrom. 15 (2000) 1161–1189.
[4] S.F. Durrant, N.I. Ward, Recent biological and environmental applications of laser ablation inductively coupled plasma mass spectrometry (LA-ICP-MS), J. Anal. At. Spectrom. 20 (2005) 821–829.
[5] J.S. Becker, Applications of inductively coupled plasma mass spectrometry and laser ablation inductively coupled plasma mass spectrometry in materials science, Spectrochim. Acta Part B 57 (2002) 1805–1820.
[6] R.E. Russo, X. Mao, H. Liu, J. Gonzalez, S.S. Mao, Laser ablation in analytical chemistry — a review, Talanta 47 (2002) 425–451.
[7] K. Novotný, T. Vaculovič, M. Galiová, V. Otruba, V. Kanický, J. Kaiser, M. Liška, O. Samek, R. Malina, K. Páleníková, The use of zinc and iron emission lines in the depth profile analysis of zinc-coated steel, Appl. Surf. Sci. 253 (2007) 3834–3842.
[8] M. Galiová, J. Kaiser, K. Novotný, O. Samek, L. Reale, R. Malina, K. Páleníková, M. Liška, V. Čudek, V. Kanický, V. Otruba, A. Poma, A. Tucci, Utilization of laser induced breakdown spectroscopy for investigation of the metal accumulation in vegetal tissues, Spectrochim. Acta Part B 62 (2007) 1597–1605.
[9] D. Günther, H. Cousin, B. Magyar, I. Leopold, Calibration studies on dried aerosols for laser ablation-inductively coupled plasma mass spectrometry, J. Anal. At. Spectrom. 12 (1997) 165–170.
[10] C. Craig, K.E. Jarvis, L. Clarke, An assessment of calibration strategies for the quantitative and semi-quantitative analysis of calcium carbonate matrices by laser ablation-inductively coupled plasma-mass spectrometry (LA-ICP-MS), J. Anal. At. Spectrom. 15 (2000) 1001–1008.
[11] L. Kleiber, H. Fink, R. Niessner, U. Panne, Strategies for the analysis of coal by laser ablation inductively coupled plasma mass spectroscopy, Anal. Bioanal. Chem. 374 (2002) 109–114.
[12] U. Narewski, G. Werner, H. Schulz, C. Vogt, Application of laser ablation inductively coupled mass spectrometry (LA-ICP-MS) for the determination of major, minor, and trace elements in bark samples, Fres. J. Anal. Chem. 366 (2000) 167–170.
[13] I. Hubová, M. Holá, J. Pinkas, V. Kanický, Examination of sol–gel technique applicability for preparation of pellets for soil analysis by laser ablation inductively coupled plasma optical emission spectrometry, J. Anal. At. Spectrom. 22 (2007) 1238–1243.
[14] A.J. Fitzpatrick, T.K. Kyser, D. Chipley, D. Beauchemin, Fabrication of solid calibration standards by a sol–gel process and use in laser ablation ICPMS, J. Anal. At. Spectrom. 23 (2008) 244–248.
[15] V. Možná, J. Pisonero, M. Holá, V. Kanický, D. Günther, Quantitative analysis of Fe-based samples using ultraviolet nanosecond and femtosecond laser ablation-ICP-MS, J. Anal. At. Spectrom. 21 (2006) 1194–1201.
[16] R.E. Russo, X.L. Mao, O.V. Borisov, H. Liu, Influence of wavelength on fractionation in laser ablation ICP-MS, J. Anal. At. Spectrom. 9 (2000) 1115–1120.
[17] J. Gonzáles, C. Liu, X. Mao, R.E. Russo, UV-femtosecond laser ablation-ICP-MS for analysis of alloy samples, J. Anal. At. Spectrom. 19 (2004) 1165–1168.
[18] D. Bleiner, D. Günther, Theoretical description and experimental observation of aerosol transport processes in laser ablation inductively coupled plasma mass spectrometry, J. Anal. At. Spectrom. 16 (2001) 449–456.
[19] M. Guillong, I. Horn, D. Günther, A comparison of 266 nm, 213 nm and 193 nm produced from a single solid state Nd:YAG laser for laser ablation ICP-MS, J. Anal. At. Spectrom. 18 (2003) 1224–1230.
[20] J. Koch, M. Wälle, J. Pisonero, D. Günther, Performance characteristics of ultraviolet femtosecond laser ablation inductively coupled plasma mass spectrometry at 265 and 200 nm, J. Anal. At. Spectrom. 21 (2006) 932–940.
[21] N.J. Seatveit, S.J. Bajic, D.P. Baldwin, R.S. Houk, Influence of particle size on fractionation with nanosecond and femtosecond laser ablation in brass by online differential mobility analysis and inductively coupled plasma mass spectrometry, J. Anal. At. Spectrom. 23 (2008) 54–61.
[22] R.E. Russo, X. Mao, J.J. Gonzales, S.S. Mao, Femtosecond laser ablation ICP-MS, J. Anal. At. Spectrom. 17 (2002) 1072–1075.
[23] C. Liu, X.L. Mao, S.S. Mao, X. Zeng, R. Greif, R.E. Russo, Nanosecond and ferntosecond laser ablation of brass: particulate and ICPMS measurements, Anal. Chem. 76 (2004) 379–383.
[24] J. Gonzáles, S.H. Dundas, C.Y. Liu, X. Mao, R.E. Russo, UV-femtosecond and nanosecond laser ablation-ICP-MS: internal and external repeatability, J. Anal. At. Spectrom 21 (2006) 778–784.
[25] C.C. Garcia, H. Lindner, A. von Bohlen, C. Vadla, K. Niemax, Elemental fractionation and stoichiometric sampling in femtosecond laser ablation, J. Anal. At. Spectrom. 19 (2008) 470–478.
[26] S.H. Jeong, O.V. Borisov, J.H. Yoo, X.L. Mao, R.E. Russo, Effects of particle size distribution on inductively coupled plasma mass spectrometry signal intensity during laser ablation of glass samples, Anal. Chem. 71 (1999) 5123–5130.
[27] J.H. Yoo, O.V. Borisov, X. Mao, R.E. Russo, Existence of phase explosion during laser ablation and its effects on inductively coupled plasma-mass spectroscopy, Anal. Chem. 73 (2001) 2288–2293.
[28] R. Jaworski, E. Hoffmann, H. Stephanowitz, Collection and separation of particles by size from laser ablated material, Int. J. Mass Spectrom. 219 (2002) 373–379.
[29] H.R. Kuhn, D. Günther, Elemental fractionation studies in laser ablation inductively coupled plasma mass spectrometry on laser-induced brass aerosols, Anal Chem. 75 (2003) 747–753.
[30] C. Liu, X. Mao, S.S. Mao, R. Greif, R.E. Russo, Particle size dependent chemistry from laser ablation of brass, Anal. Chem. 77 (2005) 6687–6691.
[31] J. Koch, A. von Bohlen, R. Hergenröder, K. Niemax, Particle size distributions and compositions of aerosols produced by near-IR femto- and nanosecond laser ablation of brass, J. Anal. At. Spectrom. 19 (2004) 267–272.

[32] C. Liu, X.L. Mao, S.S. Mao, X. Zeng, R. Greif, R.E. Russo, Nanosecond and femtosecond laser ablation of brass: particulate and ICPMS measurements, Anal. Chem. 76 (2004) 379–383.
[33] S.H. Jeong, O.V. Borisov, J.H. Joo, X.L. Mao, R.E. Russo, Effects of particle size distribution on inductively coupled plasma mass spectrometry signal intensity during laser ablation of glass samples, Anal. Chem. 71 (1999) 5123–5130.
[34] P. Weis, H.P. Beck, D. Günther, Characterizing ablation and aerosol generation during elemental fractionation on absorption modified lithium tetraborate glasses using LA-ICP-MS, Anal. Bioanal. Chem. 381 (2005) 212–224.
[35] H.R. Kuhn, D. Günther, Laser ablation-ICP-MS: particle size dependent elemental composition studies on filter-collected and online measured aerosols from glass, J. Anal. At. Spectrom. 19 (2004) 1158–1164.
[36] M. Ducreux-Zappa, J.M. Mermet, Analysis of glass by UV laser ablation inductively coupled plasma atomic emission spectrometry. Part 1. Effects of the laser parameters on the amount of ablated material and the temporal behaviour of the signal for different types of laser, Spectrochim. Acta Part B 51 (1996) 321–332.
[37] V. Kanicky, V. Otruba, J.M. Mermet, Use of internal standardization to compensate for a wide range of absorbance in the analysis of glasses by UV laser ablation inductively coupled plasma atomic emission spectrometry, Appl. Spectrosc. 52 (1998) 638–642.
[38] R. Friehmelt, S. Heidenreich, Calibration of a white light/90° optical particle counter for "aerodynamic" size measurements — experiments and calculations for spherical particles and quartz dust, J. Aerosol Sci. 30 (1999) 1271–1279.
[39] B. Sachweh, H. Barthel, R. Polke, H. Umhauer, H. Büttner, Particle shape and structure analysis from the spatial intensity pattern of scattered light using different measuring devices, J. Aerosol Sci. 30 (1999) 1257–1270.
[40] L. Mölter, P. Keßler, Partikelgrößen- und partikelanzahlbestimmung in der außenluft mit einem neuen optischen aerosolspektrometer, Gefahrst. Reinhalt. Luft 64 (2004) 439–447.
[41] J. Gebhart, Response of single-particle optical counters to particles of irregular shape, Part. Part. Syst. Charact. 8 (1991) 40–47.
[42] H. Quenzel, Influence of refractive index on the accuracy of size determination of aerosol particles with light-scattering aerosol counters, Appl. Opt 8 (1969) 165–169.
[43] W.W. Szymanski, T. Ciach, A. Podgorski, L. Gradon, Optimized response characteristics of an optical particle spectrometer for size measurement of aerosols, J. Quant. Spectrosc. Radiat. Transfer 64 (2000) 75–86.
[44] M. Holá, V. Konečná, P. Mikuška, J. Kaiser, K. Páleníková, S. Průša, R. Hanzlíková, V. Kanický, Study of aerosols generated by 213 nm laser ablation of cobalt-cemented hard metals, J. Anal. At. Spectrom. 23 (2008) 1341–1349.
[45] I. Ohlídal, M. Ohlídal, D. Franta, V. Čudek, V. Bursíková, P. Klapetek, K. Páleníková, Influence of technological conditions on mechanical stresses inside diamond-like carbon films, Diamond Relat. Mater. 14 (2005) 1835–1838.
[46] J.J. Gonzalez, C. Liu, S.-B. Wen, X. Mao, R.E. Russo, Metal particles produced by laser ablation for ICP-MS measurements, Talanta 73 (2007) 567–576.
[47] J.J. Gonzalez, C. Liu, S.-B. Wen, X. Mao, R.E. Russo, Glass particles produced by laser ablation for ICP-MS measurements, Talanta 73 (2007) 577–582.

PAPER 10

Study of aerosols generated by 213 nm laser ablation of cobalt-cemented hard metals

Holá, M.*, Konečná, V., Mikuška, P., Kaiser, J.*, Páleníková, K., Průša, S., Hanzlíková, R., Kanický, V.

Journal of Analytical Atomic Spectrometry. 2008, 23(10), 1341–1349. DOI 10.1039/B802906G

Contribution:

LA-ICP-MS and aerosol design of experiments and measurements, data evaluation, studying of ablation craters and the particle structure, manuscript writing, corresponding author.

Study of aerosols generated by 213 nm laser ablation of cobalt-cemented hard metals

Markéta Holá,*[a] Veronika Konečná,[a] Pavel Mikuška,[b] Jozef Kaiser,*[c] Kateřina Páleníková,[c] Stanislav Průša,[c] Renáta Hanzlíková[d] and Viktor Kanický[a]

Received 19th February 2008, Accepted 24th June 2008
First published as an Advance Article on the web 6th August 2008
DOI: 10.1039/b802906g

Cobalt-cemented hard metals present an example of samples with a complicated matrix consisting of components differing in chemical and physical properties and with extremely low volatility of all components. The purpose of this study was to compare particle formation of a set of real samples with similar matrices but different content of major components. The laser ablation process was studied using a Q-switched quintupled (213 nm) nanosecond Nd:YAG laser. Five samples of Co-cemented tungsten carbides, actually WC-TiC-(Ta,Nb)C-Co with a varied content of main constituents, were selected as representatives of a family of 15 miscellaneous tungsten carbide hard metal products. Physical and chemical properties vary over this specimen selection and therefore the effect on particle size formation and distribution was expected. The size distributions by number of ablated particles in different size ranges were measured using an optical aerosol spectrometer. The results proved the relationship between particle formation and sample composition. The structure of laser generated particles and the properties of ablation-craters were additionally studied by scanning electron microscopy (SEM). Spherical particles in the diameter range of 0.25–2 μm and μm-sized agglomerates composed of primary nano-particles were observed. The W and Co content in the aerosol particles was determined by energy dispersive X-ray spectroscopy (EDS). The volumes of ablation craters were measured by an optical profilometer. The laser ablation study of selected Co-cemented tungsten carbide hard metals indicates a similar total volume of formed particles with composition-dependent particle-size distributions.

1 Introduction

Knowledge of particle sizes and their number distribution in laser-generated aerosols is required for better understanding of non-stoichiometric effects observed with laser ablation inductively coupled plasma mass spectrometry (LA-ICP-MS). These effects are generally comprised within a common term called fractionation. Some works have proved the significant influence of laser parameters such as laser wavelength,[1–5] pulse duration[6–14] or energy density[14–16] on particle formation mechanisms, which reflects fractionation effects that manifest themselves as matrix interferences of an ICP-MS signal. Using shorter laser wavelengths, in fact in the ultraviolet (UV) region, leads to a decrease in the formation of larger particles (dimensions of units of micrometers) and consequently to reduced elemental fractionation within an ICP.[3,4] The pulse duration also belongs to the most important laser parameters. Generally we can say that the use of shorter pulses leads to reduction in the formation of large particles. The use of laser pulses with a duration of the order of femtoseconds (fs-LA) makes it possible to eliminate or at least substantially decrease the formation of particles with diameters on the micrometric scale, which by contrast are abundant when nanosecond pulses (ns-LA) are applied. Mechanisms of the interaction of femtosecond laser pulses with a target are associated with diminuition of thermal effects, and consequently with decreased material melting. For example, during UV-fs-LA of SRM silicate glass only nano-sized agglomerates in the range of 50–250 nm were observed whereas a UV-ns-LA generated aerosol showed a bimodal distribution formed by micro-sized molten spherical particles and nano-sized agglomerates.[7]

Besides the ablation process itself and vaporization and ionization in the ICP, it is the transport of aerosol particles to the ICP, which is critical and also contributes to fractionation.[17–24] Therefore, the shape and volume of an ablation cell, a position of target with respect to a carrier gas inlet/outlet, a carrier gas composition and flow rate, a transport tube material and length deserve the necessary attention and are studied in connection with fractionation effects.[20–24] Works studying the structure of the nanosecond laser-generated aerosol during its transport from ablation cell to ICP proved the fact that condensed nano-particles are not transported separately as single particles but as agglomerates with the sizes up to units of micrometers.[19] The rate of agglomeration is dependent on the transport conditions.

As it was mentioned, fractionation is influenced by many factors ranging from laser ablation conditions to ICP effects.

[a]*Department of Chemistry, Faculty of Science, Masaryk University, Kotlářská 2, 611 37 Brno, Czech Republic*
[b]*Institute of Analytical Chemistry, Academy of Sciences of the Czech Republic v.v.i., Veveří 97, 602 00 Brno, Czech Republic*
[c]*Institute of Physical Engineering, Faculty of Mechanical Engineering, Brno University of Technology, Technická 2896/2, 616 69 Brno, Czech Republic*
[d]*Institute of Scientific Instruments, Academy of Sciences of the Czech Republic v.v.i, Královopolská 147, 612 64 Brno, Czech Republic*

Nevertheless, the first step towards understanding these complicated processes is the acquisition of information on properties of particles generated under selected LA conditions. After this, we can investigate the changes caused by transport or ICP effects. As the study of aerosol is feasible only after particles have left the ablation cell, the influence of particle transport is always included. However, theoretical models of particle formation can be created on the basis of known patterns.

Many works are devoted to studies of fractionation of brass alloys such as metal materials containing main constituents with a significant difference in physical properties.[6,10,13,14,25–28] A cascade impactor used to collect ablated particles showed variances in zinc and copper concentration in particles with different sizes.[25] Zinc prevailed in particles smaller than 100 nm while the larger particles were enriched with copper.[26] On the basis of the experiments proving the particle size dependence on chemical composition, a theory of particle formation during laser beam interaction with a target was established. Various mechanisms were suggested and proved to be responsible for particle production during laser ablation. Small particles, enriched with the most volatile constituent (zinc), can be formed by nucleation and condensation processes from the vapor, whereas larger particles rich in lower-volatility elements (copper for example) may be ejected from the molten surface layer. Particle ejection from a liquid surface of a target occurs due to hydrodynamic instability which results from recoil pressure induced by a vapor plume expansion. Theoretical calculations of Zn/Cu ratio dependences on particle sizes were accomplished.[27]

Particle formation studies are often focused on various glass samples, frequently to certified reference materials (CRM), which are used as calibration standards in laser ablation assisted spectrometry because of their proper homogeneity and multi-elemental composition.[15,29–31] An example can be the study of elemental fractionation during 266 nm ablation of CRM silicate glass and zircon, representing a real silicate sample. Experiments showed that laser ablation of different silicate samples under identical experimental conditions produced aerosols with different particle size distribution, whereas particles with different sizes vary in their phase and chemical composition.[31]

This work is focused on the study of particle formation during 213 nm laser ablation of Co-cemented ceramic samples containing tungsten carbide (WC) as the main constituent. The sample set selection gives a great opportunity to study particle formation behaviour of real samples with similar matrices but different main components giving the specific properties of each sample – previous published works mostly focus on particle formation of one specific reference material. Tungsten carbide is frequently used for its extreme hardness and resistance as a constructional material for heavy-duty parts exposed to extreme wear and temperature. Tools and components are prepared either as sintered pieces or the surface of components is covered with a plasma-sprayed coating. Cemented carbide, or hardmetal as it is often called, is a material made by "cementing" very hard tungsten monocarbide (WC) grains in a binder matrix of tough cobalt metal by liquid phase sintering. The high solubility of WC in cobalt at high temperatures and a very good wetting of WC by the liquid cobalt binder result in an excellent densification during liquid phase sintering and in a pore-free structure. As a result of this, a material is obtained which combines high strength, toughness and high hardness. The combination of WC and metallic cobalt as a binder is a well-adjusted system not only with regard to its properties, but also to its sintering behavior.[32]

As stated above, cobalt-cemented carbide hardmetals represent materials containing a ceramic non-conductive constituent – tungsten carbide (WC) and metal cobalt, so the physical properties of both main constituents are very different (WC melting point 2870 °C, boiling point 6000 °C; Co melting point 1495 °C, boiling point 2877 °C). Hardmetals with specific properties contain also other constituents in the form of carbides such as Ti, Ta, Nb or V. By the addition of titanium carbide and tantalum carbide, the high temperature wear resistance, the hot hardness and the oxidation stability of hardmetals have been considerably improved, and the WC-TiC-(Ta,Nb)C-Co hardmetals are excellent cutting tools for the machining of steel.

The aim of this work was to investigate the behaviour of a set of samples and the particle formation process during nanosecond UV laser ablation. For this purpose, less usual and resistant WC-Co hardmetals were employed. Formerly, the cobalt content in plasma sprayed WC-Co coatings was determined by using ultraviolet[33] and infrared[34] laser ablation with inductively coupled plasma optical emission spectrometry (LA-ICP-OES). Linear calibration curves with relatively narrow coincidence bands and high coefficients of correlation were obtained for the determination of major constituents in cemented WC-TiC-(Ta,Nb)C-Co hardmetals by LA-ICP-OES.[35]

2 Material and sample preparation

Fifteen miscellaneous tungsten carbide hardmetal products were obtained from a powder metallurgy plant – Pramet Tools, L.L.C., Šumperk, Czech Republic, a subsidiary company of Seco Tools AB, Fagersta, Sweden. Five samples with varied content of main constituents were selected as representatives of the above large set of materials. Their properties were expected to vary over the whole specimen collection. Samples were routinely analysed using XRF spectrometry in the laboratory of the Research Institute of Inorganic Chemistry, J.S.C., (VÚAnCh) Ústí nad Labem, Czech Republic. Details on the XRF instrumentation and analysis have already been described by Kanický *et al.* in ref. 33–35. The composition of studied samples is shown in Table 1.

For easy manipulation, the block sample with a target area of about 1.5 cm^2 and thickness of 7 mm was embedded into polymethylmetacrylate (PMM) using a rounded mould to obtain a cast disk with a diameter of 3.5 cm. After PMM solidification, the target surface of the disk was ground down and polished.

Table 1 Composition of analysed carbide samples (wt%)

Sample	C	Co	Ti	Ta	Nb	W
1457HF3	6.13	3.33	—	1.03	0.42	89.09
3648K	5.62	6.55	0.28	0.16	0.07	87.32
554S30	6.85	8.17	6.25	3.93	1.58	73.22
2286S10	7.85	9.11	14.07	7.82	3.1	58.05
1520GH25	4.59	25.1	—	—	—	70.31

3 Instrumentation

3.1 Laser ablation device and instruments for particle classification

Laser ablation was performed using a pulsed Nd:YAG laser system UP 213 (New Wave Research, Inc., Fremont, CA, USA) operated at a wavelength of 213 nm with a pulse duration of 4.2 ns. Based on optimization experiments, the laser spot with the diameter of 100 μm, the laser pulse repetition rate of 10 Hz, and the fluence of 13 J cm^{-2} were employed thus ensuring generation of a sufficient amount of particles within the whole studied particle size range for all examined samples. Higher fluences (30 and 40 J cm^{-2}) were also tested for the experiments, but with the increasing fluence the reproducibility of the particle concentration measurements rapidly decreased (13 J cm^{-2} with 6% RSD, 40 J cm^{-2} with 20% RSD). Because the particle size distribution diagrams have the same shape differing only with the particle number, the fluency of 13 J cm^{-2} was employed for the rest of the experiments. The ablation system is equipped with a 33 cm^3 SuperCell (New Wave Research, USA) designed to enable rapid eluting of the ablation-generated aerosol in a large format cell. Helium was used as a carrier gas with the flow rate of 1.0 l min^{-1}. Aerosol was transported from the ablation cell through a 0.5 m long polyurethane transport tube (id of 4 mm) to an aerosol spectrometer.

The parameters of produced aerosol particles (*i.e.*, particle size and concentration) were measured and evaluated with the Optical Aerosol Spectrometer Welas® 2000 Series (WhitE Light Aerosol Spectrometer, Palas GmbH, Karlsruhe, Germany). The Welas® operates on the principle of the single particle scattering of white light. The intensity of the scattered-light detected at an angle of 90° is a measure of the particle size. The number of scattered-light impulses measured per time unit determines the particle quantity and therefore the concentration. Welas® sensor 2200 measures number concentration of particles in the size range 0.25–17 μm with a maximum concentration of 10^4 particles cm^{-3}. The particles are classified into 60 size channels on the basis of polystyrene-latex-equivalent diameters. The Condensation Nucleus Counter (CNC) module allows time-resolved particle counting within the nanometer range for particles larger than 8 nm in concentrations up to 10^5 particles cm^{-3}. This CNC module works on the principle of 2-propanol condensation on the particles.

The structure of the laser-generated particles was studied after their collection on polycarbonate membrane filter (25 mm diameter, 0.2 μm pores, Cyclopore, Whatman) using scanning electron microscopy (SEM). The filter was placed behind the ablation cell in the distance accordant with the ablated particle measurements (0.5 m). To collect sufficient amount of particle for SEM experiments, the ablation was performed for a 5 min time period.

The high resolution SEM (Vega, TESCAN, s.r.o., Brno, Czech Republic) was used to image both the particles collected on the filter as well as the laser ablated craters. The SEM Vega is equipped with tungsten heated cathode electron source and operates at a base pressure better than 8.0×10^{-3} Pa. The all presented SEM pictures (Fig. 4 and 6, see Results and discussion) were recorded in imaging mode with a resolution in the order of tens of nm. The standard secondary electron detector was used during collection of the images and the electron beam acceleration voltage was kept constant at 30 kV.

3.2 Energy dispersive X-ray spectrometry analysis of aerosol particles

To examine the W and Co content in the ablated aerosol particles collected on the filter, an EDS instrument (INCA x-sight, Oxford Instruments Ltd., UK) of field emission SEM (JSM-6700F, JEOL, Japan) was used. The SEM is provided with the cold auto-emission cathode that works at a pressure of 10^{-8} Pa and the pressure in the specimen chamber was maintained at 10^{-4} Pa during the analysis. The secondary electron detector providing the topographical contrast was used. All the secondary electrons producing a "lower electron image" (LEI) were collected by a conventional Everhart–Thornley (E–T) detector mounted aside the electron beam. The second in-lens system detected the true secondary electrons in the direction of the objective lens, thus producing highly resolved "secondary electrons image" (SEI). The acceleration voltage was 5 kV. The working distance (WD) was in the range of 8–15 mm so it could allow the imagining and appropriate condition for EDS analyses.

The EDS analysis was performed at the electron acceleration voltage of 15 kV. The analyzer sensitivity was sufficient to measure signals of elements from boron to uranium. The electron beam energy was high enough to excite the elements of interest. A liquid nitrogen cooled Si(Li) detector of the INCA x-sight analyzer guarantees stable output with count rate.

The elemental distribution map on filter area (Section 4.2) was obtained by a QUANTAX XFlash® (Bruker, Germany) detector coupled to the SEM Vega.

3.3 The ablation crater observation

The operation principle of the optical profilometer MicroProf (FRT, Germany) used for the measurements of the ablation crater volume is based on utilization of the chromatic aberration of the optical sensors positive lens.[36] In the device, a white light from a halogen lamp passes through the CHR 150 N lens with the high chromatic aberration. Different light monochromatic components are focused in different heights from a reference plane at the output of the optical fibre. The same optical fibre collects scattered light from a surface under study. This light is analyzed by means of a spectrometer. The intensity spectral distribution of the light processed by the spectrometer has a maximum at the wavelength of the monochromatic component exactly focused on the surface. The height of the surface irregularities is deduced by means of a calibration table from the wavelength of the intensity spectral distribution maximum. The ablation craters were measured with 1 μm lateral and 3 nm vertical resolution.

4 Results and discussion

4.1 Particle formation

The amount of aerosols produced from five Co-cemented samples was monitored under optimized laser ablation condi-

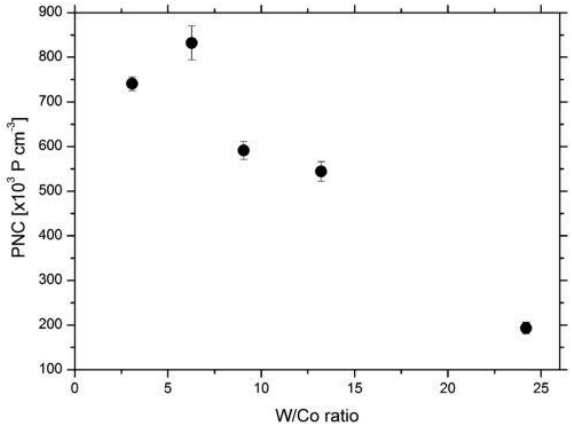

Fig. 1 Dependences of particle number concentration (PNC) on W/Co ratio for small particles (10 nm–0.25 μm).

tions (see Section 3.1) in order to investigate fractionation effects. The results indicate a relationship between particle formation and sample composition since both large (0.25–17 μm) and small (10 nm–25 μm) particles correlate with the W/Co ratios. The dependence of particle number concentration on the W/Co content ratio for all five samples is linear and is shown for both small and large particles in Fig. 1 and 2, respectively. These main constituents with different chemical and physical properties (melting point, conductivity, *etc.*) are expected to be responsible for governing the particle formation mechanism. Tungsten is the main constituent (50–90 wt%) present in a form of low-volatility tungsten carbide (melting point of 2870 °C, boiling point of 6000 °C) while cobalt represents a metal element with much higher volatility (melting point of 1495 °C, boiling point of 2877 °C). Samples with lower content of Co provided a higher concentration of large particles and a lower concentration of small particles, which is in a good agreement with theories describing particle formation – small particles are enriched with a more volatile element while large particles show significant enrichment of element with a high melting point.[26,27]

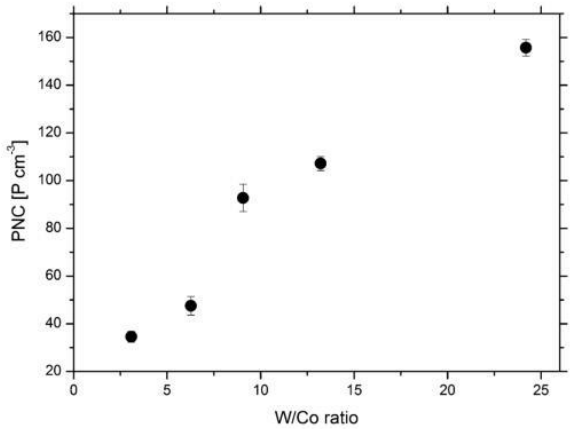

Fig. 2 Dependences of particle number concentration (PNC) on W/Co ratio for large particles (0.25–17 μm).

Except for the determination of total particle number concentration, the Welas® spectrometer allowed us to measure also particle size distribution of large particles in the size range 0.25–17 μm. In this size range, the measurements proved similar particle distribution for all tested samples with the mode diameter 0.6 μm. The number of particles larger than 2 μm in diameter is negligible (Fig. 3).

It is evident from data in the literature that both nanoparticles and vapour of ablated sample are formed during the laser ablation. The particle formation then continues both inside the ablation cell and during the transport of ablated products (*i.e.*, a mixture of particles and vapour) from the ablated cell into the ICP or measuring device (Welas®, filter) by the nucleation/coagulation processes and by vapour condensation on existed particles. The generated particles were additionally studied off-line after their collection on the polycarbonate membrane filters using the scanning electron microscope. The SEM observations showed typical pictures pointing to polydisperse particle size distribution. Spherical particles with diameters from tenths to units of micrometers and a net of "fibres" composed of primary particles with diameters in the range between tens to hundreds of nanometers were observed (Fig. 4a, 4b). In a detailed study of the "fibres" structure, clusters of agglomerated nanoparticles were observed as building units of the fibres. Visible examples of the clusters are clearly marked in a circle in Fig. 5. These clusters seem to be compact, composed of several nanoparticles. The origin of the cluster formation can probably be put into the ablation cell during the condensation process as described by Kuhn *et al.*[19] and during collision-coalescence process increasing the primary size of the condensed particles.[37] The final structure of the agglomerates is done by the rate of the hard agglomeration (particles held by stronger chemical or sintering bones) and soft agglomeration (by weak physical van der Waals forces) depending on the process conditions.[38–40] The possibility of all processes leading to the particle agglomeration can be calculated using the microplasma parameters and the particle dilution in the gas flow.[41] In our study, the agglomeration of the clusters creating the "fiber" structure should be predicated to the particle collection on the filter. The particle trajectories in the transport tube are changed because of the filter constituting an obstacle in the gas flow with the effect of the high particle concentration in specific area on the filter. To confirm this theory, SEM images of collected particles were done for both multiple laser ablation with 10 Hz repetition rate (3000 pulses) and also after application of 5 pulses with the 1 Hz repetition rate to obtain a lower particle number density (Fig. 6). The "fibre" structure is obvious in both cases as it is shown in Fig. 4 and 6. It means that although the particle concentration on the filter is minimal, the agglomeration of the primary clusters is proved. This assertion is supported by the Welas® spectrometer measurements – no particles larger than 2 μm were registered which indicates the presence of large agglomerates (fibres) only on the filter, and not during the transport into ICP.

Instead of a detailed study of the particle production mechanism, here we concentrated on the measurement of size distribution of particles produced by laser ablation of the studied samples. Although the employed on-line instrumentation (*i.e.*, Welas®) allows direct measurement of size and number concentration of particles transported from ablation

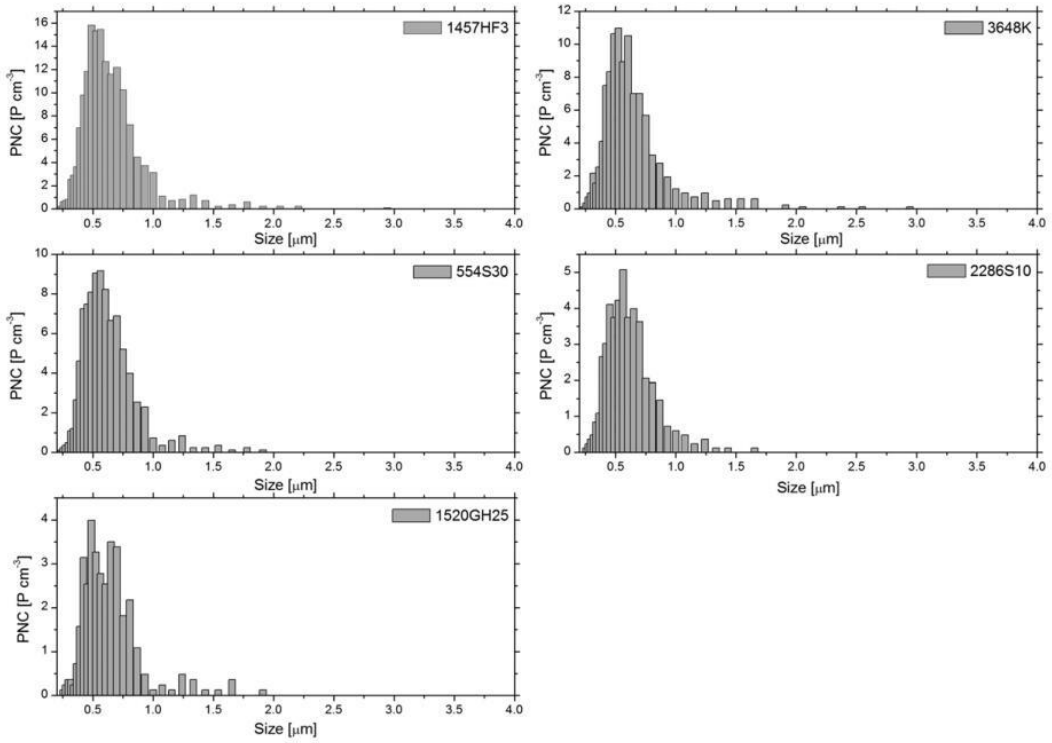

Fig. 3 The particle size distribution for large particles (0.25–17 μm) at the analysed Co-cemented tungsten carbide hardmetal. PNC – particle number concentration.

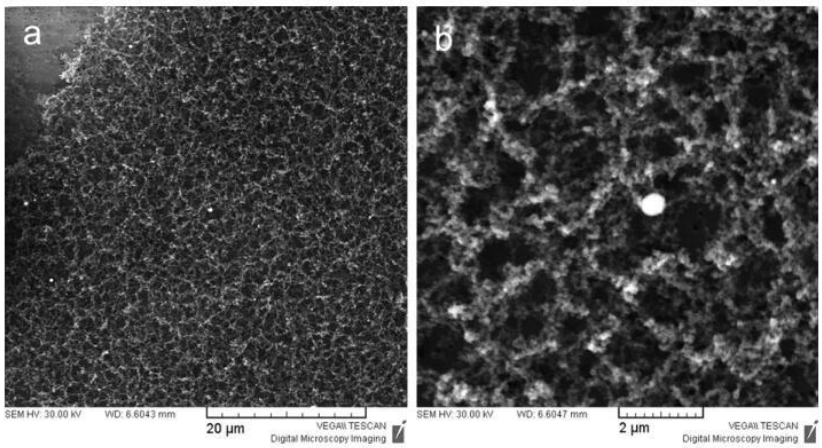

Fig. 4 SEM images of laser generated particles from sample 554S30, after their collection on a polycarbonate membrane filter; (a) overall view to the net of "fibres" composed of primary particles with a diameter between tens to hundreds of nanometers, clusters and large spherical structures and (b) detail of a large spherical particle and surrounding clusters.

cell to ICP, we cannot distinguish particles produced directly inside the ablation cell from particles/agglomerates formed during their transport to ICP by nucleation/condensation processes of vapour and/or by coagulation of smaller particles. However, we can distinguish particles formed during the ablation process and the subsequent transportation into ICP (they are measured as a sum by Welas®) from particles observed on the filter that are produced by mutual impacts of smaller particles transported from ablation cell (they are measured by SEM). The measurements performed with Welas® revealed that the majority of particles transported from ablation cell to ICP lie in the range below 250 nm. The number of

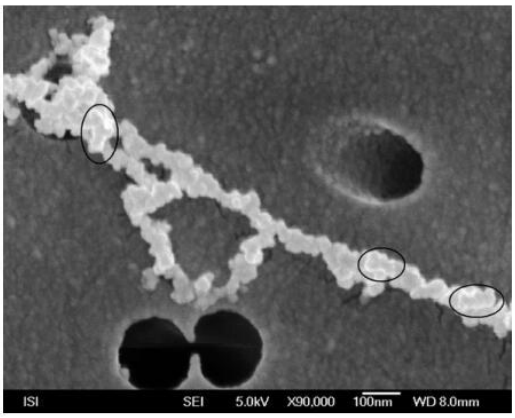

Fig. 5 The detailed SEM image of the agglomerated nanoparticles. Visible examples of the clusters are marked in a circle.

particles larger than 250 nm (0.25–2 μm) was approximately 4 orders of magnitude smaller.

The size of large spherical particles can be described using the particle size distribution graph (Fig. 3) that presents single spherical particles with diameters in the size range of 0.25–2 μm. The agglomerates forming "fibres" observed on the filter are created by impaction and coagulation of smaller particles (single particles or clusters; the majority of them smaller than 250 nm) during their collection on the filter, which proves the fact that no particles larger than 3 μm were observed during the Welas® experiments. Consequently, it follows that particles taking part in formation of agglomerates on the filter are transported either as single particles or in clusters smaller than 250 nm in diameter.

4.2 Elemental composition

For the aerosols, we have clearly demonstrated the correlation between the W/Co ratios and particle size. Ablated particles collected on the filter were analyzed using the EDS technique. Two samples with extreme values of Co content (1520GH25 and 1457HF3) were selected to demonstrate a possible influence of sample matrix on diversity of particle composition. The measurements were focused on the determination of W/Co ratio in clusters and μm-sized spherical particles. During analysis of agglomerates, the area of *ca.* 50 nm^2 was scanned. In the case of single spherical particles the scanned area was adapted to the particle size. Five different measurements of each kind of particle provided results summarized in Table 2. These results reflect a different composition of small and large particles with the same trend for both selected samples. While large particles are enriched with tungsten as the element with low volatility, depletion of W as well as Co enrichment in clusters of small particles are obvious. Material 1457HF3 represents a more illustrative example as the high cobalt content (25%) induces more significant differences in particle composition than the 1520GH25 material. High RSD values for the determination of elements in large particles indicate a considerable range of results, which is caused by the presence of small particles (smaller than ≈100 nm) adsorbed on the large particle surface. As a consequence, the analysis of only a large particle itself is impossible, because the contribution of adsorbed particles distorts the analysis. A detailed image of a spherical particle covered with a spread of smaller particles is shown in Fig. 7.

Table 2 The ratio of W and Co in laser-generated particles obtained by EDS

Sample	Declared W/Co ratio	Average W/Co ratio measured on nano-particle agglomerates	RSD (%)	Average W/Co ratio measured on single μm-sized spherical particle	RSD (%)
1457HF3	2.8	2.6	6	6.6	32
1520GH25	26.8	21.2	9	257	48

For an illustrative demonstration of elemental distribution in different-sized particles, the 5 × 4 μm filter area was mapped using EDS. The accumulation of tungsten in spherical particles is evident as well an even distribution of cobalt in agglomerates. The condensation of Co particles on larger spherical particles is also clearly visible. Fig. 8 demonstrates the elemental distribution map on a filter area for particles collected from the sample no. 1457HF3. The objects on the filter are shown on the BSE picture (Fig. 8a). For better lucidity the distribution is first illustrated for each element (wolfram and cobalt) separately in Fig. 8b and 8c, respectively. The map of all minor elements together is then shown in Fig. 8d.

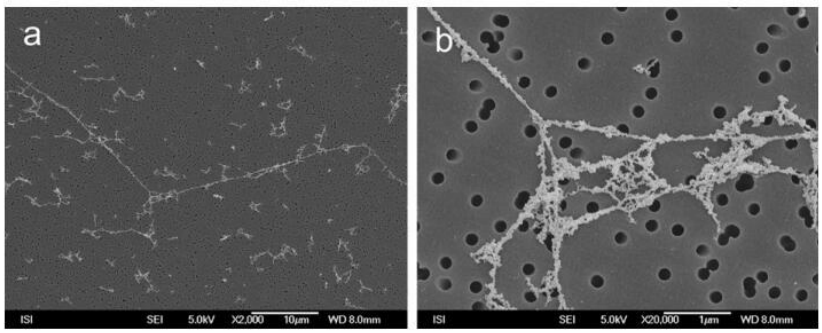

Fig. 6 SEM image of (a) the "fiber" structure formed on the filter by 5 laser pulses and (b) a detailed view of the net of fibres.

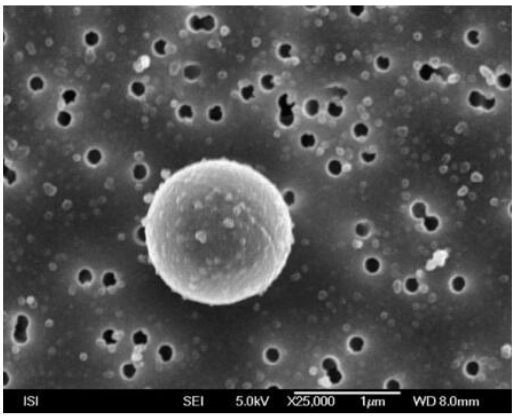

Fig. 7 SEM image of a spherical particle covered by a spread of smaller particles.

4.3 Ablation crater formation

Information about ablation rates is one of the important parameters providing comparison of the laser ablation process of different samples. The amount of ejected material during laser ablation can be estimated from the ablation crater volume with regard to amount of material remaining around the crater as a rim. The height of the crater rim and amount of material deposited around the craters for each of the five samples were studied using both the SEM and the optical profilometer. For demonstration, Co-cemented carbide no. 554S30 was chosen as a representative sample with medium cobalt content. The SEM

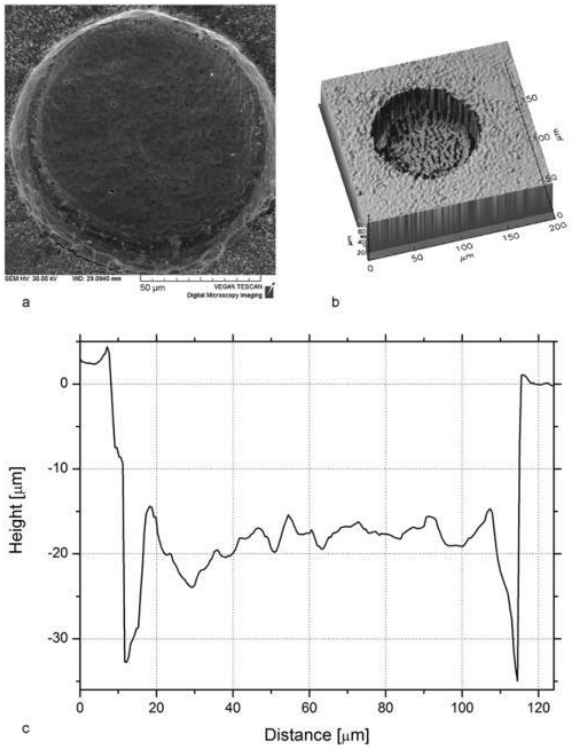

Fig. 9 (a) SEM and (b) optical micrograph of the ablation crater created on sample 554S30 together with a representative cross-section (c).

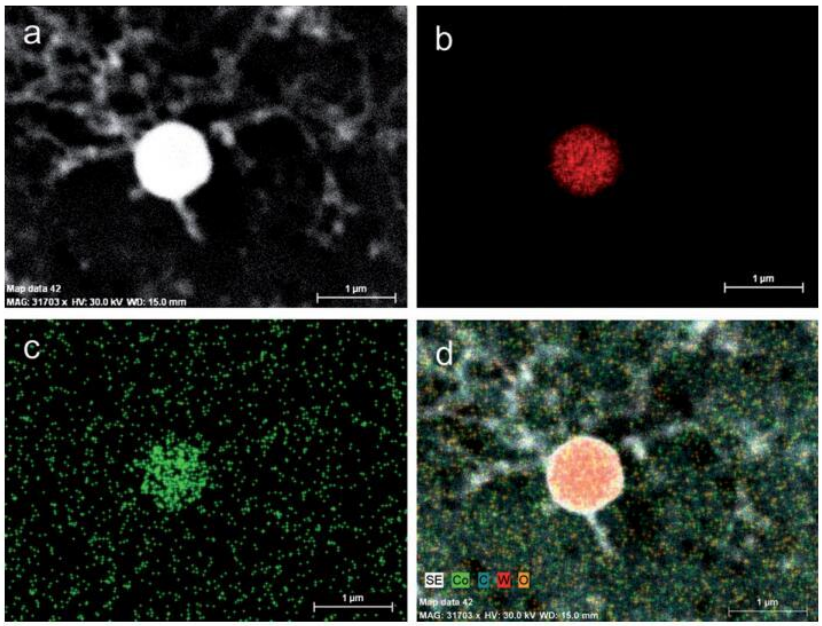

Fig. 8 The elemental distribution map of particles collected from sample no. 1457HF3, measured on a 5 × 4 μm filter area; (a) BSE picture of the particles on the filter, (b) wolfram and (c) cobalt detected in this area, and (d) the map of all minor elements (W, Co, C, O).

image of typical ablation crater (Fig. 9a) created on this sample together with the optical micrograph (Fig. 9b) shows a quasi-cylindrical structure with an irregular bottom shape (Fig. 9c). The minimal rim indicates insignificant reverse material deposition around the crater while the shape of the crater bottom points to the sample melting during laser ablation. The melted bottom surface is clearly visible both at the 3D optical micrograph and at the picture showing one selected cross-section of the ablation crater (Fig. 9c).

The ablation crater volume of all samples was calculated from ten cross-sections placed in regular angular distances across each ablation crater. Non-significant differences of released material volume and crater rim shape for samples with different W and Co contents were observed. The crater volumes fall in the interval of 120 000–160 000 μm^3 with the mean value of 145 000 μm^3 and RSD of 11%.

The mass of the ejected material for each sample was calculated from the ablation crater volume and sample density. The results fell in the region from 1.7 to 2.0 μg with the uncertainty of 10%. No dependence of the crater volume on the material mass was found. These experiments proved an insignificant difference between ejected masses of different samples.

Conclusions

The laser ablation process with Nd:YAG 213 nm of five Co-cemented carbide real samples with variable content of main constituents were studied using the optical aerosol spectrometer, the SEM, the EDS and the optical profilometer. The results give support to the theory of particle formation previously described on brass laser ablation.[25–27] The optical measurements, allowing the determination of particle number concentration at two size ranges (small particles with diameters in the size range of 10 nm–0.25 μm and large particles with diameters in the size range of 0.25 μm–17 μm), proved the relationship between particle formation and sample composition. The dependences of particle number concentration on W/Co ratio at five studied samples were linear for both small and large particles. Particles collected on membrane filters were inspected by means of SEM and analyzed using EDS. Produced particles can be divided into two categories dependent on their size: spherical particles in the diameter range of 0.25–2 μm and agglomerates composed of primary particles of diameter range tens to hundreds of nanometers. The size of agglomerates was under these laser conditions (100 μm spot size, fluence of 13 J cm^{-2}, 10 Hz repetition rate) mostly smaller than 250 nm. The results of EDS analysis proved a significant increase of tungsten content in large spherical particles while small clusters are enriched with cobalt. The surface of large particles is mostly covered with condensed cobalt which was proved by SEM images and EDS analysis. This is in good agreement with the theory of particle formation: small particles, enriched with a more volatile constituent, can be formed by nucleation and condensation from the vapor, whereas larger particles rich in low-volatility elements are ejected from the melted liquid due to hydrodynamic instability of the surface recoil pressure from the expanding vapor plume.[25–27]

The correlation between SEM results and particle size distribution graphs is evident and helps us understand the nucleation/coagulation processes during the transportation of ablated particles from the ablation cell into the ICP.

To compare ablation rates of different samples, volumes of ablation craters were measured by optical profilometer. Non-significant differences of released material volume and crater rim shape for samples with different W and Co contents were observed.

Acknowledgements

M.H. gratefully acknowledges the Czech Science Foundation for bestowing the project 203/06/P347. M.H. and V.K. acknowledge the Ministry of Education, Youth and Sports of the Czech Republic for research project MSM0021622412 and MSM0021622410, respectively. P.M. acknowledges an Institutional research plan of the Institute of Analytical Chemistry of the Academy of Sciences of the Czech Republic No. AV0 Z40310501. J.K., S.P. and K.P. acknowledge the Ministry of Education, Youth and Sports of the Czech Republic for research project MSM 0021630508.

References

1 R. E. Russo, X. L. Mao, O. V. Borisov and H. Liu, *J. Anal. At. Spectrom.*, 2000, **9**, 1115–1120.
2 J. Gonzáles, C. Liu, X. Mao and R. E. Russo, *J. Anal. At. Spectrom.*, 2004, **19**, 1165–1168.
3 D. Bleiner and D. Günther, *J. Anal. At. Spectrom.*, 2001, **16**, 449–456.
4 M. Guillong, I. Horn and D. Günther, *J. Anal. At. Spectrom.*, 2003, **18**, 1224–1230.
5 J. Koch, M. Wälle, J. Pisonero and D. Günther, *J. Anal. At. Spectrom.*, 2006, **21**, 932–940.
6 N. J. Seatveit, S. J. Bajic, D. P. Baldwin and R. S. Houk, *J. Anal. At. Spectrom.*, 2008, **23**, 54–61.
7 V. Možná, J. Pisonero, M. Holá, V. Kanický and D. Günther, *J. Anal. At. Spectrom.*, 2006, **21**, 1194–1201.
8 R. E. Russo, X. Mao, J. J. Gonzales and S. S. Mao, *J. Anal. At. Spectrom.*, 2002, **17**, 1072–1075.
9 J. Koch and D. Günther, *Anal. Bioanal. Chem.*, 2007, **387**, 149–153.
10 C. Liu, X. L. Mao, S. S. Mao, X. Zeng, R. Greif and R. E. Russo, *Anal. Chem.*, 2004, **76**, 379–383.
11 J. Gonzáles, S. H. Dundas, C. Y. Liu, X. Mao and R. E. Russo, *J. Anal. At. Spectrom.*, 2006, **21**, 778–784.
12 F. Poitrasson, X. Mao, S. S. Mao, R. Freydier and R. E. Russo, *Anal. Chem.*, 2003, **75**, 6184–6190.
13 J. Koch, A. von Bohlen, R. Hergenröder and K. Niemax, *J. Anal. At. Spectrom.*, 2004, **19**, 267–272.
14 C. C. Garcia, H. Lindner, A. von Bohlen, C. Vadla and K. Niemax, *J. Anal. At. Spectrom.*, 2008, **19**, 470–478.
15 S. H. Jeong, O. V. Borisov, J. H. Yoo, X. L. Mao and R. E. Russo, *Anal. Chem.*, 1999, **71**, 5123–5130.
16 J. H. Yoo, O. V. Borisov, X. Mao and R. E. Russo, *Anal. Chem.*, 2001, **73**, 2288–2293.
17 D. Bleiner, P. Lienemann and H. Vonmont, *Talanta*, 2005, **65**, 1286–1294.
18 D. B. Aeschliman, S. J. Bajic, D. P. Baldwin and R. S. Houk, *J. Anal. At. Spectrom.*, 2003, **18**, 1008–1014.
19 H. R. Kuhn and D. Günther, *Anal. Bioanal. Chem.*, 2005, **383**, 434–441.
20 I. Horn and D. Günther, *Appl. Surf. Sci.*, 2003, **207**, 144–157.
21 M. Guillong, I. Horn and D. Günther, *J. Anal. At. Spectrom.*, 2003, **18**, 1224–1230.
22 J. Koch, I. Feldmann, N. Jakubowski and K. Niemax, *Spectrochim. Acta, Part B*, 2002, **57**, 975–985.
23 J. Koch, M. Wälle, R. Dietiker and D. Günther, *Anal. Chem.*, 2008, **80**, 915–921.
24 D. B. Aeschliman, S. J. Bajic, D. P. Baldwin and R. S. Houk, *J. Anal. At. Spectrom.*, 2003, **18**, 1008–1014.

25 R. Jaworski, E. Hoffmann and H. Stephanowitz, *Int. J. Mass Spectrom.*, 2002, **219**, 373–379.
26 H. R. Kuhn and D. Günther, *Anal. Chem.*, 2003, **75**, 747–753.
27 C. Liu, X. Mao, S. S. Mao, R. Greif and R. E. Russo, *Anal. Chem.*, 2005, **77**, 6687–6691.
28 C. Y. Liu, X. L. Mao, J. Gonzáles and R. E. Russo, *J. Anal. At. Spectrom.*, 2005, **20**, 200–203.
29 P. Weis, H. P. Beck and D. Günther, *Anal. Bioanal. Chem.*, 2005, **381**, 212–224.
30 H. R. Kuhn and D. Günther, *J. Anal. At. Spectrom.*, 2004, **19**, 1158–1164.
31 J. Košler, M. Wiedenbeck, R. Wirth, J. Hovorka, P. Sylvester and J. Míková, *J. Anal. At. Spectrom.*, 2005, **20**, 402–409.
32 G. S. Upadhyaya, in *Cemented Tungsten Carbides: Production, Properties and Testing*, Noyes Publications, 1st edn., 1998, ch. 14, pp. 288–294.
33 V. Kanický, V. Otruba and J.-M. Mermet, *Spectrochim. Acta, Part B*, 2000, **55**, 575–586.
34 V. Kanický, V. Otruba and J.-M. Mermet, *Spectrochim. Acta, Part B*, 2000, **55**, 1601–1610.
35 V. Kanický, V. Otruba and J.-M. Mermet, *Fresenius' J. Anal. Chem.*, 2001, **371**, 934–938.
36 I. Ohlidal, M. Ohlidal, D. Franta, V. Cudek, V. Bursikova, P. Klapetek and K. Palenikova, *Diamond Relat. Mater.*, 2005, **14**, 1835–1838.
37 J. J. Gonzales, C. Liu, S. Wen, X. Mao and R. E. Russo, *Talanta*, 2007, **73**, 567–576.
38 S. Tsantilis and S. E. Pratsinis, *Langmuir*, 2004, **20**, 5933–5939.
39 S. E. Pratsinis and S. Vemury, *Powder Technol.*, 1996, **88**, 267–273.
40 S. E. Pratsinis, *Prog. Energy Combust. Sci.*, 1998, **24**, 197–219.
41 D. Bleiner and A. Bogaerts, *J. Anal. At. Spectrom.*, 2006, **21**, 1161–1174.

PAPER 11

Tungsten carbide precursors as an example for influence of a binder on the particle formation in the nanosecond laser ablation of powdered materials

Holá, M.*, Mikuška, P., Hanzlíková, R., Kaiser, J., Kanický, V.

Talanta. 2010, 80(5), 1862–1867. DOI 10.1016/j.talanta.2009.10.035

Contribution:

LA-ICP-MS design of experiments and measurements, data evaluation, studying of ablation craters, trapping particles on the filter and studying the particle structure, manuscript writing, corresponding author.

Talanta 80 (2010) 1862–1867

Contents lists available at ScienceDirect

Talanta

journal homepage: www.elsevier.com/locate/talanta

Tungsten carbide precursors as an example for influence of a binder on the particle formation in the nanosecond laser ablation of powdered materials

Markéta Holá[a,*], Pavel Mikuška[b], Renáta Hanzlíková[c], Jozef Kaiser[d], Viktor Kanický[a]

[a] Department of Chemistry, Faculty of Science, Masaryk University, Kotlářská 2, 611 37 Brno, Czech Republic
[b] Institute of Analytical Chemistry, Academy of Sciences of the Czech Republic v.v.i., Veveří 97, 602 00 Brno, Czech Republic
[c] Institute of Scientific Instruments, Academy of Sciences of the Czech Republic v.v.i, Královopolská 147, 612 64 Brno, Czech Republic
[d] Institute of Physical Engineering, Faculty of Mechanical Engineering, Brno University of Technology, Technická 2896/2, 616 69 Brno, Czech Republic

ARTICLE INFO

Article history:
Received 19 June 2009
Received in revised form 7 October 2009
Accepted 15 October 2009
Available online 24 October 2009

Keywords:
Laser ablation (LA)
Inductively coupled plasma mass spectrometry (ICP-MS)
Powder
Matrix effect
Fractionation
Binder
Particle size distribution

ABSTRACT

A study of LA–ICP-MS analysis of pressed powdered tungsten carbide precursors was performed to show the advantages and problems of nanosecond laser ablation of matrix-unified samples. Five samples with different compositions were pressed into pellets both with silver powder as a binder serving to keep the matrix unified, and without any binder. The laser ablation was performed by nanosecond Nd:YAG laser working at 213 nm.

The particle formation during ablation of both sets of pellets was studied using an optical aerosol spectrometer allowing the measurement of particle concentration in two size ranges (10–250 nm and 0.25–17 μm) and particle size distribution in the range of 0.25–17 μm. Additionally, the structure of the laser-generated particles was studied after their collection on a filter using a scanning electron microscope (SEM) and the particle chemical composition was determined by an energy dispersive X-ray spectroscope (EDS).

The matrix effect was proved to be reduced using the same silver powdered binder for pellet preparation in the case of the laser ablation of powdered materials.

The LA–ICP-MS signal dependence on the element content present in the material showed an improved correlation for Co, Ti, Ta and Nb of the matrix-unified samples compared to the non-matrix-unified pellets. In the case of W, the ICP-MS signal of matrix-unified pellets was influenced by the changes in the particle formation.

1. Introduction

Laser ablation inductively coupled plasma mass spectrometry (LA–ICP-MS) has become a method commonly used for the direct analysis and microanalysis of solid samples with a very wide field of application. The main problems that still hinder LA–ICP-MS as an ideal method for any kind of direct analysis are fractionation and quantification [1].

The common term "fractionation" comprises non-stoichiometric effects observed with the LA–ICP-MS. A lot of works describe the influence of the laser parameters on the particle formation and consequently various "suggestions" on how to reduce the fractionation effects using an appropriate laser wavelength [2–6], pulse duration [7–15] or energy density [15–17] have been proposed. However most of these parameters are dictated by the construction of the ablation laser used and so their variability becomes strongly dependent on the available experimental setup. Besides the ablation process itself, the transport of aerosol particles to the ICP [18–22,4,23] and vaporization and ionization in the ICP [24] are important and also contribute to the fractionation manifesting itself as matrix interference of the ICP-MS signal. During transportation, diffusion of the particles smaller than 2 nm and gravitational settling of particles in micrometric range (contingent on the particle density) takes place and, depending on the small and large particle representation, the mentioned factors occur [10]. In the ICP itself the main problem is that large particles cannot be completely vaporized and ionized. Some works determine 0.5 μm as a critical size for the particle vaporization [24,25], however the volatility of particles influences the limit of the maximum diameter of the particle evaporated in the ICP.

The "matrix effect" is another frequent and permanent problem arising during the LA–ICP-MS quantitative analysis. The "matrix effect" is a term for the variable ablation mechanism of materials in different matrices causing changes in volume and composition of the generated particles during the laser beam interaction with the various sample surfaces. To overcome the "matrix effect", it is necessary to create a suitable calibration strategy for the LA–ICP-MS quantitative analysis. To compensate for the matrix effect, matrix

* Corresponding author.
E-mail address: mhola@sci.muni.cz (M. Holá).

0039-9140/$ – see front matter © 2009 Elsevier B.V. All rights reserved.
doi:10.1016/j.talanta.2009.10.035

matched calibration has become the most common quantification technique relying on the use of a reference material with the same matrix as the analysed sample [1,26].

The analysis of powdered materials by LA–ICP-MS requires a preparative procedure resulting in a target with sufficient homogeneity, cohesion and stability during laser ablation. Plenty of different methods have been described for the target preparation such as melting with lithium borate [27–31], casting with a glue [32,33] or pressing into pellets [34–39]. The choice of a suitable method depends on the sample properties and laboratory facilities. Possible resulting problems must be taken into consideration like sample contamination, loss of volatile elements or sample dilution.

To press the powder into a pellet is the most common way because of its speed and simplicity. The pellets are pressed with or without other additives serving as a binder, matrix unifier or internal standard. The possibility of the matrix unification by using diverse powdered samples offers the LA–ICP-MS a great advantage in comparison to the analysis of naturally compacted samples where matrix unification is impossible. On the other hand, the presence of any kind of additive influences the ablation process. Therefore the choice of the additive should conform not only to the pellet's physical properties, but also to the suitability of the ablation mechanism providing successful quantitative analysis.

The purpose of this study is to show the effect of adding a matrix unifier into the powdered samples on the particle formation and the ICP-MS signals. Five powdered Co-cemented ceramic samples containing tungsten carbide (WC) as the main constituent were chosen as samples belonging to the same sort. The sample set selection gives a great opportunity to study particle formation behaviour of real samples with similar matrices but different main components giving the specific properties of each sample. Detailed description of the Co-cemented ceramic is made in work studying the particle formation of cemented WC samples [40]. As a matrix unifier powdered silver meeting also the criteria of the suitable binder such as easy homogenization with the sample, proper binding effect and positive price was used on the basis of previous experience with the silver as a binding material for the pellet preparation [36,38,39].

2. Experimental

2.1. Samples

2.1.1. Tungsten carbide precursors

The powdered precursors (WC/Co) for cemented carbides were obtained from Pramet Tools, L.L.C., Šumperk, Czech Republic, a subsidiary of Seco Tools AB, Fagersta, Sweden. Co-cemented carbide, or hardmetal as it is often called, is a material containing ceramic non-conductive constituent (tungsten carbide (WC)) and metal cobalt which plays the role of a binder during the sintering process, so the physical properties of both main constituents are very different (WC m.p. 2870 °C, b.p. 6000 °C, density 15.8 g cm^3; Co m.p. 1495 °C, b.p. 2877 °C, density 8.9 g cm^3). To obtain a hardmetal with specific properties, other constituents such as Ti, Ta, Nb or V are added in the form of carbides before sintering. By the addition of titanium carbide and tantalum carbide, the high temperature wear resistance, the hot hardness and the oxidation stability of hardmetals have been considerably improved, and the WC–TiC–(Ta,Nb)C–Co hardmetals are excellent cutting tools for the machining of steel [41]. The physical properties of TiC and TaC as the additives with the highest content in the final product are: TiC m.p. 3160 °C, b.p. 4820 °C, density 4.9 g cm^3; TaC m.p. 3880 °C, b.p. 5500 °C, density 13.9 g cm^3.

Five powdered precursors of hardmetals with a varied content of their main constituents were selected as representatives of a larger set of miscellaneous samples. Their properties were expected to vary over the whole sample collection. Samples were routinely analysed using XRF spectrometry in the laboratory of the Research Institute of Inorganic Chemistry, J.S.C., (VÚAnCh) Ústí nad Labem, Czech Republic. Details on the XRF instrumentation and analysis have already been described by Kanický et al. [42–44]. The composition of studied powdered tungsten carbide precursors is shown in Table 1.

Table 1
The chemical composition of the tungsten carbide precursor samples (wt%).

Sample	Co	Ti	Ta	Nb	W
3152	8.06 ± 0.41	14.4 ± 0.70	8.00 ± 0.36	3.10 ± 0.24	57.7 ± 1.5
4795	6.00 ± 0.25	3.24 ± 0.25	3.86 ± 0.21	1.59 ± 0.11	78.5 ± 1.7
5046	9.88 ± 0.44	2.48 ± 0.22	3.17 ± 0.14	1.31 ± 0.08	76.7 ± 1.2
5120	8.09 ± 0.36	6.37 ± 0.41	3.84 ± 0.19	1.58 ± 0.12	72.6 ± 0.9
5124	22.5 ± 0.8	0.04 ± 0.01	–	–	72.3 ± 1.0

2.1.2. Sample preparation for LA–ICP-MS

The powdered samples were employed for the analysis as pressed pellets with and without the binder. In both cases, the first preparation step consisted of sample grinding to obtain a fine powder. The particle size distribution, measured by laser diffractometry, showed diameter values not exceeding 5 μm after 5 min of sample grinding in a ball mill (Planetary Micro Mill Pulverisette 7, FRITSCH, Germany). The 25 ml mortars as well as milling balls (Ø 12 mm) were from Sialon material (90% Si_3N_4). To obtain binderless pellets, ground samples were pressed without any additional material, while the binder-containing ones were prepared in the ratio of 1:1 ground sample (3 g) and the silver powder (3 g, 99.99% purity, particle size <15 μm; Safina Vestec Company, Czech Republic), which was homogenized in the ball mill for 10 min. Pellets of both types were made by pressing with a hydraulic press (Mobiko Company, Czech Republic) at 1.3 GPa for 30 s. The pellet diameter and thickness was 12 mm and 1–1.5 mm, respectively. The weight of the binderless pellets was in the range of 1.3–1.7 g whilst binder-containing pellets had a weight between 1.2 and 1.5 g.

2.2. Laser ablation system

The laser ablation was realized by a pulsed Nd:YAG laser operating at a wavelength of 213 nm with a pulse duration of 4.2 ns (UP 213, New Wave Research, Inc., Fremont, CA, USA). In order to generate a sufficient number of particles within the whole particle size range studied for all examined sample types, several optimization experiments were undertaken. Based on these experiments, the following parameters of the ablation laser system were employed: a laser spot diameter of 100 μm, a laser pulse repetition rate of 10 Hz and a fluence of 13 J cm^{-2}. Higher fluences (30 and 40 J cm^{-2}) were also tested for the experiments, but with the increasing fluence the reproducibility of the particle concentration measurements rapidly decreased (13 J cm^{-2} with 7% RSD, 40 J cm^{-2} with 23% RSD). Because the particle size distribution diagrams have the same shape differing only with the particle number, the fluency of 13 J cm^{-2} was employed for the rest of the experiments. The laser spot of 100 μm diameter was used because of its suitability for the bulk analysis of powdered material where the representative sampling is very important and so larger laser spot is required. The 33 cm^3 sample chamber (SuperCell, New Wave Research, USA) of the ablation system was specifically designed to enable rapid eluting of the aerosol in a large format cell. Using helium as a carrier gas under normal operating conditions with a flow rate of 1.0 l min^{-1}, the ablation-generated aerosol was transported from the chamber through a 1-m long polyurethane transport tube (i.d. 4 mm) to either an ICP-MS system or an aerosol spectrometer.

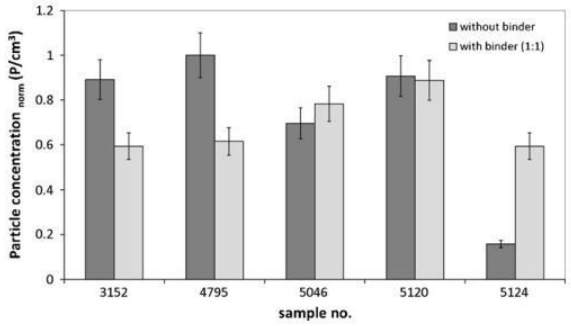

Fig. 1. Total concentration of particles (10 nm–17 μm) formed during the laser ablation of non-matrix-unified (without binder) and matrix-unified (with Ag binder) samples. The error-bars signify the standard deviation of three parallel measurements of each sample.

2.3. Inductively coupled plasma mass spectrometry

The aerosol was transported to the ICP discharge of the quadrupole mass spectrometer (ICP-MS Agilent 7500ce, Agilent Technologies, Santa Clara, CA, USA). The following isotopes were selected and used for the LA–ICP-MS analyses: ^{48}Ti, ^{51}V, ^{59}Co, ^{93}Nb, ^{181}Ta and ^{184}W.

2.4. Measurement of aerosol particles

The particle size and concentration of the laser produced aerosol particles was measured and evaluated on-line with an optical Aerosol Spectrometer Welas® 3000 Series (Palas, Germany). The Welas® operates on the principle of the single particle scattering of white light. The Welas® sensor 2200 provides a direct measurement of size distribution of particles in the size range 0.25–17 μm with a maximum concentration of 10^4 particles cm^{-3}. The particles are classified into 60 size channels on the basis of polystyrene-latex-equivalent diameters. Particles smaller than 250 nm are below the size limit for the detection by the Welas® sensors. To detect these small particles, their size is first increased by condensing 2-propanol vapor onto the small particles in the Condensation Nucleus Counter (CNC), to μm-sized particles that can be on-line detected with the Welas® sensor 2100. However, as a result of 2-propanol condensation, the former size distribution of small particles is lost and we can only count the total concentration of all particles larger than 10 nm up to 17 μm with a maximum concentration of up to 10^5 particles cm^{-3}. The number concentration of small particles (the size range 0.01–0.25 μm) was calculated as a difference between the total number concentration of all particles (measured with sensor 2100 as a result of 2-propanol condensation in the CNC; the size range 0.01–17 μm) and the number concentration of large particles (measured with sensor 2200; the size range 0.25–17 μm).

To avoid coincidence error of Welas sensors, high concentration of particles produced during the laser ablation was diluted at the output from LAS by mixing with stream of argon (5–15 l min^{-1}), part of formed mixture (5 l min^{-1}) was analysed in Welas and rest was wasted. Measuring of particles by CNC required higher dilution coefficient (12–15) than in case of sensor 2200 (dilution factor 5–7). Because of non-linear dependence of the dilution factor on the absolute particle concentration value for two types of sensors we prefer to demonstrate normalized values instead of absolute values of PC in Figs. 1 and 4. Dilution factor for PC measured by CNC was 15 (Fig. 1) while sensor 2200 used for the large particles determination worked with the dilution factor of 6 (Fig. 4).

2.5. Scanning electron microscopy and energy dispersive X-ray spectrometry

The structure and chemical composition of the laser-generated particles was studied *off-line* after their collection on a polycarbonate membrane filter (25 mm diameter, 0.2 μm pores, Cyclopore, Whatman). To collect a sufficient number of particles, the ablation was performed over a 5 min time period. The filter was placed behind the ablation cell at a distance equal to the ablated particle measurements conducted on the Welas® (0.5 m). The particles collected on the filter as well as the laser ablated craters were studied using an EDS instrument (INCA x-sight, Oxford Instruments Ltd., UK) of field emission SEM (JSM-6700F, JEOL, Japan). A secondary electron detector providing the topographical contrast was used. The acceleration voltage was 5 kV. The EDS analyses were performed at the electron acceleration voltage of 15 kV. A liquid nitrogen cooled Si(Li) detector of the INCA x-sight analyser guaranteed a stable output with a count rate.

The EDS allows analysis of W and Co as matrix elements. Method of EDS did not detect other elements as Ti, Ta and Nb due to the thickness of carbon coating used for sample conductivity that was approximately 30 nm. The carbon layer decreases the intensity of X-ray that leaves the sample for the reason of decreasing the primary electron flux and its own absorption of an output signal.

2.6. Optical profilometry

The ablation crater shape and volume was measured with 1-μm lateral and 3-nm vertical resolution by an optical profilometer MicroProf (FRT, Germany) [40]. In this device white light from a halogen lamp passes through the CHR 150 N lens with a high chromatic aberration. Different monochromatic light components are focused at different heights from a reference plane at the output of the optical fibre. The same optical fibre collects scattered light from the surface under study. This light is analysed by means of a spectrometer. The height of the surface irregularities is deduced by means of a calibration table from the wavelength of the spectral intensity distribution maximum.

3. Results and discussion

3.1. Matrix unification of different powdered samples

The real function of the silver binder as a matrix unifier was proved by two ways – by the particle concentration measurements and by the ablation crater studies. In both cases we presumed more similar results (smaller RSD) in the particle formation (measuring the particle concentration (PC)) as well as in the formation of ablation craters (more similar ablation rates and crater structure) – for samples prepared as matrix-unified pellets than for non-matrix-unified samples. The measurement of each pellet was done three times and the repeatability did not reach deviation of 10%. The RSD value used in the text as a criterion for the "level of unification" was calculated from mean values of the three repeated measurements of different samples. The matrix-unified samples represented pellets prepared by pressing of the sample and silver powder mixture as described in 2.1.2.

The total concentration of generated particles was monitored during the laser ablation of either non-matrix-unified or matrix-unified samples. The particle concentration of the five non-matrix-unified pellets differed from sample to sample very distinctly with a relative standard deviation (RSD) of 46%. It signifies a high influence of the sample composition on the particle production during laser ablation. Even if the tungsten content varies from sample to sample, the most important changes in elemental composition occur in the

Table 2
The coefficients of determination of the LA–ICP-MS signals dependent on the element concentration for the non-matrix-unified and the matrix-unified samples.

R^2	Without binder	WC + Ag (1:1)
Ti	0.9571	0.9860
Nb	0.9388	0.9782
Ta	0.9698	0.9862
Co	0.9356	0.9822
W	0.6976	0.0391

case other components such as Co, Ti and Ta (see Table 1). The RSD value, calculated from the PC values of all five samples, decreased to the value of 19% using the binder for the matrix unification. The results of PC measurements for both sets of samples are displayed in Fig. 1.

The observation of different ablation craters can also outline the similarity or difference in the laser ablation processes – the shape, structure and volume of the ablation crater can be used to explain the ablation process behaviour. One of the parameters that can be estimated from the crater depth is the ablation rate. Here the ablation crater depths were measured using the optical profilometer after 100 laser pulses. The crater depths on the non-matrix-unified samples fell in the range of 45–116 μm with the mean value of 93 μm and RSD of 36%. This result indicates the differences in the ablation rates for the samples with different compositions. The preparation of samples as matrix-unified matrix pellets caused a reduction in ablation rate differences – the depths of the ablation craters varied from 58 to 87 μm with a mean value of 70 μm. The RSD value decreased to 16%. The comparison of crater depths thus proved the results of particle formation. Both data sets confirmed our expectations that the binder unifies sample properties and consequently the ablation process.

3.2. LA–ICP-MS

The suitability of the matrix unification of the powdered hardmetal precursor for the LA–ICP-MS analysis was tested for Co, Ti, Ta, Nb and W using the conditions described above. On the basis of the LA–ICP-MS measurements, the appropriate isotope intensity (cps–count per second) dependence on the element content in the sample (simulated calibration curve) was created for each element and the regression lines were constructed. The following isotopes were used for analysis: ^{48}Ti, ^{51}V, ^{59}Co, ^{93}Nb, ^{181}Ta and ^{184}W. The measurements were done on both sets of pellets – (non)/matrix-unified samples. The coefficients of determination of the regression lines pertaining to the same element but different pellets (with or without binder) were compared.

For the matrix-unified samples, the results obtained show improved correlation of regression lines for all elements except W. It means that the Ag powder additive helps to unify the LA–ICP-MS conditions for Co, Ta, Ti and Nd while the possibility of the W quantification in the matrix-unified samples is unsatisfactory. The improvement of correlation is shown in Fig. 2, where the regression lines for Ti are displayed.

Coefficients of determination for all elements are summarized in Table 2.

3.3. Particle structure and composition

The information about the particle chemical composition can explain the behavior of the particle formation and consequently the estimation of the elemental fractionation degree during the ablation. The particle formation and elemental fractionation of Co-cemented tungsten carbides during ns laser ablation has already been described in detail elsewhere [40]. Single spherical particles with diameters in the size range of 0.25–2 μm and agglomerates

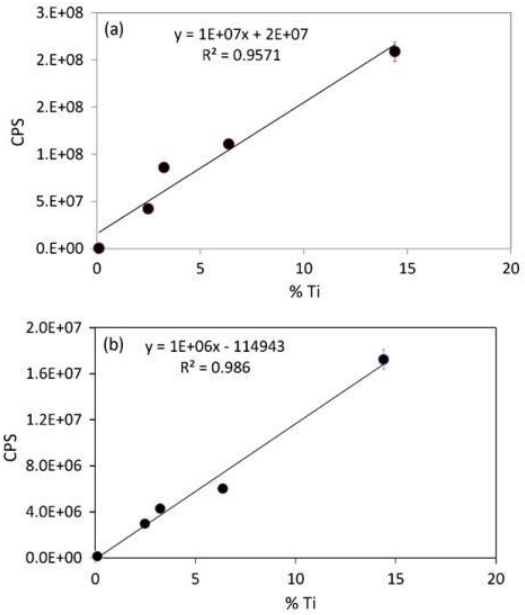

Fig. 2. The LA–ICP-MS signal dependence on the element content for 5 samples: (a) ^{48}Ti for non-matrix-unified samples and (b) ^{48}Ti for matrix-unified samples. The error-bars signify the standard deviation of three parallel measurements of each sample.

composed of primary particles of diameters ranging from tens to hundreds of nanometers were observed on the filter. The presence of tungsten (representing a low volatile element) entirely in the large spherical particles and the strong cobalt enrichment of the small particles proved the theory of particle formation: small particles, enriched with a more volatile constituent, can be formed by nucleation and condensation from the vapor, whereas larger particles rich in lowly volatile elements are ejected from the melted liquid due to hydrodynamic instability of the surface recoil pressure from the expanding vapor plume [45–47]. The elemental fractionation during ns ablation of non-matrix-unified powdered tungsten carbide precursors was identical with the above described Co-cemented samples. In the case of the matrix-unified samples, the influence of silver on the particle composition was studied. The particles were collected on the polycarbonate membrane filter during the 5 min ablation-time period. The particle structure and composition were then studied using SEM and EDS, respectively. The SEM images show, on the first sight, typical structures including single spherical particles and smaller agglomerates creating fibres and adhered to the large particle surface (Fig. 3a). With a higher magnification we can observe that the surface of the large spherical (tungsten) particle is covered by a non-homogenous layer (Fig. 3b). This is the layer where the agglomerates are bound. The EDS analysis showed the preferential presence of silver in the layer – the Ag/W mass ratio increased to the value of 25 from the declared 1.4. This finding clarifies the "destiny" of silver during ablation – the silver vapor condenses on the tungsten particle surface, which results from the much higher silver volatility than the volatility of other sample constituents (Ag melting point is 960 °C, boiling point is 2212 °C).

The EDS analysis did not allow the analysis of other elements such as Ti, Ta and Nb. On the base of the LA–ICP-MS results we can presume homogenous distribution of these elements in smaller particles. The agglomeration with the large tungsten particles seems to be logical especially for tantalum as an element with

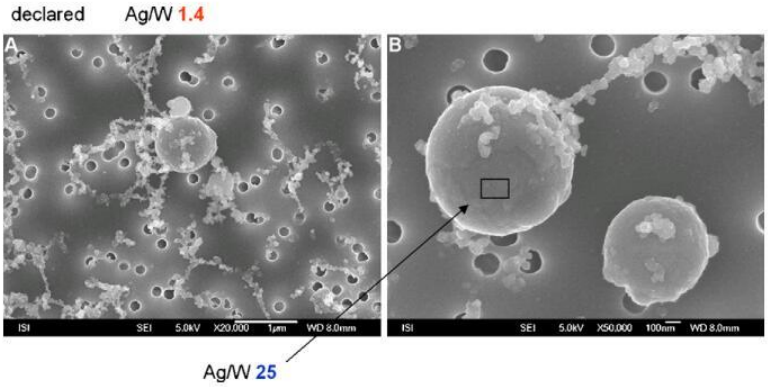

Fig. 3. The SEM images of laser-generated particles from matrix-unified sample no. 5124 after their collection on a polycarbonate membrane filter; (a) overall view, (b) detailed view with large spherical particles and surrounding clusters; a square label defines the area analysed by the EDS, the results of the EDS analysis are pasted together with the declared values.

similar physical properties to tungsten but no dependence of the analytical results on the particle formation was observed.

3.4. Particle size distribution

Silver condensation on the spherical tungsten particles leads to the growth of these particles. This fact was proved by the particle size measurements using the Welas spectrometer. The particle sizes were measured in the diameter range of 0.25–17 μm for the sample 3152 pressed in to 4 various pellets with differing amounts of the silver binder: without any added binder, 33%, 50% and 66% of the binder in the silver–sample mixture. The particle size distribution diagrams show changes in particle concentration with the increasing amount of Ag binder in the pellet (Fig. 4). For those particles with a diameter smaller than 0.31 μm the difference in the particle concentration is not significant, but the particles larger than 0.31 μm in diameter were formed in higher concentrations from the binder pellets. The dependence of particle concentration on the amount of added binder is also evident and the largest difference between the particle distribution diagrams was observed between the pellet without any binder and the pellet with the highest studied amount of added binder (i.e., 66% Ag).

Even if the analytical results of tungsten are surely influenced by the fractionation caused by the gravitational settling of the particles in the ablation cell and the transporting tube (because of the high density of W), the growth in volume of the tungsten particles caused by the Ag condensation most probably leads to another fractionation of laser formed particles inside the ICP. The incomplete particle vaporization/ionization in the inductively coupled plasma then results in problems with the tungsten quantitative analysis. The particle distribution graphs (Fig. 4) show that the concentration of the particles with a diameter larger than 0.5 μm (which can be the critical value for the particle vaporization [24,25]) increase very significantly.

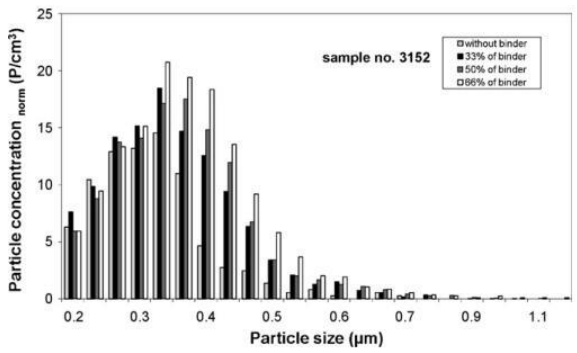

Fig. 4. Particle size distribution of the large particles (0.25–17 μm) for the sample 3152 prepared by pressing different amounts of binder. Histograms are based on a single measurement.

4. Conclusion

The reduction of the "matrix effect" by using a binder for the pellet preparation of powdered materials was investigated. Five samples representing Co-tungsten carbide precursors were prepared for ns laser ablation as pressed pellets without any binder and with the powdered silver serving as the binder and matrix unifier. The study of particle and ablation crater formation clearly demonstrated the function of the matrix unifier - the differences between studied samples in the particle concentration were reduced (RSD decreased from 46% to 19%) as well as the differences in the volumes of the ablation craters (the RSD decreased from 36% to 16%). The effect of the binder utilization on the LA–ICP-MS signals shows an improvement correlation of different samples in simulated calibration curve (increasing of the correlation coefficients of the isotope intensity *vs.* elemental content in the sample) for all elements of interest (Co, Ti, Ta, Nb) except W. In order to find a solution for the deterioration of the tungsten analytical response in the case of binder pellets, the structure and chemical composition of the particles formed during the laser ablation was investigated. The particle size distribution measurements showed an increase in the number of particles for the size range from 0.31 to 1.2 μm with the increasing binder content in the pellet. This effect was assigned to the condensation of vapor enriched by silver as a highly volatile component on the surface of the larger particles created from the melted material. It resulted in the production of large tungsten particles covered with a silver layer which was further proved by the SEM and the EDS measurements. Because the particle diameter is a critical parameter for the fractionation in the ICP, the increasing diameter of the silver-covered tungsten particle leads to their incomplete atomisation and ionization. The important role plays also the gravitational settling of W particles because of their extreme high density. Consequently, the W quantification in the matrix-unified samples is unsatisfactory.

This study shows that matrix unification can be a useful tool for the LA–ICP-MS quantitative analysis of powdered materials, but it can also cause changes in the particle formation during the ablation process leading to fractionation. The matrix unification of the Co-

tungsten carbide samples using the silver binder markedly reduced differences in the crater volumes as well as the evenly balanced concentration of generated particles during the laser ablation of different samples. On the other hand the matrix unification did not lead to complex improvement of analytical results. In general, the choice of the matrix unifier (binder) must therefore be done very carefully depending on the sample to be analysed and the ablation conditions.

Acknowledgements

M.H. gratefully acknowledges the Czech Science Foundation for bestowing the project 203/07/P439. V.K. acknowledge the Ministry of Education, Youth and Sports of the Czech Republic for the research project MSM0021622412 and MSM0021622410, respectively. P.M. acknowledges an institutional research plan of the Institute of Analytical Chemistry of the Academy of Sciences of the Czech Republic No. AV0 Z40310501. J.K. acknowledges the Ministry of Education, Youth and Sports of the Czech Republic for the research project MSM 0021630508.

References

[1] S.F. Durrant, J. Anal. Atom. Spectrom. 14 (1999) 1385.
[2] R.E. Russo, X.L. Mao, O.V. Borisov, H. Liu, J. Anal. Atom. Spectrom. 9 (2000) 1115.
[3] D. Bleiner, D. Günther, J. Anal. Atom. Spectrom. 16 (2001) 449.
[4] M. Guillong, I. Horn, D. Günther, J. Anal. Atom. Spectrom. 18 (2003) 1224.
[5] J. Gonzáles, C. Liu, X. Mao, R.E. Russo, J. Anal. Atom. Spectrom. 19 (2004) 1165.
[6] J. Koch, M. Wälle, J. Pisonero, D. Günther, J. Anal. Atom. Spectrom. 21 (2006) 932.
[7] R.E. Russo, X. Mao, J.J. Gonzales, S.S. Mao, J. Anal. Atom. Spectrom. 17 (2002) 1072.
[8] F. Poitrasson, X. Mao, S.S. Mao, R. Freydier, R.E. Russo, Anal. Chem. 75 (2003) 6184.
[9] C. Liu, X.L. Mao, S.S. Mao, X. Zeng, R. Greif, R.E. Russo, Anal. Chem. 76 (2004) 379.
[10] J. Koch, A. von Bohlen, R. Hergenröder, K. Niemax, J. Anal. Atom. Spectrom. 19 (2004) 267.
[11] J. Gonzáles, S.H. Dundas, C.Y. Liu, X. Mao, R.E. Russo, J. Anal. Atom. Spectrom. 21 (2006) 778.
[12] V. Možná, J. Pisonero, M. Holá, V. Kanický, D. Günther, J. Anal. Atom. Spectrom. 21 (2006) 1194.
[13] N.J. Seatveit, S.J. Bajic, D.P. Baldwin, R.S. Houk, J. Anal. Atom. Spectrom. 23 (2008) 54.
[14] J. Koch, D. Günther, Anal. Bioanal. Chem. 387 (2007) 149.
[15] C.C. Garcia, H. Lindner, A. von Bohlen, C. Vadla, K. Niemax, J. Anal. Atom. Spectrom. 19 (2008) 470.
[16] S.H. Jeong, O.V. Borisov, J.H. Yoo, X.L. Mao, R.E. Russo, Anal. Chem. 71 (1999) 5123.
[17] J.H. Yoo, O.V. Borisov, X. Mao, R.E. Russo, Anal. Chem. 73 (2001) 2288.
[18] D. Bleiner, P. Lienemann, H. Vonmont, Talanta 65 (2005) 1286.
[19] J. Koch, I. Feldmann, N. Jakubowski, K. Niemax, Spectrochim. Acta B 57 (2002) 975.
[20] I. Horn, D. Günther, Appl. Surf. Sci. 207 (2003) 144.
[21] D.B. Aeschliman, S.J. Bajic, D.P. Baldwin, R.S. Houk, J. Anal. Atom. Spectrom. 18 (2003) 1008.
[22] H.R. Kuhn, D. Günther, Anal. Bioanal. Chem. 383 (2005) 434.
[23] J. Koch, M. Wälle, R. Dietiker, D. Günther, Anal. Chem. 80 (2008) 915.
[24] M. Guillong, D. Günther, J. Anal. Atom. Spectrom. 17 (2002) 831.
[25] H.-R. Kuhn, D. Günther, J. Anal. Atom. Spectrom. 19 (2004) 1158.
[26] D. Günther, H. Cousin, B. Magyar, I. Leopold, J. Anal. Atom. Spectrom. 12 (1997) 165.
[27] F.E. Lichte, Anal Chem. 67 (1995) 2479.
[28] M. Odegard, S.H. Dundas, B. Flem, A. Grimstvedt, Fresenius J. Anal. Chem. 362 (1998) 477.
[29] J.S. Becker, H.-J. Dietze, Fresenius J. Anal. Chem. 365 (1999) 429.
[30] S. Nam, W.R.L. Masamba, A. Montaser, Anal. Chem. 65 (1993) 2784.
[31] C. Prokisch, A.M. Bilgic, E. Voges, J.A.C. Broeckaert, Spectrochim. Acta B 54 (1999) 1253.
[32] W. Klemm, G. Bombach, Fresenius J. Anal. Chem. 370 (2001) 641.
[33] M. Holá, P. Krásenský, V. Otruba, V. Kanický, J. Anal. Atom. Spectrom. 21 (2006) 974.
[34] J.S. Becker, Spectrochim. Acta B 57 (2002) 1805.
[35] T. Li, Q. Lou, Y. Wei, F. Huang, J. Dong, J. Liu, Appl. Surf. Sci. 181 (2001) 225.
[36] P. Musil, V. Otruba, V. Kanicky, J.-M. Mermet, Spectrochim. Acta B 55 (2000) 1747.
[37] O.V. Borisov, C.J. Bannochie, R.E. Russo, Appl. Spectrosc. 55 (2001) 1304.
[38] J. Mikolas, P. Musil, V. Stuchlikova, K. Novotny, V. Otruba, V. Kanicky, Anal. Bioanal. Chem. 374 (2002) 244.
[39] M. Holá, V. Otruba, V. Kanický, Spectrochim. Acta B 61 (2006) 515.
[40] M. Holá, V. Konečná, P. Mikuška, J. Kaiser, K. Páleníková, S. Průša, R. Hanzlíková, V. Kanický, J. Anal. Atom. Spectrom. 23 (2008) 1341.
[41] G.S. Upadhyaya, Cemented Tungsten Carbides: Production, Properties, and Testing, Noyes publications, New Jersey, USA, 1998.
[42] V. Kanický, V. Otruba, J.-M. Mermet, Spectrochim. Acta B 55 (2000) 575.
[43] V. Kanický, V. Otruba, J.-M. Mermet, Spectrochim. Acta B 55 (2000) 1601.
[44] V. Kanický, V. Otruba, J.-M. Mermet, Fresenius J. Anal. Chem. 371 (2001) 934.
[45] R. Jaworski, E. Hoffmann, H. Stephanowitz, Int. J. Mass Spectrom. 219 (2002) 373.
[46] H.R. Kuhn, D. Günther, Anal. Chem. 75 (2003) 747.
[47] C. Liu, X. Mao, S.S. Mao, R. Greif, R.E. Russo, Anal. Chem. 77 (2005) 6687.

PAPER 12

The effect of nanoparticle presence on aerosol formation during nanoparticle-enhanced laser ablation inductively coupled plasma mass spectrometry

Holá, M., Salajková, Z., Hrdlička, A.*, M., Ondráček, J., Novotný, K., Pavliňák, D., Vojtíšek-Lom, M., Čelko, L., Pořízka, P., Kanický, V., Prochazka, D., Novotný, J., Kaiser, J.

Journal of Analytical Atomic Spectrometry. 2020, 35(12), 2893-2900. DOI 10.1039/d0ja00324g

Contribution:

LA-ICP-MS design of experiments and measurements, data evaluation, studying of ablation craters, trapping particles on the filter and studying the particle structure, manuscript writing.

JAAS

ROYAL SOCIETY OF CHEMISTRY

PAPER

View Article Online
View Journal | View Issue

Cite this: *J. Anal. At. Spectrom.*, 2020, **35**, 2893

The effect of nanoparticle presence on aerosol formation during nanoparticle-enhanced laser ablation inductively coupled plasma mass spectrometry

Markéta Holá,[a] Zita Salajková,[b] Aleš Hrdlička,*[a] Jakub Ondráček,[c] Karel Novotný,[a] David Pavliňák,[d] Michal Vojtíšek-Lom,[e] Ladislav Čelko,[b] Pavel Pořízka,[b] Viktor Kanický,[a] David Prochazka,[b] Jan Novotný[b] and Jozef Kaiser[b]

The changes in aerosol physical properties were studied by applying Nanoparticle-Enhanced Laser Ablation Inductively Coupled Plasma Mass Spectrometry (NE-LA-ICP-MS). This approach was compared to conventional LA-ICP-MS method. Analyte signal enhancement was related to the particle number concentration of aerosol for three sizes of Au nanoparticles (NPs) applied on the metal sample surface in the form of droplets. The dependence of the number of generated particles on the laser fluence in the range from 0.5 to 10 J cm^{-2} was studied. A different shape of the particle size distribution (PSD) of NE-LA-ICP-MS and LA-ICP-MS aerosol was determined. The aerosol structure was additionally studied on filters using scanning electron microscopy (SEM). Compared to LA-ICP-MS, NE-LA-ICP-MS produced a larger proportion of small particles (<30 nm), and was approaching the ideal monodisperse aerosol that is evaporated in ICP with a high efficiency. The measurements proved that NPs on the sample surface could influence the evaporation, condensation and coagulation processes in aerosol formation as well as the signal of analytes in ICP-MS.

Received 13th July 2020
Accepted 21st September 2020

DOI: 10.1039/d0ja00324g

rsc.li/jaas

1. Introduction

Searching for relations between laser ablation phenomena and yielded results of laser ablation inductively coupled plasma mass spectrometry (LA-ICP-MS) is a very traditional topic. Although the LA process is reckoned to be "poorly understood" during the LA-ICP-MS era, numerous studies have been published about partial processes that are involved. In general, the process of laser–matter interactions is influenced by two main factors – the laser ablation conditions and properties of the sample itself.[1–3] In addition to the wavelength of the laser, the pulse duration, fluence, repetition rate and crater size are very important parameters influencing the results, sensitivity of analysis and fractionation effects.[4]

Under the same LA-conditions, different fractions of sizes and numbers of particles and clusters are launched from different materials. Matrix effects are observed in ICP[5] because the evaporation and atomization efficiency differs for various types of particles. Achieving a correct analysis is thus not only the question of appropriate LA-sampling at minimum selective evaporation during the laser impact, but also of the composition of partial aerosol fractions. Big micrometer-sized particles suffer from lower transport efficiency and they cannot be completely evaporated if delivered to ICP.[6] Some size fractions of aerosol particles might be enriched by different elements. It is typical for the aerosol from brass[4] but also for widely used NIST glass standard reference materials.[7,8] Short wavelengths, the pulse duration down to fs[9] and He as a carrier gas are advantageous.[8,10] The processes behind the ultrashort laser ablation start with the electronic absorption of the laser beam in a time scale of 10^{-15} s and end with the particle ejection from 10^{-6} s.[11]

Formation of nanoparticles (NPs) during LA of solid samples has been studied for a long time.[12] It was recognized that the mass of the particle aerosol could increase through the metal oxidation during aggregation.[12] The number of particles may increase by two orders of magnitude depending on the gas environment (air *vs.* Ar); moreover, shorter pulses produce

[a]*Department of Chemistry, Faculty of Science, Masaryk University, Kotlářská 2, 61137 Brno, Czech Republic. E-mail: ahrdlicka@chemi.muni.cz*

[b]*Central European Institute of Technology, Brno University of Technology, Purkyňova 656/123, CZ-612 00 Brno, Czech Republic*

[c]*Department of Aerosol Chemistry and Physics, Institute of Chemical Process Fundamentals of the ASCR, Rozvojová 135, CZ-165 00 Prague, Czech Republic*

[d]*Department of Physical Electronics, Faculty of Science, Masaryk University, Kotlářská 2, CZ-611 37 Brno, Czech Republic*

[e]*Faculty of Mechanical Engineering, Czech Technical University of Prague, Zikova 4, 160 00 Prague, Czech Republic*

smaller particles.[13] The set of processes accompanying the particle creation, nucleation, condensation, and agglomeration was described theoretically and experimentally demonstrated on mainly silicate and metallic materials.[10] Mass load matrix effects differing by the material, lasing wavelength, and element represent another problem. Complexity and entanglement of the particular matrix effects make their recognition quite difficult.[14] Direct and easy evaporation of small particles in ICP is not the only process that leads to higher signals. Ion distribution and ion beam density are also changed in the plasma plume[15] as well as ion extraction and transport to detector.

Any aerosol modification can then lead to a positive or negative change of the measured element (isotope) signal. It has been experimentally proved that a restriction of big particles and a selection of smaller ones from the aerosol lead to a diminution of elemental fractionation.[16] Systematic signal enhancement would be profitable for any analytical technique. In the case of LA-ICP-MS, the Limit of Detection (LOD) could be improved. Moreover, both the integration time for sequential MS and the time of analysis could be shortened. The required sample area and ablation spot may be smaller, which means a lower damage of the sample. As a result, spatial resolution would be better.

One of the signal enhancement techniques in the field of LA is enhancement by nanoparticles. This method has been mainly used in Laser-Induced Breakdown Spectroscopy (LIBS) as nanoparticle enhanced (NE) LIBS.[17] NPs are applied onto a sample surface. The photons of the incident laser beam polarize NPs and induce elongation of free electron clouds from equilibrium positions around static ions in the crystal lattice of NPs. NPs can behave as secondary antennas producing radiation which can locally be very intense, mainly between NPs and the sample surface. The local field enhancements make LA more intense, consequently enhancing the measured emission of the microplasma. In the case of conductive surfaces, appropriate NP diameters, distances between NPs and lasing wavelength surface plasmon resonance might occur and the enhancement could be orders of magnitude. Non-conductive samples of NELIBS can be plant leaves[18] or gemstones where NPs protect the surface from a visible damage at keeping an intensive analyte emission.

NPs are an intermediator which indirectly delivers the laser beam energy to the surface under the ablation threshold.[19] NELIBS can be optimized not only by searching for the best NP size and concentration, fluence/irradiance and gate delay[20] but also the ambient low pressure which was shown as a dominant parameter.[21] Surface deposited NPs may also be modified by the incident laser beam. They are rounded, partially evaporated or they even undergo laser-induced breakdown at irradiances above 10^9 W cm^{-2}.[17] Although the question of the ablation mechanism with NPs has been solved,[17,19] the post-breakdown aerosol modification is another topic which is, however, out of the scope of the classical LIBS.

Concerning NE-LA-ICP-MS, there are currently only two studies.[22,23] The relations among the ablation crater morphology, aerosol composition, sample material, used NPs and the fluence during NE-LA-ICP-MS have been shown in our recent study.[22] The second study presents the effect of NPs on a wider range of materials including NIST glass and more deeply explores the role of the NP concentration. The maximum enhancement is 2 for the glass and about one order of magnitude for metallic materials.[23] The 213 nm laser is the same as in our study[22] where the maximum enhancement exceeded 2 orders of magnitude. The difference of observed enhancement is mainly a result of variation in the NP surface concentration. The second study also mentions that the enhancement of Ag presented as a trace element in a pure Cu sample, varies depending on its concentration; the enhancement grows with decreasing concentration of Ag. This behaviour differs from that of NELIBS, where the enhancement is almost independent of the elemental concentration. This observation supports the assumption that NP enhancement in LA-ICP-MS cannot be simply explained by NELIBS theory and the effect of NPs on the formation, transport and ionisation of aerosol should be investigated.

The dominant factor influencing the number of big primary particles is the sample material.[3] A suggested hypothesis is that aerosol particles of the metallic target might condense or aggregate on the NPs which serve as cores. Both the transport and evaporation efficiency might then increase and more intense element signals can be measured. In this work, we would like to show the influence of the NP size and laser fluence on the measured element signal and aerosol physical properties.

2. Experimental

2.1 Samples and chemicals

Aluminum alloy AW 2030 was used as a model sample. This sample was selected on the basis of experience from a previous study describing the principle of the method.[22] The composition was (wt%) Al (92), Cu (3.9), Pb (1.2), Mg (0.8), Mn (0.6), and Fe (0.1). The sample surface was carefully polished (FEPA 800, 1000, 4000, diamond pastes 3 and 1 μm, cleaned with IPA) prior to the application of drops containing nanoparticles (NPs). One drop corresponded to 5 μl of a water suspension containing spherical Au NPs and was freely dried in open air on a sample surface. Typically, the created drop was almost in a circular shape with a diameter of about 2.7–3 mm. Gold spherical nanoparticles in three sizes (10, 40 and 100 nm) were selected (citrate, BBI Solutions, UK) as model NPs. The same mass concentration was maintained for all sizes (Au $\sim$ 57 μg ml^{-1}), resulting in a different particle number (PN) concentration: 5.7 $\times$ 10^{12} particles per ml for 10 nm NPs, 9 $\times$ 10^{10} particles per ml for 40 nm NPs and 5.6 $\times$ 10^9 particles per ml for 100 nm NPs. For more detailed information on the sample preparation see ref. 22.

2.2 Instrumental equipment and operating conditions

All experiments were performed with an LA-ICP-MS system consisting of an LSX-213 G2+ laser ablation device (Teledyne Cetac Technologies, USA) and Agilent 7900 ICP-MS analyser (Agilent Technologies, Japan). The LA system operates at

a wavelength of 213 nm with a pulse duration of ~4 ns using helium as a carrier gas with a 2-volume ablation cell (HelEx). An ablation spot of 100 μm diameter was used to ensure the existence of a sufficient isotopic signal and a representative area containing NPs on the sample surface.

A line scan was performed, with an ablation speed of 0.5 mm s^{-1} at a repetition rate of 5 Hz, *i.e.*, a chain of adjacent 100 μm ablation spots was produced. In the case of the clean sample surface measurements, line scans outside the droplet area were performed. In the case of the experiments with NPs, line scans were positioned only inside the area of the droplets. Fluences in the range of 0.5–10 J cm^{-2} were applied. The ICP-MS system was a quadrupole analyser with an octopole reaction cell. This instrument was operated at a forwarded power of 1550 W, Ar gas flow rates of 15 (outer plasma gas) and 0.7 (auxiliary) l min^{-1}, a He carrier flow rate of 0.8 l min^{-1}, and an Ar makeup gas flow rate of 0.6 l min^{-1} (for LA-ICP-MS set-up) or 1.6 l min^{-1} (for the LA-aerosol spectrometer set-up). The ablated material was transported through a FEP (Fluorinated Ethylene Propylene) tube (i.d. 2 mm, length 1 m) to the ICP-MS system. Five measured isotopes were selected to represent the sample: ^{27}Al for the matrix element, ^{57}Fe, ^{63}Cu, ^{26}Mg, and ^{208}Pb as minor elements and ^{197}Au representing nanoparticles. The total integration time per all isotopes was adjusted to 0.225 s (0.05 per minor and 0.005 per major).

The aerosol generated by laser ablation of non-overlapping spots was alternately sampled into either an ICP-MS instrument or aerosol spectrometers in two arrangements (see Fig. 1): classical set-up LA-ICP-MS or LA – Engine Exhaust Particle Sizer (EEPS) + Condensation Particle Counter (CPC) as described below. The separate sampling into the set of aerosol spectrometers and ICP-MS was selected to avoid unwanted negative effects of common sampling in many instruments at the same time. The reproducibility of results was verified by repeated experiments resulting in similar results obtained by ICP-MS and aerosol spectrometers. Moreover, in order to minimize the effects of changing conditions within one droplet containing Au nanoparticles, the sampling into aerosol spectrometers and ICP-MS was performed in the alternating pattern of odd (aerosol spectrometers) and even (ICP-MS) lines of one drop.

The change of the sampling method between ICP MS and aerosol spectrometers was carried out after measuring all fluences of the respective nanoparticle size for the respective sampling method. The results of measurements of both ICP-MS and aerosol spectrometers were averaged over 30 s – the duration of one cycle over the droplet. Each cycle was repeated 3 times (one cycle = one droplet). The averaging over the whole scan and the repetition of the experiment should minimize the influence of the possible inhomogeneous distribution of NPs on the sample caused by the coffee stain effect and corresponded to the mapping of almost the entire surface of the droplet. The resulting data consisted of the elemental composition obtained from ICP-MS supplemented by the total particle number concentration (CPC) and particle size distribution of nanoparticles <560 nm (EEPS) from identical NP drops under the same LA setup. For a detailed scheme of the performed line scans on a droplet see Fig. 2.

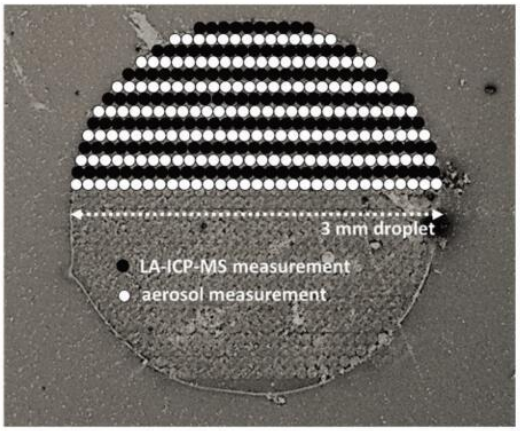

Fig. 2 An overview SEM image of the layout of line scans on a droplet after laser ablation.

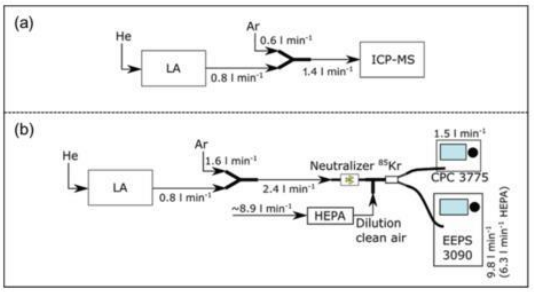

Fig. 1 Measurement setup: (a) LA-ICP-MS, and (b) LA with CPC and EEPS.

The size distribution of aerosol particles and the total number concentration was measured in the following setup: the flow of the carrier gas with aerosol particles produced by LA was first led through a bipolar aerosol neutralizer (^{85}Kr, 10 mCi) in order to prevent excessive losses of particles due to the electrostatic deposition on the sampling lines and in order to ensure a correct charge distribution for the aerosol spectrometers. After neutralization, the aerosol was diluted with HEPA (High-Efficiency Particulate Air) filtered air to lower the high aerosol concentration and to maintain a sufficient flow into the aerosol spectrometers. The diluted aerosol was then split using an isokinetic flow splitter in order to ensure representative aerosol sampling into used aerosol spectrometers.

The setup of aerosol spectrometers (see Fig. 1) contained a CPC (CPC 3775, TSI) and EEPS (EEPS 3090, TSI). The CPC was used to count the total number of particles >4 nm (d_{50} = 4 nm) with a high time resolution (1 s). The EEPS allows for fast measurements (0.1 s) of the particle number size distribution in the range of 5.6–560 nm resolved in 32 size channels. The individual aerosol spectrometers require specific gas flows as shown in Fig. 1. Aerosol dilution was performed with air cleaned through a HEPA filter. Furthermore, the shape and

structure of laser-generated particles were studied after their collection on a polycarbonate membrane filter (25 mm in diameter and 0.2 μm pores, Cyclopore, Whatman) using scanning electron microscopy (SEM; Mira 3, Tescan Orsay Holding, Tescan Brno, Czech Republic; 10 kV, backscattered electron mode). To obtain a sufficient amount of particles, the samples were completely covered with contacting drops, and ablation proceeded over the entire area of the sample line by line for 30 minutes. To achieve a better visualization and to prevent charging, the filters were covered with a 10 nm silver layer.

3. Results and discussion

In order to understand more deeply the phenomena of nanoparticle-enhanced LA, obtaining detailed knowledge of the generated aerosol is one of the most important tasks. Experiments were performed as a comparative study for laser ablation of a clean sample (common LA) and NE-LA of a sample surface covered with Au nanoparticles of three different sizes (10, 40 and 100 nm). These sizes were selected also with respect to recently published NELIBS results where the size effect of NPs on the laser–matter interaction was reported. For the spot size of 100 μm in diameter, LIBS signal enhancement was observed only for nanoparticles smaller than 50 nm.[14] Fluences in the range of 0.5–10 J cm^{-2} were applied.

The basic information is the total particle number concentration (PNC), measured using a CPC in the range from 4 nm to >3 μm in our study. The results show different trends in PNC dependences on the used laser fluence. Theoretically, it can be assumed that increasing the fluence increases linearly the ablation rate.[24] A larger ablation rate means the release of a larger volume of material. Postulating that the ablation process does not change, there should also be a proportional increase in the number of particles. But this statement is usually only valid for low laser fluences (up to 10 J cm^{-2}). The models show that especially at higher fluences the increase in the ablation rate and loose matter is not linear and the shape of the curve depends on the physical properties of the ablated material. Individual materials will have different surface temperatures during ablation. This results in varying thickness of the melt layer on the surface and the evaporation of the material will be different. The thicker melt layer also causes larger particle formation due to hydrodynamic sputtering.[25]

For our range of fluences (0.5–10 J cm^{-2}), it has been shown that by applying nanoparticles to the sample surface, we change its properties to such an extent that this is also reflected in the graph shape of the total number of particles *versus* fluence. Although we are aware that the number of particles does not exactly match the total mass released, this information points to a different process of aerosol formation for LA and NE-LA. While the PNC produced from the clean sample surface increases proportionally with increasing laser fluence (Fig. 3, full squares), the surfaces covered with NPs provide an increase in particle production only at lower fluence rates.

The PNC remains more or less constant from the value of 5 J cm^{-2}, as shown in Fig. 3. The CPC results proved a higher particle production in the case of NE-LA compared to common

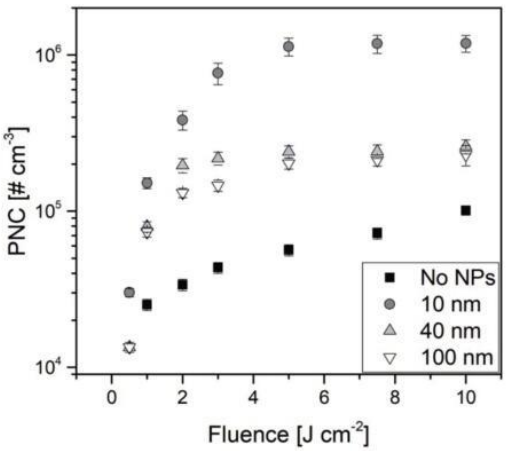

Fig. 3 Dependence of the PNC on the laser fluence for a clean surface and surface covered with: 10 nm Au, 40 nm Au, 100 nm Au NPs.

LA, most effective for 10 nm Au NPs where the total PNC increased more than ten times depending on the used fluence.

Each CPC measurement corresponds to LA-ICP-MS results (the same drop) for a group of measured isotopes. For better clarity, selected isotopes are presented in separate graphs for three values of fluence representing the steep part of the curve from Fig. 3 (1, 3 and 5 J cm^{-2}). It is possible to compare the PNC (Fig. 4a), LA-ICP-MS signal of gold (Fig. 4b) and LA-ICP-MS signal of analytes (Fig. 4c–f). In the first approximation, it is obvious that the presence of NPs on the sample surface is the cause of aerosol formation with a rather large number of particles. On the other hand, a large particle number does not automatically implicate a high signal amplification for all elements. The highest particle production for 10 nm NPs is related to a significant enhancement of Pb and Mg while the Al and Fe enhancements work better with 40 nm NPs. Copper did not show any signal amplification, and therefore it is not shown in the graph. In our previous study copper showed certain signal enhancement but rather lower fluencies and Ag NPs were used.[22] The low or no signal enhancement apparently correlates

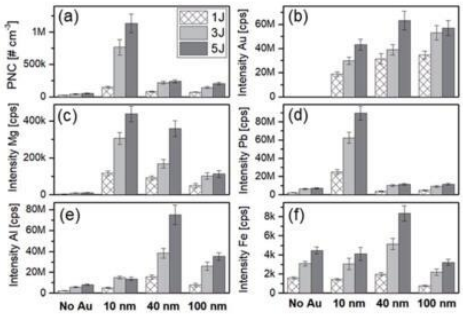

Fig. 4 Total particle number concentration (a), ICP-MS intensities for ^{197}Au (b), ^{26}Mg (c), ^{208}Pb (d), ^{27}Al (e), and ^{57}Fe (f), for clean sample and sample covered with Au nanoparticles (10, 40 and 100 nm).

with high solubility of copper and iron in gold.[26] Besides, the selectivity enhancement is also associated with the physical characteristics of the individual elements. Mg and Pb represent the most volatile parts of the sample (with boiling points of the macroscopic material being 1091 °C and 1749 °C respectively) compared to other components (2519 °C for Al and 2861 °C for Fe). Assuming that the mechanism of the laser interaction with the sample and also the subsequent particle condensation are different in the presence of NPs compared to standard LA, the volatility of the individual components is likely to play a role as well. During NE-LA, it is assumed that the Au NPs are either vaporized together with the sample and the vapours then condense together in the nanoparticles, or only a partial evaporation occurs and can then serve as condensation nuclei for the surrounding sample vapours.

The principle of the signal enhancement still remains unclear. However, the measurements proved production of a higher number of particles in the presence of NPs. This can be caused by more effective energy transfer from the laser beam to the sample surface, altered condensation conditions of the particles (other vapor compositions and the possibility of the presence of desorbed Au NPs). The results of the experiments can be compared with the studies of NELIBS,[17] where similar consequences of the presence of nanoparticles on the sample surface were observed. When the laser interacts with NPs on the sample surface, the collective oscillation of electrons is excited in the NPs. This results in the enhancement of the electromagnetic field that is the strongest in the gaps between close NPs (gaps are smaller than the particle diameter). When NPs are deposited on a metallic surface, this laser field enhancement can switch the production of seed electrons from a typical multiphoton ionization to a field emission. In this way, the gaps between close NPs work as ignition points of plasma. Even if the system is not in the plasmon resonance, the locally enhanced electric field facilitates the escape of the electrons from the surface.[17] Assuming the described NELIBS processes in NE-LA, we can expect changes in the laser–sample interaction, microplasma dynamics as well as in particle production compared to classical LA. This can result in ablation of larger mass of material or the formation of aerosol with different particle size distributions (discussed below), or a combination of both. Moreover, to a certain extent, it will be true that more nanoparticles mean a higher rate of the described process. The higher the surface concentration of NPs, the higher the number of ignition points, which implies a higher PNC in the end of process. Therefore, we obtained the highest PNC for 10 nm NPs, where the surface concentration of NPs is the highest (Fig. 4a). The question of whether more mass is released using NE-LA has been partially discussed in the previous study.[22] The measurements of the ablation crater depths did not confirm the removing of more material in the case of NE-LA. However, estimating the released material only from the volume of the ablation crater can be misleading. The melted bottom changes its density, so the conversion of volume is inaccurate. It was also shown in the study of ablation craters that the rate of thermal effects was higher for LA compared to NE-LA.[22] So part of the material from classical LA is splashed around the ablation crater and does not participate in the analytical signal of ICP-MS. Since each element responds differently to NE-LA, it is clear that the effect of NE-LA will not only be due to a possible increase in the mass transported to the plasma but also more importantly the change in the dynamics of the process of aerosol formation, which is then more efficiently transported, evaporated and ionized in ICP-MS.

Fig. 4b points to an interesting phenomenon. Although the Au mass concentration in all droplets is the same regardless of the size of the NPs, the LA-ICP-MS signal for Au is higher for larger nanoparticles. From this relation we can deduce that not all Au NPs are removed from the sample surface by the one pulse ablation. To verify this assumption, the SEM photos of the ablation crater surface were recorded. Fig. 5 shows images for the 40 nm NP sample surface before (Fig. 5a) and after (Fig. 5b) one shot ablation using a fluence of 3 J cm^{-2}. Fig. 5b shows NPs on the crater bottom (visible as contrasting white dots). It should be noted that it was not possible to record pictures exactly from the same spot before and after NE-LA, so the photos are only illustrative that after NE-LA some particles are still on the surface unchanged. Re-ablation measurements of the sample surface confirmed that the mass of the remaining nanoparticles is less than 15%. Thus, particle numbers in Fig. 5 cannot be taken as a measure of their loss.

The information about the particle size distribution (PSD) was obtained using an EEPS within the size range of 5.6–560 nm. Fig. 6 shows the average PSD of 60 s laser ablation as complementary data to Fig. 4. In order to accurately compare the PSD shape for different NP sizes on sample surfaces, the curves for the same fluences are presented in the same graph after their normalization on the total number of particles.

Focusing on NE-LA, it has been found that the different sizes of NPs have only a minimal effect on the PSD shape. This is shown by a significant peak at about 15 nm that represents primary condensed nanoparticles (see first maximum at Fig. 6a). The rest of the PSD curve does not exhibit any distinct peak (>30 nm) for all Au NP diameters. Moreover, no visible peak at the position of original NP sizes can be found on the curves. The shape of the PSD curves, and the position of the main peak support the theory that an addition of Au NPs on the sample surface enhances the sample evaporation. At the same time, NPs themselves are released intact in a very small number and/or the NPs also evaporate and subsequently condense to form new particles with the same mechanism to the compounds of the original sample. Moreover, if the Au NPs are

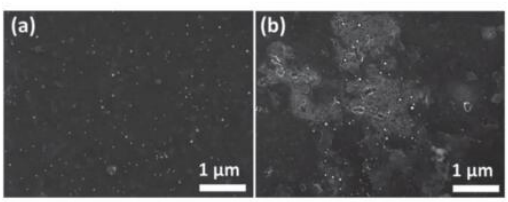

Fig. 5 Sample surface of a 40 nm Au NP droplet before (a) and after (b) NE-LA-ICP-MS.

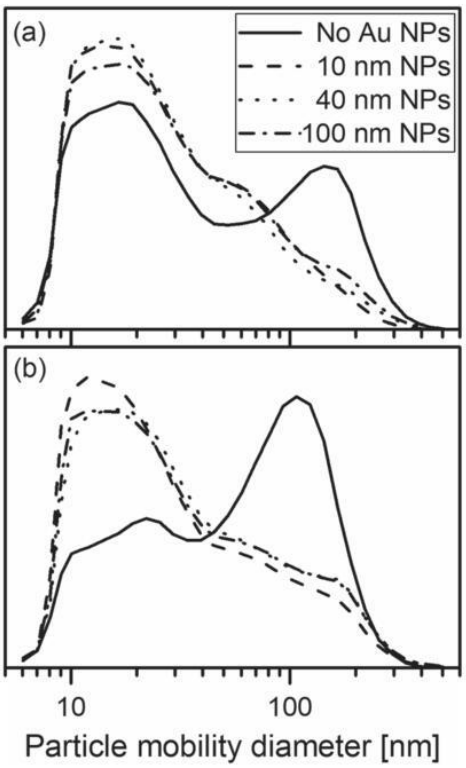

Fig. 6 Particle size distribution (5.6–560 nm, arbitrary concentration units) of LA and NE-LA aerosol using different sizes of nanoparticles for fluences 1 J cm^{-2} (a) and 3 J cm^{-2} (b).

released intact from the sample surface, they represent only a small fraction compared to the amount of new particles formed by condensation of vapours.

Thus the peak of the original Au NPs is negligible in the PSD for all studied Au NP sizes. Specifically, the maximum number of 10 nm NPs from the crater area results from the known amount of NPs in the pipetted volume per area unit. A 100 μm crater makes 3.17×10^7 NPs. The total number of measured particles from the CPC is 3.2×10^7 NPs per pulse for a density of 7.5×10^5 cm^{-3} (Fig. 3) of 10 nm NPs and a fluence of 3 J cm^{-2}. The number of 10 nm NPs in the crater area is anyway comparable with the total measured number of the aerosol particles and no specific maxima are observed in the yielded PSD (Fig. 6) except for 10–20 nm.

This maximum, however, gives evidence on the increased total amount of the small particles at the expense of the bigger ones. Most of the NPs must be re-melted and incorporated into the newly formed particles during the ablation and condensation process. The total numbers of particles are much higher compared to the numbers of 40 and 100 nm. In principle, large NPs cannot substantially increase the corresponding size of the PSD by direct rejection from the surface.

On the other hand, the difference between the PSD of the aerosol generated by NE-LA and LA is clear. For LA we have a typical bimodal PSD shape with a small peak at the very beginning of the PSD that was already shown[3,27] for nanosecond LA of polished surfaces of solid samples. Particles peaking at 10 nm represent the smallest primary particles produced by evaporation and following condensation of the material released during laser ablation. The second peak shows the primary particles with condensed vapours growing the particles to larger sizes (for higher fluence 3 J cm^{-2} more vapours are available, so the second peak is shifted towards larger particle sizes compared to lower fluence 1 J cm^{-2}). Particles >30 nm are most probably a product of coagulation/agglomeration of primary nanoparticles together with particles originating from the droplet solidification (the sample heats up and easily creates a pool of melted components, which may result in splashes of the melt). This means that the last maximum of PSD (>100 nm) is dependent on the degree of sample melting; in our case a higher fluence means higher sample melting and a greater tendency to form larger particles (comparing Fig. 6a and b – full line). Applying NPs on the sample surface causes a decrease of the magnitude of the particle mode >100 nm. The presence of Au NPs promotes a different energy transfer of the laser beam to the sample compared to conventional LA resulting in a higher production of primary particles at the expense of larger particles formed by thermal effects.

A different agglomeration process for NE-LA and LA is also possible. All effects lead to aerosol size unification towards smaller particles if NE-LA is introduced. The aerosol structures were additionally studied by SEM. Particles from LA and NE-LA were collected on membrane filters for 30 minutes using a laser fluence of 3 J cm^{-2}. Nanoparticles that are formed from a clean sample surface create a typical picture – chain structure together with large spheres[28] (Fig. 7a). NE-LA also produces

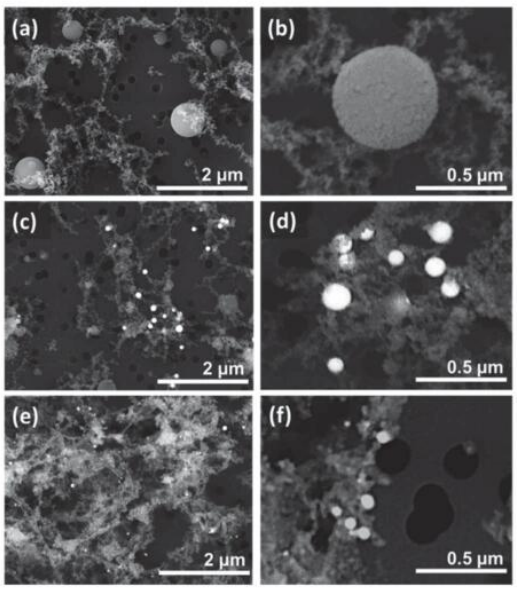

Fig. 7 SEM images of aerosol particles captured on the filter at a fluence of 3 J cm^{-2} – clean surface (a and b), 100 nm NPs on the surface (c and d), and 40 nm NPs on the surface (e and f).

a chain structure but with visible Au NPs in the structure, with the large spheres almost missing. The gold NPs can be distinguished from the other material using SEM by material contrast and our photographs display them as white dots. The size of Au NPs corresponds to their original size of 100 nm in Fig. 7b and 40 nm in Fig. 7c (the filter pores have a diameter of 200 nm).

This means that some of the Au NPs can "survive" the laser ablation process in their original form by direct release from the surface without any evaporation and without any following condensation process. However, the quantity is very small in comparison with other populations of particles, and therefore not visible in the distribution graph (Fig. 6) as a separate peak. Another fact is that there is no layer of smaller particles on their surface and it is therefore very likely that they did not participate in the condensation of the ablated material. The explanation may be that they admixed to already condensed vapours in the later phase of ablation by the pressure wave. It is also possible that these particles were not directly affected by the laser, but they only were lying in the peripheral circle close to the impact of the laser pulse to the surface. We can expect that some of the Au NPs directly ablated by the laser pulse are evaporated together with the sample matter and are incorporated into the structure of the condensed material particles. If the evaporation of Au NPs is not complete, vapour condensation will occur on the remainder of the NPs leading to larger structures with the composition of the Au core + condensed envelope. However, a significant proportion of Au NPs is not involved in the aerosol formation process because it remains lying on the surface, as mentioned earlier (Fig. 5). The SEM investigation of the collected particles proved also a more significant reduction of the splashed material (hydrodynamic sputtering) from the surface if using NE-LA, compared to LA. Almost no large spheres (products of splashed melt) were present on the filters as shown in Fig. 7b and c. This supports an observation previously documented in the investigation of ablation craters[22] *i.e.* thermal effects commonly present during ns LA may be significantly reduced by NE-LA.

4. Conclusions

This study characterizes the aerosol produced by two methods, NE-LA and conventional LA, and would contribute to further understanding of the NE-LA mechanism. The total number of generated particles (>4 nm) measured using the CPC was monitored for LA and NE-LA using three sizes of Au NPs (10, 40 and 100 nm) under fluences ranging from 0.5 to 10 J cm^{-2}. While in LA the number of particles increased in proportion to the used fluence, in the case of NE-LA, it only increased to 5 J cm^{-2}, then a saturation occurred and the effect of NPs was no longer intensified. Nevertheless, the presence of NPs on the ablated surface increases the number of generated particles substantially compared to the clean surface. The highest number of particles was generated using 10 nm Au NPs, where the increase in the PNC compared to the clean surface was up to 20 times. The origin of this behaviour most likely comes from the plasmon properties of NPs and their influence on LA, as described previously in the NE-LIBS publication.[17] The gaps between close NPs work as ignition points of plasma, and in this way whole plasma dynamics changed. To a certain extent, more NPs cause a higher rate of the described process. In our observations it also means more particles in produced aerosol. This can be due to the formation of smaller particles at the expense of larger ones resulting in more efficient transport, evaporation and ionization in ICP. The presence of NPs on the sample surface can also change the optical properties of the surface and thus increase the energy transfer of the laser. This additional energy then results in more efficient ablation of the surface. This increased mass production can also contribute to the enhancement but it has not been proven from the crater volume estimation. It will be necessary to use an accurate method to verify this, for example gravimetry. Most likely a combination of both the different aerosol structure and higher effective mass production will play a role. Although SEM pictures demonstrated that a small portion of Au NPs survived and remained unchanged after NE-LA, no increase in the PNC in the size mode corresponding to the original nanoparticle size was observed in PSD graphs. This suggests that Au NPs do not occur alone in the aerosol, but only as a part of the agglomerates or as a part of newly formed particles formed by evaporation followed by condensation. Most likely they form cluster centres and contribute to the vapor condensation of the ablated material. The shape of the PSD remained almost the same for different NP sizes. The difference in the PSD was obvious only when comparing a clean surface and a surface with the presence of nanoparticles. The NE-LA-ICP-MS method produced a larger proportion of small particles (<30 nm) at the expense of particles with a diameter around 100 nm and larger. The first reason could be explained by a different clustering mechanism for both methods. The second reason is a reduction of sample melting during NE-LA which leads to a reduced formation of large spherical particles formed directly by solidification of the sprayed sample melt (hydrodynamic sputtering). Suppression of sample melting has been already observed during studies of the NE-LA craters.[22] This has been confirmed by a current study of aerosol collected on filters. SEM observations proved a reduced number of large spherical particles in the case of NE-LA. The effect of nanoparticle-enhancement on ICP-MS signals is partly dependent on the physical properties of the analyte. The signal enhancement in relation to the boiling points of the individual components was compared. The highest enhancement was obtained for Pb (macroscopic b.p. 1749 °C) and Mg (b.p. 1090 °C) using 10 nm Au, which was also associated with the largest particle production. However, for less volatile components such as Al (b.p. 2519 °C) or Fe (b.p. 2861 °C), the enhancement effect was greatest in the case of 40 nm particles. The boiling point, however, certainly will not be the only indicator of the enhancement rate. In the case of copper, signal enhancement was not observed although it should be classified as Al and Fe with its boiling point of 2562 °C. Other circumstances, such as the miscibility of the particular metal with Au,[26] the structure of the material and the melt composition formed on the surface of the sample when interacting with the nanosecond laser pulse will also play a role.[25,26] The clear result of experiments is that while using the NE-LA-ICP-MS method,

a larger proportion of small particles (<30 nm) is produced (compared to conventional LA-ICP-MS). This is approaching the ideal monodisperse aerosol that can provide a highly efficient evaporation in ICP. This knowledge could serve as the basis for further research that might eventually lead to a strategy that would correct unwanted fractionation effects in LA.

Conflicts of interest

There are no conflicts to declare.

Acknowledgements

This work (MH) was financially supported by the Czech Science Foundation under the project GA17-12774S. AH acknowledges the project MUNI/A/1421/2019 from the Grant Agency of Masaryk University. This research has also been partially supported (DPav) by the project LO1411 (NPU I) funded by Ministry of Education, Youth and Sports of Czech Republic. MV acknowledges the Czech Science Foundation project no. GA19-04682S. ZS, LC, PP and JK gratefully acknowledge that this research has been financially supported by the Ministry of Education, Youth and Sports of the Czech Republic under the project CEITEC 2020 (LQ1601).

Notes and references

1 P. M. Outridge, W. Doherty and D. C. Gregoire, *Spectrochim. Acta, Part B*, 1997, **52**, 2093–2102.
2 D. Marla, U. V. Bhandarkar and S. S. Joshi, *Appl. Phys. A: Mater. Sci. Process.*, 2014, **116**, 273–285.
3 M. Holá, J. Ondráček, H. Nováková, M. Vojtíšek-Lom, R. Hadravová and V. Kanický, *Spectrochim. Acta, Part B*, 2018, **148**, 193–204.
4 C. Liu, X. Mao, S. S. Mao, R. Greif and R. E. Russo, *Anal. Chem.*, 2005, **77**, 6687–6691.
5 J. Koch, *Appl. Spectrosc.*, 2011, **65**, 155A–162A.
6 M. Guillong, H.-R. Kuhn and D. Günther, *Spectrochim. Acta, Part B*, 2003, **58**, 211–220.
7 H.-R. Kuhn and D. Günther, *J. Anal. At. Spectrom.*, 2004, **19**, 1158–1164.
8 M. Guillong and D. Günther, *J. Anal. At. Spectrom.*, 2002, **17**, 831–837.
9 B. Fernandez, F. Claverie, C. Pecheyran and O. F. X. Donard, *TrAC, Trends Anal. Chem.*, 2007, **26**, 951–966.
10 R. Hergenroeder, *Spectrochim. Acta, Part B*, 2006, **61**, 284–300.
11 R. E. Russo, X. L. Mao and S. S. Mao, *Anal. Chem.*, 2002, **74**, 70A–77A.
12 M. Ullmann, S. K. Friedlander and A. Schmidt-Ott, *J. Nanopart. Res.*, 2002, **4**, 499–509.
13 V. Dudoitis, V. Ulevičius, G. Račiukaitis, N. Špirkauskaite and K. Plauškaite, *Lith. J. Phys.*, 2011, **51**, 248–259.
14 I. Kroslakova and D. Günther, *J. Anal. At. Spectrom.*, 2007, **22**, 51–62.
15 L. M. Moses and P. B. Farnsworth, *Spectrochim. Acta, Part B*, 2015, **113**, 138–146.
16 M. Guillong, H.-R. Kuhn and D. Günther, *Spectrochim. Acta, Part B*, 2003, **58**, 211–220.
17 M. Dell'Aglio, R. Alrifai and A. De Giacomo, *Spectrochim. Acta, Part B*, 2018, **148**, 105–112.
18 T. Ohta, M. Ito, T. Kotani and T. Hattori, *Appl. Spectrosc.*, 2009, **63**, 555–558.
19 C. Koral, M. Dell'Aglio, R. Gaudiuso, R. Alrifai, M. Torelli and A. De Giacomo, *Talanta*, 2018, **182**, 253–258.
20 A. De Giacomo, R. Gaudiuso, C. Koral, M. Dell'Aglio and O. De Pascale, *Anal. Chem.*, 2013, **85**, 10180–10187.
21 L. Sládková, D. Prochazka, P. Pořízka, P. Škarková, M. Remešová, A. Hrdlička, K. Novotný, L. Čelko and J. Kaiser, *Spectrochim. Acta, Part B*, 2017, **127**, 48–55.
22 M. Holá, Z. Salajková, A. Hrdlička, P. Pořízka, K. Novotný, L. Čelko, P. Šperka, D. Prochazka, J. Novotný, P. Modlitbová, V. Kanický and J. Kaiser, *Anal. Chem.*, 2018, **90**, 11820–11826.
23 A. Magnone, F. Mastrorocco, L. C. Giannossa, R. Comparelli, M. Dell'Aglio and A. De Giacomo, *Spectrochim. Acta, Part B*, 2020, **163**, 105731.
24 I. Horn, M. Guilong and D. Günther, *Appl. Surf. Sci.*, 2001, **182**, 91–102.
25 R. Hergenröder, *J. Anal. At. Spectrom.*, 2006, **21**, 505–516.
26 G. V. Raynor, *Gold Bull.*, 1976, **9**, 12–19.
27 H. Nováková, M. Holá, M. Vojtíšek-Lom, J. Ondráček and V. Kanický, *Spectrochim. Acta, Part B*, 2016, **125**, 52–60.
28 M. Holá, V. Konečná, P. Mikuška, J. Kaiser, K. Páleníková, S. Průša, R. Hanzlíková and V. Kanický, *J. Anal. At. Spectrom.*, 2008, **23**, 1341–1349.